

Automated Mode Recovery and Electronic Stability Control for Wendelstein 7-X Gyrotrons

Zur Erlangung des akademischen Grades eines

**DOKTORS DER INGENIEURWISSENSCHAFTEN
(Dr.-Ing.)**

von der KIT-Fakultät für
Elektrotechnik und Informationstechnik
des Karlsruher Instituts für Technologie (KIT)

genehmigte

DISSERTATION

von

M.Sc. Fabian Wilde

geb. in Gehrden

Tag der mündlichen Prüfung: 22.06.2021

Hauptreferent: Prof. Dr.-Ing. John Jelonnek

Korreferent: Prof. Dr. rer. nat. Robert C. Wolf

Dedicated in affection and gratitude to the people
who went through my darkest times with me

Kurzfassung

Die vorliegende Arbeit dokumentiert die Entwicklung einer schnellen Steuerung und die Ermittlung einer Echtzeit-Signatur für den drohenden Verlust der Arbeitsmode für die Hochleistungs gyrotrons (von Thales Electron Devices) von Wendelstein 7-X, dem weltgrößten Fusionsexperiment vom Typ Stellarator.

Das Hystereseverhalten nach einem Sprung zur Satellitenmode und das Verhalten bei gleichzeitiger Aktivität mehrerer Moden wird in Simulationen und Experimenten für das W7-X Gyrotron untersucht. Basierend auf den gewonnenen Erkenntnissen wurde eine automatische Wiederherstellung der Arbeitsmode (mode recovery, abgekürzt als MORE) auf einem FPGA implementiert und erfolgreich in dafür geplanten Experimenten, sowie während der letzten Experimentkampagne OP1.2b von Wendelstein 7-X getestet. Im Gegensatz zu bereits existierenden, vergleichbaren Lösungen wird dabei zum ersten Mal das Hystereseverhalten des Gyrotrons nach einem Sprung zur konkurrierenden Satellitenmode ausgenutzt und ein kompletter Durchlauf aller Moden beim Startup vermieden. Zur Bewertung des Effekts von MORE auf die Betriebsstabilität wurde eine statistische Analyse durchgeführt, welche die Erste ihrer Art hinsichtlich des Umfangs der analysierten Daten ist. MORE war in 99 % der Fälle in der Lage die Arbeitsmode bei Tests mit zwei Gyrotrons wiederherzustellen. 91 % der Modenverluste bei sieben Gyrotrons konnten während OP1.2b wieder hergestellt werden. Im Vergleich zum Betrieb ohne MORE konnte die zuverlässige Ausgangsleistung pro Gyrotron um bis zu 100 kW bei gleicher mittlerer Fehlerwahrscheinlichkeit gesteigert werden. Die resultierende Leistungssteigerung der W7-X ECRH entspräche einer Kosteneinsparung in Höhe von circa einer Million Euro gemessen an dem Beschaffungspreis eines Gyrotrons. Die automatische Modenwiederherstellung wurde von Fusion For Energy (F4E) zur Verwendung bei ITER vorgeschlagen und soll am Swiss Plasma Center am EPFL für den Prototypen des EU ITER Gyrotrons erprobt werden.

Weiterhin wurden in dieser Arbeit die Streustahlung der Parasitären und Satellitenmoden (der azimuthalen Nachbarmoden) am Relief-Window des Gy-

rotrons untersucht um eine Echtzeit-Signatur für einen bevorstehenden Modenverlust zu identifizieren. Letzterer wird als Feedback in einer elektronischen Stabilitätskontrolle für Gyrotrons benötigt. Die Satellitenmoden wurden als mögliche Kandidaten in Streustrahlungsspektrogrammen und in ersten Untersuchungen entdeckt. Ein exponentielles Wachstum des durchschnittlichen Streustrahlungsniveaus wurde nahe der maximalen Leistung des Gyrotrons beobachtet.

Ein Hochpassfilter und ein quasi-optischer Bandpassfilter wurden für zwei Messanordnungen der Satellitenmodenaktivität realisiert. Beide Messanordnungen dienten der Beobachtung der Satellitenmodenaktivität während stabiler und instabiler Pulse mit Modenverlusten, bei denen MORE aktiv war. Stochastische Muster von simultanem Abfall des Leistungssignals der Arbeitsmode mit Anstieg des Aktivitätssignals der Satellitenmoden wurden als mögliches, temporäres, reversibles multi-moding identifiziert. Das Phänomen wird reproduziert, kurz bevor der Modensprung von der Arbeitsmode zur Nachbarmode durch den langsam abfallenden Kathodenstrom, auf Grund der Emitterabkühlung, erfolgt. Als mögliche Erklärung für die Zeitskala der Muster wurde die Wahrscheinlichkeitsverteilung des Rauschens auf den Versorgungsspannungen identifiziert.

Die Transinformation oder gegenseitige Information (mutual information) wurde für ein gleitendes Zeitfenster zwischen dem Leistungssignal und den gemessenen Streustrahlungssignalen für 170 bzw. 174 Gyrotronpulse bestimmt, um die nicht-lineare Korrelation der Signale zu bestimmen und die Signalverarbeitung in einer späteren, möglichen Implementierung in einer schnellen Gyrotronsteuerung zu simulieren. Das oben genannte Muster zeigt sich dabei in einem (schnellem) Abfall der gegenseitigen Information bis zu 400 ms vor einem bevorstehenden Modenverlust als statistische Häufung. Daher könnte die Transinformation als Vorläufersignatur für den Modenverlust und als Feedback in einer künftigen elektronischen Stabilitätskontrolle für Gyrotrons verwendet werden.

Abstract

This work documents the development of a fast feedback controller and the investigation of a real-time mode loss precursor for the high-power gyrotrons of Wendelstein 7-X, the world's largest fusion experiment of the stellarator type.

The hysteretic behavior after a mode switch to the competing satellite and multi-moding behaviour of the W7-X gyrotron is investigated in simulations and experiments. Based on the findings, an automated recovery of the nominal operating mode (MORE) was implemented on a FPGA and successfully tested in dedicated experiments and during the last experimental campaign OP1.2b of Wendelstein 7-X. In contrast to other already existing solutions, the hysteretic gyrotron behaviour after a switch to the competing satellite mode is exploited for the first time and the whole gyrotron mode startup is avoided. In order to evaluate the effect of MORE in terms of operational reliability, a statistical analysis was performed being the first in terms of the analyzed amount of data. MORE was able to recover the nominal gyrotron mode among two gyrotrons in 99 % of the cases during dedicated experiments. 91 % of the mode losses could be recovered among seven gyrotrons during W7-X OP1.2b. The reliable output power per gyrotron was increased by up to 100 kW with the same mean failure probability when compared to an operation without MORE. The total output power increase of the W7-X ECRH facility translates to possible cost savings of up to one million euros. The automated mode recovery was proposed by F4E to be applied for ITER and an evaluation is planned at the Swiss Plasma Center (SPC) in Lausanne for the prototype of the ITER EU gyrotron.

The stray radiation of parasitic and satellite modes (e.g. the azimuthal neighbour modes) at the gyrotron relief window was examined in order to identify a real-time mode loss precursor. The latter is required as feedback for an electronic stability control for gyrotrons. The satellite modes of the gyrotron working mode were identified as possible candidates in stray radiation spectrograms and in exploratory measurements. An exponential growth of the average stray

radiation level was observed during pulses approaching the practical output power limit of the gyrotrons.

A cutoff high pass filter and a quasi-optical band pass filter were designed and realized for two satellite mode activity measurement setups. Both setup were used to monitor the satellite mode activity during stable and unstable pulses with mode losses were MORE was active. A stochastic pattern of simultaneous dips in the nominal mode power signal and peaks in the satellite mode activity signal was identified as possible temporary reversible multi-moding. The phenomenon is reproduced prior to an imminent mode switch from the nominal working mode to the azimuthal neighbor mode during a slowly decreasing cathode current as a consequence of the emitter cooling effect. As possible explanations for the time scale of the patterns, besides the time constant of the decreasing cathode current, the supply voltage ripple and the probability distribution of the supply voltage noise were identified.

Table of Contents

Kurzfassung	i
Abstract	iii
Abbreviations and Symbols	ix
1 Introduction	1
1.1 Motivation	1
1.2 State of the Art for Gyrotron Controllers	3
1.3 Scope and Structure of this Work	4
1.4 Thermonuclear Fusion	7
1.4.1 The Stellarator Wendelstein 7-X	11
1.4.2 The Wendelstein 7-X ECRH Facility	14
1.5 The Gyrotron: An Electron-Cyclotron Maser	17
1.5.1 Electron Beam Generation and Properties	19
1.5.2 Beam-Wave Interaction in the Cavity	24
1.5.3 Quasi-Optical Mode Conversion	28
1.5.4 Energy Recovery in the Depressed Collector	30
1.5.5 Mode Competition and Stability	31
1.5.6 Parasitic Oscillations	33
1.5.7 Noise and Chaos in Gyrotrons	37
1.5.8 Long-pulse Behaviour	38
1.5.9 The Wendelstein 7-X Gyrotron	40
1.5.10 Simulation Codes	43
1.5.11 Experiment Setup and Data Acquisition	46

2	Hysteretic and Multi-Mode Behaviour	47
2.1	Nominal Mode Voltage Hysteresis	48
2.1.1	Simulations	48
2.1.2	Mode Recovery Experiment	53
2.2	Emitter Cooling Behaviour	55
2.3	Impact of Technical Noise	58
2.3.1	Empirical Noise Distribution	59
2.3.2	Simulations	68
2.4	Summary	70
3	Automated Mode Recovery	71
3.1	Gyrotron Controller	71
3.2	FPGA Implementation	74
3.3	Experimental Results	80
3.3.1	Operation Regimes	80
3.3.2	Improvement of Output Power and Reliability	84
3.3.3	Spectrogram of a Mode Recovery Cycle	86
3.3.4	Performance in dedicated Experiments	86
3.3.5	Performance during Wendelstein 7-X OP1.2b	92
3.4	Summary and Outlook	96
4	Development of Microwave Filters	97
4.1	Filter Design Code - MMWFR	98
4.2	Cutoff High Pass Filter	100
4.2.1	Design	100
4.2.2	Realization	102
4.2.3	Measurement	102
4.3	Quasi-Optical Filter	105
4.3.1	Design	105
4.3.2	Realization	116
4.3.3	Lab Measurement with tuneable RF source	118
4.3.4	In-situ Measurement with Gyrotron	120
4.4	Summary	123
5	Stray Radiation Measurements	125
5.1	Pulse Spectrograms	126

5.1.1	Measurement Setup	127
5.1.2	Post-processing	129
5.1.3	Spectrogram of the Nominal Mode	131
5.1.4	Spectrogram of Mode Switching Behaviour	132
5.2	Explorative Measurements	135
5.2.1	TED #2i Gyrotron with 142 GHz High Pass Filter	135
5.2.2	TED #5i Gyrotron with 142 GHz High Pass Filter	144
5.2.3	TED #5i Gyrotron with 140 GHz Notch Filter	147
5.3	Advanced Measurements	151
5.3.1	Mono-mode Setup	151
5.3.2	Quasi-Optical Setup	160
5.4	Summary	169
6	Moving-Window Activity Data Statistics	171
6.1	Time-Delayed Mutual Information	171
6.2	Moving Mutual Information	177
6.2.1	Mono-mode Setup	177
6.2.2	Quasi-optical Setup	184
6.3	Summary	189
7	Conclusion and Outlook	191
A	Appendix	193
A.1	Data Normalization Methods	193
A.1.1	Min-Max Normalization	193
A.1.2	Z-Score Normalization	194
A.2	Implemented Expressions in MMWFR	195
A.2.1	Circular Waveguide	195
A.2.2	Rectangular Waveguide	196
A.3	Supplementary Figures	198
	Bibliography	203

Abbreviations and Symbols

Abbreviations

ADC	Analog Digital Converter
ANN	Artificial Neural Network
API	Application Programming Interface
ASDEX	Axially Symmetric Divertor EXperiment (fusion experiment in Garching, Germany)
CDF	Cumulative Distribution Function
CNN	Convolutional Neural Network
COVID-19	CoronaVirus Disease 2019
CPI	Communications & Power Industries (USA)
CTS	Collective Thomson Scattering
CVC	Current-Voltage Characteristics
CVD	Chemical Vapor Deposition
CW	Continuous Wave
DBSCAN	Density-Based Spatial Clustering of Applications with Noise
DEMO	DEMONstration Power Plant
ECE	Electron Cyclotron Emission

ECCD	Electron Cyclotron Current Drive
ECDF	Empirical Cumulative Distribution Function
ECM	Electron Cyclotron Maser
ECRH	Electron Cyclotron Resonance Heating
EEG	Electro Encephalo Graphy
EMA	Exponential Moving Average
EOL	End Of Life
FAT	Factory Acceptance Test
FEM	Finite Element Method
FIFO	First In First Out
FNN	False Next Neighbour Method
FPGA	Field-Programmable Gate Array
FSM	Finite State Machine
FVE	Fraction of Variance Explained
GO	Geometrical Optics
GPIO	General Purpose Interface Bus (IEEE 488)
GSM	Generalized Scattering Matrix
HEB	Helical Electron Beam
HVPS	High-Voltage Power Supply
ICRH	Ion Cyclotron Resonance Heating
IGBT	Insulated Gate Bipolar Transistor
IHE	Institut für Hochfrequenztechnik und Elektronik

IHM	Institut für Hochleistungsimpuls- und Mikrowellentechnik
IIR	Infinite Impulse Response
ITER	International Thermonuclear Experimental Reactor
JET	Joint European Torus (Culham, United Kingdom)
JT-60	Japanese Torus (Ibaraki Prefecture, Japan)
KDE	Kernel Density Estimate
KIT	Karlsruhe Institute of Technology
LHD	Large Helical Device (Toki, Japan)
LSTM	Long-Short Term Memory
MMWFR	Multi-Mode Multi-Window Frequency Response
MAST	Mega Ampere Spherical Tokamak (Culham, United Kingdom)
MCA	Maximum Credible Accident
MFP	Mean Failure Probability
MI	Mutual Information
MIG	Magnetron Injection Gun
MISTRAL	Experiment at Wendelstein 7-X to test in-vessel components in an environment with microwave stray radiation
MTTF	Mean Time To Failure
NBI	Neutral Beam Injection
NRMSE	Normalized Root-Mean-Square Error
NTP	Network Time Protocol (computer network protocol)
OLS	Ordinary Least Squares (method to estimate the parameters of a regression model)

OP	Operational Amplifier
PIC	Particle-In-Cell
PDF	Probability Density Function or Probability Distribution Function
PLC	Programmable Logic Controller
PSD	Power Spectral Density
PSM	Pulse Step Modulation
QO	Quasi-Optical
RAMI	Reliability Availability Maintainability Inspectability
RBW	Resolution Band Width
REST	Representational State Transfer (programming paradigm in web application development)
RF	Radio Frequency
RMSE	Root-Mean-Square Error
SAGE	Statistical Analysis of Gyrotron Experiments
SAT	Site Acceptance Test
SDC	Single-stage Depressed Collector
MDC	Multi-stage Depressed Collector
TDMI	Time-Delayed Mutual Information
TE	Transverse Electric
TED	Thales Electron Devices (France)
TEM	Transverse ElectroMagnetic
TM	Transverse Magnetic

TMMI	Total Mean Mutual Information
TTML	Time Till Next Mode Loss
TTFML	Time Till First Mode Loss
VBW	Video Band Width
W7-X	Wendelstein 7-X (Greifswald, Germany)

Constants

A_0	Richardson constant: $\frac{4\pi m_e k_B^2 e}{h^3} = 1.20173 \cdot 10^6 \text{ A} \cdot \text{m}^{-2} \cdot \text{K}^{-2}$
c_0	speed of light in vacuum: $3 \cdot 10^8 \text{ m} \cdot \text{s}^{-1}$
e	elementary charge: $1.602 \cdot 10^{-19} \text{ C}$
ϵ_0	vacuum permittivity: $8.854 \cdot 10^{-12} \text{ F} \cdot \text{m}^{-1}$
μ_0	vacuum magnetic permeability: $4\pi \cdot 10^{-7} \text{ H} \cdot \text{m}^{-1}$
h	Planck constant: $6.626069 \cdot 10^{-34} \text{ J} \cdot \text{s}$
k_B	Boltzmann constant: $1.380649 \cdot 10^{-23} \text{ J} \cdot \text{K}^{-1}$
$m_{e,0}$	electron rest mass: $9.1 \cdot 10^{-31} \text{ kg}$
π	mathematical constant: 3.14159...

Latin Symbols and Variables

Letters

b	beam compression ratio
d_{\min}	minimum embedding dimension

f_{cycl}	cyclotron frequency [Hz]
$f_{\text{ec},n}$	n-th harmonic electron cyclotron frequency [Hz]
f_{c}	cutoff frequency
$f_{\text{c},\text{mp}}$	cutoff frequency for a TE_{mp} or TM_{mp} mode
k	wave number
k_0	free space wave number
k_{c}	cutoff wave number
$k_{\text{c},\text{mp}}$	cutoff wave number for a TE_{mp} or TM_{mp} mode
m_0	(particle) rest mass
n	density [m^{-3}]
r_{b}	electron beam radius [m]
r_{c}	caustic radius (of a mode) [m]
r_{w}	waveguide radius [m]

Capitals

B_0	(initial) magnetic flux density [T]
B_{c}	magnetic flux density at cavity center [T]
B_{e}	magnetic flux density at emitter surface [T]
C	criticality of a working point
E	energy [J] or scalar electric field strength [$\text{V} \cdot \text{m}^{-1}$]
H	entropy [bits]
I_{b}	beam current [A]
I_{cath}	cathode current [A]
I_{body}	body current [A]

J_n	n-th Bessel function of the first kind
J'_n	first derivative of the n-th Bessel function of the first kind
MI	mutual information [bits]
P_{coll}	electrical power recovered by the collector [W]
P_{RF}	generated or output RF power [W]
P_0	total power flow [$J \cdot s^{-1} = W$]
P_b	electron beam power [W]
P_l	power loss per unit length [$dB \cdot m^{-1}$]
P_{out}	RF output power [W]
R_S	surface resistance [$\Omega \cdot m^{-2}$]
T	temperature [K]
T_p	pulse length [s]
U_{acc}	accelerating voltage [V]
U_b	beam voltage [V]
U_{body}	body voltage [V]
U_{cath}	cathode voltage [V]
U_{coll}	collector voltage [V]
ΔU_{dep}	beam voltage depression [V]
U_{dep}	retarding or depression voltage [V]
W	material work function [J]

Greek Symbols and Variables

α	pitch factor
$\alpha_{\text{cmp}}^{(\text{TE})}$	conductive loss attenuation constant for a TE_{mp} mode
$\alpha_{\text{cmp}}^{(\text{TM})}$	conductive loss attenuation constant for a TM_{mp} mode
$\alpha_{\text{dmp}}^{(\text{TE})}$	dielectric loss attenuation constant for a TE_{mp} mode
$\alpha_{\text{dmp}}^{(\text{TM})}$	dielectric loss attenuation constant for a TM_{mp} mode
β	normalized electron velocity
β_{mp}	propagation constant for a TE_{mp} or TM_{mp} mode
γ	relativistic Lorentz factor
ϵ_{r}	relative permittivity
ϵ^*	complex permittivity
λ	wavelength [m^{-1}]
λ_{R}	material-specific correction factor for A_0
$\rho_{\text{mp}}^{(\text{TE})}$	reflection coefficient for a TE_{mp}
$\rho_{\text{mp}}^{(\text{TM})}$	reflection coefficient for a TM_{mp} mode
μ	mean
σ	standard deviation
σ_{c}	conductivity [$\text{S} \cdot \text{m}^{-1}$]
τ_{E}	energy confinement time [s]
τ_{opt}	optimum time delay [s]
ω	angular frequency [$\cdot \text{s}^{-1}$]
χ_{mp}	mode eigenvalue

η	efficiency [%]
η_{coll}	collector efficiency [%]
η_{elec}	electrical efficiency [%]

Operators and mathematical Symbols

\times	vector product
\cdot	(scalar) product
	(arithmetic) mean

General Indices

\perp	perpendicular component of a quantity
\parallel	parallel component of a quantity

1 Introduction

This chapter gives the motivation, an overview of already existing solutions and the scope of this work. The reader then receives a short introduction into the topic of nuclear fusion, the importance of gyrotrons for this field and a presentation of the world's largest fusion experiment of the stellarator type - Wendelstein 7-X (W7-X) - and its Electron-Cyclotron Resonance Heating (ECRH) facility. The improvement of the operational stability and reliable output power of the W7-X gyrotrons is the main subject of examination in the present thesis. It thus continues with the necessary theoretical background about the gyrotron and its components in general, a description of the most important transient phenomena during long-pulse operation and a description of the W7-X gyrotron in particular. This enables the reader to grasp the applied methods and the results presented in the subsequent chapters.

1.1 Motivation

The importance of thermonuclear fusion for mankind's future energy supply is undeniable. All fusion experiments and fusion power plants in the near future will need reliable continuous heating power since the conditions for a self-ignited plasma are not yet feasible. The electron cyclotron resonance heating (ECRH) using high-power microwave oscillators (gyrotrons) has the potential to be the heating method of choice for future fusion devices of power plant scale [TDST19]. The reliable ECRH operation was also crucial for the success of the first experimental campaigns of Wendelstein 7-X [WBD⁺18]. Therefore, any achievable improvement in terms of output power and reliability for the gyrotrons is greatly desired.

The feasible cooling sets an upper limit for the thermal load of the gyrotron cavity. Therefore high-order modes in oversized cavities have to be considered for the design of megawatt gyrotrons as desired by fusion research.

Unfortunately the spectrum of cavity modes becomes more dense and the frequency separation of the modes is worsening with increasing cavity size being necessary to satisfy the demand of growing output power [KBT04]. Consequently the excitation of competing parasitic and satellite modes is more likely, leading to an increased stray radiation level and consequently often to a loss of the nominal operating mode when the output power limit of the tube is approached. The gyrotrons (at W7-X) are therefore operated below their maximum possible output power with a safety margin as trade-off between output power and reliability. In case of a mode loss during a gyrotron pulse, a gyrotron at W7-X is shutdown after 2 to 3 ms without RF (RF grace time period) to avoid any damages and is then no longer available for the current plasma discharge [MWB⁺19, WBD⁺18]. The gyrotron needs to be reset manually by an operator afterwards.

An innovative solution for the existing W7-X gyrotrons to increase their achievable output power while maintaining or even increasing their operational reliability is desired. The challenge is that the solution must not include any technical modifications of the gyrotrons itself, possibly affecting their design, or the high voltage power supplies. Under these circumstances, the only possible solution is a fast feedback gyrotron controller allowing to minimize the probability of mode loss or allowing to avoid any mode loss by taking counter-measures in advance. Also an automated fast recovery of the output power during the pulse would be beneficial since the current plasma discharge would remain unaffected and no human intervention would be necessary. Fast in this context means that the time necessary to recover the heating power should be (much) smaller than the energy confinement time τ_E of the fusion experiment. In case of W7-X, τ_E is in the order of 100 to 200 ms depending on the injected heating power [WAA⁺17]. W7-X achieved a record of $\tau_E = 220$ ms [WA19]. Such a gyrotron controller would significantly enhance the ECRH capabilities of W7-X, also addressing the needs of other and future ECRH facilities of fusion experiments, like ITER.

1.2 State of the Art for Gyrotron Controllers

The already existing gyrotron controllers can be distinguished by their control parameters and the controlled quantities. Among those, the gyrotron frequency and output power are the most prominent. Various approaches for frequency stabilization were applied on low-power gyrotrons for DNP-NMR spectroscopy [IKUK14, KIK⁺15, FGG⁺18] and also on high-power gyrotrons for fusion applications [KMT⁺06, OIT⁺12]. In order to achieve the frequency [Gei91] or output power stabilization, injection locking, a Phase-Locked Loop (PLL) [GKL⁺06, DFG⁺17, FGG⁺18] and a PID feedback control of the acceleration voltage [KIK⁺15] and/or heater current [IKUK14] were the most popular methods.

Only very few solutions exist for the general stability control or post-failure handling of (multiple) high-power gyrotrons, hence a fast automated recovery of the normal gyrotron operation after a failure. Of course the demand for and the realization of such solutions is limited to large-scale fusion facilities, thus limiting the number of publications in this field.

At the DIII-D facility [PBC⁺18, PLT⁺11] exists a fast FPGA-based controller which restarts a gyrotron when it ceases RF operation, interrupts an imminent body current fault or pauses the gyrotron operation when a critical plasma density is exceeded. In case a gyrotron ceases RF operation, it is restarted within 10 to 30 ms by a temporary shutdown, reducing the body and the cathode voltage to zero [PBC⁺18]. At ASDEX Upgrade, a gyrotron is shutdown and restarted within 100 ms after a failure which could be arcing or the loss of the nominal gyrotron mode. In this case another idle gyrotron attempts to take over immediately the operation [WSL⁺16].

These solutions have in common that the gyrotron is completely shutdown before its normal operation state is restored and that no precursor for the loss of the nominal operating mode is implemented. Although the time required for the recovery of the normal gyrotron operation is still smaller than the energy confinement time of the experiment, the required time should be as short as possible. At the stellarator Wendelstein 7-X, no active post-failure handling solution exist so far, meaning that a gyrotron is no longer available for the running plasma discharge in case of a failure (e.g. arcing, overcurrent, body current fault etc.) during a pulse. The gyrotron needed then to be reset manually by an operator after the end of the discharge.

A fast oscillation recovery for gyrotrons is of even greater importance for the

future operation of the ITER tokamak or future fusion power plants where a sudden drop in microwave heating power could lead to a premature end of the plasma discharge, hence a disruption in a tokamak [TDST19]. Due to the enormous thermal and electromagnetic (hence mechanical) loads acting on the vessel and the magnetic coil structures [LAA⁺15, SPB10, Sch95], ITER is only designed to withstand a limited number of disruptions. Therefore, solutions to predict, mitigate and avoid disruptions are currently under investigation [SBB⁺19, PdVH⁺18]. In this context, a fast oscillation recovery for gyrotrons would be desired to reduce the probability of such disruptions and it could be crucial to ensure the reliability of future fusion power plants [TDST19].

1.3 Scope and Structure of this Work

The present work documents the development of a fast innovative controller for gyrotrons to increase the achievable pulse duration and the maximum reliable output power. In case of W7-X, it helps to increase the reliable heating power and the achievable pulse duration available for experiments allowing for higher plasma densities and discharge durations.

In order to achieve this goal, a combination of fast control algorithms acting on the acceleration voltage is proposed and partly integrated in a FPGA-based controller. The first innovation is an algorithm for a fast automated recovery of the nominal gyrotron working mode after a switch to the competing satellite. The hysteretic gyrotron behaviour is exploited instead of simply switching the gyrotron off and on again after a while, unlike other already existing solutions. This way a full gyrotron mode startup is avoided which could potentially have a side effect on W7-X diagnostic systems operating in a similar frequency range (e.g. ECE, CTS). This allows a very fast recovery of the output power within ≤ 1 ms, much smaller than the energy confinement time τ_E of the Wendelstein 7-X device which is in the order of up to 400 ms. It reacts in case of a loss of the nominal working mode using a calibrated RF detector diode signal. This is thought of to be the backup solution in case the second algorithm fails.

The second algorithm is proposed as a possible approach for a fast feedback control, an electronic stability control, using a real-time measurement of the satellite mode stray radiation as feedback and precursor for mode loss. It would allow to stabilize the gyrotron operation at a given working point close where a mode switch from the nominal working mode to its azimuthal neigh-

bour mode is more likely. The gyrotron could be operated with even smaller safety margins and hence at a higher output power level. Using a real-time modelless precursor signal, the controller would be able to detect temporary multi-moding behaviour prior to a mode loss and could reduce the accelerating voltage in advance in order to avoid it. To the best of the author's knowledge, this is attempted for the first time, in particular applied on high-power gyrotrons for fusion. The development of custom microwave components for two stray radiation measurement setups is as well documented. The stray radiation measurements are the basis for a real-time measurement of a modelless precursor. This work is organized in four major parts: The first introductory part gives the motivation for this work and the state of the art for gyrotron controllers. Afterwards the novelties and the scope of this work are described. The chapter is complemented by an introduction into nuclear fusion, the fusion experiment Wendelstein 7-X and its ECRH facility. Finally an overview for gyrotrons is given including its working principle and key components to enable the reader to grasp the following investigations and methods.

The second part investigates hysteretic and multi-moding behaviour in simulations and experiments to evaluate the feasibility of a controller as described above. The hysteretic behaviour after a switch to the competing satellite mode is examined in simulations. An experiment to demonstrate the hysteretic behaviour due to mode competition and repeated mode switching with subsequent recovery of the nominal mode was performed. This is done in order to evaluate the feasibility of an automated recovery of the nominal gyrotron working mode. The emitter cooling behaviour is simulated, since this is the most common scenario and reason for mode loss observed for long gyrotron pulses during experiments at Wendelstein 7-X. Multi-mode simulations are performed taking into account technical noise on the acceleration voltage. This is done to investigate the effect on mode competition and stability and to support the existence of a precursor for mode loss. Spectrograms are acquired for the stray radiation at the gyrotron relief window during mode switching experiments. The measurement setup using a spectrum analyzer as well as the software for data-aquisition and post-processing are presented. The spectrogram measurement setup is validated with spectrograms of the nominal working mode by comparison to already existing spectrograms in [Sch15] acquired with the pulse spectrum analysis (PSA) system presented in [SGJT13b]. In order to provide a real-time precursor measurement, two measurement setups were developed for which custom microwave components were designed, built and tested. The design, construction and measurement of a waveguide high-pass

filter and a quasi-optical dielectric disc filter as satellite mode band pass are presented in detail. The performance of the proposed mode loss precursor using the two measurement setups is evaluated.

The third part continues with the proposed solutions: an automated mode recovery and a proposed electronic stability control for gyrotrons. The mode recovery (MORE) algorithm, its implementation and experimental results during dedicated experiments and the last experimental campaign W7-X OP1.2b are shown. In order to automate the statistical analysis of a large number of gyrotron pulses, a framework named SAGE (*Statistical Analysis of Gyrotron Experiments*) developed in the programming language Python is presented as well. This software is used to create a searchable database of all performed gyrotron experiments. Based upon this database the performance of MORE is evaluated. Finally two possible approaches for an electronic stability control using a real-time modelless precursor are described and their performance is simulated in software. One of the approaches makes use of a phase space reconstruction with Takens theorem (1981) [Tak81, Sha06] and a special type of neural network based on the Koch-Poggio-Torre model [KPT83]. The phase space reconstruction technique known from the analysis of chaotic time series is powerful to reconstruct the high-dimensional state space of a complex system without the need to know its governing differential equations [PCFS80, KBA92, YEW14]. The special neural network, an approximate logic dendrite morphological neuron model [JGC⁺16], has a straightforward hardware implementation and can be easily implemented in a FPGA. The other approach uses a Savitzky-Golay filter for signal preprocessing and a simple control algorithm.

1.4 Thermonuclear Fusion

The world population is growing and projections indicate that a stabilization in population numbers is not expected before the end of this century [GRS⁺14, Coh03]. This translates to a fast growing demand for energy whereof the vast majority has been and is still nowadays covered by burning of fossile fuels [KLT12]. Due to enormously increasing CO₂-emissions since the beginning of the industrialization at the end of the 19th century, evidence for anthropogenic climate change and global warming is emerging since the seventies of the 20th century [MS64, KBB⁺76]. More recent studies conclude that a global warming of around 1.0°C was already caused compared to pre-industrial levels. A global warming of 1.5 °C is predicted with high confidence for the period of 2030 to 2052 if CO₂-emissions will remain with the current rate [MDZP⁺18, ZRZ16, MBH98].

Therefore mankind has to cover this demand with preferably CO₂-neutral technologies. Unfortunately the renewable energy sources like photovoltaics, wind and water power are inherently not suitable to cover the base load under all weather conditions at any location on earth. Nuclear fission as quasi CO₂-neutral alternative on the other hand faces only low acceptance by the public due to multiple reasons: Firstly, the risk and severe consequences of radioactive contamination in case of a maximum credible accident (MCA) like in Chernobyl (1986) or Fukushima (2011). Secondly, the problematic disposal, treatment and unsolved final-storage problem for the highly radioactive waste produced by operating nuclear fission power plants. But since Bethe's discovery in 1938 [Bet39] that the stars harness their energy from the process of thermonuclear fusion, science attempts to mimick a similar process on earth to generate electrical power in the long-term future. Since the nuclear binding energy increases with increasing proton number upto the element Fe [CG01], fusion of lighter nuclei releases the energy difference equivalent to the mass defect, the difference of the rest masses, as described by Einstein's mass-energy-equivalence [Ein35]. From an economical point of view, fusion of hydrogen, the lightest nuclei, has the highest fusion energy gain, as investigated in 1956 by Lawson [Law57]. An important quantity in this context is the fusion triple product $n \cdot T \cdot \tau_E$ proposed by Lawson with n being the density, T the temperature and τ_E the energy confinement time. The fusion triple product is a key quantity to measure the performance of fusion devices as well as to describe the conditions required for a specific fusion reaction. Among the pos-

sible hydrogen fusion reactions, the D-T reaction, the fusion of the hydrogen isotopes deuterium ${}^2_1\text{D}$ and tritium ${}^3_1\text{T}$ to helium ${}^4_2\text{He}$, is considered to be the most promising one [KLT12, Che15]. The required resources for this reaction are abundant: Deuterium can be extracted from sea water and tritium can be bred from lithium which is the second most abundant element on earth. Moreover the end product helium is a harmless inert gas in contrast to the highly radioactive, hazardous waste consisting of depleted fuel rods produced by nuclear fission power plants.

In order to achieve nuclear fusion, the repelling Coulomb barrier has to be overcome with sufficient collective kinetic energy of the nuclei. At very small distances in the order of 10^{-15} m, the strong attractive nuclear force then dominates, allowing for nuclear fusion. The maximum reaction rate for the D-T reaction can be achieved at temperatures in the order 100 Million K, which is equivalent to 10 keV. This is a unit typically used in plasma or particle physics, since hydrogen (the reactant gas) is fully ionized at such temperatures and is called plasma. Degrading effects are drift and diffusion need to be minimized by a proper confinement, since the plasma needs to retain its density and temperature long enough to allow thermonuclear fusion to happen. Among the experimental concepts towards the realization of fusion power, the magnetic confinement devices are the most popular [Che15]. A magnetic confinement device is a circular, closed setup of magnetic field coils. The idea is to achieve a confinement of the charged particle species (ions and electrons) in the plasma by a toroidally closed magnetic field via the Lorentz force.

Within the class of magnetic confinement devices, there exist two main concepts which are currently pursued in large-scale experiments: the tokamak [SBG⁺01] and the stellarator [Spi58] both developed in the 50s of the last century. Nowadays large-scale tokamak experiments to name are JET¹ [RBK85, SdP06] and MAST² [MAD⁺15] in the UK, ASDEX³ Upgrade [HG03] in Germany, JT-60 [NAH⁺90, KIKN05] in Japan and ITER [Big18, Mot15] in France which is still under construction. ITER⁴ will be the world's largest tokamak and a large-scale international research project with 35 participating countries, representing two third of the world population, with a first plasma expected for 2025 [ite19, Hol07, Big18]. The large helical device (LHD) [KYI⁺10] in

¹ Joint European Torus

² Mega Amp Spherical Tokamak

³ Axially Symmetric Divertor EXperiment

⁴ latin: the way, previously: acronym for International Thermonuclear Experimental Reactor

Japan and Wendelstein 7-X⁵ [GM93, BWA⁺13, KAB⁺16] in Germany are the largest stellarators currently in operation.

A tokamak and a stellarator both consist of a toroidal plasma vessel and a magnetic coil system allowing the plasma confinement. The key difference between both is that for the stellarator no current needs to be induced in the plasma in order to create the poloidal field component which is crucial for the confinement. In a stellarator both magnetic components (toroidal and poloidal) are created externally by its magnetic coil system. The stellarator is therefore intrinsically capable of steady-state operation in contrast to the pulsed operation of the tokamak. The drawback of the stellarator was a worse particle confinement compared to the tokamak in the past. But with the generation of optimized stellarators, like Wendelstein 7-X, competitive confinement properties can be achieved and the stellarator is considered again as possible candidate with regard to a future fusion power plant.

In order to achieve the required temperatures, one or more of the following methods are used in fusion experiments: Ohmic Heating (OH) [PW05, GR95], Neutral Beam Injection (NBI) [HTA08, SBC⁺16] and Radio-Frequency (RF) plasma heating [HAB⁺07, EBB⁺07, REGK98, MKL⁺14].

The method of ohmic heating works with an induced current in the plasma which is heated due to its electrical resistance, similar to a kettle, where a current flows through a resistor which then heats up. This method has the disadvantage that it is only suitable for the initial heating since the method becomes increasingly ineffective with increasing plasma temperature or respectively decreasing plasma resistance [GR95, Che15, PW05, Spi06].

Plasma heating with neutral beam injection requires the generation of a high-energy beam of neutral hydrogen (H^0) or deuterium (D^0) atoms by ionization of the neutral gas to typically their negative ion counterparts and the subsequent acceleration and neutralization. Typically a neutral D^0 beam with an energy in the order of several tens of keV (which translates to an injected power in the MW range) is injected into the plasma [HFH⁺96, TNN⁺00]. Since the neutral high energy atoms are not influenced by the magnetic field, power can be deposited deeper in the plasma core where the atoms transfer their energy by electrostatic collisions after ionization, simultaneously fueling the plasma. The disadvantages of NBI are the size, costs and complexity of the required

⁵ The stellarator Wendelstein 7-X to which this work is closely related, is presented in the following section.

machinery reducing the availability for experiments and the low efficiency towards high beam energies.

Higher efficiency can be achieved with RF plasma heating based on the resonant absorption of RF power near the cyclotron frequency or one of its n -th harmonics of charged particles in a magnetic field. Depending on the particle species in the plasma, electrons or ions, electron cyclotron resonance heating (ECRH) [WBD⁺18, EBB⁺07] and ion cyclotron resonance heating (ICRH) [OMVE⁺14, MKL⁺14] are distinguished.

In case of ECRH, the frequency of the injected RF power has to be equal to a multiple (or n -th harmonic) of the electron cyclotron frequency f_{cycl} in a magnetic field B given by (e.g. [KBT04, Che15])

$$f_{\text{cycl},n} = \frac{n \cdot q \cdot B}{2\pi \cdot m_{e,0} \cdot \gamma} \text{ with } n = 1, 2, 3, \dots \quad (1.1)$$

with $m_{e,0}$ and e being the electron rest mass and charge and γ being the relativistic Lorentz factor which is approximately 1 for a typical plasma temperature. In case of Wendelstein 7-X with $B_0 \approx 2.5 \text{ T}$ on the central plasma axis inside the vessel the non-relativistic electron cyclotron frequency accounts to

$$f_{\text{ec},n} = \frac{n \cdot e \cdot B_0}{2\pi \cdot m_e} \approx n \cdot 70 \text{ GHz with } n = 1, 2, 3, \dots \quad (1.2)$$

where $m_e \approx 9.1 \cdot 10^{-31} \text{ kg}$ is the electron rest mass and $e \approx 1.602 \cdot 10^{-19} \text{ C}$ is the elementary charge. The circular arrangement of the main magnetic field coils creates a magnetic field decreasing from the inner side to the outer side of the torus. This allows to centrally heat the plasma. The RF power with a discrete frequency is injected from the outer side of the torus (low magnetic field side), so that the resonance condition is only fulfilled in the plasma center and the RF power is transferred to thermal electrons. Depending on the polarization, O-mode (ordinary) and X-mode (extraordinary) heating are distinguished. Often the 2nd harmonic electron cyclotron frequency is used for X2-mode heating for the startup, followed by O2-mode heating, in order to achieve higher densities [Che15, GR95]. This can be illustrated in a Clemmow–Mullaly–Allis (CMA) diagram for the electromagnetic wave propagation in a cold plasma as shown in [KLT12].

The so called Q-factor, the ratio $P_{\text{output}}/P_{\text{input}}$ between the input heating power and the expected output power, is nowadays still well below 1 for fusion exper-

iments. The thermal energy released by the fusion reaction is insufficient to sustain itself and continuous reliable heating power is required. The opposite would be an ignited, self-sustaining plasma with $Q \rightarrow \infty$. A Q-factor of 10 is planned for ITER with a target output power of 500 MW achieved with 50 MW of heating power whereof 24 MW are provided by ECRH [OHA⁺11]. Therefore a reliable microwave source with an output frequency in the range of 100 to above 200 GHz (e.g. 170 GHz / 204 GHz planned for DEMO, 280 GHz planned for Tokamak Energy) and an output power in the order of megawatts is crucial for the success of fusion experiments and future fusion power plants. The only suitable source which fulfills the mentioned requirements is the gyrotron [Thu11, Thu14]. Since all fusion experiments, in particular Wendelstein 7-X [BWA⁺13], aim towards steady-state operation, the gyrotrons need to be suitable for continuous wave (CW) operation. The working principle and components of a gyrotron and the stellarator Wendelstein 7-X and its ECRH facility are presented the following sections.

1.4.1 The Stellarator Wendelstein 7-X

The optimized stellarator Wendelstein 7-X (W7-X) located in Greifswald, Germany, is currently the world's biggest stellarator in operation with a major radius of 5.5 m and a plasma volume of 30 m² (see Figure 1.1). The stellarator has a five-fold symmetry allowing a modular construction consisting of five modules. The main goal of W7-X is to demonstrate a quasi steady-state operation (1800 s) with hydrogen and deuterium plasmas having properties relevant for a future fusion power plant and in particular to demonstrate confinement properties, plasma densities and triple products which are competitive with tokamaks. Parts of this goal have been already achieved in setting several new records for stellarator devices [KAB⁺19, BWA⁺13].

The name stellarator originates from a mountain in the state of Bavaria, Germany, having a shape comparable to the nested magnetic surfaces and helical field line geometry. The magnetic field geometry has been optimized with regard to seven criteria, among those are fast-particle confinement, neo-classical transport, plasma stability issues and engineering feasibility of the non-planar coils [GLM⁺92]. The magnetic confinement is achieved with a system of 50 modular non-planar and 20 planar superconducting NbTi coils operating at a temperature of 3.4 K [KAB⁺16, KAB⁺19]. The optimization

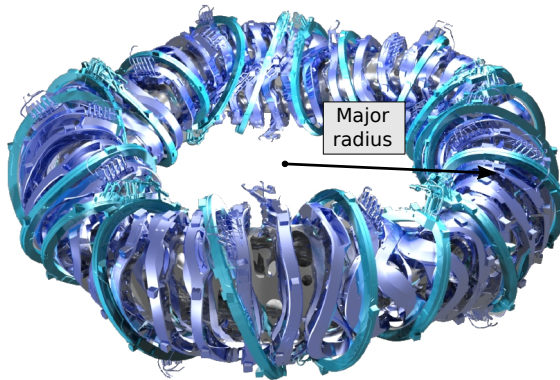


Figure 1.1: Rendered image of the Wendelstein 7-X device showing its magnetic coil system: Non-planar modular coils (dark blue) and planar coils (cyan) threaded on the inner plasma vessel with a major radius of 5.5 m - modified version based on [KAB⁺16].

is reflected by the complex three-dimensional shape of the coils which were an engineering challenge on their own due to very high manufacturing precision demands [BWA⁺13]. The manufacturing precision is of great importance since even small errors of the magnetic field can lead to big perturbations of the confinement quality. Measurements of the magnetic field topology showed that the fields produced by the magnetic coil system meet the expectations with astonishing precision [POL⁺16]. An overview of the inner structure of the Wendelstein 7-X device is given in Figure 1.2. The first ideas for W7-X date back to 1986 by Nührenberg [NZ86] and 1992 by Grieger [GLM⁺92], but it took till 2015, when finally, after a 15 year construction and one year commissioning period, the first plasma has been created. The first helium plasma with a duration of 0.1 s has been created on 10th December 2015 and the first hydrogen plasma with a duration of 0.25 s on 3rd February 2016 during an inauguration ceremony in presence of the German Chancellor Dr. Merkel [KAB⁺16, DeV16, IPP16]. During the last operation phase OP1.2b a pulse length of up to 100 s has been achieved with reduced heating energy keeping in mind the limits of the uncooled in-vessel components [KAB⁺19]. For the next operation phase OP2, expected to begin in 2022 (delayed due to the COVID-19 pandemic), all the in-vessel components will be equipped with water cooling allowing to extend further the pulse length (up to 1800 s) and

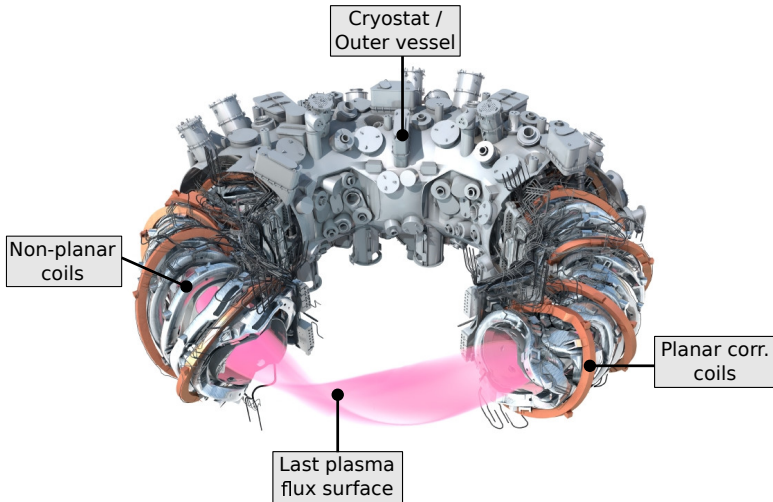


Figure 1.2: Rendered image of the Wendelstein 7-X device showing its inner structures: The last plasma flux surface is shown in magenta, surrounded by the complex shaped inner plasma vessel. The non-planar (steel colored) and planar correction (copper colored) coils are threaded along the inner plasma vessel. The superconducting coils are bolted to the central support structure and operated at 3.4 K, cooled with liquid helium, in the cryostat volume between the inner plasma vessel and the outer vessel. The diagnostic ports are clearly visible from the outside - modified version based on [KAB⁺16].

heating energy (up to 18 GJ). Wendelstein 7-X will use three different heating methods till OP2: ECRH, NBI and ICRH. NBI started its operation with one of two boxes during OP1.2b with up to 3.5 MW of injected power limited to a possible pulse length of up to 10 s [MBB⁺13]. ICRH is planned for next operation phase OP2 with an initial heating power of 1.5 MW. ECRH was and will be the dominant heating method which provided up to 4.3 MW with six gyrotrons during the first operation phase OP1.1 and 7.5 MW of injected power in the plasma vessel provided by ten gyrotrons during the last operation phase OP1.2b. An upgrade up to 15 MW ECRH power is planned for OP2. ECRH is so far the only heating method capable of providing heating power for 30 min. This is the maximum duration of an experiment for which W7-X and its cooling systems was designed. Therefore it is expected to be the favoured heating method for future fusion power plants [WBDa16, KAB⁺19, Thu11].

1.4.2 The Wendelstein 7-X ECRH Facility

The Wendelstein 7-X ECRH facility is the world's biggest of its kind with maximum output power of up to 8.5 MW provided by ten 140 GHz gyrotrons being capable of continuous operation for up to 30 min [SLB⁺17, WBD⁺18]. The ten gyrotrons have an output power in the range of 600 kW to 1 MW [LBB⁺18], depending on the target pulse length and individual tube condition. Other comparable facilities like ASDEX Upgrade, DIII-D or LHD deliver less power with shorter pulse lengths, see for example [TDST19, WSL⁺16, CCE⁺17, KYI⁺10, TSK⁺10]. One of its unique features are the two identical quasi-optical multi-beam transmission lines operating in air (see figure 1.3). The gyrotrons are installed in two rows of five, symmetrical to an underground beam duct, connecting the ECRH hall with the torus. The RF power is transported over a distance of typ. 60 m towards their vacuum windows and finally the four front steering launchers directing the power in the plasma vessel. Figure 1.3 shows a simplified rendered image of one half of the gyrotron arrangement and one transmission line [EBB⁺07, SLB⁺17]. Each transmission line handles the individual RF beams generated by five gyrotrons plus a reserve of two for remote steering launcher experiments and an additional future gyrotron.

The remote steering launcher without movable plasma facing components is an important concept for a future fusion reactor [LBB⁺18, WBD⁺18]. The overall power loss of the transmission line is about 6 % leading to an injected power of up to 7.5 MW used in OP 1.2. A power loss of the transmission line per meter is hard to estimate since it is composed by the losses from absorption on the surfaces of the metallic mirrors and the atmospheric attenuation depending on the humidity of the air in the beam duct. The auxiliary systems like high-voltage power supplies, water cooling and liquid nitrogen storage are not shown and located in separate building parts. The ECRH launchers are located in neighboring modules 1 and 5 of the W7-X torus as illustrated in Figure 1.4. The gyrotrons are organized into 12 independent modules named after the NATO alphabet followed by the number of the W7-X module section, they belong to: Alpha 1, Alpha 5, Bravo 1, ... etc. Nine gyrotrons were built in Europe by Thales Electron Devices (TED) and one was built in the USA by Communications & Power Industries Inc (CPI). Commissioning and maintenance can be done independently from each other, so that the operation of the other gyrotrons is not affected. Two additional gyrotrons can be installed in the future. An overview of the available gyrotrons in operation

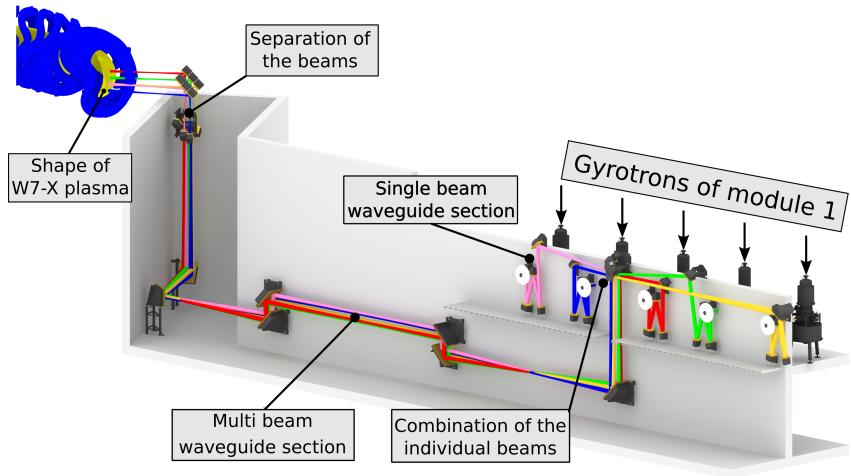


Figure 1.3: Rendered image showing one of the two identical quasi-optical transmission lines to transport the RF power from five gyrotrons to the W7-X vessel - modified version based on [SLB⁺17].

and their individual continuous and maximum output powers is given in Table 1.1 [WHL⁺17, BSL⁺17].

The gyrotrons built by TED and the transmission line were developed at the Institute for Pulsed Power and Microwave Technology (IHM) part of the Karlsruhe Institute of Technology (KIT, formerly FZK: ForschungsZentrum Karlsruhe) within the PMW-project ("Projekt Mikrowellenheizung für W7-X") in collaboration with the Institute of Interfacial Process Engineering and Plasma Technology (IGVP) at the university of Stuttgart.

The transmission line was planned with a safety margin (factor 2 to 3) regarding its power handling capability, so that already existing gyrotrons could be replaced with more powerful gyrotrons (> 1 MW). An upgrade of one gyrotron by a 1.5 MW gyrotron based on a slightly modified old design of the series tube is planned [ARM⁺19]. The transmission line even already satisfies the ITER requirement (24 MW) without modifications, if safety margins are reduced [EBB⁺07].

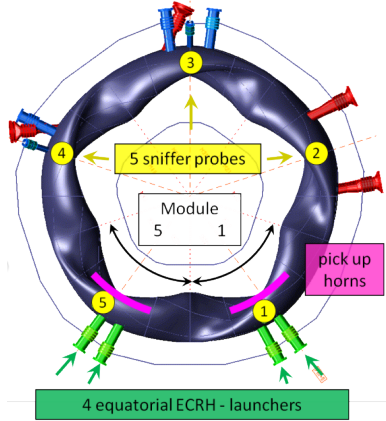


Figure 1.4: Rendered image showing a top view of the Wendelstein 7-X vessel with its 5 modules [MWC⁺17].

Module	Gyrotron	P_{heat} [MW]	P_{out} [MW]	τ_P [s]
Alpha 1	TED #7	0.85	>0.9	1800
Alpha 5	TED #5i	0.85	>0.9	1800
Bravo 1	TED Maquette	0.5 ¹	0.55	10 ¹
Bravo 5	TED #2i	0.85	>0.9	1800
Charly 1	TED #1	0.65 ²	0.65 ²	1800
Charly 5	TED #4	0.93	1.02	1200
Delta 1	TED #6	0.9	0.95	1800
Delta 5	TED #3	0.65	0.7	1800
Echo 1	TED #8	0.85	>0.9	1800
Echo 5	CPI	0.75	0.82	1800

Table 1.1: Overview of available gyrotrons in the Wendelstein 7-X ECRH facility with their individual continuous (long-pulse) output power available in the plasma P_{heat} and at the gyrotron P_{out} in 2019 [MWB⁺19]. The installation of an additional 11th 1.5 MW conventional cavity gyrotron is planned.

¹ outgassing problem due to aging

² unusual big frequency shift of ≥ 500 MHz during the pulse indicates a cavity cooling problem

1.5 The Gyrotron: An Electron-Cyclotron Maser

A gyrotron is a vacuum electron device able to generate microwave power in the frequency range from GHz to THz with a power range from kilowatts to megawatts. The working principle of the gyrotron is the electron cyclotron maser instability (ECMI) in a longitudinal magnetic field [FGPY77, TDST19, KBT04, Nus04]. This is also the origin of its name: weakly relativistic electrons are gyrating perpendicular to an external magnetic field while following the field lines, forming a helical electron beam (HEB). Coherent stimulated emission of bremsstrahlung is achieved by electron phase bunching due to the relativistic mass dependence changing the electron cyclotron frequency. Figure 1.5 shows an illustration of a high-power gyrotron and its components. First, a filament heats up a metal ring, a surface, where electrons are thermionically emitted. The emitter is the key component of a magnetron injection gun (MIG) generating the electron beam. Usually, so called dispenser emitters made of porous tungsten impregnated with metal oxides (having a low work function) are used [Thu15, TDST19, Thu20]. The MIG determines the properties of the electron beam and its quality has a big impact on the gyrotron operation characteristics. The electrons are then accelerated in a strong electric field between the cathode (emitter) and the anode of the electron gun. The normal conducting gun coils are used to adjust electron beam parameters.

Before entering the cavity, the electron beam passes the so-called beam tunnel. The increasing, strong magnetic field (up to 7 T) in this region produced by a superconducting coil (main coil) then compresses the HEB adiabatically to increase the transverse kinetic energy (since only that portion of the electron kinetic energy is transferred to the cavity mode) of the electrons and to adjust the electron beam radius. The beam tunnel contains a structure of stacked rings of alternating isolating and conducting material or wall corrugations. The purpose of this structure is to suppress the possible excitation of parasitic modes by the electron beam in the region of increasing pitch factor before the cavity [PAH⁺98]. The strong magnetic field (up to 7 T) produced by a superconducting coil (main coil) then compresses the HEB adiabatically to increase the transverse kinetic energy (since only that portion of the electron kinetic energy is transferred to the cavity mode) of the electrons and to adjust the electron beam radius.

Since the cavity is a circular waveguide imposing boundary conditions on the Maxwell's equations, only certain solutions exist, called modes. The HEB then

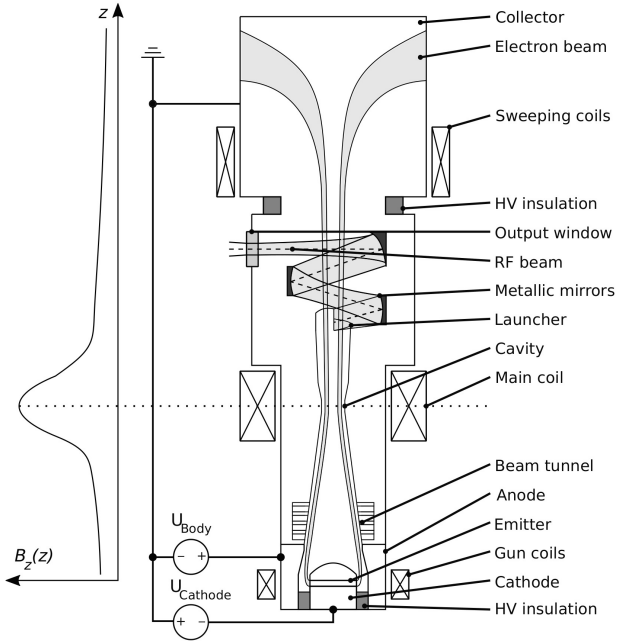


Figure 1.5: Illustration of a high-power gyrotron, its components and supply voltages (adapted from [Zha16, Sch15]).

transfers energy to the electromagnetic field of a TE-mode in the cavity when the cyclotron resonance condition is met. The cavity is located at the position of maximum magnetic flux density in the center of the coil. High-power gyrotrons use oversized cavities which exhibit a dense spectrum of modes which can be excited beside the desired mode.

After the interaction in the cavity, the wave propagates towards the quasi-optical mode converter. The high-order TE-mode which can only exist in the waveguide is converted to a quasi-Gaussian beam (TEM_{00}) with high efficiency [TYA⁺05] which can propagate freely in free space. This beam is then guided by an arrangement of metallic mirrors outside the gyrotron through the output window. The output window is made of a material with high thermal conductivity and low absorption in the microwave range, for high-power gy-

rotrons, it is often chemical-vapor deposition (CVD) diamond.

The "spent" electron beam then defocusses and hits the inner collector surface. Since the electrons still possess a significant kinetic energy, the electron beam should be moved along the whole inner collector surface to distribute the heat load and avoid thermal damage. For most high-power gyrotrons, this is achieved by the collector sweeping coils, see e.g [DIP⁺05, SID⁺07]. In order to increase the electrical efficiency of the gyrotron, the collector is depressed, hence the collector potential is lowered with respect to the anode. The remaining kinetic energy of the electrons after the interaction in the cavity is converted to electrical energy, hence recovered.

The gyrotron working principle, its key components and long-pulse effects are described in more detail in the following sections.

1.5.1 Electron Beam Generation and Properties

The component in a gyrotron generating the electron beam is the Magnetron Injection Gun (MIG) [Edg93, Tsi07]. The MIG itself consists of a ring-shaped emitter heated by a filament (emitter, cathode) and one (diode-type MIG) or two separated (triode-type MIG) anodes at different potentials. The emitter is preferably made of a material with a low work function. A MIG is typically operated in the temperature-limited regime where the Richardson-Dushman equation with Schottky effect correction holds for the current density of the emitter surface [Cro65]

$$J_S = A_G T^2 e^{\frac{W - \Delta W}{k_B T}} \quad (1.3)$$

$$\Delta W = \sqrt{\frac{e^3 E}{4\pi\epsilon_0}} \quad (1.4)$$

$$A_G = A_0 \lambda_R \quad (1.5)$$

$$A_0 = \frac{4\pi m_e k_B^2 e}{h^3} \quad (1.6)$$

where T is the absolute emitter temperature, W the work function of the emitter material and E is the electric field strength at the emitter surface. h denotes the Planck's constant and k_B the Boltzmann constant. λ_R is a material specific factor and A_0 is the Richardson constant. ΔW is taking into account the

Schottky effect being the influence of an electric field on the emitter surface. In particular for electron guns, the cathode is biased to a negative potential, lowering the material work function, hence supporting the electron emission. Typically the emitter filament is white glowing, therefore the typical working temperature is around 800 to 1000°C. According to equation 1.3, the current density and thus the beam current are controlled by the cathode voltage and the emitter temperature controlled via the heating filament current.

Due to the thermal inertia of the gun, the beam current reacts faster to changes of the cathode voltage (Schottky effect) than to changes of the filament heating current. This circumstance leads to the phenomenon of emitter cooling causing a drop in the beam current potentially limiting the stable mono-mode operation of the gyrotron for long pulses. The issue of emitter cooling and its relevance for long pulse operation of gyrotrons will be discussed in a following section. Since typical accelerating voltages for high-power gyrotrons are 75 to 90 kV, the electrons are accelerated to slightly relativistic velocities, as shown by [KBT04]

$$E_{\text{kin}} = U_{\text{be}} = E_0(\gamma - 1) = m_e c_0^2(\gamma - 1) \quad (1.7)$$

$$\Delta U_{\text{dep}} = U_{\text{acc}} - U_{\text{b}} \quad (1.8)$$

where $U_{\text{acc}} = U_{\text{cath}} - U_{\text{body}}$ is the accelerating voltage with typically $U_{\text{cath}} < 0$ and $U_{\text{body}} \geq 0$. Figure 1.6 shows the MIG, the magnetic field coils and the inner waveguide structure with beam tunnel, down-taper, cavity and up-taper. The gun cathode is on negative potential $U_{\text{cath}} < 0$ where as the gun anode and the beam tunnel are on positive potential $U_{\text{body}} > 0$ which sum up to the applied technical acceleration voltage U_{acc} . In practice the absolute value for the accelerating voltage is mentioned only. In the gyrotron the negative charge of the HEB itself (beam space charge) and the external potential of its body have a shielding effect. So the applied technical voltage U_{acc} is reduced by the beam voltage depression ΔU_{dep} , leading to an effective beam voltage U_{b} . This effect is called voltage depression [KBT04]. The voltage depression of an azimuthally symmetric annular electron beam in a conventional hollow cavity is defined as [DK81]

$$\Delta U_{\text{dep}} = \frac{I_{\text{b}}}{2\pi\epsilon_0 v_{\parallel}} \ln\left(\frac{r_{\text{w}}}{r_{\text{b}}}\right) \quad (1.9)$$

Since the electron beam ionizes neutral molecules of residual gas present in the tube, the ions can partially, but not fully compensate or neutralize the beam space charge during longer pulses or cw-operation [KBT04]. Therefore, the

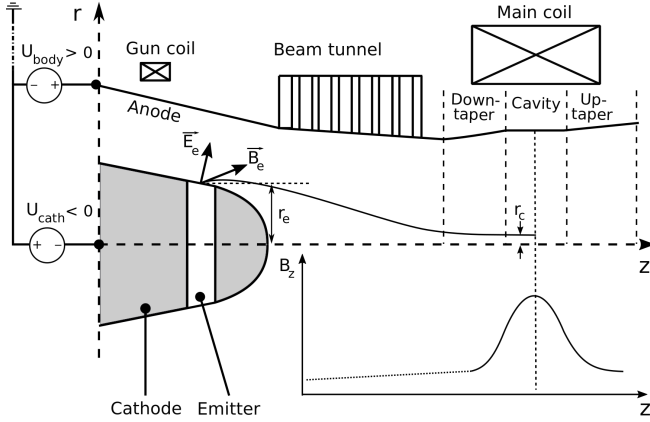


Figure 1.6: Illustration of the symmetric cross-section of a typical diode-type MIG (not true scales) with \vec{E}_e and \vec{B}_e being the electric and magnetic field at the emitter surface, r_e the emitter radius and r_c the electron beam radius at the cavity center.

depression voltage decreases (and consequently the pitch factor increases) and takes a stationary value on a time scale of tens of ms depending on the pressure in the tube. For the W7-X gyrotron, the voltage depression in the nominal operation parameter is 5 to 6 kV around 50 ms after the startup due to the beam charge neutralization [SCP⁺ 14, SWP⁺ 15].

The relativistic Lorentz factor γ defined as

$$\gamma = 1/\sqrt{1 - \beta^2} = 1 + \frac{E_{\text{kin}}}{E_0} \approx 1 + \frac{E_{\text{kin}}}{511 \text{ keV}} \quad (1.10)$$

is typically $\gamma > 1$, but in case of the gyrotron close to 1 (slightly relativistic). The electron velocity v is therefore often normalized to the speed of light c_0 in vacuum

$$\beta = \frac{v}{c_0} = \sqrt{\beta_{\perp}^2 + \beta_{\parallel}^2} \quad (1.11)$$

The orbital-to-axial velocity ratio or pitch factor is defined by

$$\alpha = \frac{\beta_{\perp}}{\beta} = \frac{v_{\perp}}{v_{\parallel}} \quad (1.12)$$

Here, the subscripts \perp and \parallel denote the orbital (perpendicular to the magnetic field) and the axial (parallel to the magnetic field) component of the electron velocity v . The quantities α , β and γ are important quantities to characterize the electron beam. The external electric \vec{E} and magnetic fields \vec{B} act on the electron leaving the emitter surface with e.g. [KBT04] or [Jac99]

$$\vec{F} = \vec{F}_e + \vec{F}_L = -e \left(\vec{E} + \vec{v} \times \vec{B} \right) \quad (1.13)$$

determining the electron motion. The electrons drift in the electric field and gyrate simultaneously due to the Lorentz force forming a helical electron trajectory around the magnetic field lines. The magnetic field lines are the guiding centers for the electron gyrotron with the Larmor radius

$$r_L = \frac{\gamma m_e v_\perp}{eB} = \frac{v_\perp}{2\pi f_{ec}} = \frac{v_\perp}{\omega_{ec}} \quad (1.14)$$

where m_e denotes the electron rest mass, B the magnetic flux density and f_{ec} respectively ω_{ec} the electron cyclotron (angular) frequency which was introduced previously. The external electric and magnetic fields can be considered as homogeneous in the interaction region of the cavity.

The initial pitch factor at the emitter is small, but only the transverse component of the kinetic electron energy can be used in the beam-wave interaction in the cavity. Hence, the pitch factor at the cavity center should be maximized. This is achieved by a slowly increasing magnetic field from the emitter towards the cavity, so that the adiabatic invariance of the magnetic momentum (Busch theorem) [Bus26, Nus04]

$$\frac{(m_e v_\perp)^2}{B} = \frac{p_\perp^2}{B} = \text{const} \quad (1.15)$$

holds with p_\perp being the orbital electron momentum. The electron beam is compressed according to Busch's theorem [Bus26] and for the electron beam compression ratio holds [KBT04]

$$b = \frac{B_e}{B_c} = \frac{r_E^2}{r_w^2} \quad (1.16)$$

with B_e denoting the magnetic flux density at the emitter and r_E the emitter radius. B_c and r_w are the magnetic flux density and the electron beam radius

at the cavity center.

Due to the conservation of energy (and momentum), equation 1.15 implies that the perpendicular electron velocity can be maximized by gradually increasing the magnetic flux density B along the drift movement, hence achieving the adiabatic compression of the electron beam. The electron velocity is transferred from the axial to the perpendicular component, hence increasing the pitch factor α . The typical value for α at the cavity center of a high-power gyrotron varies between 1.2 to 1.5. Due to inhomogeneous emission, surface roughness, space-charge effects or a non-uniform magnetic field, α exhibits some spread [KBT04].

As a consequence, some electrons with already high α can loose all axial velocity v_{\parallel} and are reflected back to the emitter, so that the electrons are trapped by the increasing magnetic field acting as a magnetic mirror. Electron trapping increases the spread and lowers the maximum achievable pitch factor, therefore deteriorating the beam quality and a stable mono-mode operation of the gyrotron. Trapped electrons are also considered to be responsible for low frequency parasitic oscillations in the region between the emitter and the cavity [PPZ⁺16]. The maximum achievable α is limited by the spread δ_{α} defined by

$$\delta_{\alpha} = \frac{\sigma_{\alpha}}{\bar{\alpha}} \quad (1.17)$$

where σ_{α} denotes the standard deviation and $\bar{\alpha}$ the mean of α , assuming an approximate Gaussian distribution. This assumption can be easily violated by beam-wave interactions, so that mean and expectation value are not necessarily identical anymore. In this case a relative spread $\delta_{\alpha_{\text{rel}}}$ is proposed in [Tsi01], using the difference between the 90 % and 10 % quantiles instead.

The spread δ_{α} is hence an important quantity to describe the beam quality. Also the axial and perpendicular electron velocity spreads $\delta\beta_{\parallel}$ and $\delta\beta_{\perp}$ are common.

The expression for the perpendicular electron velocity at the cavity center $\beta_{\perp c}$ [Edg93]

$$\beta_{\perp c} = \frac{\sqrt{b} |\mathbf{E}_e \times \mathbf{B}_e|}{\gamma c_0 B_e^2} \quad (1.18)$$

indicates that $\beta_{\perp c}$ depends on both, the electric \vec{E}_e and magnetic field \vec{B}_e on the emitter surface. For a diode-type MIG with a single anode, an increasing cathode voltage thus leads to an increasing pitch factor. A triode-type MIG with a separate modulation anode would allow for a better control of the electric

field \vec{E}_e and consequently better control of the pitch factor α at the cost of additional technical complexity (an additional voltage power supply).

1.5.2 Beam-Wave Interaction in the Cavity

As the compressed HEB advances through the gyrotron, it reaches the gyrotron resonator where the beam-wave interaction takes place. A gyrotron resonator or cavity is usually a circular waveguide structure with variable radius: the down-taper (or input taper) with increasing radius, a uniform middle section or cavity with constant radius and the up-taper with further increasing radius as shown in Figure 1.6. In contrast to the simplified illustration in Figure 1.6, the transitions between the resonator sections are usually smoothed to avoid undesired mode conversion due to sharp transitions [KBT04]. A part of the wave is reflected at the transition between the cavity and the up-taper. The down-taper avoids a backpropagation of a wave to the MIG. An open-ended resonator towards the up-taper is obtained. The up-taper is followed by the output waveguide and the quasi-optical (QO) mode converter. This component will be explained more in detail in a following section. The interaction between the HEB and the electromagnetic fields takes place in the cavity section with constant radius where the external magnetic field has its maximum.

The electromagnetic fields in a (circular) waveguide are the solutions of the Maxwell's equations under the given geometric boundary conditions and are divided into Transverse Electric ($TE_{mp,s}$) and Transverse Magnetic ($TM_{mp,s}$) modes [Poz05]. Depending on the direction of the azimuthal polarization of the mode with respect to the gyration of the electrons, co- (or co) and counter-rotating (+ or ct) modes are distinguished with superscripts. In this work, the superscripts are omitted and co-rotating modes are meant, except explicitly stated otherwise. The indices m , p and s are the azimuthal, radial and axial indices of the mode denoting the number of field maxima along the respective direction. For example, the electric field of a TE_{0p} mode has only an azimuthal component. The design mode of a high-power gyrotron has usually an axial index of 1 and it is therefore omitted in this thesis.

For a TE-mode, the electric field component E_z is always zero where the transverse field components in cylindrical coordinates E_r and E_ϕ do not vanish propagating along the z -axis. In contrast, the transverse electric field components E_r and E_ϕ of a TM-mode vanish propagating along the z -axis of a cavity

having a resonance close to the cutoff frequency. TM-modes also have a non-vanishing field component $E_z > 0$ which would also affect the parallel electron velocity β_{\parallel} , increasing the axial velocity spread and potentially counteracting the efficient beam-wave interaction.

Since the electrons gyrate in the plane perpendicular to their drift along the z -axis, only the transverse electric field components E_r and E_{ϕ} can and should contribute to the beam-wave interaction. Therefore a stable and efficient gyrotron operation is only possible with TE-modes where $E_{\perp} \gg E_z$ holds [Ber11]. Usually the excitation of co-rotating modes is desired and excitation of counter-rotating modes should be avoided, often leading to arcing inside the gyrotron (see e.g. [IKO⁺15, SGJT13a, DIP⁺05]) due to enlarged stray radiation caused by the beam launcher. The beam launcher is designed for co-rotating modes, therefore counter-rotating modes are scattered in the beam launcher.

An electron entering the interaction region either transfers energy to the perpendicular electric field of the TE-mode or gains energy from it. This depends on the phase difference between the electric field and the electron's gyration phase. A net energy transfer between the electron beam and the TE-mode is possible due to the relativistic mass dependence of the electrons: When the electron's gyro motion is in phase with the electric field, the electron loses energy to the field, hence reducing its mass and consequently increasing its cyclotron frequency defined by

$$\Omega_{ec} = \frac{\Omega_0}{\gamma} = \frac{eB}{m_e \gamma} \quad (1.19)$$

If the frequency of the rotating electric field is slightly higher than the electron cyclotron frequency $\omega_{RF} \gtrsim \Omega_{ec}$, the electron stays longer in the favorable phase, decreasing its phase difference, synchronizing with the electric field of the mode. This effect is called "phase bunching": electrons accumulate in the same gyro phase [KBT04, FGPY77]. Note that this is a sensitive, dynamic process. If the cavity transit time is too long and therefore the time for the electrons to interact with the field, "overbunching" can occur. The RF field would then transfer energy back to the electrons which should be avoided. The interaction with the preferred design mode should therefore take place near the end of the cavity where the axial field profile of the design mode should have its maximum. Furthermore the beam radius should be close to the radial maximum of the RF field to maximize the beam-mode coupling. For the co-rotating excitation, it should be slightly smaller than the radial position

of the field maximum. The simplified resonance condition for this interaction is given by [Chu04, Nus04]

$$\omega_{\text{RF}} - k_{\parallel} v_{\parallel} \approx \Omega_{\text{ec}} = \frac{\Omega_0}{\gamma} \quad (1.20)$$

where k_{\parallel} is the axial wavenumber of the mode. For the propagation of waveguide modes, the dispersion relation

$$k_0^2 = k_{\parallel}^2 + k_{\perp}^2 \quad (1.21)$$

$$k_0 = \frac{2\pi f}{c_0} = \frac{\omega}{c_0} \quad (1.22)$$

$$k_{\perp} = \frac{\chi_{\text{mp}}}{r_w} \quad (1.23)$$

holds with k_0 being the free space and k_{\perp} the transverse wave number. The latter depends on the mode eigenvalue χ_{mp} which is defined for TE-modes as

$$J'_m(\chi_{\text{mp}}) = 0 \quad (1.24)$$

being the n -th zero of derivative of the m -th order Bessel function of the first kind. Finally with (1.21), (1.22) and (1.23), we obtain the dispersion relation for a TE-mode defined as following

$$f = \frac{c_0}{2\pi} \sqrt{\left(\frac{\chi_{\text{mp}}}{r_w}\right)^2 + k_{\parallel}^2} \quad (1.25)$$

which in particular yields for $k_{\parallel} = 0$

$$f_c = \frac{c_0 \chi_{\text{mp}}}{2\pi r_w} \quad (1.26)$$

which is the cutoff frequency for the mode. This is the lowest frequency with which a TE-wave can propagate through the waveguide (so that k_{\parallel} is a real number and bigger than zero). Note that (1.25) describes a parabola in the dispersion diagram, also called Brillouin diagram, as shown in figure 1.7.

The dispersion of a wave in free space (1.22) and the electron beam (1.20) are represented by linear graphs. An interaction thus can only take place near the intersections of (1.25) and (1.20) where the resonance condition (1.20) is met.

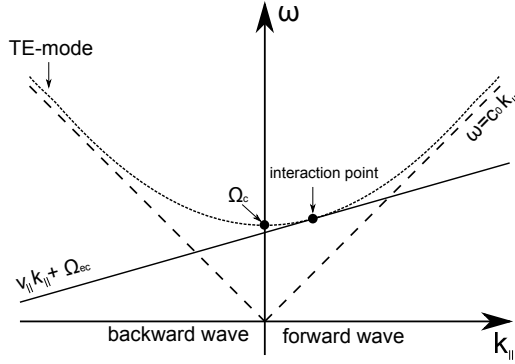


Figure 1.7: Exemplanic Brillouin diagram (adapted from [KBT04]) showing the dispersion parabola for a TE-mode, the electron beam line, the speed-of-light line and a typical interaction (or resonance) point near the mode cutoff.

A typical gyrotron interaction point is shown where the resonance point is given near the cutoff for a forward wave with small $k_{\parallel} > 0$, but a large $k_{\perp} > 0$ according to (1.21) as desired. Since the interaction point in the dispersion diagram is above the speed-of-light line, hence the phase velocity is bigger than for a wave in free space, the term "fast wave" interaction is used.

Note that a beam line can have several intersections with different modes. More sophisticated and realistic models are used for interaction simulations in practice [APIV12, Jel00, Ker96]. The electrons cannot transfer their whole perpendicular kinetic energy to the cavity mode. The theoretical limit for the (orbital) interaction efficiency η_{\max} [KDST85, KBT04]

$$\eta_{\max} = \frac{\alpha^2}{1 + \alpha^2} \quad (1.27)$$

given by the pitch factor α . In reality, the maximum achievable efficiency is lower due to electron beam parameter spreads and electron beam space charge effects [Nus04]. The typical achievable interaction efficiency for a megawatt-class gyrotron is between 35% and 40% [TDST19].

1.5.3 Quasi-Optical Mode Conversion

After the interaction in the cavity, the cavity mode propagates towards a mode converter. In general mode conversion is required to adapt the high-order TE_{mn} cavity mode to the fundamental mode required for the external transmission line. Most common are the HE_{11} hybrid mode for oversized corrugated circular waveguides and the fundamental Gaussian mode TEM_{00} used for quasi-optical (QO) transmission lines. For modern high-power gyrotrons built-in QO mode converters and transmission lines are used [TDST19]. The latter is in use at the W7-X ECRH facility [EBB⁺07, TBB⁺08] and the KIT high-power gyrotron test stand.

The QO mode converter consists of a mode converting antenna, the beam launcher, and an arrangement of metallic mirrors to reflect the RF beam outside the gyrotron through the output window. The mode conversion efficiency to TEM_{00} is above 97 % for the QO mode converter of the W7-X gyrotron, meaning only about 3 % of the RF power is converted to undirected stray radiation [TYA⁺05]. Furthermore the QO beam launcher separates the electron from the RF beam, so that the dump for the "spent" beam, the collector, can be optimized discarding the RF power.

The mode conversion to a QO beam with quasi Gaussian field intensity distribution is achieved by a superposition of a selected set of phase and amplitude matched modes which are radiated by the beam launcher [TYA⁺05]. In the geometrical optics (GO) limit of a rotating mode propagating in a (circular) waveguide, the mode can be represented by a superposition of linear polarized waves and treated as a set of optical rays. The propagation is described as helical reflections along the waveguide walls in axial direction under the Brillouin angle θ_B [TYA⁺05, Nus04, Thu97]

$$\theta_B = \sin^{-1} \left(\frac{\chi_{mp}}{k_0 r_w} \right) \quad (1.28)$$

where the cross-section of the waveguide within the caustic radius r_c

$$r_c = \frac{m r_w}{\chi_{mp}} \quad (1.29)$$

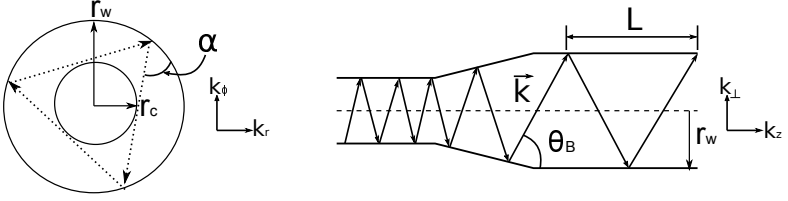


Figure 1.8: Mode propagation in a circular waveguide in the limit of geometrical optics (adapted from [Nus04]).

stays field-free. The area between r_w and r_c is filled by uniformly distributed geometrical rays. The angle between subsequent reflections is 2α where α is defined as

$$\alpha = \cos^{-1} \left(\frac{r_c}{r_w} \right) = \cos^{-1} \left(\frac{m}{\chi_{mp}} \right) \quad (1.30)$$

Between two subsequent reflections in the axial direction, the beam propagates along a distance L

$$L = 2r_w \cot \theta_B \sqrt{1 - \left(\frac{m}{\chi_{mp}} \right)^2} \quad (1.31)$$

The total distance required for the rays to rotate by 2π on the surface is π/α times bigger and is called the Brillouin length L_B .

The propagation and the related quantities are illustrated in Figure 1.8. This translates to a portion of the inner waveguide surface where a certain mode is reflected. If now the remaining part of the waveguide is removed, the waveguide antenna or beam launcher is obtained with a helical cut.

All other modes or the modes responsible for the quasi Gaussian field distribution at a different frequency contribute to the stray radiation in the tube heating up the inner gyrotron surface. Consequently an increased stray radiation level can lead to a sudden increase of the gyrotron vacuum pressure due to increased outgassing of the gyrotron body material. Note that also the modes being part of the defined set for superposition contribute to the stray radiation level, but just with a small power fraction depending on the efficiency of the QO mode converter.

Taking the W7-X gyrotron and its QO mode converter as an example, the stray radiation level during nominal working mode operation amounts already to 30 kW, assuming 1 MW output power and 97 % mode conversion efficiency.

1.5.4 Energy Recovery in the Depressed Collector

After the q.o. mode converter separated the electron from the RF beam, the widened electron beam hits the inner collector surface. After the interaction, the electrons still possess a significant axial (and transverse) velocity and hence kinetic energy. The electron beam therefore heats up the collector which is problematic in particular during CW operation of the gyrotron. In order to avoid thermal damage for the collector, megawatt-class high-power gyrotrons operating at long pulses have sweeping coils to permanently move the "spent" electron beam over the inner collector surface to distribute the heat load [SID⁺07, DIP⁺05]. Another measure which increases the electrical efficiency of the gyrotron and leading to reduced power consumption and operation costs, is the so called single-staged (SDC) or multi-staged "depressed" collector (MDC). The potential of the collector surface is depressed with respect to the anode potential [PIDT96]. In case of the W7-X gyrotron, the collector is at ground potential and a retarding or depression voltage $U_{\text{dep}} > 0$ (at W7-X called body voltage, not to confuse with the beam voltage depression) is applied between the cavity and the collector [GEI⁺11, TAA⁺07]. So the remaining kinetic energy of the electrons is converted back to electrical energy and is recovered.

The collector efficiency η_{coll} is defined as $P_{\text{coll}}/(P_{\text{b}} - P_{\text{RF}})$ being the ratio of the power recovered by the collector P_{coll} to the remaining power of the "spent" electron beam ($P_{\text{b}} - P_{\text{RF}}$) [PIDT96]. Here for a SDC $P_{\text{coll}} = U_{\text{coll}} I_{\text{coll}}$.

The total electrical efficiency of the gyrotron η_{tot} is defined by $P_{\text{out}}/(P_{\text{in}} - P_{\text{rec}})$ where $P_{\text{in}} = U_{\text{acc}} I_{\text{cath}}$ and $P_{\text{rec}} = (P_{\text{in}} - P_{\text{RF}}) - P_{\text{dis}}$. Here P_{dis} is the fraction of power dissipated in the collector walls, P_{RF} is the RF power generated in the cavity and P_{rec} the power recovered by the collector. Beside the increased total electric efficiency of the gyrotron, the advantages of using a depressed collector are the lowered required voltage for the main power supply, a lowered collector head load resulting in an increased gyrotron reliability and reduced required capabilities of the collector cooling system [TDST19].

The maximum retarding voltage is limited by the lower bound for the axial electron velocity after the interaction. In case an electron reaches $\beta_{\parallel} \approx 0$, it is reflected back to the towards the emitter where it is either trapped in the region between collector and launcher or emitter and cavity [PPZ⁺16, PIDT96]. Typically the electronic efficiency of a high-power gyrotron is around 30 % to 40 % which can be improved by a SDC to 50% [PIDT96]. The more collector

stages are used, the higher is the achievable efficiency. For the W7-X gyrotron, a total electrical efficiency of 40 % to 50 % and an electronic efficiency of 26 % to 28 % up to 37 % was achieved with a depressed collector at a lower output power [GEI⁺11].

1.5.5 Mode Competition and Stability

The growing demand for heating power in fusion research led to the development of high-frequency multi-megawatt gyrotrons [TDST19]. Due to the technical limitation for the ohmic losses at the cavity wall of 2 kW/cm² the cavity size had to be increased along with the order of the design working mode. Therefore modern high-power gyrotrons for fusion use volume modes e.g. TE_{28,8} or TE_{34,19}, TE_{mp} modes with $m > p$, as nominal working mode [KBT04]. There are new technical approaches to mitigate the cavity cooling problem allowing to exceed the limitation, like mini-channel cooling [BAA⁺17, KBR⁺19].

For each mode in the cavity, a minimum beam current at which the mode starts to oscillate at a given beam voltage, can be defined. As a consequence of the oversized cavity, the mode spectrum in the cavity is very dense. The problem of lacking frequency separation of the modes is in particular severe since the cyclotron resonance is not arbitrarily sharp, but rather a band.

The width of a cyclotron resonance band is given by [KBT04]

$$\frac{\Omega_0}{\gamma_0} - \frac{\pi}{t_{tr}} \approx \omega_{RF} \approx \frac{\Omega_0}{\gamma_0} + \frac{\pi}{t_{tr}} \quad (1.32)$$

with t_{tr} being the electron transit time $t_{tr} = L/v_{||,0}$ for the cavity interaction region with length L . So the resonance bands might overlap and the beam current I_b can be above the starting current I_{start} for more than one mode simultaneously.

Figure 1.9 shows an example plot of starting current curves for a set of 32 relevant modes with the I_{start} -curve for the nominal working mode emphasized with a thicker line. The dashed line is the beam current curve indicating which modes could be excited. If $I_b > I_{start}$, inside the region denoted by the starting current curve, we speak of "soft excitation" [KBT04]. Since the soft-excitation regions of multiple modes can overlap, one of most challenging tasks for high-power gyrotrons is to ensure stable mono-mode operation. Coaxial

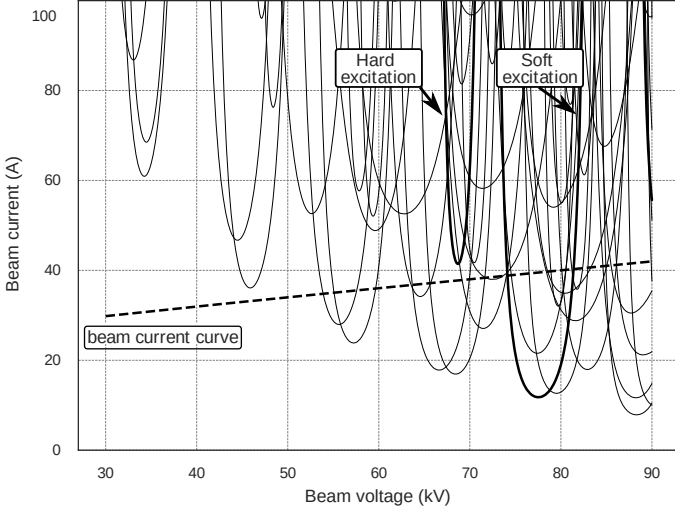


Figure 1.9: Exemplaric plot of the starting current curves for a set of 32 modes obtained with ISTART being part of the EURIDICE code package [APIV12]. The starting current curve for the desired design mode in this case is bold. The beam current curve is shown as dashed line, indicating which modes could be excited.

cavities with an insert possess a less dense mode spectrum and are already tested for future high-power gyrotrons, also at the KIT [RGJ⁺14, RAG⁺18]. Note that the result shown in Figure 1.9 is obtained with the cold-cavity, fixed-field approximation, meaning that no other mode is active before and a fixed axial Gaussian field profile is assumed. In reality another weak mode is always present and the starting current curves look different in that case. If a mode starts to oscillate, it tends to grow in power and suppresses other modes [Nus81, Nus99]. This allows stable mono-mode operation in the presence of other competing modes [NSV⁺04]. A mode oscillation is considered to be stable, if the power of the nominal mode $\partial P_1 / \partial t > 0$ while the power of a competing mode $\partial P_j / \partial t \leq 0$ [KBT04].

If $I_b < I_{\text{start}}$ holds, we speak of "hard excitation" [KBT04]. Very often the optimum efficiency for the nominal mode is achieved in the hard excitation region which is not directly accessible. But since the active mode suppresses other competing modes, the hard excitation region can be reached from a

neighboring soft-excitation region.

Consequently, the operating (and dominant) mode of the gyrotron depends on the path previously taken in the gyrotron (operation and hence beam) parameter space over time. This is the case for the startup, the begin of a gyrotron pulse, where the operation parameters (e.g. the applied voltages and currents) have a finite rise time and the desired working point cannot be instantaneously reached. In particular for gyrotrons with a diode-type MIG, the electron pitch factor α depends on the accelerating voltage. Consequently, several mode switches or hoppings can be observed during the startup (the voltage (and current) rise time) before the stable mono-mode operation is eventually achieved, see for example [ARM⁺19, ADV08, NSV⁺04]. Therefore, the dynamic behaviour of the gyrotron can be described as highly non-linear, sometimes chaotic [ADRS01, AAA⁺12] and exhibiting a strong hysteresis [DII⁺03, SKT⁺07, DI08].

1.5.6 Parasitic Oscillations

In general, any undesired excitation of an oscillation in- or outside the cavity interaction region is considered to be a parasitic oscillation.

An oversized hollow cavity which is typical for nowadays high-power fusion gyrotrons exhibits a dense mode spectrum. Therefore, such a cavity is sensitive for small deviations of the electron beam radius, the beam alignment within [SDG⁺13, IKF⁺17] or the remaining electron beam parameters (pitch factor α , relativistic factor γ and their respective spreads). Of course, manufacturing tolerances for the waveguide structure (and the inner conductor in case of a coaxial cavity) [IKF⁺17] or the emitter ring of the MIG [PIT16, RGI⁺17] can also lead to a more likely excitation of other modes than the design mode, resulting in increased undesired parasitic activity.

The situation when other modes are active simultaneously with the nominal cavity mode is called multi-moding behaviour. The modes involved in multi-moding behaviour are often coupled, appear in sets of modes and likely start together [APPV07, SNA12]. Typical competing modes are the $TE_{|m|-1,p+1}$, $TE_{|m|-2,p+1}$ and $TE_{|m|-3,p+1}$ counter-rotating modes and the azimuthal neighbour or satellite modes $TE_{m\pm 1,p}$ of the nominal cavity mode

[Ber11, Ker96]. This can be explained with the squared coupling factor $G_{e,mp}$ between a counter-rotating mode and the electron beam [KBT04, Ker96]

$$G_{e,mp}(r_b) = \frac{1}{\sqrt{\pi (\chi_{mp}^2 - m^2) J_m(\chi_{mp})^2}} k_{c,mp} J_{m+s}(k_{c,mp} r_b) \quad (1.33)$$

with s being the cyclotron harmonic and m and p being the azimuthal and radial indices of the mode. For a co-rotating mode with $m < 0$ using the property of the Bessel function $J_{m+s} = (-1)^{m+s} J_{-m-s}$ follows [Ker96]

$$G_{e,mp}(r_b) = \frac{(-1)^{m+s}}{\sqrt{\pi (\chi_{mp}^2 - m^2) J_m(\chi_{mp})^2}} k_{c,mp} J_{|m|-s}(k_{c,mp} r_b) \quad (1.34)$$

In order to give an illustrative example without loss of generality, the squared coupling factors $G_{e,mp}^2$ are plotted over the beam radius r_b normalized to the cavity wall radius r_w for the desired mode $TE_{-28,16}$ and its aforementioned competitors in Figure 1.10. Clearly, the modes compete since they have their first maximum of the squared coupling factor G_e^2 close to the coupling factor maximum of the desired design mode $TE_{-28,16}$ for which the beam radius has been optimized. The azimuthal neighbors become more important for high mode eigenvalues χ_{mp} since the frequency separation decreases with $\Delta f/f_{mp} \approx \pi/2\chi_{mp}$ [Ber11]. The azimuthal or satellite modes and are investigated more in depth in the present work.

Furthermore, parasitic modes can be also excited outside the cavity interaction region where Before-Cavity Interactions (BCI) and static (or stationary) and dynamic After-Cavity Interactions (ACI) are distinguished [AIK⁺15, Sch15, SCG⁺11, CSD⁺11, SFG⁺10, KAC⁺10].

BCI is a very common type of parasitic oscillation in high-power gyrotrons located in the so-called beam tunnel before the cavity [ATA⁺11, KSF⁺09] (see Figure 1.6) Beam parameter deterioration, in particular an increase of beam parameter spreads δ_α and δ_γ , can be an important effect of BCIs with parasitic modes. The startup scenario, the achievable output power in the nominal cavity mode and the parameter range for stable mono-mode operation are therefore strongly affected by BCIs. High-order $TE_{0,p}$ backward-waves which are hard to attenuate, seem to be a source of parasitic oscillations in this region since the reconstructed axial interaction positions (based on the measured frequencies of the parasitic oscillations) were found to be in the beam tunnel before the

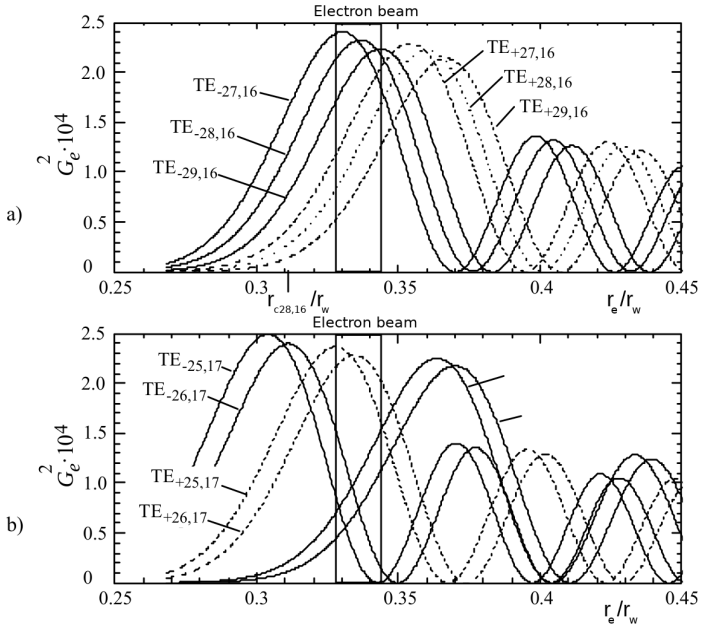


Figure 1.10: The most important competing modes have their first maximum of the squared coupling factor G_c^2 close to the maximum of the desired $TE_{-28,16}$ mode for which the beam radius was optimized (adapted from [Ker96]).

cavity. Additionally, interaction simulations exhibited a high growth rate for these modes [GDF⁺10]. Since the magnetic field is lower in this region, the parasitic oscillations originating from BCIs have a lower frequency than the nominal cavity mode [SFG⁺10, SCG⁺11, Sch15]. Various technical solutions exist to damp the undesired oscillations in the beam-tunnel region between the gun and the cavity, e.g. [LST11, RGI⁺13]. Among those a structure of stacked rings of alternating material (copper/ceramic) is most prominent, lowering the quality factor in order to increase the starting current of possible parasitic modes [TDST19, GDF⁺10]. Such a beam tunnel is also used for the W7-X gyrotron.

An After-Cavity Interaction (ACI) is a time-varying, second interaction of the "spent" electron beam (with reduced γ and α and broadened beam parameter distributions due to the power extraction) after leaving the cavity. The

interaction takes place at lower frequencies (due to the lower magnetic field in the up-taper section and beyond) with the nominal mode or other competing modes [AIK⁺15, RC14]. In particular, the gyrating electrons are already phase-bunched when leaving the cavity. Therefore, ACIs can reduce the efficiency since energy can be transferred back from the RF field to the electrons due to over-bunching taking place. Since the electron energy distribution is broadened, a SDC is less suitable for an energy recovery because it can be only optimized for a particular electron energy. However, a MDC where the individual stages act on different electron energy intervals, are a promising solution to address this issue [Wu19]. ACIs can also degrade the gyrotron performance causing electron beam reflections leading to low-frequency oscillations (LFO) by trapped electrons in the region between the gun and the cavity [PPZ⁺16]. An important distinction between ACIs and BCIs is that ACIs depend on a pre-bunching introduced by a first interaction in the cavity, where in contrast, BCIs are independent from the cavity mode.

The parasitic mode activity by BCIs and ACIs lead then to an increased stray radiation level in the tube. The stray radiation which can only partly leave the gyrotron causes increased component heat loads, consequently resulting in a degradation of the vacuum quality due to increased outgassing of the materials. Therefore the increased stray radiation level due to parasitic modes worsens the gyrotron reliability, hence the achievable pulse length and output power [GEI⁺11].

1.5.7 Noise and Chaos in Gyrotrons

Ideally the radiation linewidth of a gyrotron should be zero, but in reality this is not the case due to various noise sources and the finite width of the cyclotron resonance band. This is in particular of interest for applications based on the Doppler effect e.g. Doppler radars or collective Thomson scattering (CTS) plasma diagnostics. Noise sources in gyrotrons can be categorized as intrinsic or extrinsic noise sources [Nus04].

Intrinsic noise can originate from shot, thermal and flicker noise. Shot noise is caused by the discretization of the electrical charge. Thermal noise is caused by the finite temperature of the microwave circuit e.g. the waveguide walls (Kirchhoff radiation). Flicker noise is caused by a locally different emissivity of the cathode due to impurities in the emitter material (Schottky 1926) [DN97]. Extrinsic noise stems from the stochastic fluctuations in the gyrotron operation parameters like beam voltage and current (indirectly via a residual ripple voltage on the supply voltages) and magnetic fields from the main and gun coils. The effect of noise from the heating filament current is negligible due to the thermal inertia of the emitter. The noise in superconducting solenoids can be as well discarded. Of all the noise sources, the supply voltage noise, hence a residual ripple voltage and noise on the body and cathode voltage, should have the strongest effect. As a rule of thumb, extrinsic technical noise is much more significant regarding its order of magnitude than natural intrinsic noise [DN97]. The voltage ripple imposed on the body and cathode voltage often requires the gyrotron to be operated with a safety margin to avoid mode loss, in particular when operated in the hard-excitation regime for the nominal cavity mode [ARM⁺19].

The effect of technical noise on the radiation linewidth for free-running gyrotrons has been investigated in [ND97, DN97] but not with a self-consistent gyrotron interaction model. The technical noise was assumed to be a stationary stochastic process with small amplitude and the gyrotron parameters were chosen far away from critical behaviour (observed as bifurcations in the gyrotron dynamics, hence chaotic behaviour). It was found that the sensitivity to fluctuations in beam voltage or magnetic field strongly depend on the operation regime.

The regimes of non-stationary oscillations in the normalized gyrotron parameter plane, stochastic processes and chaos in gyrotrons have been investigated for a self-consistent model in [ADRS01, AD03, AD02]. In gyrotrons three

major processes were identified: stochastic (chaotic) electron trajectories, stochastic RF oscillations and spatio-temporal chaos of the RF field in the resonator [AD03]. For -power gyrotrons with oversized cavity, the latter is most relevant. Generation of stochastic RF radiation was found to be unfeasible with regard to achievable operation parameters [ADRS01]. Possible routes in the normalized gyrotron parameter plane to spatio-temporal chaos (and hence unstable behaviour) were investigated in [AD02] but without technical noise. Ways how to control (and avoid) chaos were not investigated so far, but the author of [AD02] hypothesized that it could be possible by small fast time-dependent adjustments of a control parameter, e.g. beam voltage. This is a hint how to possibly realize a kind of electronic stability control for gyrotrons.

To the best of the author's knowledge, no self-consistent multi-mode simulations have been performed so far incorporating technical noise e.g for the beam voltage. This would be helpful to investigate the effect of noise on the startup scenario, mode switching behaviour and competition, hence potential multi-modding behaviour and the stability of mono-mode operation. The latter is of great importance when the gyrotron is operated near the nominal cavity mode cutoff at the output power limit. Self-consistent multi-mode simulations with EURIDICE [APIV12] incorporating technical noise are presented in this work. In this way, the feasibility of stable mono-mode gyrotron operation close to the cutoff in the presence of noise could be evaluated and a possible precursor for mode switching (hence mode loss) could be found with a more realistic model.

1.5.8 Long-pulse Behaviour

The long-pulse and cw-behaviour of a gyrotron is mainly characterized by four major transient processes on different time scales with respect to the pulse length: thermal expansion of the cavity, beam space charge neutralization, cathode emission or emitter cooling and outgassing [NSA⁺06, SGI⁺15].

Due to ohmic heating of the cavity walls (with heat loads up to 2 kW cm^{-2}), even with sophisticated cooling methods, a temperature increase and therefore a thermal expansion of the cavity occurs which is observable as a frequency drift of the nominal cavity mode. If a very short gyrotron pulse is performed ($< 10 \text{ ms}$), the thermal inertia of the cavity avoids a sudden increase in temper-

ature and no frequency downshift is observed. Otherwise, the cavity expands till thermal equilibrium and a stationary state is reached. Typically the frequency downshift is in the order of several 100 MHz happening during several 100 ms [NSA⁺06]. The observed frequency downshift for the W7-X gyrotron was about 200 MHz during 1 s as presented in [Sch15]. This result was confirmed in tests to validate a spectrogram measurement method developed in this thesis.⁶ Once a stationary state is reached after 1 to 2 s, the frequency drift is normally reduced to 1 to 2 MHz per minute [Sch15]. More recent works incorporate the thermal expansion of the cavity in self-consistent multi-mode simulations to obtain more realistic results [ABA⁺18]. New technical cavity cooling approaches attempt to reduce the cavity temperature difference and therefore the impact of thermal cavity expansion on the gyrotron operation and performance [KBR⁺19, BAA⁺17].

The observed effect of the frequency downshift is the result of both, the thermal cavity expansion and the effect of the transient beam space charge neutralization. An approach to distinguish the contributions of the two processes to the frequency downshift was followed in [SCP⁺14, SWP⁺15]. Despite the good technical vacuum inside the tube (with pressures lower than 10^{-6} bar [Dam95]), residual gas is present in the tube which is first ionized and then gradually neutralizing the electron beam space charge. During this process on a time scale of a few hundred ms, depending on the pressure inside the tube, the pitch factor is increasing due to the decreasing beam voltage depression till a stationary state is reached [FGN15, NSA⁺06, DAB⁺05]. For a typical pressure of 10^{-8} bar, the time scale for neutralization is in the order of 100 ms [PAA⁺19, TAA⁺07]. The beam voltage is increased by a few kV, hence a few percent, during the neutralization. In contrast to previous assumptions (e.g. in [NSA⁺06]), full neutralization is not achieved [PAA⁺19]. The stationary neutralization level for the W7-X gyrotron was determined in [SWP⁺15] based on a frequency measurement. The stationary neutralization level was found to be around 60%. The third important effect is the emitter or cathode cooling effect occurring during long pulses, resulting in a decreasing beam current [NSA⁺06]. The optimum efficiency working point for high-power gyrotrons is often in the hard-excitation regime for the nominal mode. If the beam current drops below the break current (being the minimum current to sustain the mode in the hard-

⁶ A measurement setup to obtain (time-averaged) spectrograms of gyrotron stray radiation is presented in a following chapter.

excitation regime), the result is a mode switch to a competing mode, thus a loss of the nominal mode [NSA⁺06, KMT⁺05]. So the emitter cooling phenomenon causes a transition of the working point which can degrade the gyrotron reliability in particular when already operated in the hard-excitation regime. If no heating filament current boosting scheme is used, the mode is usually lost after a few seconds. Even when such a boosting scheme is applied prior and during the gyrotron pulse, a fast beam current drop by up to 30 % within the first two seconds is typically observed for the W7-X gyrotrons, arriving at a local minimum after around 2 to 3 s. The beam current then slightly increases and stabilizes later-on [WMS⁺19]. Another possible counter-measure against the emitter cooling phenomenon besides an appropriate boosting scheme for the cathode heater filament current is a safety margin for the acceleration voltage to avoid mode loss. A safety margin is also necessary because of the supply voltage ripple as mentioned in the previous section. Of course, a safety margin for the acceleration voltage can decrease the maximum achievable output power of the gyrotron [ARM⁺19]. The phenomenon of mode loss due to emitter cooling is frequently observed during experiments at Wendelstein 7-X. Consequently this phenomenon was investigated in simulations and experiments in this thesis.

The last relevant and slowest phenomenon is outgassing and the resulting degradation of vacuum quality inside the tube during long pulses or cw-operation. The gyrotron walls are heated by RF and the collector heats up being hit by the spent electron beam. The situation is complicated when different physico-chemical processes are taken into account in modeling the inhomogeneous outgassing and the different heat loads for the components of a gyrotron [Sch15].

1.5.9 The Wendelstein 7-X Gyrotron

The development of cw-capable megawatt-class gyrotrons was pursued in world-wide research activities driven by the heating requirements of W7-X and ITER. Thales Electron Devices (TED) in Europe and Communications & Power Industries (CPI) were found in 1998 as industrial partners in the development of the W7-X gyrotron [TAA⁺07]. The Karlsruhe Institute of Technology (KIT), formerly Forschungszentrum Karlsruhe (FZK), and the University of Stuttgart together with the Max Planck Institute for Plasmaphysics in Garching

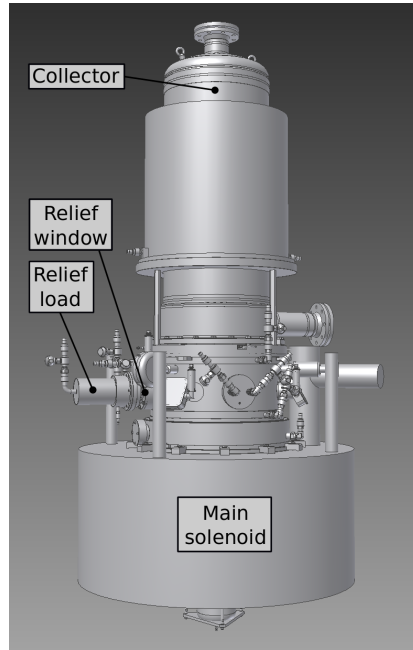


Figure 1.11: 3D CAD model of the Wendelstein 7-X gyrotron manufactured by Thales Electron Devices (TED) with installed main solenoid.

initiated the joint project "Projekt Mikrowellenheizung für W7-X" to develop a 140 GHz gyrotron with a target output power of 1 MW. The W7-X gyrotron is equipped with a diode-type MIG (without additional control anode) and a single-stage depressed collector to increase the electrical efficiency. The gyrotron works on the $TE_{28,8}$ -mode (TED) or on the $TE_{28,7}$ -mode (CPI) as nominal operating mode with an average pitch factor of 1.3 and magnetic field of 5.56 T in the interaction region center. The W7-X gyrotron has a conventional, hollow cavity made of Glidcop with a design quality factor between 885 (cold/fixed-field Gaussian) and 1100 (hot/self-consistent approximation). The gyrotron uses a high-efficiency QO mode converter with a mode conversion efficiency of 98% [TYA⁺05]. The rest is converted to stray radiation which can be observed e.g. at the gyrotron relief window in case of the TED series tubes. This is an additional window facing the QO output coupler and

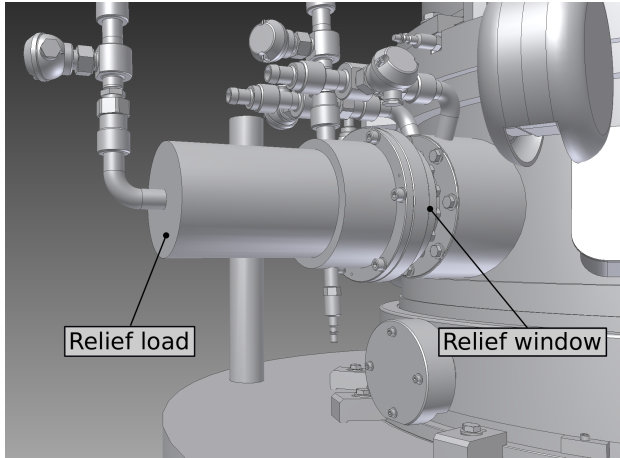


Figure 1.12: Zoom-in of the 3D model section showing the gyrotron relief window with installed water-cooled relief load.

the metallic mirror arrangement. It is used in this thesis for stray radiation measurements of parasitic and satellite modes. The prototype tube Maquette (Bravo 1) does not have a relief window. In that case, stray radiation measurements can be performed by picking up RF in the periphery of the output beam waist.

The RF output power converted to a Gaussian beam is finally led through the output window. It consists of an actively-cooled diamond disc with 106 mm diameter produced in a chemical-vapour deposition (CVD) process with an aperture of the output window of 88 mm. The thickness of the disc is 1.8 mm is a compromise between the losses at the target RF output power frequency of 140 GHz, mechanical strength (protection of the high vacuum inside the tube) and manufacturability [GDA⁺06]. A typical design working point with depressed collector is found at an accelerating voltage of $U_{\text{acc}} = 81$ kV, a beam current of $I_b = 40$ A and a collector depression voltage of $U_{\text{dep}} = 27 \dots 30$ kV. The theoretical total efficiency was found to be 48 % in depressed operating mode but in reality the achievable values range between 30 to 44 % [TAA⁺07]. Until 2018 9 tubes were built by TED and one by CPI. During the final site acceptance test (SAT) at Wendelstein 7-X, an output power of 0.92 MW for 30 min was targeted with the first series tube (TED SN1) [TAA⁺07]. Results

with following series tubes differed in terms of performance and reliability e.g. SN3a [GEI⁺11], compare also with table 1.1. So each gyrotron shows an individual behaviour with its individual, empirically found, optimum high-power working point. Possible reasons are e.g. emitter surface quality deviations, manufacturing tolerances and outgassing behaviour. To cope with the issues limiting the output power and reliability (due to mode hopping), slight design modifications and an improved beam tunnel were introduced in the manufacturing process of the eight series tubes [TAA⁺07, GEI⁺11].

A 1.5 MW gyrotron design operating on the TE_{28,10}-mode based on the old design with conventional cavity was investigated in [ARM⁺19]. The installation of an additional 11th 1.5 MW conventional-cavity gyrotron is planned and will be also manufactured by TED. Since the cavity dimension and nominal mode order will be increased in this design, the problems with mode hopping and competition are expected to be more severe. The gyrotron controller developed in this thesis could be therefore required to ensure stable gyrotron operation with maximum output power.

1.5.10 Simulation Codes

Simulation models are required in the design process of a gyrotron as well as to examine the electron beam parameters, since they cannot be measured directly, but are verified by comparison of an experiment with a simulation. The magnetic field profile in axial direction of the electron beam (for the W7-X gyrotron main and gun coil) are also computed. Deviations between simulated and measured magnetic field profiles are also due to differences between the cold and the warm dewar and coil geometry. The gyrotron behavior at a nominal working point is dominated by the external control parameters (coil currents I_{gun} and I_{main} and their resulting magnetic fields, acceleration and depression voltage V_{acc} and V_{dep} respectively), as well as by the electron beam parameters governed by gun geometry and emitter surface properties [Sch15]. Emitter surface roughness is neglected in the simulations performed for this thesis since it is not an effect relevant for mode switching or multi-moding behavior on an individual gyrotron pulse time scale. Its influence is rather a static shift in interaction simulations, gradually changing over gyrotron lifetime due to aging of the emitter, which could be modeled by increasing emitter surface roughness in simulations as presented in [Zha16]. Increasing emitter surface

roughness can be measured in experiments by acquisition of the current-voltage characteristics (CVC) and a subsequent fitting procedure [ZIP⁺17].

Different interaction models exist with their own numerical solution approach: The most simple linear interaction model turned out not to be suitable to yield a qualitative agreement for experiments with W7-X gyrotrons [Sch15]. The most common approach is a self-consistent slow-time interaction simulation, incorporating the following assumptions:

The RF fields in the waveguide are represented as superposition of waveguide resonator eigenmodes and mode conversion is neglected. So only smooth transitions (tapering $\leq 5^\circ$) in the waveguide geometry and high wall conductivity should be used [APIT13, DN13] and participating modes have to be carefully selected in advance [Sch15]. However, the generalized scattering matrix (GSM) method would allow self-consistent simulation without these limiting assumptions as demonstrated in [Jel00, JGS99].

Another assumption is the so called slow-time approach: electron trajectories are described as orbits around a fixed guiding center. Additionally the RF field envelope is assumed to be constant during the electron transit time through the resonator geometry. So the electrons can be propagated through the geometry before the RF fields are updated. This leads to a decoupling from the fast interaction regime, relaxing the requirement for a small time discretization step size to the electron cyclotron period (typ. 0.01 to 0.1 ns), hence reducing the computational effort for the simulation. Of course, the base-band treatment implies that the bigger the RF frequency f_{RF} deviation from the carrier frequency f_{carrier} is, the less the slow-time approach holds. This and the fact that the beam electrons are represented by a discrete number of beamlets of macro electrons, implies that only gyrotron type interactions (with a frequency close to the cyclotron frequency f_{cycl}) can be reliably modeled. Furthermore often axisymmetry and a conservation of axial electron momentum are assumed and the magnetic RF fields are discarded as well [Avr15, Fra17, Sch15].

The codes SELFT (Kern et al., 1997 - 2011, [Ker96]) and more recent EVRIDIKI from the code package EURIDICE (Avramidis et al., 2006 - 2016, [APIV12]), both developed at KIT, use the self-consistent slow-time approach. Other prominent codes are MAGY [BAL⁺98] and TWANG [ATA⁺11]. Another approach contrasting the slow-time treatment are the class of Particle-In-Cell (PIC) codes. Electrons are treated as point-wise macro particles moving through a mesh having magnetic and electric fields assigned to each node. Due to the high required time and frequency precision, the computational effort is greatly increased and is hence out of question for a gyrotron simulation.

The full-PIC approach can be used to validate the simplified design codes and investigate physical effects, but faces itself the inherent problems considering the formulation of proper boundary conditions, convergence and the non-trivial mode analysis afterwards. Under the quasi-PIC approach there are 2 1/2 dimensional PIC codes with azimuthal symmetry or fast design codes (trajectory codes) with PIC-style extensions. The quasi-PIC codes are located between the fast simplified design codes and the full-PIC codes. The first quasi-PIC code was the TUHH code (Technical University Hamburg-Harburg) [Jel00,JGS99]. It uses the PIC approach for the treatment of the electron beam, employs the aforementioned GSM approach, the field expansion in eigenmodes of the resonator and a physical model taking reflections into account. EVRIDIKI is a trajectory code offering PIC-style extensions.

The quasi-PIC approach of EVRIDIKI is used in this thesis to identify possible non-physical simulation results. This is done by checking the energy balance W_{bal} which should be smaller than 15% for a credible simulation result [Avr19].

Furthermore the code ARIADNE [PV04] is used in this thesis to calculate electron beam parameters which are then used in multi-mode interaction simulations with EVRIDIKI. ARIADNE allows the self-consistent calculation of electron trajectories using the finite element method (FEM) on curvi-linear meshes. It has its own scripting language to perform all steps from geometry and model definition, mesh creation and calculation of magnetic fields and beam parameters. It also can take into account the space charge neutralization and its effect on the beam parameters.

1.5.11 Experiment Setup and Data Acquisition

Each gyrotron of the W7-X ECRH plant is integrated in the central W7-X control and data acquisition environment (see figure 3.1). Gyrotron experiments can be performed either manually without W7-X Control using the beam dump or the gyrotrons are controlled remotely by W7-X Control as part of a W7-X experiment program. In the latter case, the RF power is directed into the torus. All relevant gyrotron experiment data like cathode and body voltage, cathode current, coil and filament heating currents, collector temperatures, ion-getter pump current etc. are stored in the W7-X ArchiveDB [HMG⁺16]. The ArchiveDB is a high-performance, scalable database storing continuously all technical and scientific data with various sampling rates of the Wendelstein 7-X experiment. In case of the gyrotron data, low resolution channels are sampled with down to 1 Hz and up to 1 MHz (high resolution). Most channels are sampled with 25 kHz (medium resolution) as default setting. A time window around the begin and the end of each pulse is acquired in a triggered manner with a high time resolution. The data can be accessed via an application programming interface (API) in Java or using the representational state transfer (REST) API of the web service and the programming language Python. The latter method is used throughout this thesis to download the experiment data from the W7-X ArchiveDB experiment data archive.

2 Hysteretic and Multi-Mode Behaviour

The present chapter investigates the hysteretic and multi-mode behavior of the W7-X gyrotron in multi-mode interaction simulations and experiments. The hysteretic gyrotron behavior [DII⁺03,DI08] after a loss of the nominal working mode is examined in multi-mode interaction simulations and in an experiment. The latter is done to demonstrate the feasibility of a fast oscillation or mode recovery during a gyrotron pulse. The critical acceleration voltages and beam currents for loss and recovery of the nominal gyrotron mode are extracted from a big parameter sweep exploring the working point plane. Since a mode loss due to emitter cooling was most frequently observed during the last experimental campaigns of W7-X, the emitter cooling is investigated in interaction simulations as well.

In the introductory chapter of this thesis, noise in gyrotrons and its effect on the operational stability was discussed. It was stated that extrinsic noise on gyrotron control parameters like coil currents and supply voltages could have the biggest effects on gyrotron mode stability in particular close to the mode switching regime where a mode loss is more likely. The quality of the supply voltages during gyrotron experiments is examined. The residual voltage ripple and the empirical probability distribution of the acceleration voltage noise are given based on the experimental data of more than 100 gyrotron pulses. Even though the acceleration voltage cannot be directly measured and other noise sources along the measurement chain contribute to the observed noise as well, the noise of the sum of the body and cathode voltage could serve as upper-limit for an estimation of the real noise. In an attempt to obtain a more realistic simulation, multi-mode interaction simulations with EURIDICE [APIV12] are performed with synthetic noise imposed on the acceleration voltage.

2.1 Nominal Mode Voltage Hysteresis

2.1.1 Simulations

The hysteretic gyrotron behaviour after a loss of the nominal operating mode is examined in multi-mode interaction simulations using the W7-X resonator geometry and a set of 34 modes including the nominal mode $TE_{28,8}$, its azimuthal neighbours and other parasitic modes which were identified in [Sch15]. Since a great number of simulations was performed for this thesis, the execution of the simulations for e.g. all combinations in a parameter sweep was automated for convenience. For this purpose, a wrapper and job manager for the gyrotron interaction code EURIDICE [APIV12] (named *pyEURIDICE*) was implemented in the programming language Python. It allows to automate more complex simulation scenarios each consisting of multiple steps (continuation runs). Multiple simulations can be run in parallel and a defined set of subsequent tasks is automatically performed. The most frequent task is a ramp for a simulation parameter, mostly the acceleration or beam voltage. Finally, all results from the individual simulations are aggregated in a simulation database allowing for an easier post-processing of the data for the visualization.

In order to examine the hysteresis of the nominal working mode in a simulation, two continuation runs are performed and concatenated. One for the startup and mode switch (ramping up the voltage) and another one for the possible recovery of the nominal working mode (ramping down the voltage). Figure 2.1 shows the simulation scenario for all simulations in the parameter sweep. The sweep parameters in this case are the reference electron beam pitch factor α_0 , the reference (cathode) voltage U_0 and the reference cathode current I_0 in the Schottky approximation. This means the pitch factor α reaches α_0 with $I_b = I_0$ and $U_{\text{cath}} = U_0$. Since the purpose of this study is to identify just the general trends (and not to exactly reproduce the experimental results), the Schottky approximation and no spreads are used to reduce the computational effort with regard to the large number of simulations.

Figures 2.2 and 2.3 show the results for $U_0 = 80 \text{ kV}$, $I_0 = \{38, \dots, 52\}$ and $\alpha_0 = 1.3$. Every line represents the result of a simulation run. The first onset of the nominal mode $TE_{28,8}$ is visible and the transition voltage increases non-linearly with increasing beam voltage. The region for stable mono-mode operation of $TE_{28,8}$ becomes smaller with increasing beam current.

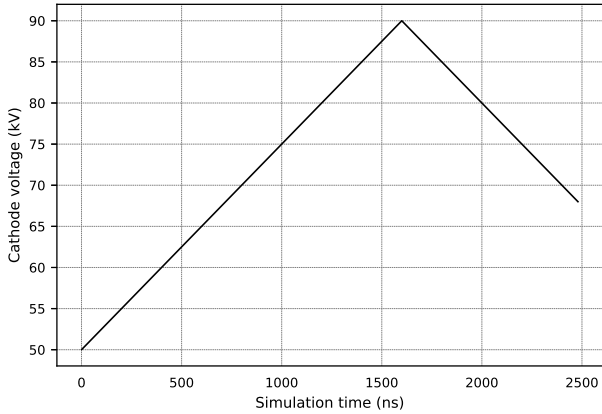


Figure 2.1: Simulation scenario to investigate the hysteretic gyrotron behaviour: concatenated voltage ramps for startup and mode loss and subsequent mode recovery.

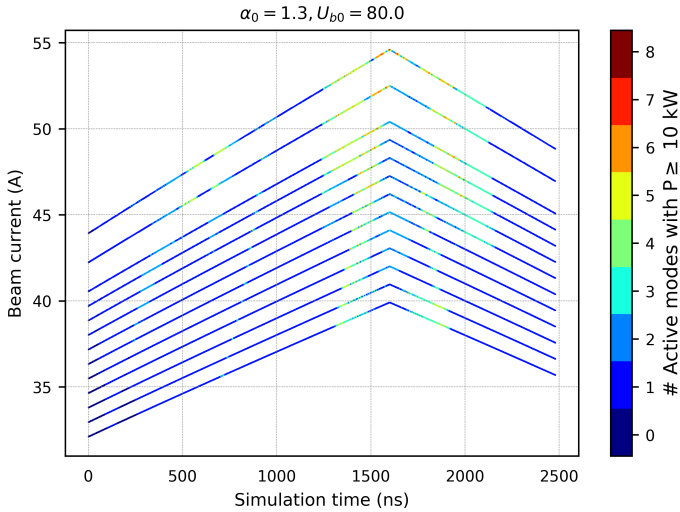


Figure 2.2: Number of simultaneously active modes with $P \geq 10$ kW (together with figure 2.3). The first onset of the nominal mode and the mode switching regime to the next azimuthal neighbour are visible.

If α is increased to pathological, hence unrealistically high values ($\alpha_0 > 1.3$), Figure 2.4 exhibits broadened mode transitions and negligible small regions for stable-mode operation (of the $TE_{28,8}$ mode).

Figure 2.5 shows the cathode voltages and beam currents for the mode loss and recovery. The mode loss voltage is taken here where an onset of multi-mode behaviour and a subsequent mode switch are observed. The mode recovery voltage is taken where a stable mono-mode operation of $TE_{28,8}$ is again achieved. The plot shows two distinct cases with an intermediate zone: For low beam currents (≤ 44 A), the mode switching regime seems to be rather short and the simulation predicts that a small voltage decrease (of 1 to 2 kV) would be sufficient to recover the nominal mode again. Such a regime was not observed in experiments (see also section 2.1.2). In a real gyrotron operation scenario, the beam current is higher at the begin of the pulse (hence at the end of the startup) due to the emitter cooling effect. Also electron beam parameter spreads, the effect of the depressed collector on the electron beam properties and the effect of extrinsic, technical noise from the supply voltages are neglected here. For higher beam currents, one passes an intermediate regime with prolonged multi-moding behaviour prior to the mode switch and a much larger voltage decrease (of 8 to 9 kV) is required to switch back to the nominal mode.

In order to obtain a more realistic result with parameters closer to the real-world gyrotron operation, the mode recovery simulation was repeated with a higher number of electrons spreads and more realistic beam parameters for α and γ and magnetic field profiles along the cavity computed with the code ARIADNE [PV04]. Figure 2.6 shows the result where a mode switch from $TE_{28,8}$ to its azimuthal neighbour or satellite mode $TE_{27,8}$ is observed at a cathode voltage of 87.5 kV. After a ramp down of around 10 kV, the nominal mode is recovered at 78 kV. The critical voltage where the mode switch is observed, is higher than in the gyrotron experiments because of the fact that the simulation did not take electron beam parameter spreads, the effect of the depressed collector or technical noise into account.

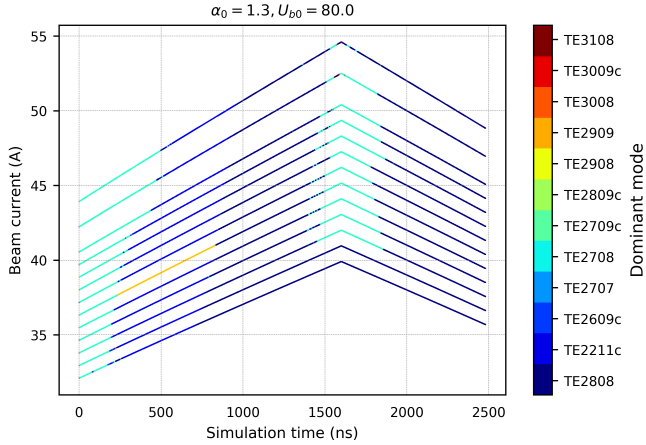


Figure 2.3: Dominant mode during the simulations. The mode transitions are visible. The region for stable mono-mode operation of $TE_{28,8}$ becomes smaller with increasing beam current.

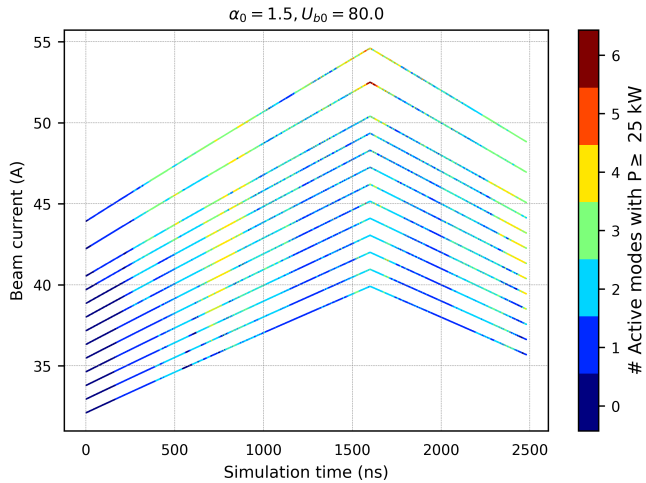


Figure 2.4: Number of simultaneously active modes with $P \geq 25$ kW. The region for stable mono-mode operation is negligible and the operation mostly is chaotic due to an increased α .

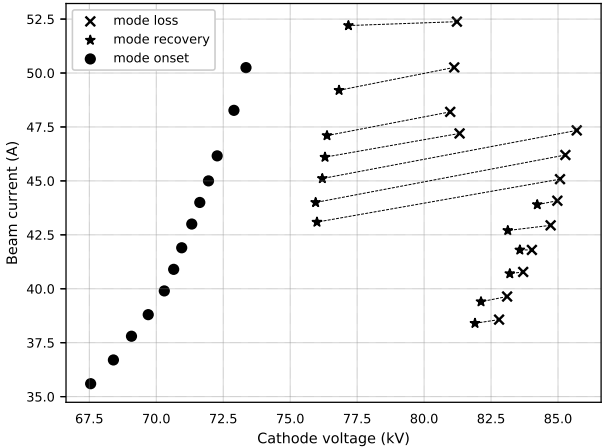


Figure 2.5: Extracted cathode voltages and beam currents for mode loss (=onset of multi-mode behaviour) and mode recovery (=return to stable mono-mode operation) from figure 2.2.

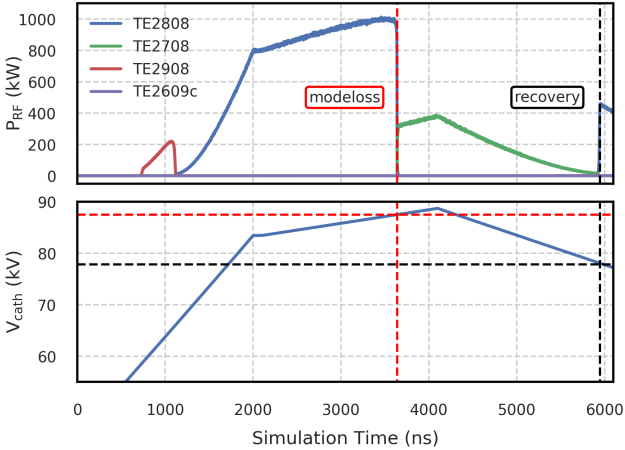


Figure 2.6: Multi-mode simulation of the hysteretic gyrotron behaviour with spreads for α , γ and beam parameters computed with ARIADNE. Mode switching behaviour and subsequent mode recovery of the nominal mode after a voltage decrease of around 9 kV.

2.1.2 Mode Recovery Experiment

In order to evaluate the feasibility of a fast oscillation or mode recovery during a gyrotron pulse, the following experiment was performed:

By a sawtooth modulation of the acceleration voltage $V_{\text{acc}} = V_{\text{body}} - V_{\text{cath}}$ (only the body voltage V_{body} was modulated, see Figure 2.7), the critical acceleration voltage for the nominal working mode TE_{28,8} is exceeded for the current beam current. Therefore, a mode loss is intentionally provoked in a repeated manner, but the mode was recovered subsequently. The voltages U_{body} and U_{cath} are measured using two separate high-voltage dividers directly at the high-voltage power supplies. The direct measurement of the technical, actual applied acceleration voltage is difficult [BBK⁺05]. The two HVPS types used for the body and the cathode voltage are discussed more in detail in section 2.3 where the technical noise is discussed.

The result of the mode recovery experiment is shown in figure 2.7. It was already published in [WLM⁺17]. The first author of the publication is also the author of this thesis.

It was observed that the voltage reduction after a mode loss has to exceed at least 8 to 9 kV in order to ensure a successful mode recovery. This indicates an acceleration voltage hysteresis for the nominal gyrotron working mode TE_{28,8}. The mode was repeatedly lost around 82.0 ± 0.2 kV and recovered during the subsequent ramp down around 75.5 ± 0.2 kV. The average required voltage difference amounted to 9.91 kV. In comparison to the more realistic simulation with spreads, a small deviation was observed for the required voltage decrease (9.65 kV vs. 9.91 kV).

Judging the experimental result, it should be possible to implement a fast oscillation recovery after a mode loss as a fast gyrotron controller. This way, the complete gyrotron startup scenario with several mode hoppings could be avoided in comparison to a complete temporary shutdown of the gyrotron (with a reduction of the supply voltages to zero) implemented by others (see e.g. [PBC⁺18]) or [WSL⁺16].

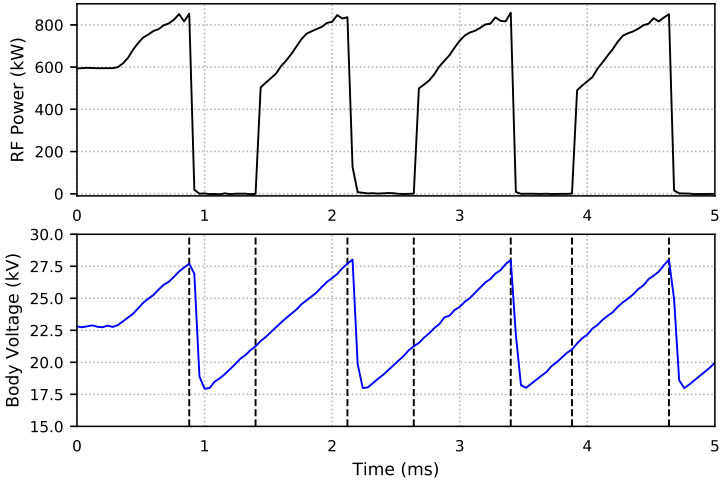


Figure 2.7: Mode recovery experiment with the Bravo 5 (TED SN002i) tube. Repeated intentional mode loss and successful subsequent recovery with a sawtooth-modulated body voltage. The acceleration voltage reduction after mode loss has to exceed 9 kV to ensure a successful mode recovery indicating a hysteresis. The dashed line indicates the moment of mode loss.

2.2 Emitter Cooling Behaviour

The emitter cooling phenomenon, the fast decrease of the cathode current after the begin of the pulse, was for example observed prior to a loss of the nominal operating mode during the experiment programs and the dedicated gyrotron experiments performing long gyrotron pulses ($\tau \gg 1$ s) at W7-X. The emitter cooling is therefore investigated in multi-mode interaction simulations to observe a possible multi-moding behaviour prior to a mode loss when the nominal mode break current is approached.

In order to simulate the emitter cooling in EURIDICE [APIV12], the simulation scenario contains two steps: The first step is a mode startup with increasing voltage and beam current to $U_{\text{cath}} = U_0$ and $I_b = I_0$. The emitter cooling behaviour is then approximated by the so-called "fake ramps", allowing to simulate a drop in beam current with technically constant acceleration voltage. The same number of electrons and the Schottky approximation without spreads for α or γ were used as in the previous section.

Figures 2.8 and 2.9 show the simulation results for the emitter cooling with a fixed reference beam voltage U_{b0} . The mode switch to the nominal mode is visible during the startup (first half). The general trend of an increasing break current for the nominal mode (minimum required beam current to support the nominal mode) is visible during the emitter cooling (second half). Decreasing the current has a similar effect as increasing the voltage. But in this case, the mode switch is approached more slowly by the decreasing current and the transition zones are prolonged. This way multi-moding behaviour could become observable in an experiment since it would appear on a longer time scale. Figures 2.10 and 2.11 draw a more differentiated picture: The simulation results for different reference voltages are shown here, while the reference current is held constant. First, a non-linearly increasing current is visible where first multi-mode behavior occurs. On the other hand, the actual mode switch where the azimuthal neighbour mode $TE_{27,8}$ takes over, seems to happen at a much lower current. This is a contradiction compared with the experiment where the mode switch is observed already at higher currents above 40 A. Note that this simulation is strongly simplified since no spreads and no realistic beam parameter curves were used. Furthermore, the emitter cooling is only taken into account by a decreasing beam current. Other effects on the electron beam parameters from a decreasing emitter temperature are neglected.

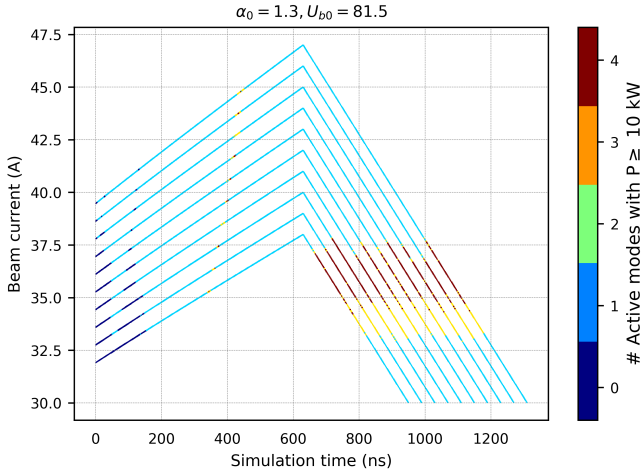


Figure 2.8: The number of simultaneously active modes for startup and subsequent emitter cooling simulation for $U_0 = 81.5$ kV and various reference beam currents. Multi-moding behaviour is visible with decreasing current.

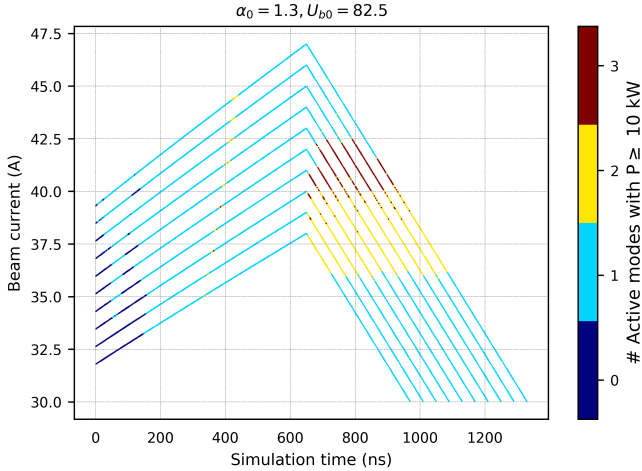


Figure 2.9: The number of simultaneously active modes for startup and subsequent emitter cooling simulation for $U_0 = 82.5$ kV and various reference beam currents. Multi-moding behaviour is visible with decreasing current.

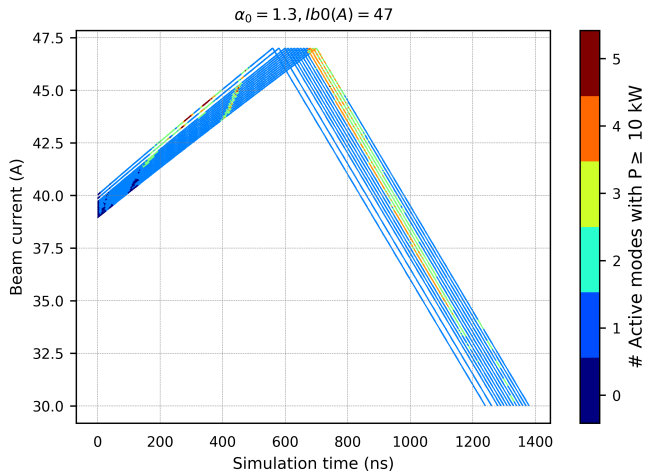


Figure 2.10: The number of simultaneously active modes for startup and subsequent emitter cooling simulation for $I_0 = 47$ A and various reference cathode voltages. Multi-moding behaviour is visible with decreasing current.

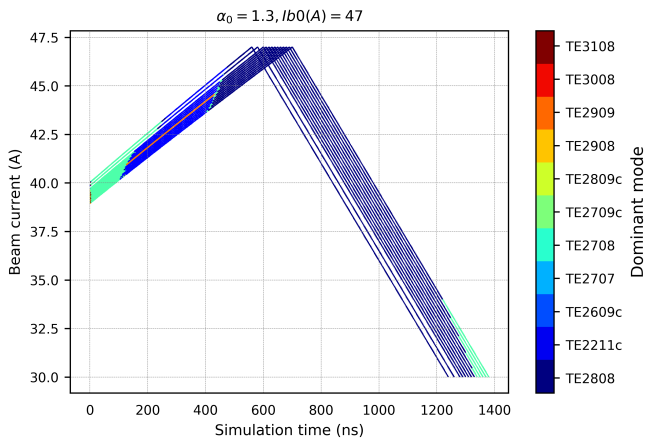


Figure 2.11: Dominant mode during startup and subsequent emitter cooling simulation for $I_0 = 47$ A and various reference cathode voltages. Although multi-moding was visible very early at higher currents in figure 2.10, the actual mode switch happens at a much lower current.

2.3 Impact of Technical Noise

As stated in section 1.5.7, extrinsic technical noise of external operation parameters has the strongest impact compared to all other intrinsic noise sources of the gyrotron. In practice, the technical noise of the acceleration voltage can have in particular a significant impact on the gyrotron mode startup and mode stability near the mode switching regime at the maximum output power of the gyrotron [DN97]. A safety margin for the acceleration voltage is therefore often applied for the gyrotron operation [ARM⁺19]. Hence, noise amplitude, voltage ripple and overshoot should be minimized in the design of power supplies for gyrotrons to ensure a stable operation.

In case of W7-X, the main high voltage power supply is a solid-state switching power supply based on the Pulse Step Modulation (PSM) principle [BBK⁺05]. It consists of 84 IGBT (Insulated Gate Bipolar Transistor) modules connected in series. An IGBT is a high-power semiconductor switch suitable for high forward currents [LSSD11]. The output voltage can be controlled by switching the individual IGBT modules in series on or off. In order to suppress voltage noise in the supply voltage, a low pass filter with a cutoff frequency around 100 kHz was used [BBK⁺05]. Despite using a low pass filter, a significant amount of noise and a residual ripple voltage are visible in the signal as shown in Figure 2.12.

The properties of the extrinsic, technical noise from gyrotron experiments performed at W7-X are investigated first with data from a large number of gyrotron pulses. Although the acceleration voltage could not be measured directly (no direct measurement point is available without time-consuming modifications) and other noise sources (mainly signal conversion (optical/coaxial), AD-conversion and possible cross talk between long signal lines) along the measurement chain surely contributed to the observed noise, the simple sum of the body and the cathode voltage could serve as a worst-case, upper estimate for the real noise. Then multi-mode gyrotron interaction simulations with Gaussian (white) noise and synthetic noise, imposed on the acceleration voltage, are performed here for the first time to study the mode switching hysteresis and the multi-mode behaviour.

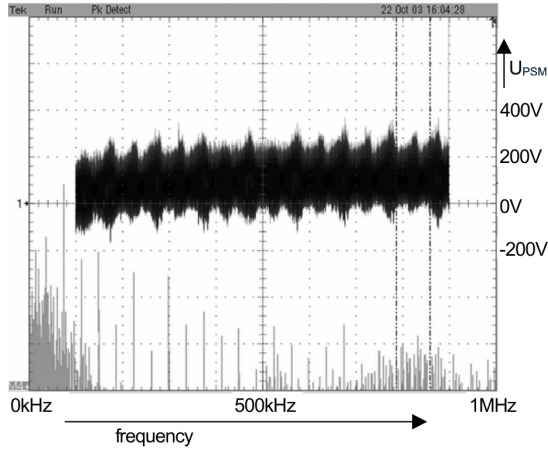


Figure 2.12: Excerpt of the measured PSM output voltage: time trace (above) and noise frequency spectrum (below) from [BBK⁺05].

2.3.1 Empirical Noise Distribution

The statistical terms probability $p(x)$, probability density function (PDF) $f_X(x)$, percentile $p_{k\%}$ and median μ of a random sample X which are used in the following, relate to each other as follows

$$1 = \int_{-\infty}^{\infty} f_X(x) dx \quad (2.1)$$

$$p(y \leq X \leq z) = \int_y^z f_X(x) dx \quad (2.2)$$

$$p(X \leq y) = \int_{-\infty}^y f_X(x) dx \quad (2.3)$$

$$y = p_{k\%}(X) \leftrightarrow p(X \leq y) = \frac{k}{100} \% \quad (2.4)$$

$$\mu = p_{50\%}(X) \quad (2.5)$$

The first equation shows the normalization property of a probability density. The second equation gives the probability to find a value in the interval $[y, z]$.

The percentile $p_k \%$ is the threshold below which $k \%$ of the values of the random sample are located. The 50 % percentile $p_{50\%}$ is called median μ which is the value most likely to occur. The popular standard deviation σ assumes normal-distributed values. In contrast, the percentile can be reasonably applied to random samples whose values can have any kind of probability distribution (also skewed or asymmetric). In the limit of a large sample size $N \rightarrow \infty$, the normalized histogram can approximate the underlying PDF of the random variable as implied by (Borel's) law of large numbers.

Figure 2.13 and 2.14 show the (zoomed) the body, cathode and resulting sum voltage (as substitute or estimate for the acceleration voltage signal which was not available) along with the cathode current and the RF output power signal. The red dashed envelope lines denote the 10 % and 90 % percentiles for a moving window over the signal with a duration of 20 ms. The red solid line in between is the moving median over the same duration. Hence, the percentile difference could be interpreted as the noise voltage peak-to-peak value. In the time signals, a phase delay between the body and the cathode voltage is visible leading to a modulation of the noise amplitude or noise distribution width. Also without noise (the moving median), a significant voltage ripple is visible.

The statistical properties of the acceleration voltage noise were determined with data from 110 gyrotron pulses performed with the Alpha 1 tube with a duration of up to 20 s. The noise signal is computed as difference between the actual acceleration voltage value $V_{\text{acc}}(t_n)$ and the moving median over a window with a duration of 20 ms. Thus, the voltage ripple is interpreted to be independent from the noise and not seen as consequence of the super-imposed noise of the body and the cathode voltage. The mean ripple voltage without noise (using the moving median) over all shots is 0.24 kV. No obvious correlation was visible between the ripple voltage and the working point ($V_{\text{acc}}, I_{\text{cath}}$). The slow modulation of the acceleration voltage manifests itself also in the power spectral density (PSD) of the noise signal as shown in figure 2.15. The PSD was estimated using Welch's method [Wel67] with an overlap of 0.1 and 2^{16} values per segment. The Python implementation of Welch's method from the SciPy library (<https://docs.scipy.org/doc/scipy/reference/>) was used to compute the PSD.

The most dominant frequency contributions are located at 4.3 Hz, 34 Hz and odd multiples of the power grid frequency of 50 Hz where 150 Hz is the strongest. High-frequency contributions around 6 kHz and 12 kHz could originate from the switching power supply. The PSD of white (Gaussian) noise is also shown for comparison and is near zero across all frequencies as expected.

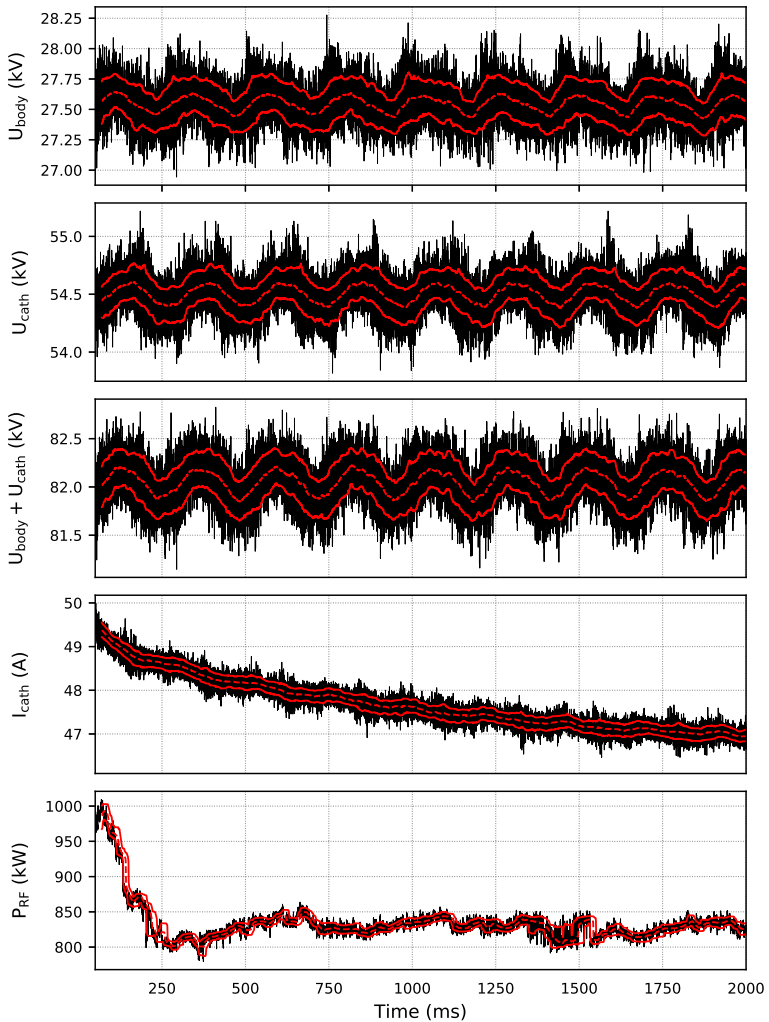


Figure 2.13: Body U_{body} , cathode U_{cath} , resulting sum voltage signal $U_{\text{body}} + U_{\text{cath}}$, cathode current I_{cath} and RF output power signal from a gyrotron experiment. Red envelope lines denote the $p_{10\%}$ and $p_{90\%}$ percentiles of a moving window with a duration of 20 ms. The red dashed lines denote the moving median over the same window duration. Apparent slow modulation in voltage, cathode current and RF signals. A phase delay between the body and cathode voltage is observed.

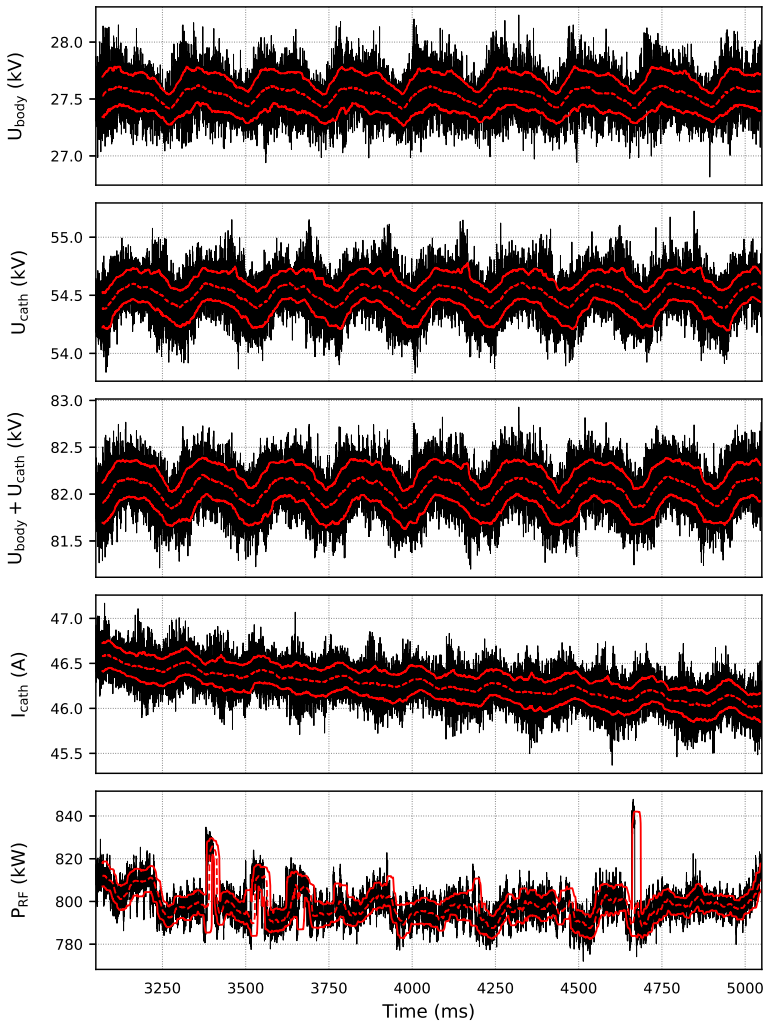


Figure 2.14: Zoomed body U_{body} , cathode U_{cath} , resulting sum voltage signal $U_{\text{body}} + U_{\text{cath}}$, cathode current I_{cath} and RF output power signal from a gyrotron experiment. Red envelope lines denote the $p_{10\%}$ and $p_{90\%}$ percentiles of a moving window with a duration of 20 ms. The red dashed lines denote the moving median over the same window duration. Apparent slow modulation in voltage, cathode current and RF signals. A phase delay between the body and cathode voltage is observed.

noise type	percentile [%]	$p_{x\%}$ [kV]
observed	90	0.216
	99	0.438
	99.9	0.609
	99.99	0.751
	99.999	0.879
white	90	0.225
	99	0.408
	99.9	0.542
	99.99	0.652
	99.999	0.749

Table 2.1: Comparison of percentiles for the observed noise and synthetic white (gaussian) noise with the standard deviation of the observed noise.

Figure 2.16 shows the logarithmic probability density functions (PDF) of the observed acceleration voltage noise during all pulses compared to the log PDF of synthetic white noise. $5 \cdot 10^7$ values in total were used for both cases, so that the histograms approximate well enough the PDFs. The observed noise PDF is obviously not purely Gaussian, but has fat tails for values bigger than 0.5 kV. The percentiles are compared for the observed noise and white noise in Table 2.1. The generated white noise has the same standard deviation computed from the observed noise (assuming the observed noise would be Gaussian). This gives an impression how big the voltage overshoot due to noise is at a given probability level.

For example, 99.99 % of the values for the observed noise are ≤ 0.751 kV. In contrast for the synthetic white (Gaussian) noise, 99.99 % of the values are ≤ 0.652 kV. We could also invert the question by asking:

How big is the probability $S_X(x) = 1 - F_X(x) = p(X > x) = 1 - p(X \leq x)$ that the noise voltage (overshoot) is bigger than x ?

$S(x)$ is called the survival function and $F(x)$ is the cumulative distribution function (CDF) of the random sample. The CDF $F_X(x)$ gives the probability that a random value X of the sample is smaller or equal to x , hence $F_X(x) = p(X \leq x)$. In case the analytic expression for the PDF is unknown, the empirical cumulative distribution function (ECDF) can be easily determined. The result is compared for both noise types in figure 2.17.

To give some numbers: the probability that the noise voltage is bigger than 0.5 kV is 0.43 % (observed) vs. 0.2 % (synthetic white noise). For a noise voltage bigger than 0.75 kV the difference is one order of magnitude, 0.01 % (observed) vs. 0.001 % (synthetic white noise). The probability of 0.43 % seems small, but actually means for a sampling frequency $f_s = 25$ kHz that every 243 samples or 9.3 ms, at least one sample with a noise voltage ≥ 0.5 kV is observed. This is of importance in particular when the gyrotron is operated close to the nominal mode cutoff. A more detailed investigation of the various noise sources along the measurement and data acquisition chain is necessary to distinguish the superimposed, additional noise from the real noise present on the gyrotron supply voltages. Of course, in the example above, the contribution of the noise introduced by the data acquisition system (e.g. noise introduced by AD-conversion, quantization noise) is neglected.

Figure 2.18 shows the noise percentile difference, hence the peak-to-peak noise voltage during an exemplary 20 s shot (hence the slow modulation by the residual voltage ripple is not taken into account). From this plot, we can conclude that a safety margin of at least 0.6 to 0.7 kV (0.2 kV ripple + 0.5 kV noise) is necessary here in particular close to the mode switching regime of the nominal mode. During the last maintenance of the power supplies by the company Ampegon, the noise voltage was determined to be around 400 V_{pp} (peak-to-peak) [Mue]. A part of it is compensated by the body voltage modulator. This is close to the mean of the $p_{90\%} - p_{10\%}$ percentile difference determined here. In fact, the $p_{99\%} - p_{1\%}$ percentile difference is in agreement with experiences operating gyrotrons at W7-X where on average a safety margin for the acceleration voltage of at least 1 kV is used (depending on the gyrotron). A voltage safety-margin of 2 kV is proposed in [ARM⁺19] for a possible future 1.5 MW conventional-cavity gyrotron. Though, it cannot be excluded that the real noise is super-imposed by noise from the hardware used for the AD conversion and data acquisition.

For the following multi-mode interaction simulations with noise, synthetic noise is generated using the inverse ECDF of the observed noise PDF. The PSD of the observed noise is not reproduced this way, but this would not be reasonable as well since the simulation time scale is orders of magnitude smaller than the time scale of the noise modulation. The PSD could be reproduced using the Lanczos algorithm [LG75] or other methods. Anyway, by reproducing the observed noise in the multi-mode interaction simulations, more realistic results could be expected.

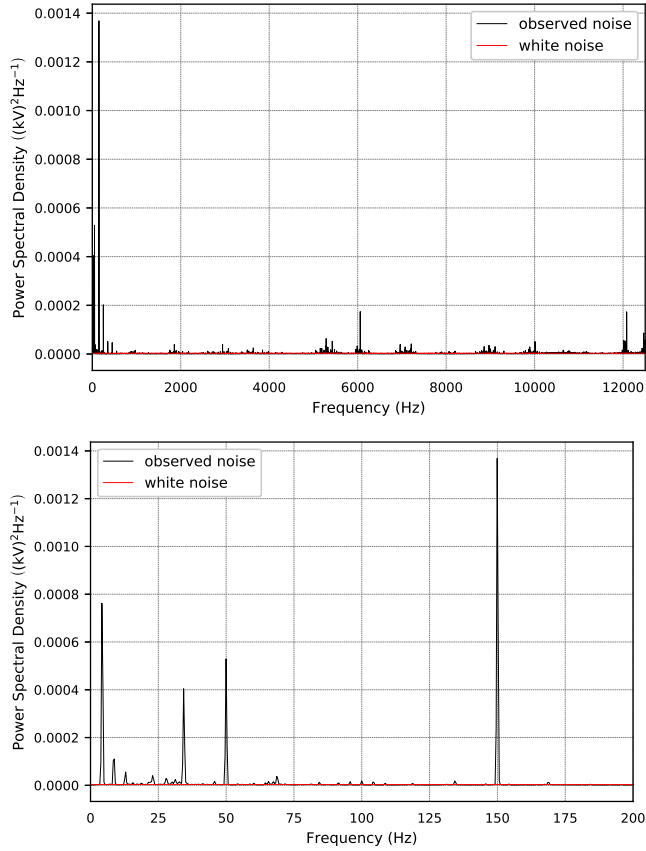


Figure 2.15: The power spectral density of the sum voltage $U_{\text{body}} + U_{\text{cath}}$ noise obtained with Welch's method (overlap 0.1, 2^{16} values per segment). Most prominent frequency components around 4.3 Hz (see figure 2.13), 34 Hz and odd multiples of 50 Hz from the power line.

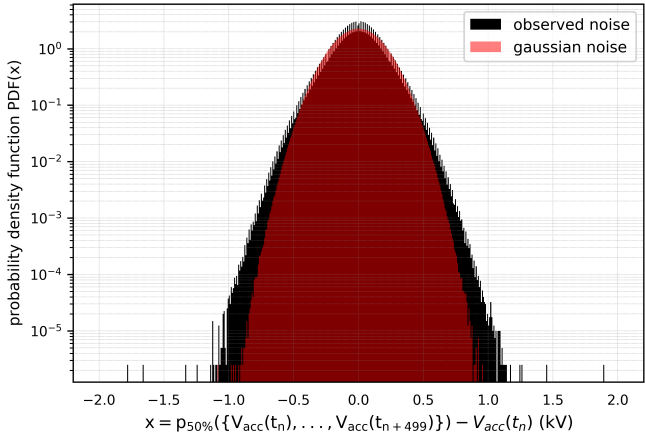


Figure 2.16: Comparison of the probability density functions (PDF) for the observed noise of the acceleration voltage and random Gaussian (white) noise using $5 \cdot 10^7$ values. The vertical axis is logarithmic. The observed noise PDF is not purely Gaussian, but has tails for values bigger than ± 0.5 kV.

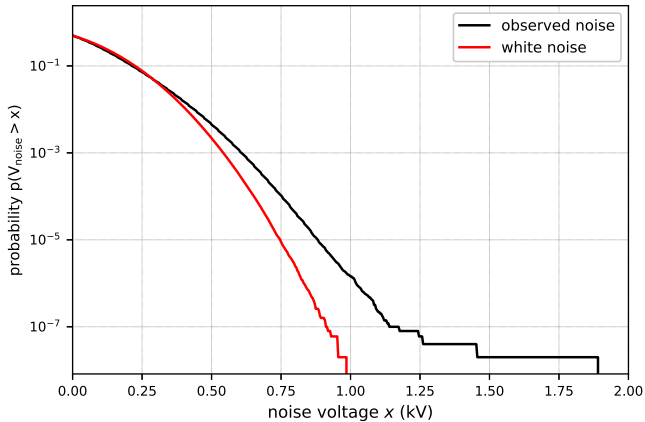


Figure 2.17: Comparison of noise voltage threshold probabilities for observed and synthetic white noise. For a noise voltage > 0.3 kV the probabilities diverge. The probability for a noise voltage of 1 kV is about two orders of magnitude bigger for the observed noise compared to white noise.

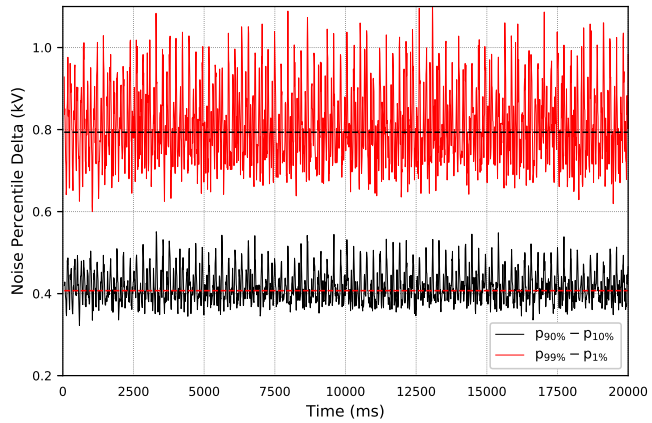


Figure 2.18: Percentile differences of the noise for a moving window with a duration of 20 ms. The dashed lines indicate the mean value over the time period.

2.3.2 Simulations

Multi-mode interaction simulations with EURIDICE were performed with technical noise imposed on the cathode voltage. The results are compared for white noise (using a normal distribution with different standard deviations) and synthetic noise based on the empirical noise distribution presented in the previous section. The effect of noise on the mode switching is examined. In this case, the simulations were performed with spreads (about 2000 electrons) and a more realistic $I_b - \alpha$ curve from ARIADNE for a rather low current of 38 A at 80 kV.

Figure 2.19 shows the mode switch from $TE_{28,8}$ to $TE_{27,8}$ and the recovery to the nominal mode for various noise levels, hence standard deviations σ for the normal distribution, imposed on the cathode voltage. Only a slight difference is visible between the noise levels with the tendency to an earlier mode switch and earlier mode recovery with increasing noise amplitude. Figure 2.20 shows an excerpt around the first mode switch $TE_{28,8} \rightarrow TE_{27,8}$ exhibiting an elevated background noise level for increasing standard deviation. The simulation with the empirical noise probability distribution leads to a slightly earlier growth of power in a satellite mode compared to Gaussian white noise.

In order to give a well-founded statement about the effect of the technical noise on the mode switching behaviour and (nominal mode) stability, the simulations for the noise levels need to be repeated for a statistically significant number, a higher beam current and an increased pitch factor.

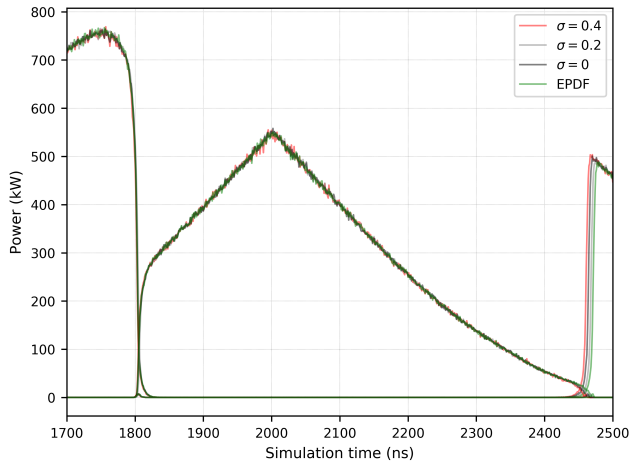


Figure 2.19: Multi-mode simulation of the mode loss and recovery with higher electron count, spreads and $I_b - \alpha$ curve from ARIADNE (38 A at 80 kV) for various noise levels imposed on the cathode voltage. Only the nominal mode $TE_{28,8}$ and its satellites $TE_{27,8}/TE_{29,8}$ are shown.

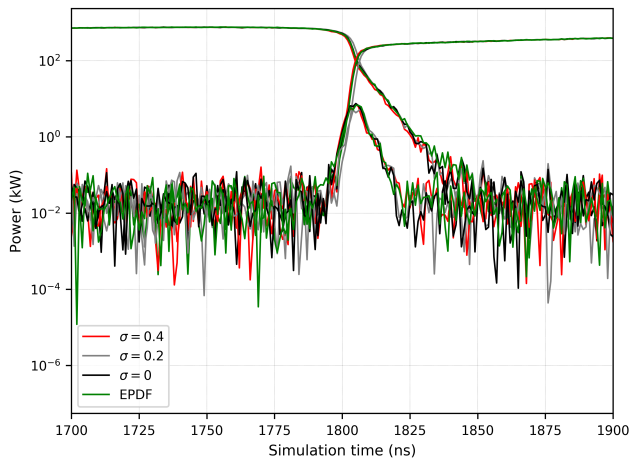


Figure 2.20: Zoom of figure 2.19 with logarithmic y-axis for the mode switch $TE_{28,8} \rightarrow TE_{27,8}$. An elevated background noise for other modes and a slightly shifted mode switching is observed for an increasing standard deviation of the noise.

2.4 Summary

Multi-mode interaction simulations of the mode switching behaviour were performed to investigate the hysteretic gyrotron behaviour after a loss of the nominal mode. The results show a varying required voltage decrease between 2 kV up to 10 kV in order to recover the nominal mode after a mode loss. A more realistic interaction simulation with a higher electron count, spreads and a realistic $I_b - \alpha$ curve from ARIADNE yielded a higher required voltage decrease of 9.6 kV. An experiment was performed to demonstrate the technical feasibility of the mode recovery. The mode was repeatedly recovered reducing the voltage on average by 9.9 kV which confirms the prediction given by the simulation.

The emitter cooling was simulated since it is one of the most frequent causes for mode loss during gyrotron pulses at W7-X. The simulations predict a multi-moding behavior with decreasing beam current over extended time periods. The mode switching is predicted to happen at much lower beam currents (below 38 A) compared to the observations in experiments (see also Figure 3.5). This could be explained with the drastically simplified simulation model without spreads for α or γ using the Schottky approximation, the absence of technical noise in the simulation and the simplified representation of the emitter cooling effect in the simulation ramping down the cathode current to reduce the computational effort.

3 Automated Mode Recovery

Based on the findings presented in the previous chapter, an algorithm for an automated recovery of the nominal working mode (a fast oscillation recovery) during the gyrotron pulse after a mode switch to the competing satellite is developed. In this chapter, the automated mode recovery (MORE) algorithm and its implementation on a field-programmable gate array (FPGA) as finite state machine (FSM) are presented. Based on experiments performed with MORE, the gain in terms of gyrotron performance and reliability using MORE are evaluated in a first statistical analysis. The impact on gyrotron reliability during the last experimental campaign OP1.2b at Wendelstein 7-X is also presented in a statistical analysis for nine out of ten gyrotrons. This is the first gyrotron reliability analysis for the ECRH facility of a large-scale experiment with regard to its extent of the experimental data used. The contents of sections 3.2 have been already published in parts in [WMS⁺ 19]. The first author of that paper is also the author of this thesis.

3.1 Gyrotron Controller

The automated mode recovery uses the already existing gyrotron controllers at W7-X. Each gyrotron has its own controller implementing the fast real-time control of the high voltage power supplies (body and cathode voltage power supply), gyrotron output power modulation and fast gyrotron protection interlocks invoking the immediate shutdown of the gyrotron to avoid damages. An example for such a fast protection interlock is the so called "RF interlock". It is triggered when a gyrotron pulse is running (hence supply voltages are switched on), but no RF output power is measured for a time period longer than the RF grace time (default value 2 ms). An RF interlock often occurs during the pulse due to loss of the nominal operating mode or as consequence of arcing inside the gyrotron or outside along the QO transmission line. Each

gyrotron controller works independently for dedicated gyrotron experiments, but also remotely controlled by the central W7-X control for W7-X experiment programs. Slow control tasks ($\gg 1$ ms, e.g. magnet, cathode heater) and interlocks are realized using conventional programmable logic controllers (PLC) for industrial applications (Siemens Simatic S7) which are connected via Ethernet to the gyrotron controller. These aforementioned functionalities were first implemented in a gyrotron controller developed by IPP in 2011 based on an open-source FPGA implementation of a real-time Java Virtual Machine (JVM) [MS11]. Due to the error-prone architecture, difficult handling and no-longer guaranteed hardware maintainability (e.g. the Altera Cyclone FPGA which is used, has reached end-of-life (EOL) status), the gyrotron controller functions were ported to a National Instruments compactRIO 9039 using LabView FPGA [MWC⁺17]. This is an Intel Atom based real-time Linux system combined with a FPGA and configurable input/output modules which is fully integrated in the National Instruments LabView environment.

Figure 3.1 shows the overview of the ECRH control system for a single gyrotron and how the gyrotron controller is connected to the power supplies and the periphery. The set point values for the acceleration and cathode voltage supply are set separately, as well as there are distinct gate signals for the two HVPS (main / cathode and body power supply). The body power supply receives a set point for the acceleration voltage. The acceleration voltage is then internally feedback controlled measuring both the cathode and the body voltage and acting on the body voltage. The HVPS allow the quasi real-time control of the acceleration voltage during the pulse. The set point values for both voltages are stored in a ring buffer on the FPGA. How a change of the acceleration voltage is shared among body and cathode voltage modulator for the voltage ramps during MORE cycles is defined by a parameter (typically set to 0.5) defining a $U_{\text{body}}/U_{\text{cath}}$ voltage ratio. During normal operation, the cathode and the acceleration voltage are linearly controlled within the defined limit values resulting in a previously defined, fixed depression ratio. The signal " μ -wave power" denotes the signal for the nominal mode at 140 GHz measured at the periphery of the RF output beam waist using a RF detector diode. The output voltage signal is power-calibrated with long gyrotron pulses using a (rather inert) calorimeter. This signal is used for the fast protection RF interlock to shutdown the gyrotron in absence of RF power in the nominal working mode during a pulse. In order to reduce the sensitivity of MORE towards noise, the measured diode signal is buffered and averaged to obtain a more stable signal. This does not hold true for the RF interlock to guarantee a very low latency.

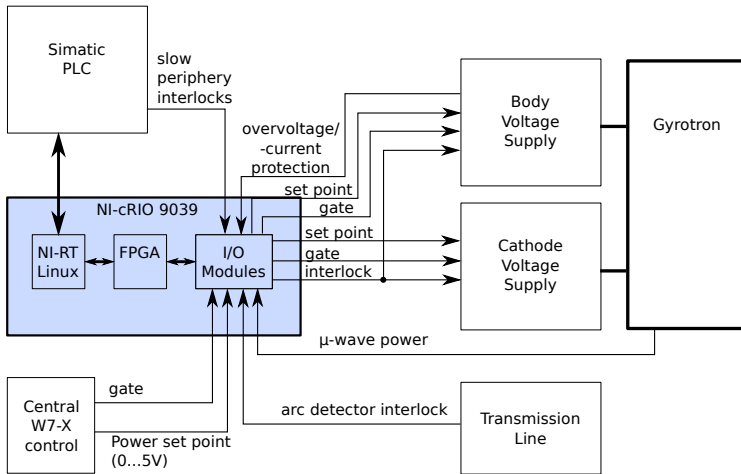


Figure 3.1: Overview of the ECRH control system showing the gyrotron controller and its connections to the power supplies and W7-X central control (from [MWC⁺17]).

The RF signal is connected to a fast analog input module (up to 1 MS^{-1}) as shown in Figure 3.2. Seven more analog inputs with high sampling rate are available for future extensions. The gyrotron controller can be administered conveniently with a web interface.

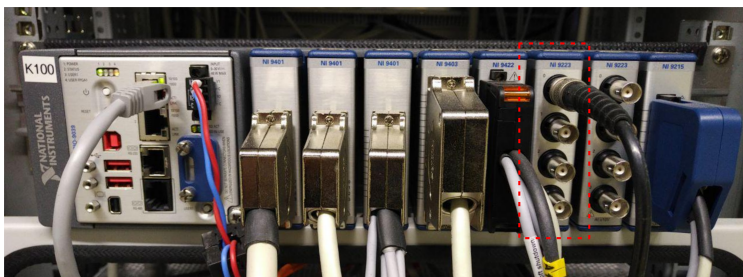


Figure 3.2: Photo of the new gyrotron controller based on a National Instruments cRIO 9039 with plugged-in input/output modules. The fast analog input module is highlighted (own work).

3.2 FPGA Implementation

As found in the investigations of the previous chapter, the gyrotron exhibits a strong hysteretic behaviour after a mode switch to the competing satellite. A simple, small reduction of the acceleration voltage is insufficient to recover the nominal mode. The reduction of the acceleration voltage has to exceed a certain threshold value depending on the pulse history and therefore on the past trajectory in the gyrotron parameter space. The MORE algorithm acts on the acceleration voltage since this parameter can be controlled very fast and it has an immediate effect (μs time scale). The required time to change other gyrotron parameters and the time delay of a reaction to such a change of e.g. the coil currents (coil currents are ramped slowly) or the filament heater current (thermal inertia of the emitter) is much greater (ms to multiple seconds). This is by all means too slow since the available time to recover the nominal mode is constrained by the collector heat load. Therefore a RF grace time (typically 2 ms which is very conservative value) is defined. The attempts to recover the nominal mode should not require more time in order to protect the gyrotron against thermal damage when operated too long on the false (satellite) mode. MORE can act on both the body voltage and the cathode voltage. As mentioned above, the ratio how an acceleration voltage change is shared between the two, can be adjusted via a parameter. As shown in [WLM⁺17], it is also possible to recover the nominal mode by a modulation of the body voltage only (changing the collector depression ratio).

In order to reliably recover the nominal mode, the following mode recovery algorithm is proposed and was implemented as FSM on the FPGA of the gyrotron controller [WMS⁺19]:

1. Wait for clearance. Clearance is given if MORE is enabled and a pulse is running longer than a defined ignore period (typically 20 ms to 100 ms). The "ignore period" or delay time is a defined time period after which the MORE algorithm is allowed to act on the acceleration voltage. If clearance is given, go to step 2.
2. Wait for a mode loss indicated by a RF interlock state. If clearance is lost because another interlock occurred due to e.g. arcing, body current fault or the pulse has ended, go back to step 1.
If a mode loss occurs, store actual acceleration voltage $U_{\text{ML},n}$ and relative

time of the mode loss during the running pulse. Check if this is the first mode loss in the current pulse ($n = 0$). If false,

- a) compute time distance Δt to the previous mode loss.
- b) check if time distance Δt is bigger than a defined minimum time distance Θ between subsequent mode losses. If true, go to step 3, else go to step 6 and set MORE into a halt state.

else continue and go to step 3. In order to avoid continuous mode recovery attempts and minimize the duty cycle for the gyrotron operating on the false mode or without emission, this safety measure was implemented. Otherwise the increased collector heat load and the additional heat loads for other gyrotron components could lead to a decreased lifespan.

3. Perform fast ramp down (RD) of the acceleration voltage (within $\leq 100 \mu\text{s}$) to the target voltage $U_{RD,n} = U_{RD,n-1} - \Delta_{RD}$ where $U_{RD,0}$ is the default target for the first mode recovery attempt (typ. 71 kV) and Δ_{RD} a defined voltage step (typ. 0.1 ... 1 kV). The minimum ramp down target is the minimum allowed acceleration voltage of typ. 65 kV since this is the hard-coded lower limit in the low-level Programmable Logic Controller (PLC). The index n is incremented and hence $U_{RD,n}$ is decreased after each unsuccessful mode recovery attempt. If clearance is lost during the ramp down (e.g. because the RF grace time is over), go back to step 1, else continue to step 4.
4. Perform fast ramp up (RU) of the acceleration voltage with a defined duration (typ. 300 μs) to the target value $U_{RU,n} = U_{ML,n} - \Delta_{RU}$ where Δ_{RU} is a defined voltage step (typ. 0.1 ... 1 kV). The shortest possible ramp duration is only limited by the achievable slew rate of the HVPS (here at W7-X 4 $\mu\text{s}/\text{kV}$).
If the clearance is lost during the ramp up, go back to step 1. If the mode is still active at the end of the ramp up (and hence was successfully recovered), continue to step 5 else try again and go back to step 3.
5. Perform another slow (power) ramp up (PRU) either with
 - a) a constant defined slew rate SR_0 (typ. 20 ... 100 ms / kV)

- b) a variable slew rate $SR_n = SR_{n-1} + \Delta SR$ with $\Delta SR \approx 0.1SR_0$ after each consecutive mode loss during the pulse

where the target value for the (power) ramp up is either

- a) the momentary set-point value $U_{PRU,n} = U_{acc}(t_n)$, if the algorithm priority is maximum output power
- b) $U_{PRU,n} = U_{ML,n} - \Delta_{PRU}$ with Δ_{PRU} being a defined voltage step (typ. 0.2 ... 1 kV), if the algorithm priority is operational stability. The acceleration voltage is limited to $U_{PRU,n}$ afterwards for the remaining pulse in order to avoid any further mode loss.

In case another mode loss occurs during the (power) ramp up, try again and go back to step 2. If the (power) ramp up has finished and the mode is still active, also go back to step 2 and wait for another mode loss to happen.

- 6. Wait for the end of the current pulse or the RF grace time period. This is a kind of halt state for the MORE algorithm. MORE remains inactive till the end of the current pulse. If the clearance is lost, go back to step 1 and wait for another pulse to begin.

Figure 3.3 illustrates the mode recovery algorithm with a state diagram including the intermediate preparatory states (Prep#) before (to compute necessary values) and wait states (Wait#) after each ramp. Transitions back to the state "wait clear" (equivalent to step 1 of the algorithm description) were omitted in the diagram for the sake of clarity and comprehensibility. Furthermore the states "wait RFint", "RD", "RU" and "PRU" equal steps 2, 3, 4 and 5 respectively in the description of the algorithm.

The externally given, actual set point values during the pulse are stored in two ring buffers for the body and the cathode voltage each with a size of 2^{14} values. A floating-point precision of 16 bits was chosen, since it turned out during experiments that rounding errors lead to missed voltage ramp target values.. The MORE algorithm intervenes by overwriting the externally given set point values in the ring buffer during MORE cycles. The ignore period introduced in step 1 of the algorithm defines a minimum pulse length before MORE is responsive. This is done for multiple reasons: First to guarantee the neutralization process is finished to support a successful mode recovery. Second to minimize the false mode duty cycle. MORE was intended to be used for longer

and long pulses (or cw operation) only. Using MORE for short pulses could lead to a high false-mode duty cycle, if the minimum time distance Θ between subsequent mode losses is set to a small value. By adjusting the minimum allowed time distance Θ between subsequent mode losses, the slew rate SR_0 for the 2nd power ramp up and the voltage step Δ_{PRU} , the expected false-mode duty cycle can be controlled.

Since the cathode current drops during the first seconds of the pulse (despite a boosted filament heating current) and the critical acceleration voltage U_{ML} (where the nominal mode is lost) was observed to follow the decreasing current, step 5b was introduced in the algorithm.

Figure 3.4 presents an example for a MORE cycle during a pulse from an experiment with the Alpha 1 (TED SN007) tube. Due to the time delay between the body and the cathode voltage modulator (typically 50 to 100 μs) and the time required to process the buffer of the RF diode signal, wait states had to be introduced between the fast ramps.

Since MORE is a software solution, it was easily transferred to all gyrotron controllers but was not of practical use for the Echo 5 tube manufactured by CPI. In this case, a rising body current triggers an interlock before a mode switch could be observed and MORE could have intervened. This problem will be mitigated in future by implementing a similar recovery algorithm triggered by transient increases of the body current.

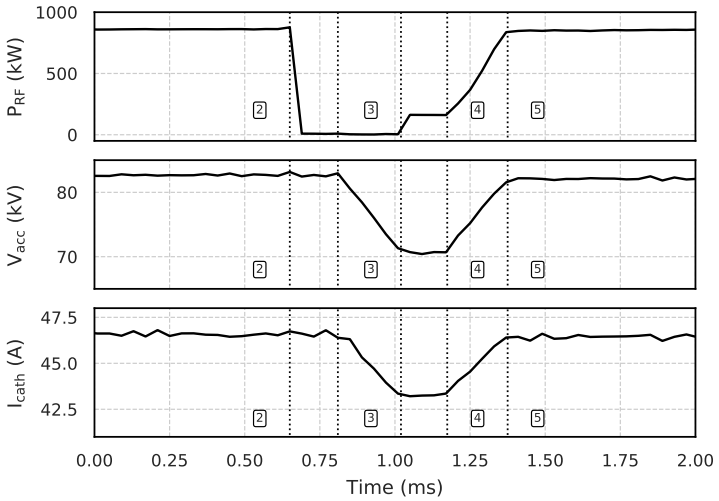


Figure 3.4: Example for a MORE cycle during a pulse from an experiment with Alpha 1 (TED SN007) tube. The numbers indicate the actual state of the FSM. Wait states were introduced to compensate the delay between the body and cathode voltage modulator and the required time to process the RF diode signal.

3.3 Experimental Results

The results presented in this section are extracted from a database of reduced gyrotron experiment data from dedicated tests with MORE and the last operational campaign OP1.2b of Wendelstein 7-X. The database creation was automated by the help of a Python framework named SAGE (Statistical Analysis of Gyrotron Experiments) which was created for this thesis. It allows the automated evaluation, visualization and reduction of big amounts of gyrotron experiment data to a small-sized searchable database. It can facilitate the statistical analysis of gyrotron experiment data e.g. for a gyrotron reliability study significantly. The RF output power is measured by a power-calibrated detector diode signal where the contribution of the nominal operating mode at 140 GHz is measured. The calibration is achieved by comparing the diode voltage signal to the integrated cooling water temperature difference in the beam dump. Transmission line losses were also taken into account to obtain the RF power at the gyrotron output window. In the following section, gyrotron pulses are labeled either as "stable" (finished normally without intervention of MORE), "unstable" (finished normally with at least one MORE cycle) and "failed" (pulse ended prematurely with at least one MORE attempt) In all experiments with MORE, it was used with maximum output power being set as priority for the algorithm. Therefore the target value for the 2nd (power) ramp-up is the actual set-point value (see step 5 of the algorithm) and a fixed slew rate was used.

3.3.1 Operation Regimes

Based on the database of reduced gyrotron experiment data from dedicated MORE experiments and the last operational campaign Wendelstein 7-X OP1.2b, the mode-loss line in the working point plane for the nominal operating mode was found. Figure 3.5 shows all 3963 mode loss events during 162 unstable and failed pulses in the $(U_{\text{acc}}, I_{\text{cath}})$ working point plane. Additionally, the average acceleration voltages and cathode currents of 425 stable pulses (green triangles) are shown as well. It is reasonable to assume that the initial cathode current for these pulses is higher due to emitter cooling. The pulses with a duration of up to 55 s were performed with the Alpha 1 (TED SN007) tube at same magnetic fields.

The depression ratio $U_{\text{body}}/U_{\text{cath}} \approx 0.51$ was approximately constant across all pulses with a maximum deviation of 4 % for 8 out of 162 pulses. The dashed red line in figure 3.5 fits the mode losses in the working point plane with

$$U_{\text{max}}(I) = \alpha_0 \ln(I + \alpha_1) + \alpha_2 \quad (3.1)$$

or respectively

$$I_{\text{min}}(U) = \exp\left(\frac{U - \alpha_2}{\alpha_0}\right) - \alpha_1 \quad (3.2)$$

with $\alpha_0 = 1.1$, $\alpha_1 = -42$ and $\alpha_2 = 81.135$.

The stable pulses are located in the upper left area and are enclosed by the fit line. The conclusion is that the fit denotes the center of a boundary region for the nominal operating mode where mode loss and multi-moding behaviour are more likely to occur. For a given acceleration voltage U_{acc} exist a minimum critical cathode and breaking current I_{min} . The width of the mode loss point cloud (around 1 kV) could be partly explained by the technical noise from the supply voltages itself and the additional noise introduced in the measurement chain. As shown in section 2.3.1, the individually observed noise amplitude on the body and cathode voltage amounts up to 500 V_{pp}. In the resulting sum signal $U_{\text{body}} + U_{\text{cath}}$ used as estimate for U_{acc} , the mean observed noise amplitude varied between 400 V_{pp} (10 %/90 % percentile difference) and 800 V_{pp} (1 %/99 % percentile difference) with rarely up to 1 kV_{pp}. Another contributing factor could be the hysteresis for the cathode current after a mode recovery. The existence of such a boundary region for the nominal working mode is supported by satellite mode stray radiation measurements presented in [WLM⁺17]. The increasing stray radiation level of the satellite modes approaching the output power limit is proposed there as a mode loss precursor. Additionally, multi-moding behaviour of the nominal operating mode TE_{28,8} and its satellites TE_{27,8} and TE_{29,8} is observed in multi-mode interaction simulations with EURIDICE [APIV12] where the emitter cooling behaviour is simulated with decreasing beam current. The shape of the mode-loss line is consistent with the experimental observations: When the gyrotron is operated close to the mode-loss line, a small voltage change (e.g. due to technical noise on the acceleration voltage) is enough to cause a mode switch. In the contrary, the mode-loss line is slowly approached by a slowly decreasing cathode current, allowing to observe (temporary) multi-moding behaviour.

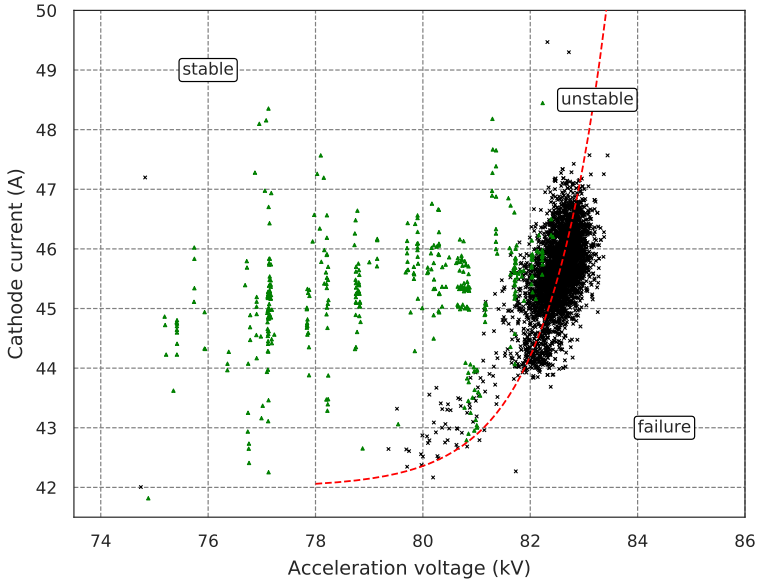


Figure 3.5: 3963 Modelosses (black crosses) and 425 stable pulses (green triangles) in the working point plane from dedicated MORE experiments and W7-X OP1.2b operation performed with the Alpha 1 (TED SN007) tube. The red dashed line is a fits the mode losses denoting the mode-loss line of the nominal working mode in the working point plane.

A new quantity called "criticality" C is proposed to denote the stability of the momentary gyrotron working point defined as

$$d_{\min}(U_i, I_i) = \min \left(\left\{ \sqrt{(x - U_i)^2 + (I_{\min}(x) - I_i)^2} \mid x \in [a, b] \right\} \right) \quad (3.3)$$

$$C(U_i, I_i) = \text{sgn}(U_i - U_{\max}(I_i)) \cdot \text{sgn}(I_{\min}(U_i) - I_i) \cdot d_{\min}(U_i, I_i) \quad (3.4)$$

where the criticality C is the minimum distance d_{\min} from the actual working point (U_i, I_i) to the cutoff line $(x, I_{\min}(x))$ computed for all $x \in [a, b]$. The signum function $\text{sgn}(x)$ is defined by

$$\text{sgn}(x) = \begin{cases} -1 & x < 0 \\ 0 & x = 0 \\ +1 & x > 0 \end{cases} \quad (3.5)$$

All working points (U_i, I_i) for which the criticality C shall be computed, should be contained in the voltage interval $[a, b]$. The criticality is negative for working points far away from the cutoff in the stable region and approaches zero with decreasing distance to the cutoff line. The criticality exceeds zero if the mode-loss line has been passed and the working point is located in the failure region. An increasing criticality can be, but is not necessarily, proportional to the output power. For example, in the case of emitter cooling with decreasing cathode current, the criticality is increasing, but the output power is decreasing.

In order to comply with physical units and ensure comparability of C with datasets from other gyrotrons, a min-max or z-score normalization (see section A.1 in the appendix) could be applied on the union sets of the individual features (U, I) of the working points and the mode loss fit curve $(U, I_{\min}(U))$. A normalization is not applied here since a comparison between different gyrotrons was not intended. A normalization of the dataset would also not qualitatively change the results in section 3.3.4.

3.3.2 Improvement of Output Power and Reliability

Since MORE allows a fast recovery of the nominal mode during the pulse (fast oscillation recovery), the gyrotron can now be operated closer to its individual output power limit at more unstable working points near the mode-loss line of the nominal working mode. In the past a safety margin had to be used which lowered the achievable output power to ensure a reliable operation [ARM⁺ 19]. Therefore, fast oscillation recovery methods like MORE are promising to fulfill the reliability- availability-maintainability-inspectability (RAMI) requirements of future high-power gyrotrons for fusion power plants [TDST19].

Figure 3.6 shows a comparison of the maximum achievable output power for the Alpha 1 (TED SN007) tube without (black trace) and with MORE (red trace). The frequent mode losses and subsequent recoveries of the nominal mode during the pulse are clearly visible as vertical lines in the red signal.

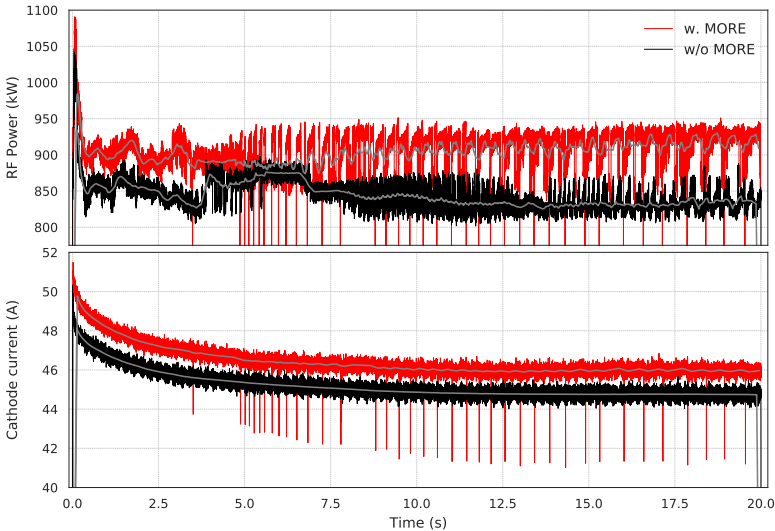


Figure 3.6: Comparison of maximum achievable output power and cathode current without (black) and with MORE (red) for Alpha 1 tube (TED SN007) measured at the gyrotron output window. Frequent MORE cycles are clearly visible as vertical lines. The emitter cooling effect is clearly visible, reaching a stationary state after 10 s. The grey line denotes the moving time-average with a window length of 250 ms.

The emitter cooling phenomenon is clearly visible in the plot for the cathode current. The average output power of a 20 s pulse could be increased by 7 % from 859 kW to 916 kW for the fundamental gaussian mode at the output window. The values are a conservative estimate based on the achieved integrated temperature difference in the water-cooled load (beam dump) including 3.5 % transmission line loss and 1 % reflection in the load. A comparable result was achieved with the Bravo 5 (TED SN002i) tube with an improvement of up to 7 % using the conservative estimate. The maximum achievable output power without MORE is defined as the output power which was reproducibly achieved without any mode losses for a pulse of the same duration (20 s).

Note that these values do not take into account the reduced gyrotron reliability at the maximum output power level without using MORE. If the achievable output power with the same pulse length and reliability level are compared, the power increase is higher (see Figure 3.8). Based on the available data presented in figures 3.8c and 3.8d, the mean failure probability (MFP) levels are comparable for the criticality range $[-0.5, -0.25]$ without MORE and the criticality range $[0, 0.25]$ with MORE. If the maximum achieved average output power at the same MFP level is compared, the reliable output power is even increased by 9.4 % from 866 kW to 948 kW. In Figure 3.6, the output power seems to stabilize and slightly increase towards the end of the pulse with MORE. This can be explained with the increasing time distance between subsequent MORE cycles (visible as sharp drops for the RF output power and the cathode current) during the pulse since the cathode current is stabilizing after 5 to 10 s. Another hypothesis is that the MORE cycles help to improve the beam quality by removing trapped electrons. This hypothesis is evaluated in the following section. The improvement for steady state operation is expected to be higher since the momentary output power towards the end of the pulse could be increased by up to 11 % around 100 kW.

3.3.3 Spectrogram of a Mode Recovery Cycle

The collective Thomson scattering (CTS) diagnostic at W7-X [MSS⁺19] was used to acquire stray radiation spectrograms of the Alpha 1 gyrotron (TED # 7) during MORE cycles. The question was whether or not the ion neutralization level in the gyrotron is changed during a MORE cycle. A change in the frequency of the gyrotron nominal mode in the stationary operating regime (after the thermal cavity expansion and the space-charge neutralization process are finished) can indicate a change of the neutralization level [SWP⁺15]. A rough estimation yields that trapped ions should not be able to escape during the MORE cycle with lowered voltage, since the time period is too short. Figure 3.7 shows a spectrogram for the nominal mode (TE_{28,8}-mode at 140 GHz) and its azimuthal neighbour (TE_{27,8}-mode at 137.5 GHz). The frequency of the nominal operating mode remains unchanged comparing the frequency before and after the MORE cycle. Therefore the ion neutralization level is not changed by MORE cycles during a gyrotron pulse. Though it cannot be excluded that trapped electrons are freed during MORE cycles, helping to improve the beam quality [Pag].

3.3.4 Performance in dedicated Experiments

In order to quantify and evaluate the impact of MORE in terms of achievable output power and operational reliability, a statistical analysis has been performed. For the analysis, 178 pulses with a duration of up to 20 s were performed using the Alpha 1 (TED SN007) tube at nominal fields to test the automated mode recovery in preparation for the operational campaign OPI.2b at Wendelstein 7-X. The overall success rate of the automated mode recovery amounts to 99 % of 3755 mode loss events during 178 pulses, whereof 50 were stable, 84 were unstable and 44 had failed.

The average achieved pulse length, the mean time to failure (MTTF) and the mean failure probability (MFP) were computed to quantify the effect of MORE on the operational reliability and the achievable output power. The latter two were calculated for different criticality intervals representing working points with varying distance to the cutoff line of the nominal working mode in the working point plane (see figures 3.8b and 3.8c).

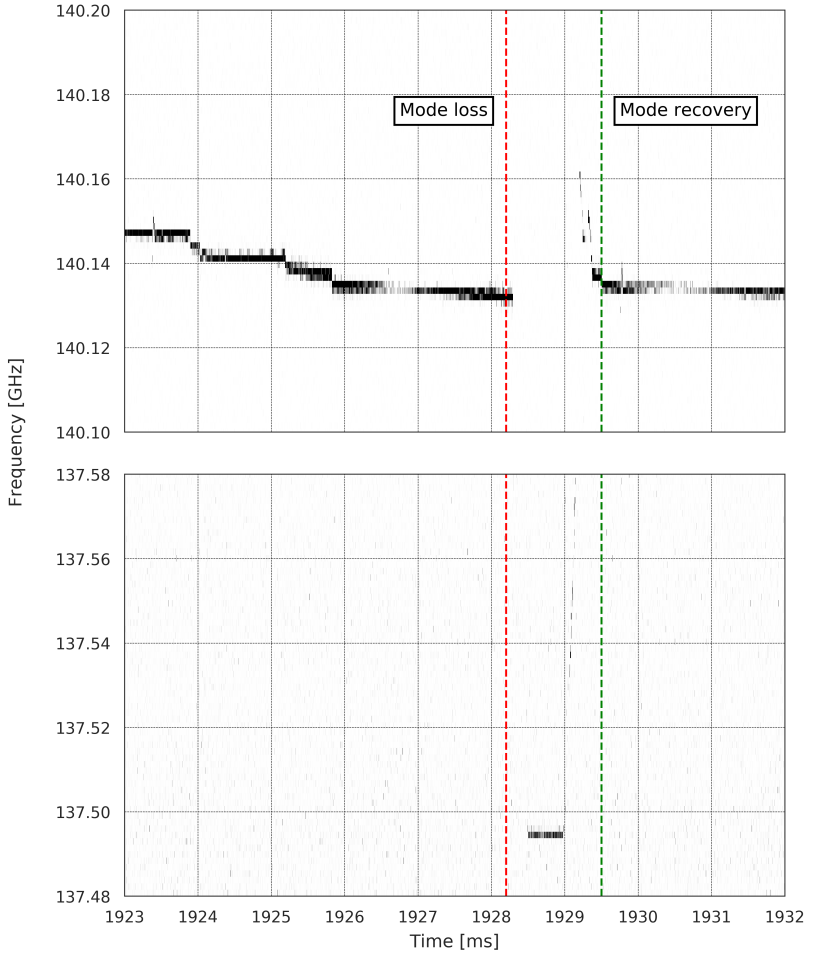


Figure 3.7: Spectrogram (frequency resolution $\Delta f = 1.5$ MHz, time resolution $\Delta t = 0.3$ ms) of a MORE cycle acquired with the W7-X CTS diagnostic. The frequency, hence the neutralization level, is not changed by a MORE cycle.

The criticality is the independent variable in this case. The mean time to failure (MTTF) was computed using the simple approach

$$\text{MTTF} = \frac{1}{N_{\text{failed}}} \sum_i \tau_i \quad (3.6)$$

for each criticality interval where τ_i are the achieved pulse lengths and N_{failed} the number of failed pulses of a corresponding criticality interval. The mean failure probability (MFP) is defined as

$$\text{MFP} = \frac{N_{\text{failed}}}{N_{\text{total}}} \quad (3.7)$$

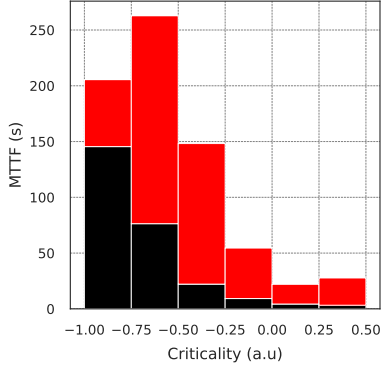
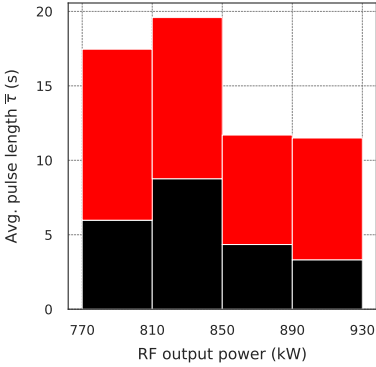
which is the ratio between the number of failed pulses N_{failed} and the total number of pulses N_{total} in every criticality interval. The average achieved pulse length was calculated for different RF output power intervals, hence the RF output power was the independent variable in that case (see figure 3.8a). Of course, this result is biased by the varying number of pulses in the RF output power intervals. The achieved pulse length without MORE is defined as time till the first mode loss since the pulse would have ended prematurely without MORE. Figure 3.8a shows a comparison of average achieved pulse lengths for different RF output power intervals. The average achieved pulse length is improved by +123.4 % up to +246.4 % from 3.32 s to 11.5 s. This indicates reliability improvements for pulse in all given RF output power intervals with a fixed target pulse length. The effect of MORE on the achieved pulse length is stronger for higher output powers. The overall average achieved pulse length across all output power intervals using MORE is 14.7 s in contrast to 4.9 s without MORE. The overall achieved MTTF using MORE is 42.8 s compared to 12.7 s achieved without MORE. Note that the definition of the MTTF in equation 3.6 is independent from a pre-set target pulse duration (20 s in this case).

In section 3.3.1 the criticality was introduced which is a better independent variable for a statistical analysis since it takes both the cathode current and the acceleration voltage into account. Figures 3.8b and 3.8c show the consistent trends of a decreasing MTTF and an increasing MFP with increasing criticality, the latter resembling a cumulative Weibull distribution known from failure analysis in engineering. Figure 3.8c shows that MORE reduces the MFP significantly in particular close to the modeloss by -27.3% up to -77%

from 53.7 % to 12.2 %. Simultaneously, the MTTF is increased by +41.2 % up to +753.5 % for high criticality values as shown in figure 3.8b. Since also stable pulses were taken into account, the effect of MORE is reduced for low criticality values far from where the nominal mode is lost.

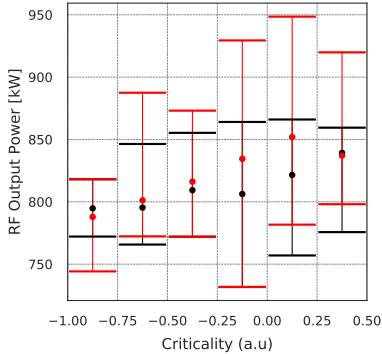
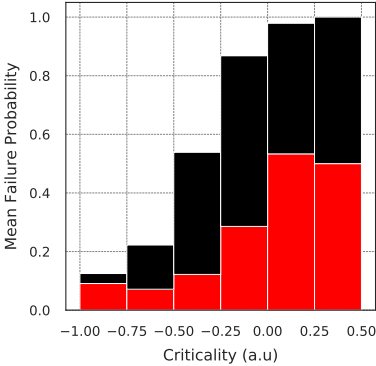
The average achieved pulse length, the MTTF and the MFP indicate an improvement in terms of gyrotron reliability close to its output power limit when MORE is used.

The average duration of MORE cycles is 532 μs , but in figure 3.9c it is clearly visible that the histogram is broadened having two major peaks. This is due to the fact that the number of attempts to recover the nominal mode and the duration of the involved ramps varies. Apparently, the nominal mode has been recovered in most cases after one or two attempts consisting each of a fast ramp down (with a duration of 100 μs) and a fast ramp up (with a duration of 200 μs). The time available for MORE attempts is limited by the aforementioned RF grace time which is set to 2 ms by default. The overall average false mode duty cycle is 9.6×10^{-4} and the average voltage modulation frequency amounts to 2.2 kHz. For a cyclic load with $f \geq 1$ kHz with low duty cycle, no significant effect on the collector lifespan is expected [MNP⁺16]. Therefore the additional expected collector heat load using MORE is negligible and a significant reduction of the collector lifespan is unlikely. Figure 3.9 gives an overview of the temporal distribution of mode loss events and the duration of MORE cycles. Evidently in Figure 3.9a, the first mode losses accumulate during the first 2 to 5 s of the analyzed pulses. This is due to the emitter cooling effect and the consequently decreasing cathode current which stabilizes after 5 to 10 seconds (see figure 3.6). In Figure 3.9b, the first mode losses overlap with the repeated mode losses during the pulse. The mode losses are nearly uniformly distributed later-on when the gyrotron is operated close to the cutoff, since the cathode current has stabilized then.



(a) Increased pulse lengths near the output power limit with MORE (red)

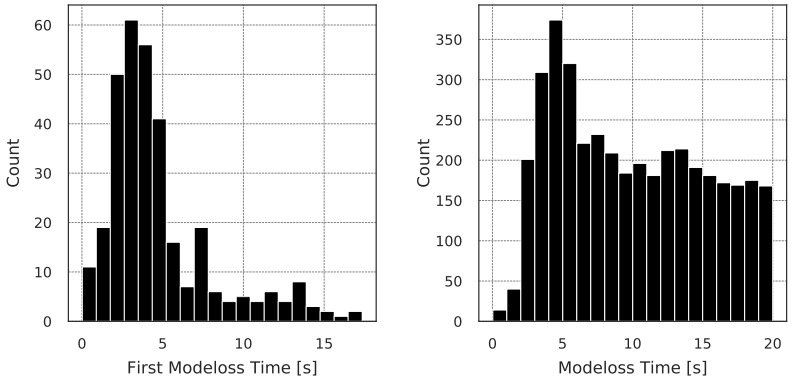
(b) Increased MTTF for high criticality near the cutoff with MORE (red)



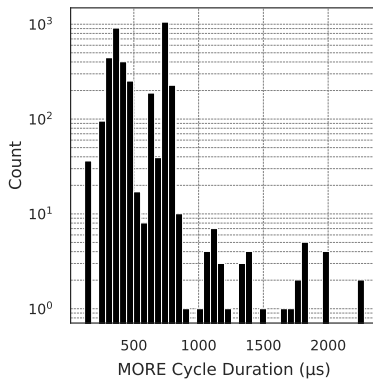
(c) Reduction of the MFP for high criticality near the cutoff with MORE (red)

(d) Relation between criticality intervals and min./max./avg. RF output power.

Figure 3.8: Statistical results for dedicated experiments to evaluate the gyrotron performance and reliability with (red) and without (black) MORE.



(a) Accumulation of first mode losses during the first 2 to 5 s of the pulses (b) Uniformly distributed mode losses later-on during the pulse with MORE



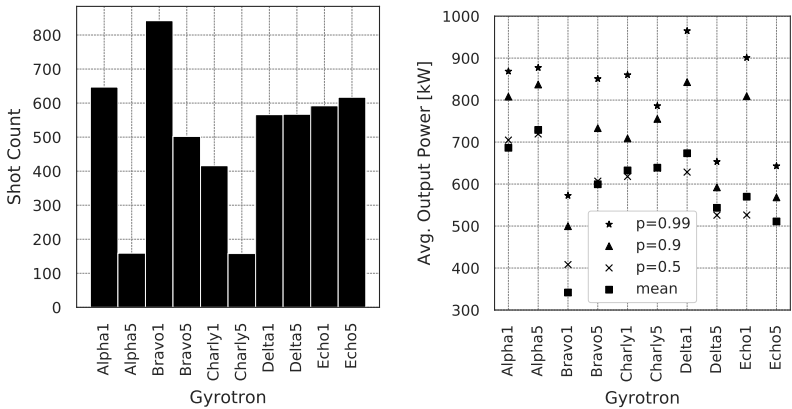
(c) Histogram of the MORE cycle duration

Figure 3.9: Statistical results for mode loss events and MORE cycles

3.3.5 Performance during Wendelstein 7-X OP1.2b

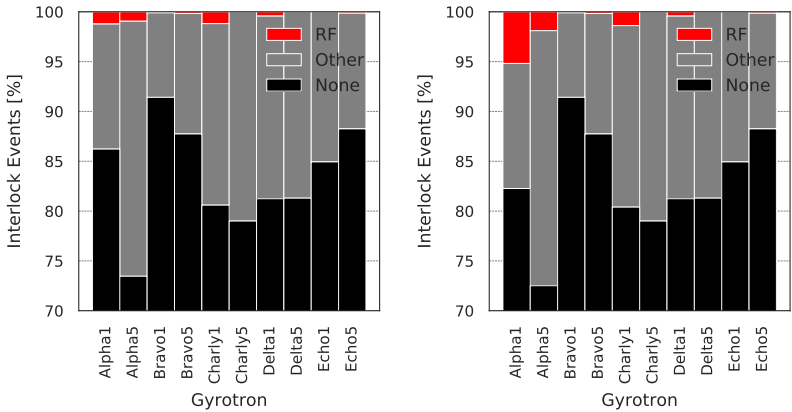
During the last operational campaign at Wendelstein 7-X OP1.2b from July to October 2018, 9813 gyrotron pulses were performed in total with duration of up to 100 s during more than 1500 experiment programs. MORE was not fully operationable before end of August 2018. Only pulses where MORE was enabled with a duration of at least 100 ms were analyzed. The lower duration limit was set since MORE was configured so that it becomes active after 100 ms. Given the above conditions, 8651 pulses for nine gyrotrons remained in total and were analyzed to evaluate the impact of MORE on the gyrotron operation during the campaign. MORE was not implemented for the 10th Echo 5 gyrotron (CPI) since a body current interlock occurred always before the nominal mode was lost. Increased ambient temperatures and insufficient air conditioning in parts of the transmission line during the experiment campaign caused massive arcing. Therefore high power pulses close to the maximum power were hardly feasible and the loss of the nominal mode was less frequently observed.

This is also reflected by the statistics for the W7-X ECRH in figures 3.10b and 3.10c. The reliability is mainly reduced due to other interlocks, like arc interlocks (arcing inside the gyrotron or along the transmission line) and modulator interlocks. The fraction of RF interlock events compared to other interlock events is small, in particular when MORE was used. Comparing figures 3.10c and 3.10d, MORE was able to improve the reliability by reducing the percentage of RF interlocks during the experimental campaign. This was in particular the case for Alpha 1 where the base reliability was improved by 4.8 % and the percentage of RF interlock events was reduced from 5.2 % to 1.1 % with MORE. The overall reliability across all gyrotrons of the W7-X ECRH facility was slightly improved from 82.9 % to 83.4 % with MORE. The improvement in the overall reliability is small since only Alpha 1 and Alpha 5 were operated at high power (see figure 3.10b). For the comparison and the evaluation of the reliability improvement, the gyrotron pulses containing MORE cycles were counted as pulses with RF interlocks without MORE. These pulses would have been terminated prematurely by a mode loss and the resulting RF interlock if MORE would not have been used. The count of these pulses was then compared to the number of pulses terminated by an RF interlock despite the fact that MORE was used.



(a) Absolute number of pulses performed for all gyrotrons

(b) Percentiles and mean for the avg. pulse output power for all gyrotrons



(c) Percentages of interlock events for all gyrotrons with MORE. Majority of interlock events due to arcing in transmission lines.

(d) Percentages of interlock events for all gyrotrons without MORE. High-power operation mainly with Alpha 1 and Alpha 5.

Figure 3.10: Statistics for the Wendelstein 7-X ECRH facility during the last experimental campaign OP1.2b using 8651 gyrotron pulses during > 1500 experiment programs with a minimum duration of 100 ms from 25th August on-wards for ten gyrotrons. The base reliability is mostly reduced due to insufficient air conditioning in beam duct limiting high-power gyrotron operation.

Name	Serial No.	Pulses	Mode losses	Mode recoveries	Success [%]
Alpha 1	7	65	331	308	93
Alpha 5	5	6	15	13	87
Bravo 1	M	8	23	23	100
Bravo 5	2i	8	10	7	70
Charly 1	1	15	14	9	64
Delta 1	6	25	66	58	87
Delta 5	3	4	5	3	60
Total		131	464	421	91

Table 3.1: Results from W7-X OP1.2b operation with MORE: the number of mode losses compared to the number of successful mode recoveries yields the success rate. Most data available for the Alpha 1 and Delta 1 tubes.

Name	$\bar{\tau}$ [s]	$\overline{\tau_{MORE}}$ [s]	Δ [%]
Alpha 1	3.10	4.61	49
Alpha 5	4.54	6.66	47
Bravo 1	3.47	4.25	22
Bravo 5	3.26	4.45	36
Charly 1	3.56	3.76	47
Delta 1	1.69	2.87	70
Delta 5	3.07	3.11	1
Total	3.07	4.31	40

Table 3.2: Average achieved pulse length without and with MORE during W7-X OP1.2b experimental campaign

Table 3.1 shows the success rate of the automated mode recovery for all gyrotrons for which data was available. Pulse data with MORE cycles could be acquired only for seven gyrotrons, mostly for Alpha 1 and Delta 1. Please note that the MORE parameters were optimized for Alpha 1, Bravo 1 and Bravo 5 and the sample size is much smaller for the other gyrotrons. The mode recovery success rate is therefore less reliable for the cases where only few data was available. The overall success rate for the automated mode recovery across seven gyrotrons was 91% during the campaign.

Table 3.2 shows the average achieved pulse lengths for seven gyrotrons without and with MORE and the respective relative improvements. The overall average pulse length extension across the gyrotrons was +40% during the last experimental campaign. No parasitic effects like cross talk between the simultaneously operated gyrotrons was observed so far when MORE was used. The amount of data was insufficient to further resolve it for different RF output power or criticality intervals.

3.4 Summary and Outlook

The first implemented version of MORE already yields very promising results as shown in the previous sections. The success rate of MORE in dedicated experiments amounts to 99 % with more than 3000 modeloss events during pulses of up to 20 s with two gyrotrons. The average pulse length could be significantly increased with MORE from 4.9 s to 14.7 s. This means a great enhancement of the ECRH capabilities for experiments being part of the W7-X physics program where at least 10 s of stable, reliable heating power are required to achieve a stationary state at high plasma densities.

The success rate of MORE during W7-X OP1.2b was 91 % with 464 modeloss events during pulses with seven gyrotrons. The average pulse length was extended by 40% using MORE during these pulses. The reliable average output power could be increased by 9.4 % or absolute 82 kW at the same mean failure probability level for the Alpha 1 gyrotron. In general, an improvement of the reliable output power between 5 and up to 10% is expected per gyrotron. This results in a potential increase of at least 500 kW up to 800 kW for the total output power of the W7-X ECRH facility. This is equivalent to an additionally installed gyrotron, leading to significant cost savings amounting to the acquisition costs of a new gyrotron of about one million euros.

The first results using MORE with gyrotron pulses up to 20 s were revealing that most of the mode losses occur during the first 5 s of the gyrotron pulse (see Figure 3.9) and that the event frequency of mode losses stabilizes later-on. Therefore, longer gyrotron pulses for future experiment programs with a duration of up to 30 minutes should not be problem to achieve using MORE. Nevertheless, the following improvements could be implemented:

So far, only the momentary acceleration voltage when the mode was lost is taken into account and a fixed duration or slew rate is defined for the voltage ramps. A significant improvement could be achieved by taking also the rate of the decreasing cathode current due to the emitter cooling into account. Mode losses occur more frequently in the phase where the cathode current is dropping fast due a fixed ramp slew rate and the fact that the target of the slow power ramp up is not adapted to the decreasing cathode current. Furthermore, the acceleration voltage could be ramped up exponentially instead of linearly to reduce the duration of the MORE cycles and the false-mode duty cycle.

4 Development of Microwave Filters

Due to the nature of stray radiation fields and their measurement, it is challenging to obtain a stable power-proportional measured time signal. Therefore, first preliminary measurements of the satellite mode activity turned out to be insufficient. Observed correlations between the measured activity signal and mode loss events was weak. In an attempt to improve the signal stability of the measurement, two more advanced measurement setups were developed in this thesis.

This chapter documents the development of two custom microwave filters being part of a new gyrotron diagnostic for the real-time measurement of the satellite mode activity. First, the common filter design code, named MMWFR (multi-mode multi window frequency response), is presented which was used to design both microwave filters.

Then the development of the first filter, a rather simple cutoff high pass filter, is described. Its design is presented as well as the realized filter. Finally the filter characteristics are verified by measurements in the lab with a network analyzer.

The second filter developed in this thesis is a quasi-optical satellite mode band pass. It was realized as a dielectric disc filter in an oversized circular waveguide. The implemented filter optimization procedure and the final filter design are described in detail. Possible manufacturing tolerances were taken into account in the design phase, facilitating the evaluation of the feasibility of a specific quasi-optical filter design. The characteristics of the quasi-optical filter are verified both in lab measurements with a low-power tuneable RF source and in in-situ measurements attached to a gyrotron.

4.1 Filter Design Code - MMWFR

The design code MMWFR (Multi-mode Multiple Window Frequency Response) was created for this thesis in the programming language Python. It was used for the design of the cutoff high pass filter and the quasi-optical dielectric disc filter. It originates from a MATLAB script created by J. W. Oosterbeek implementing the S-matrix and reflection coefficients as shown in the paper by Nickel and Thumm [NT91] and the T-matrix concatenation for the dielectric layers as presented by Geist and Hartfuss in [Gei98]. It was used to calculate the frequency response of a dielectric window and was significantly extended. The code calculates the frequency response of arbitrary stacks of material layers with defined relative permittivity. In order to model dielectric disc filters in waveguides, the code computes for rectangular and circular waveguides which modes exist in a given frequency range along with their cutoff frequency f_c , wavenumber k_{mn} , eigenvalues χ_{mn} , propagation constant β_{mn} , Brillouin angles θ_B and attenuation constants $\alpha_{\text{tot},mn}$. The frequency response of a dielectric filter for the different modes in the waveguide is then computed using their the Brillouin angle $\theta_B(f)$ as incidence angle. The code can also handle oblique incidence (layer tilt). The attenuation constant takes the dielectric loss (for a filled waveguide) and conductive wall loss into account by using own reformulations based on chapter 3 in [Poz05]. All implemented expressions can be found in detail in the appendix of this thesis. Since in reality manufacturing tolerances exist, the code estimates their impact by imposing random normal-distributed errors on the material layer thicknesses and tilt angle. The computation of the frequency response is then repeated multiple times (typically 10^1 to 10^3) for a defined set of modes. This way, the average expected filter characteristics (transmission, reflection, absorption over frequency) with error bars for a given manufacturing tolerance and frequency range (here: 120 GHz to 150 GHz) are obtained. This facilitates the feasibility evaluation of a specific quasi-optical filter design. In order to speed up the computation, the code was parallelized. Figure 4.1 shows a flow diagram for the computation of the frequency response for multiple modes with random manufacturing errors. To find the optimum stack under defined constraints for e.g. the transmission of the filter at defined frequencies, a brute-force approach was used computing all possible combinations for layer thicknesses and count. This procedure is described in detail in section 4.3.1.

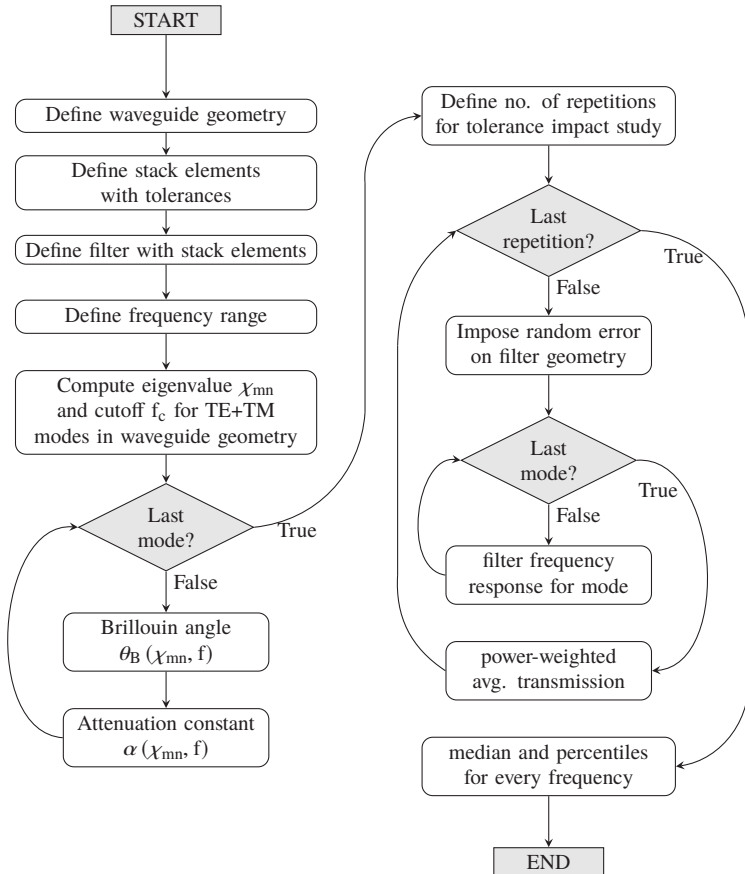


Figure 4.1: Flowchart of the filter design code MMWFR for the computation of the multi-mode frequency response with random manufacturing errors

4.2 Cutoff High Pass Filter

For the mono-mode measurement of the satellite mode activity, a high pass filter with a cutoff frequency of around 136 GHz was designed, built and validated. The high pass filter is necessary to attenuate all parasitic modes below the satellite mode $TE_{27,8}$ at 137.5 GHz of the nominal gyrotron $TE_{28,8}$ mode at 140 GHz. The measurement setup in which this high pass filter is used, is described in section 5.3.1.

4.2.1 Design

The function of a cutoff high pass filter is accomplished by a section of a rectangular wave guide with reduced inner dimensions to increase its cutoff frequency. The optimum inner dimensions of the section are determined by a grid search (with typically around 10^4 candidate solutions) for the two dimension variables a and b while candidate solutions are kept which fulfill defined conditions e.g. the desired minimum or maximum attenuation for given frequencies. Figure 4.2 shows a plot for the attenuation of the fundamental rectangular waveguide mode TE_{10} over frequency. The standard D-band WR4 (inner dimensions: 1.0922 mm x 0.5461 mm) and WR5 (inner dimensions: 1.2954 mm x 0.6477 mm) waveguides, possible alternative designs and the final chosen design are presented for comparison. The starting point for the search are the dimensions of the WR4 waveguide since its cutoff frequency is already very close to the frequency of the satellite mode $TE_{27,8}$ around 137.5 GHz. The target cutoff frequency for the design was chosen to be 135 GHz, so that in case the achieved manufacturing tolerances for the designed high pass filter would be bigger in reality than expected, material can still be removed to achieve the desired cutoff frequency of 136 GHz.

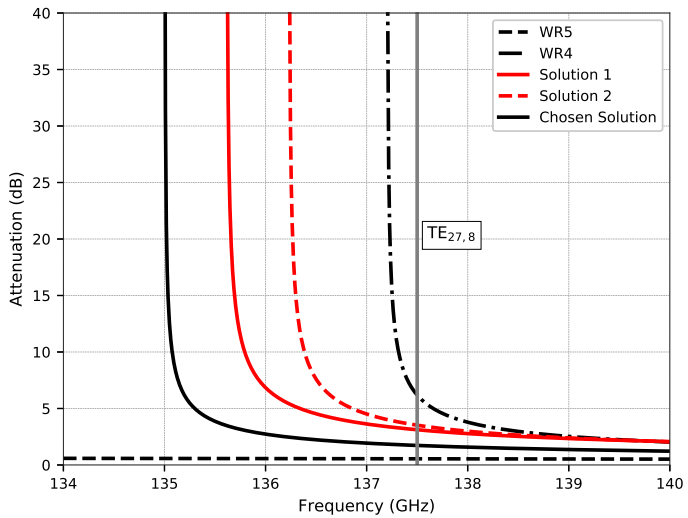


Figure 4.2: Attenuation over frequency for the standardized WR5 and WR4 waveguides, some exemplaric high pass filter solutions and the final chosen solution for the filter design.

4.2.2 Realization

In order to use the high pass filter with other D-band microwave components, the waveguide section defining the cutoff is linearly tapered to the standardized dimensions of the WR5 waveguide and the usual UG-387 flanges are used. A technical drawing of the mechanical filter design is shown in figure 4.3. The mechanical filter design is adapted from a sketch by W. Kasperek (IPF, University of Stuttgart). The filter is assembled from two parts which are screwed together. The bulk material was chosen to be copper which is soft enough, so that the filter could be tuned after the assembly by increasing the tightening torque of the screws. The filter was successfully fabricated in-house in the IPP workshop in Greifswald. Figure 4.4 shows a photograph of the assembled filter.

4.2.3 Measurement

The attenuation over frequency of the high pass filter was measured in the lab with a low-power tuneable RF source and an Anritsu 68087A network analyzer combined with D-band frequency range extender. The measurement was repeated while sandpaper was used to remove excess material from the inner surface of the filter parts. This procedure was repeated several times. The cutoff frequency could be shifted this way closer towards the desired cutoff frequency of around 136.5 GHz.

The cutoff frequency of the filter was found to be 136.8 GHz close to the frequency of the satellite mode $TE_{27,8}$ around 137.5 GHz. The high pass filter was therefore successfully manufactured.

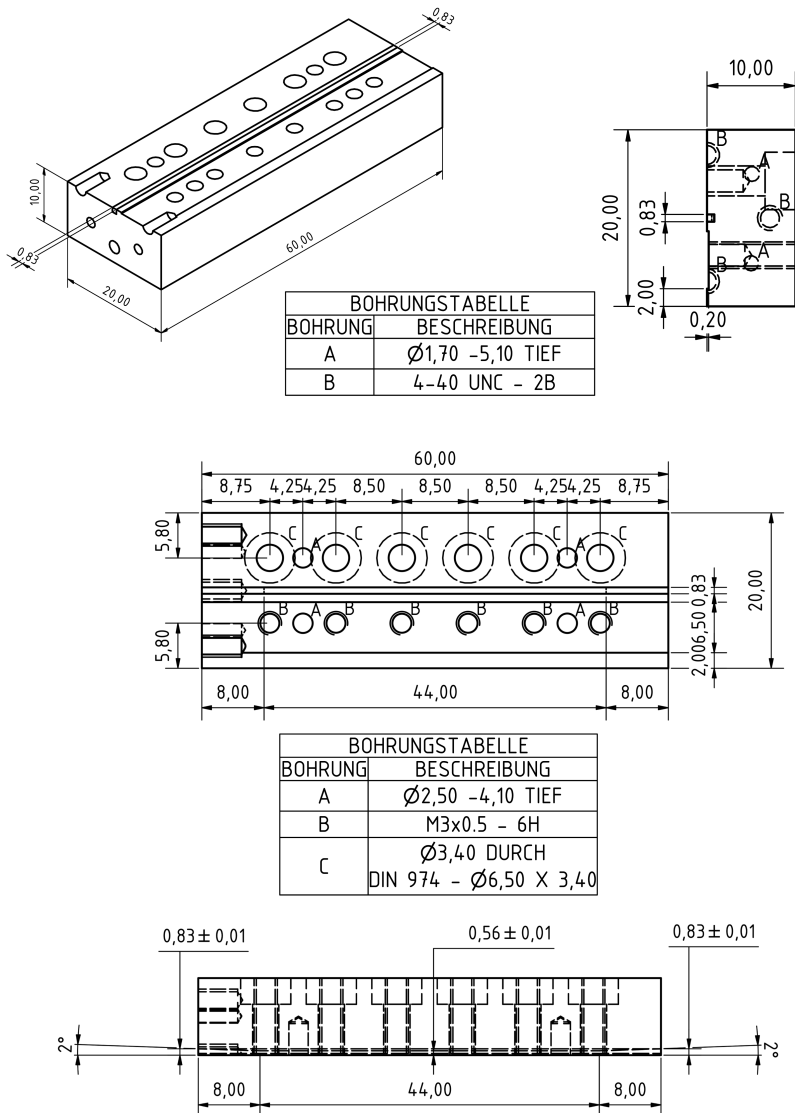


Figure 4.3: Technical drawing for the mechanical design of the cutoff high pass filter. The filter is assembled of two parts which are screwed together. The chosen filter bulk material is copper so that it can be tuned by variable tightening torque of the screws.

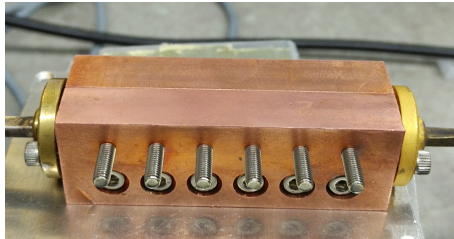


Figure 4.4: Photograph of the manufactured cutoff high pass filter

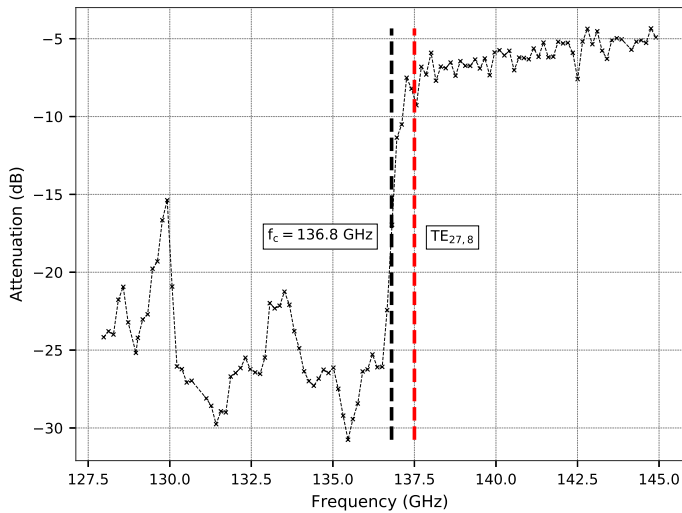


Figure 4.5: Plot of the measured attenuation over frequency for the cutoff high pass filter. The measured cutoff frequency is around 136.8 GHz sharply before the frequency of the satellite mode $TE_{27,8}$ around 137.5 GHz.

4.3 Quasi-Optical Filter

For the quasi-optical measurement of the satellite mode activity, a quasi-optical filter implementing a satellite mode band pass for both satellite modes $TE_{27,8}$ at 137.5 GHz and $TE_{29,8}$ at 142.5 GHz and a notch for the nominal gyrotron mode $TE_{28,8}$ around 140 GHz was required. Furthermore other parasitic modes below 136 GHz and above 143 GHz should be attenuated. Since such a filter was not commercially available, it was designed, built and validated in this thesis. The measurement setup in which this quasi-optical filter is used, is described in section 5.3.2.

4.3.1 Design

The structure of a dielectric disc filter is rather simple as shown in figure 4.6. It simply consists of dielectric layers with alternating relative permittivity or refractive index. The difference in the refractive index should be maximized to realize a compact filter with good frequency separation. Prior to the design of the quasi-optical satellite band pass, a much simpler stack with zinc selenide (ZnSe) windows was built as proof of principle and measured in the 90 to 110 GHz range. Good quantitative agreement was found between the computed and measured transmission. ZnSe has a high refractive index of 3.015 in the microwave frequency range between 100 GHz and 250 GHz [Lam96], but is rather expensive. In the end, sapphire (Al_2O_3) was chosen as dielectric material. It is cheap and has an even higher refractive index of 3.065 in the microwave frequency range 100 GHz to 200 GHz [AC94, Lam96]. Since sapphire is a birefringent material, z-cut sapphire was chosen so that any unwanted birefringence is excluded. The optical and the crystallographic axes are congruent for z-cut crystals. In order to maximize the refractive index difference, air gaps are used in between the dielectric layers. Since a 16 mm WG16 flange already exists for diagnostic stray radiation measurements at the gyrotron, a circular waveguide with the same diameter is used.

The design of a dielectric disc filter fulfilling all of the aforementioned requirements above is rather complicated and challenging. Usually, only a periodic notch filter can be easily realized with dielectric layers having a thickness of $(2n + 1)\lambda/4$. Another particularity in the design of this filter was that it should be transparent for multiple modes (beside the fundamental $TE_{1,1}$

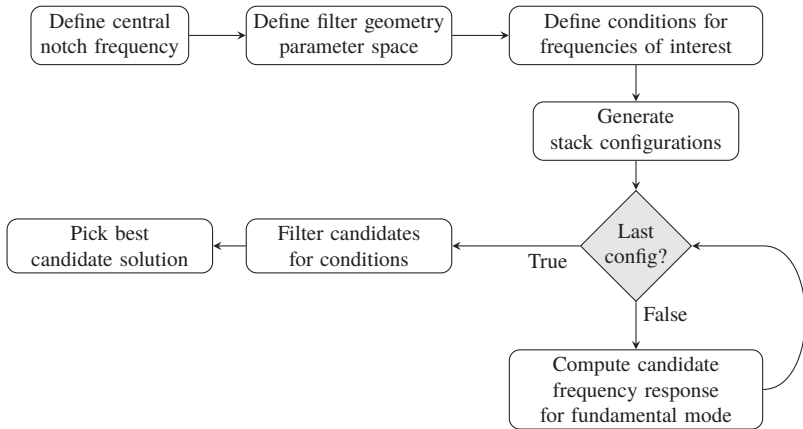


Figure 4.8: Flowchart for the brute-force approach to find the optimum notch filter stack

In order to realize the desired filter characteristics, multiple stacks each realizing a notch for a specific frequency, had to be concatenated. In order to identify the best individual stacks, a brute-force approach was used. Figure 4.8 illustrates the brute-force approach to find the best stack fulfilling defined conditions for the transmission at defined frequencies. The frequency response of all possible configurations, the cartesian product of the sets for the layer thickness, air gap distance and number of layers, was computed for the frequencies of interest and the fundamental waveguide $TE_{1,1}$ mode only. This was done in order to reduce the computational effort. To evaluate the feasibility of a specific design and its sensitivity to manufacturing errors, the computation of the frequency response is repeated for at least $10^1 \dots 10^2$ realizations of the filter geometry, each with a random normal-distributed error imposed on the layer thicknesses and air gaps of the stack. Typically $\geq 10^4$ configurations are investigated, leading to 10^6 to 10^7 individual computations, of which typically 10^2 candidate solutions fulfill the requirements.

Figure 4.9 shows the result of this brute-force approach for the 140 GHz notch filter stack. The error bars and configuration labels on the y-axis were omitted for better readability. Each configuration represents a tuple (number of repetitions, dielectric layer thickness, air gap distance). In case of the 140 GHz notch, the requirements were that the attenuation for the satellite modes $TE_{27,8}$ at 137.3 GHz and $TE_{29,8}$ at 142.5 GHz should not exceed 6 dB with a maximum

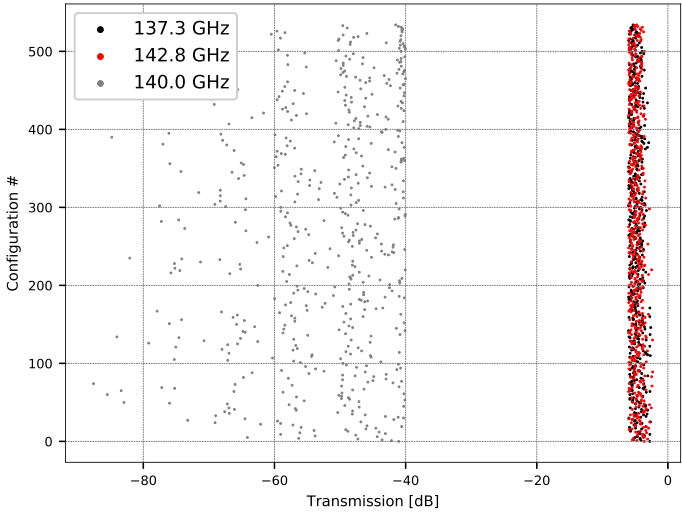


Figure 4.9: Remaining candidate solutions for the 140 GHz notch stack fulfilling the constraints for the frequencies of interest. Every configuration stands for a tuple (no. repetitions, layer thickness, air gap distance). The horizontal error bars are omitted for better visibility.

allowed deviation of 10 dB. For the notch at 140 GHz, the attenuation should be at least 40 dB also with a maximum allowed deviation of 10 dB. Among the remaining candidate solutions, the best solution was selected manually. Table 4.2 shows the specifications of the final design for the quasi-optical satellite mode band pass. A design was chosen which minimizes the number of different required dielectric disc thicknesses (see Table 4.1).

In order to achieve the desired filter properties, six different notch filter stacks for 125 GHz, 129 GHz, 132 GHz, 135 GHz, 140 GHz and 147 GHz were concatenated. The length of the resulting filter stack is 522.1 mm which is still a convenient size. Figure 4.11 shows the transmission of the individual notch filter stacks to visualize this circumstance.

material	refractive index n	loss tangent δ	thickness [mm]	count
Al ₂ O ₃	3.065	$1.5 \cdot 10^{-3}$	2.1	4
			2.6	9
			2.7	5
			2.8	12
Air	1.0006	0	4.3	4
			5.3	5
			9.6	2
			10.7	5
			21.8	5
			24.2 (24.1)*	9

* before multi-mode correction of the filter design.

Table 4.1: Bill of materials for the final quasi-optical filter design.

stack element name	layer thickness [mm]	air gap [mm]	count
Notch 125	2.1	4.5	4
Notch 129	2.8	5.3	5
Notch 132	2.8	9.6	2
Notch 135	2.7	21.8	5
Notch 140	2.6	24.2	9
Notch 147	2.8	10.7	5

stack element order:

Notch 132, Notch 125, Notch 129, Notch 140, Notch 147, Notch 135

Table 4.2: Final design specifications for the quasi-optical filter

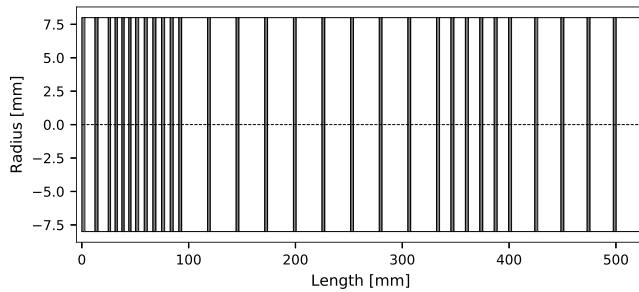


Figure 4.10: Illustration of the stack geometry for the final quasi-optical filter design from Table 4.2

Figure 4.12 shows the computed transmission of the final quasi-optical filter design for the TE_{1,1} mode including a 3σ manufacturing tolerance of 100 μm both for each of the dielectric discs and the air gaps. Therefore in 99.73 % (3σ) of the cases, the random normal-distributed error imposed on the filter element geometry was assumed to be ≤ 100 μm. The computation of the frequency response was repeated for 10² realizations of the filter geometry for every frequency in the defined range between 125 GHz and 150 GHz. Although the imposed errors were gaussian, the resulting error distribution for the transmission was not which is expressed by the non-symmetric error around the median. Therefore the error range is given by the 10 % and 90 % percentile difference instead of the standard deviation. Obviously, the desired filter characteristics were successfully achieved by the concatenation of multiple stacks each realizing a notch filter. Even when the possible random manufacturing errors are taken into account, the errors are within acceptable limits for the

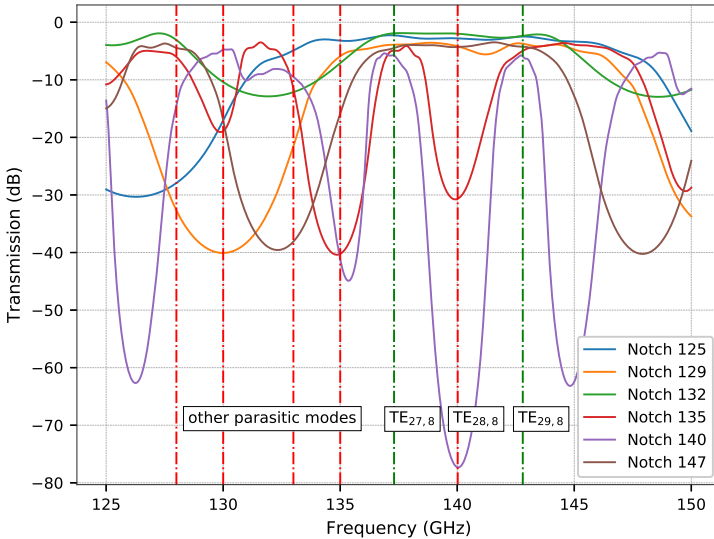


Figure 4.11: Transmission of the individual notch stacks for the TE_{1,1} fundamental mode. The stacks are shifted in frequency so that they yield a very broad notch between 125 GHz to 135 GHz and above 145 GHz when concatenated as presented in figure 4.12. Manufacturing errors were omitted for better readability.

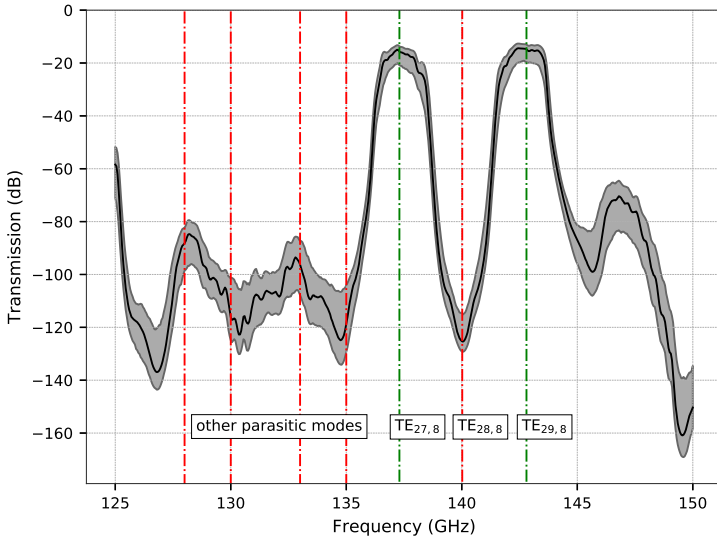


Figure 4.12: Computed transmission of the final quasi-optical filter design for the fundamental $TE_{1,1}$ mode. The grey shaded area around the graph denotes the difference between the 10% and 90% percentiles around the median of the transmission due to random errors imposed on the filter geometry. A 3σ manufacturing tolerance of ≤ 0.1 mm was assumed for 10^2 realizations of the filter geometry.

critical frequency range between 137 GHz and 143 GHz where the frequencies of the three gyrotron resonator modes of interest are located.

In the previous computations of the quasi-optical filter transmission only the fundamental $TE_{1,1}$ mode of the circular waveguide was taken into account. It can be reasonably assumed that most of the power is contained in the fundamental mode $TE_{1,1}$ of the circular waveguide, since the attenuation constants are higher for the other modes. Another reason is that ideally in absence of corrugations or steps in the axial or radial profile of the waveguide, no mode conversion should take place. Anyway, the effect of the other waveguide modes should be investigated in particular with regard to the goal of multi-mode transparency for the filter. In total 164 (TE and TM) modes exist in the 16 mm circular waveguide within the frequency range between 120 GHz and 150 GHz. To determine the possible relevant modes in the waveguide, the mode eigenvalues and their cutoff frequencies were computed. If the mode

cutoff frequency was less or equal to the upper bound of the defined frequency range, the mode was considered. Figure 4.15 compares the expected filter transmission for different modes with increasing eigenvalue and Brillouin angle. Clearly, the modes are increasingly attenuated over the whole frequency range with increasing Brillouin angle. This can be explained in terms of non-orthogonal or oblique incidence using the Brillouin angle as incidence angle in the quasi-optical approximation. The desired filter transmission is generally only conserved up to a Brillouin angle of around ≤ 10 deg. Therefore the filter design is only transparent for the first five modes while conserving the filter characteristics: $TE_{1,1}$, $TM_{0,1}$, $TE_{2,1}$, $TM_{1,1}$ and $TE_{0,1}$. The remaining modes with a Brillouin angle > 10 deg would only deteriorate the filter performance, if same mode content would be assumed, or attenuated by the filter. If a relative mode content $P_{\text{rel}}(\alpha, \chi_0, \chi)$ for the different modes is assumed as follows

$$P_{\text{rel}}(\alpha, \chi_0, \chi) = e^{\alpha(\chi_0 - \chi)} \quad (4.1)$$

where χ_0 is the eigenvalue of the fundamental mode, $\chi \geq \chi_0$ a mode eigenvalue and α a scaling factor. Therefore the content in the other modes is expressed as multiple of the content in the (fundamental) mode with eigenvalue χ_0 . Then an effective average transmission $T_{\text{eff}}(f)$ could be expressed as

$$T_{\text{eff}}(f) = 10 \cdot \log_{10} \left(\frac{\sum_{i=1}^N P_{\text{rel}}(\alpha, \chi_0, \chi_i) T(\chi_i, f)}{\sum_{i=1}^N P_{\text{rel}}(\alpha, \chi_0, \chi_i)} \right) \quad (4.2)$$

as weighted average for all possible or a defined set of N modes. Figures 4.13 and 4.14 illustrate the fact, that with increasing scaling factor α , the relative mode content is decreasing faster and the number of relevant modes to be taken into account decreases.

Figure 4.16 shows the computed effective transmission of the quasi-optical filter for different number of modes and different scaling factors α . Again, the error range has omitted in the plot to improve the readability. Obviously when other modes are taken into account, the filter characteristics are deteriorated. The effect is reduced with increasing scaling factor since higher order modes, potentially deteriorating the filter performance, become less important.

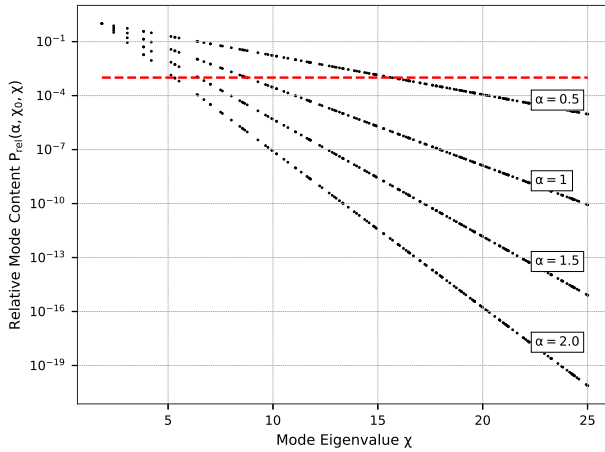


Figure 4.13: Relative mode content distribution for different scaling factors with eigenvalue χ_0 of the $TE_{1,1}$ fundamental mode.

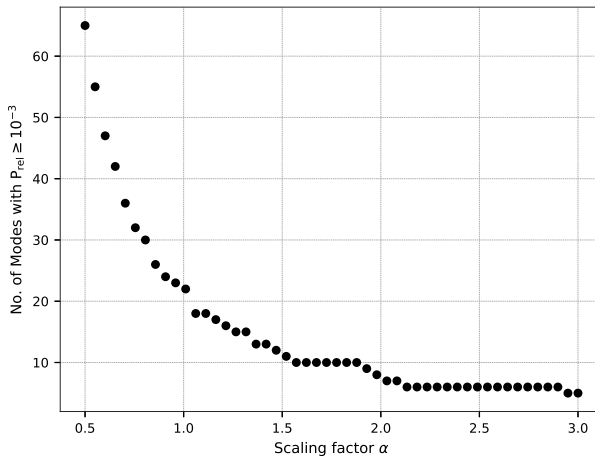


Figure 4.14: Number of modes with relative mode content above threshold of 10^{-3} . An increasing scaling factor α leads to a decreasing number of relevant modes.

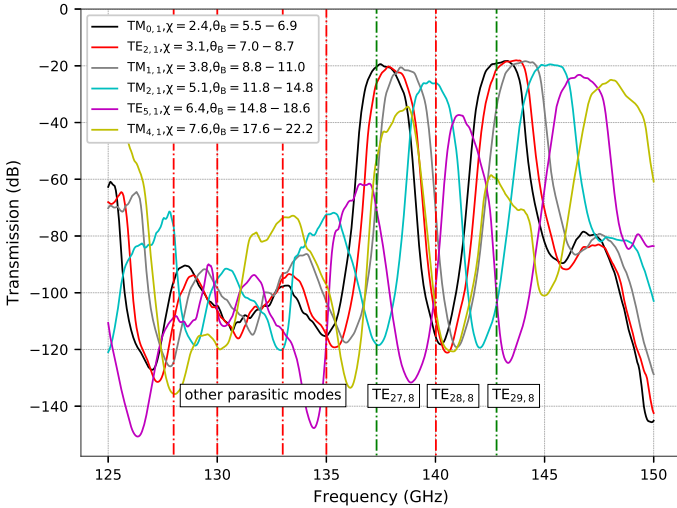


Figure 4.15: Comparison of the quasi-optical filter transmission for different modes with increasing eigenvalue and Brillouin angle. The additional modes either deteriorate the filter characteristics or are strongly attenuated. Errors are omitted for better readability.

In this case, a correction of the filter design is necessary to take into account the effect of other modes since the 140 GHz notch is shifted by 700 MHz to 1 GHz. A correction is necessary to achieve a downshift of the 140 GHz notch frequency. Therefore the air gap distance of the 140 GHz notch stack was slightly increased. The result of this correction is shown in Figure 4.17. Therefore, if a relative mode content distribution over mode eigenvalues is assumed where the major portion is in the fundamental waveguide mode, a reasonable solution for a quasi-optical filter can be found which is transparent for multiple modes.

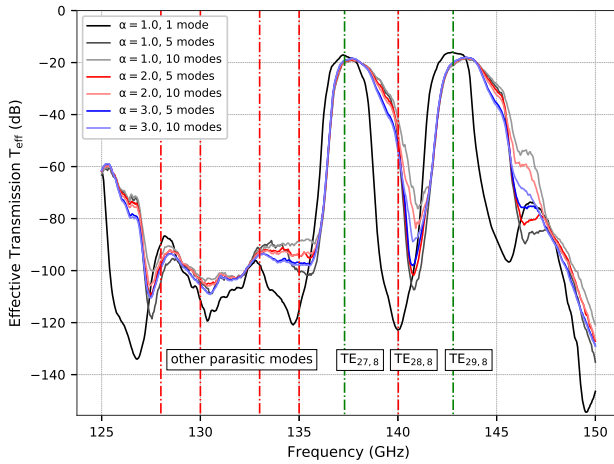


Figure 4.16: Computed effective transmission $T_{\text{eff}}(f)$ of the quasi-optical filter for variable number of modes and scaling factor α . Only the median values are shown for the sake of readability. Obviously a correction of the design is required for the 140 GHz notch when multiple modes are taken into account.

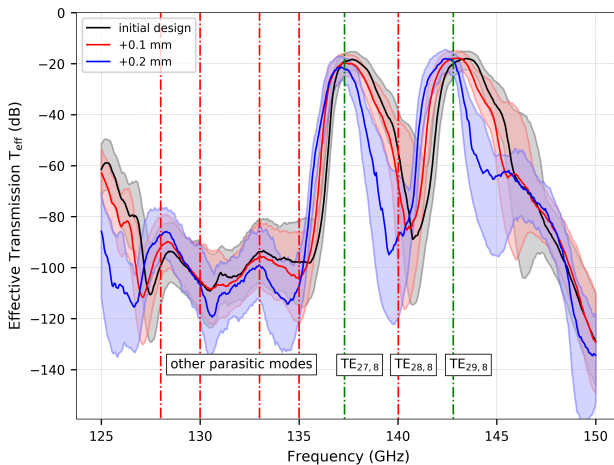


Figure 4.17: An increased air gap distance for the 140 GHz stack leads to the desired downshift of the notch frequency when multiple modes (here: 10) are considered with $\alpha > 1$ (here: 3).

4.3.2 Realization

The quasi-optical filter was made of simple ring elements, once screwed together, realizing a filter in a circular waveguide with a WG16 flange. Each ring element type constitutes a stack element housing a sapphire disc with different thickness, realizing the required air gap to the subsequent sapphire disc. Figure 4.19 shows the technical drawing for one of the six ring element types. 30 ring elements were fabricated in total in-house with aluminium as material in the IPP Greifswald workshop.

Obviously this design leaves some space for improvements: Once the ring elements are screwed together, the filter cannot be easily tuned, except thin foils are inserted in between ring elements. Second, a slight corrugation is introduced for the waveguide by the mechanical design to house the dielectric discs. This potentially supports mode conversion (e.g. to the $HE_{1,1}$ hybrid mode) which could deteriorate the filter performance.



Figure 4.18: Photograph of the assembled quasi-optical dielectric disc filter to realize a satellite mode band pass.

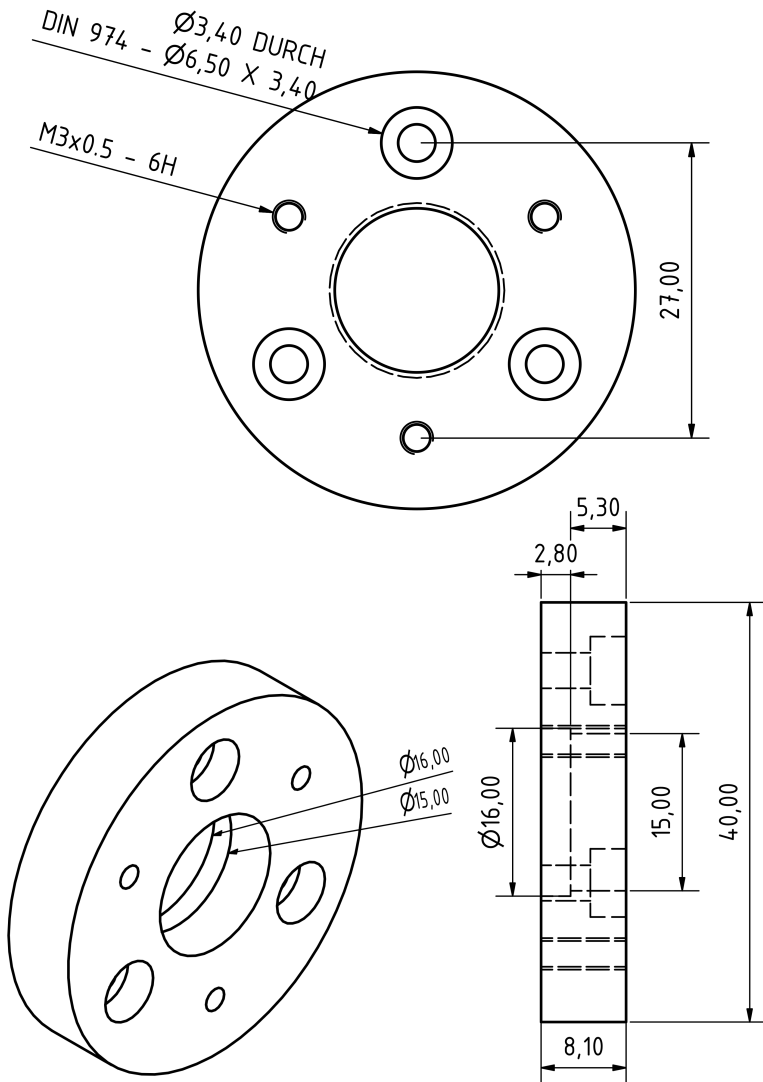


Figure 4.19: Technical drawing of one of the ring element types housing a sapphire disc and realizing the required air gap to the next dielectric layer. A maximum tolerance of $50 \mu\text{m}$ was demanded.

4.3.3 Lab Measurement with tuneable RF source

In order to verify the filter function and the computed transmission of the quasi-optical filter, a measurement with a manually tuneable low-power RF source and a Tektronix 2784 spectrum analyzer was performed. At the time of measurement, the Anritsu spectrum analyzer used for the measurement in section 4.2.3, providing an automated measurement sweeping the RF source frequency, was not available yet. Therefore, the output power level over frequency of the RF source was measured first without filter as reference.

Figure 4.20 shows the measurement result, revealing a non-uniform output power level over the relevant frequency range. The measurement was then repeated using two circular horn antennas with the quasi-optical filter in between.

Figure 4.21 shows the filter attenuation over frequency for the measurement after the first assembly without correction. For the satellite $TE_{27,8}$ mode around 137.3 GHz and for the satellite $TE_{29,8}$ mode around 142.8 GHz a low attenuation of 6.1 dB and respectively 10.2 dB were achieved. For the nominal gyrotron $TE_{28,8}$ mode between 140.0 GHz and 140.5 GHz an attenuation of 20.3 dB up to 42.0 dB was achieved. For the other parasitic modes below 136.5 GHz an average attenuation around 40 dB was measured.

The measurement was repeated after a second assembly and a third assembly with thin steel foils (0.1 mm) in between the ring elements for the 140 GHz notch stack. Furthermore, the in- and output of the filter and the whole filter itself were covered in ECCOSORB[®] in an attempt to create a proper isolated measurement environment to see an improvement. It is a broadband microwave absorbing material based on polyurethane foam. Unfortunately, due to the noisy RF source, the manual frequency sweep and the lack of a proper isolated measurement environment, the measurement is inconclusive and imprecise. An bigger attenuation than -40 dB could not be reasonably measured with the available equipment. A deterioration of the filter performance was visible after each reassembly of the filter. This can be explained by the ductility of aluminum altering the filter geometry with every reassembly. Comparing the measurement qualitatively with the computed filter transmission, the desired frequency characteristics were achieved as far as the limited measurement capabilities allow such a statement.

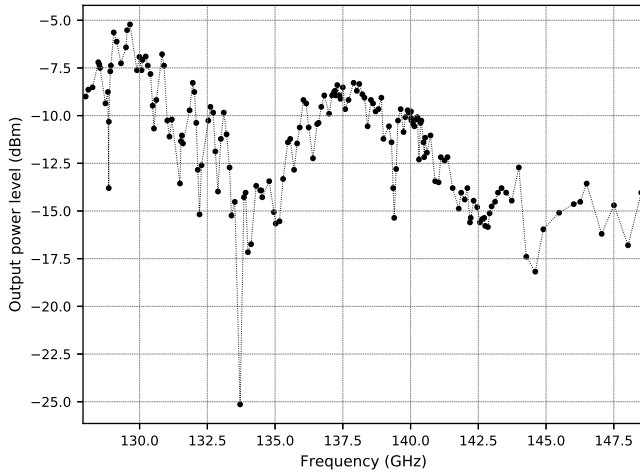


Figure 4.20: Measured output power level over frequency for the low-power manually tuneable RF source. The output power level is not stable over the relevant frequency range.

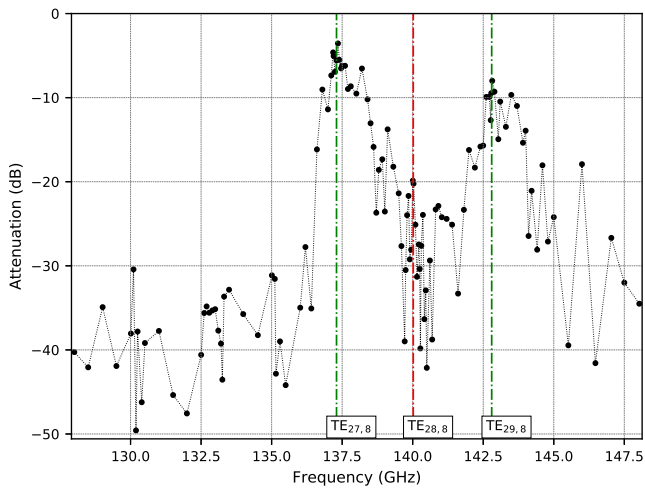


Figure 4.21: First measurement of the quasi-optical filter attenuation over frequency. The intended frequency characteristic was achieved qualitatively.

4.3.4 In-situ Measurement with Gyrotron

In order to evaluate the performance of the quasi-optical filter under real conditions, two gyrotron pulse spectrograms of the stray radiation at the gyrotron relief window were acquired with a frequency resolution of 10 MHz. A detailed description of the method is given in section 5.1.1 of this thesis. One spectrogram of the gyrotron nominal mode was acquired without filter to obtain a reference spectrogram, shown in figure 4.22. The gyrotron nominal mode was chosen, since the filter performance in this frequency range is most important and the nominal mode appearance is highly reproducible. The measurement was then repeated with the quasi-optical filter attached to the diagnostic flange between the relief load and the relief window of the gyrotron (see figure 4.23). The two spectrograms were then subtracted to obtain a rough estimate of the filter attenuation over frequency (and time) as shown with figure 4.24. Of course, this result is not reliable since the frequency over time of the nominal mode is maybe well reproducible, but the same presumably does not hold for the power level over frequency (and time). As we remember, the most prominent property of stray radiation was its highly unstable and fluctuating intensity in time. So we would need many spectrograms (at least 10 to 100) to approximate the spectrogram noise distribution to obtain a reliable value with an error estimate for the attenuation of the quasi-optical filter. This method would be extremely tedious. Anyway, to obtain a result comparable to the previous lab measurement, the frequency over time was extracted from the mode traces in both spectrograms. For that purpose a gaussian and a Savitzky-Golay filter [SG64] was used to suppress the noise and a histogram-based image processing method was applied to detect the edges of the mode trace. Consequently the amplitude over frequency for the spectrograms with and without filter and the attenuation of the quasi-optical filter were determined. The latter result is shown in figure 4.25, but is, as previously mentioned, probably unreliable due to insufficient data used.

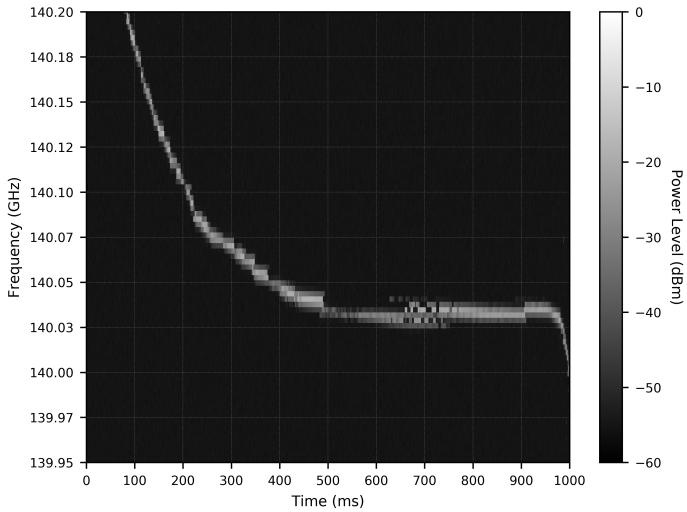


Figure 4.22: Gyrotron stray radiation pulse spectrogram ($\Delta f = 10$ MHz) without quasi-optical filter as reference. For $t \geq 980$ ms, the body voltage was ramped up to provoke a mode loss.



Figure 4.23: Photo of the quasi-optical filter (silver rod) attached to the diagnostic flange between the gyrotron relief window and relief load (black cylinder).

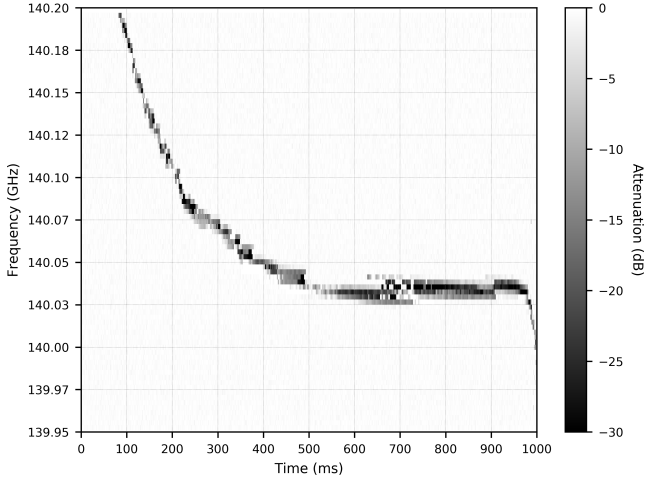


Figure 4.24: Subtraction result of the gyrotron pulse stray radiation spectrograms ($\Delta f = 10$ MHz) without and with quasi-optical filter showing the gyrotron nominal mode. The filter attenuation over frequency and time is obtained.

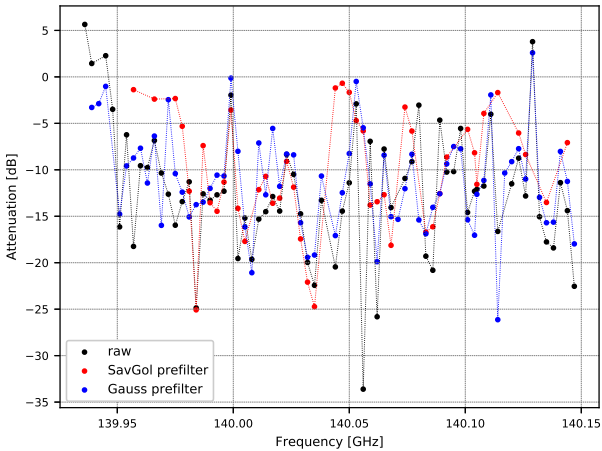


Figure 4.25: Extracted attenuation over frequency for the quasi-optical filter obtained from the spectrogram mode traces. Noise is dominating, no clear frequency selectivity visible despite pre-filtering. More spectrogram data is required to obtain a less noisy result.

4.4 Summary

The filter design code MMWFR was presented implementing the T-matrix concatenation approach to compute the frequency response of multi-layered dielectric disc filters for multiple modes taking into account the effect of manufacturing tolerances. The code can also be used to design cutoff-waveguide filters. The design and construction of a 136 GHz cutoff high pass filter is documented and its intended function was successfully verified in a measurement. An attenuation around 25 dB for frequencies below 136.5 GHz was achieved. A quasi-optical satellite mode band pass was designed and realized as dielectric disc filter in a circular, oversized waveguide. During its design process, emphasis was put on the feasibility evaluation of a design by taking realistic manufacturing tolerances and the possible effect of higher order modes in the circular waveguide into account. Finally, the quasi-optical filter was verified in a lab measurement using a tunable low-power RF source and in an in-situ measurement attached to the diagnostic flange between the gyrotron relief load and relief window. The lab measurement showed good qualitative agreement of the measured filter attenuation with the simulation. A very good attenuation around 40 dB for frequencies below 137 GHz and low attenuation around the satellite mode frequencies between 6 dB for the $TE_{27,8}$ mode to 10 dB for $TE_{29,8}$ mode was achieved. The measurement result for the attenuation around 140 GHz for the nominal gyrotron $TE_{28,8}$ mode is ambiguous and probably affected by the badly isolated measurement environment, noise, filter geometry deviations and the crude measurement method applied due to the limitations of the available equipment. The achieved attenuation around 140 GHz varies between 20 dB and 40 dB. The in-situ measurement with the quasi-optical filter being attached to the gyrotron is inconclusive due to insufficient data.

5 Stray Radiation Measurements

As stated in sections 1.5.3 and 1.5.5 of the introduction, a variety of modes beside the intended design mode can be excited and the quasi-optical output coupler (beam launcher) of a gyrotron converts all other modes than the design mode to stray radiation. The W7-X gyrotron has a so-called "relief window" which is another window additionally to the output window. Originally intended as sink for the stray radiation, it is used here for diagnostic purposes since it is facing the quasi-optical output coupler. Therefore the gyrotron relief window is suitable to observe the stray radiation from parasitic and satellite mode activity.

This chapter presents and compares the results of stray radiation measurements at the gyrotron relief window with various measurement setups in order to identify a precursor for the loss of the nominal working mode in a gyrotron. A measurement setup to acquire pulse spectrograms of arbitrary duration was developed for this thesis with no additional costs. The activity level of the azimuthal neighbours $TE_{27,8}$ and $TE_{29,8}$, the satellite modes of the nominal working $TE_{28,8}$ mode for the W7-X gyrotron, is identified in pulse spectrograms and preliminary single-detector measurements as possible candidate for a mode-loss precursor. Two more advanced measurement setups are presented in this chapter for which custom microwave components were designed, built and tested. For the first setup, the mono-mode setup using a power combiner (triple hybrid ring), a 136 GHz cut-off high pass filter was designed, built and tested. For the second setup, the quasi-optical setup using multiple RF detectors, a quasi-optical satellite mode band pass was designed and built as dielectric disc filter in an oversized circular waveguide. The results achieved with both setups for the satellite mode activity are compared and used to derive possible mode loss precursors.

5.1 Pulse Spectrograms

Spectrograms of long gyrotron pulses could be helpful to observe transient multi-moding, mode switching behaviour and slower processes in order to identify a modelless precursor. A Pulse Spectrum Analysis (PSA) system to acquire unambiguous pulse spectrograms was developed by Schlaich and presented in his doctoral thesis [Sch15]. Unfortunately the PSA system was not suitable for the purposes of the present thesis: The maximum spectrogram duration is limited by the amount of built-in fast memory of the real-time oscilloscope (RTO) depending on the sampling rate and the number of receiver channels used. Spectrograms with the full bandwidth of 6 to 12 GHz in the frequency range between 100 to 170 GHz are limited to a duration of 28 ms when only one receiver channel is used. Therefore the alias frequency elimination and/or the usable bandwidth has to be sacrificed for a longer spectrogram acquisition [Sch15]. Additionally it was difficult to move the PSA system from the gyrotron teststand at KIT to the W7-X ECRH facility in Greifswald. The PSA system itself and/or parts of it were simultaneously in use for investigations at the gyrotron teststand at that time.

Therefore a solution to acquire spectrograms of gyrotron pulses with arbitrary duration was developed for this thesis using already available resources in Greifswald. The measurement setup and data post-processing workflow of this solution are presented in the following sections. A spectrogram of the nominal mode is presented to validate the method by comparing it with the results obtained with the PSA system. The mode switching behaviour during an experiment was made visible in a spectrogram of a 1s pulse which is also presented here. The results presented in this section were already published in parts in [WLM⁺17]. The first author of that publication is also the author of this thesis..

5.1.1 Measurement Setup

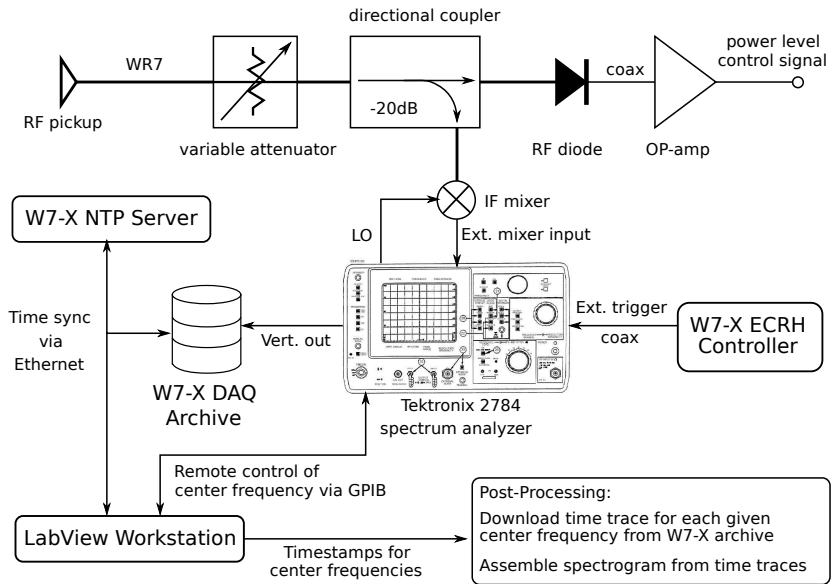


Figure 5.1: Schematic overview of the provisional measurement setup for the gyrotron pulse spectrogram acquisition at Wendelstein 7-X. A spectrum analyzer in zero span mode is remotely controlled and its central frequency is incremented at each external pulse gate trigger provided by the W7-X ECRH control.

Figure 5.1 shows a schematic overview of the improvised measurement setup to acquire gyrotron pulse spectrograms at Wendelstein 7-X. In order to protect the input mixer of the spectrum analyzer, a variable attenuator is used in series with a directional coupler. The actual power level is checked with a calibrated RF diode signal. The central component is a Tektronix 2784 spectrum analyzer operated in zero-span mode. Therefore a time signal of the input power level for a specific frequency is obtained when the spectrum analyzer is triggered. The analog vertical and horizontal output signal of the spectrum analyzer is continuously sampled with 25 kHz by the W7-X data acquisition and the time signal for a given central frequency is stored in the W7-X experiment data archive. The spectrum analyzer is triggered externally by a rising edge of the

pulse gate signal for a specific gyrotron provided by the W7-X ECRH control. The spectrum analyzer is remotely controlled via general purpose interface bus (GPIB (IEEE 488)) with a LabView program running on a workstation. Each time the spectrum analyzer is triggered by the external gyrotron pulse gate signal, its central frequency is incremented. After the end of the pulse, the spectrum analyzer waits for another external trigger. The LabView program running on the workstation records the actual timestamp and the central frequency set when the spectrum analyzer is triggered. To guarantee data consistency between the LabView workstation and the W7-X experiment data archive, the actual system time set on the workstation is synchronized with the W7-X network time protocol (NTP) server down to millisecond accuracy. This way, a spectrogram of a gyrotron pulse with arbitrary duration can be assembled from the time signals for each given central frequency.

Of course, this solution has several drawbacks: First of all, this spectrogram acquisition procedure is tedious depending on the central frequency increment stepsize and the desired frequency range, requiring many gyrotron pulses to obtain one spectrogram. Also the download and post-processing of the time trace data is time consuming. Secondly, it is only possible to acquire a kind of average spectrogram with this method, therefore requiring a certain degree of reproducibility of the phenomena to be observed in the spectrogram. In addition, elimination of alias frequencies (hence the mixing products) is possible, but doubles the time required to acquire a spectrogram. The Tektronix 2784 spectrum analyzer can switch between two different local oscillator frequencies for the input mixer. So the alias frequencies in the time trace or the spectrum (when the frequency span is greater zero) can be ruled out by comparison. The PSA system mentioned above uses a similar approach to eliminate the alias frequencies, but acquires simultaneously the time traces using two different oscillator frequencies with two mixers. The spectrogram is then computed on a workstation using a short time Fourier transform (STFT) [Sch15].

5.1.2 Post-processing

Figure 5.2 shows a simplified flow chart of the post-processing workflow for the gyrotron pulse spectrogram acquisition. As mentioned above, the gyrotron pulse spectrogram is assembled from time signals for different center frequencies set for the spectrum analyzer operated in zero-span mode. The whole data post-processing to create a pulse spectrogram is automated in the programming language Python and is part of the aforementioned framework SAGE. First the file created by the LabView workstation, containing the trigger timestamps and the actual center frequencies, is read. Since the majority of the gyrotron experiments were conducted independently from a W7-X experiment program, the begin and end of the individual gyrotron pulses had to be identified afterwards during the data post-processing. This procedure is necessary since, when the gyrotrons are operated manually which means independent from a W7-X experiment program, the begin, end and duration of gyrotron pulses is saved nowhere and cannot be simply requested from the W7-X experiment data archive. A finite state machine was therefore implemented to detect gyrotron pulses of arbitrary length (e.g. longer than the defined data chunk duration of 4 seconds in the W7-X experiment data archive) and if the pulse was modulated. A list of available data chunks for the body voltage channel is requested via the REpresentational State Transfer Application Programming Interface (REST API) of the W7-X experiment data archive. A REST API is a common standard in software development for the communication with web-based services. Then data chunks are downloaded and simultaneously held in the working memory, up to a maximum number of data chunks equivalent to the maximum expected pulse duration. Then concatenated chunks are analyzed using the kernel density estimate (KDE) to determine if the pulse was modulated and to determine the proper threshold signal level to identify the begin and the end of gyrotron pulses with falling and rising edge pairs. When all available data chunks within the time period given by the timestamp list are analyzed, the full pulse data consisting of multiple defined data channels is downloaded for each detected pulse. For each downloaded pulse data, the relative time index of either a possible mode loss event or the pulse startup is identified.

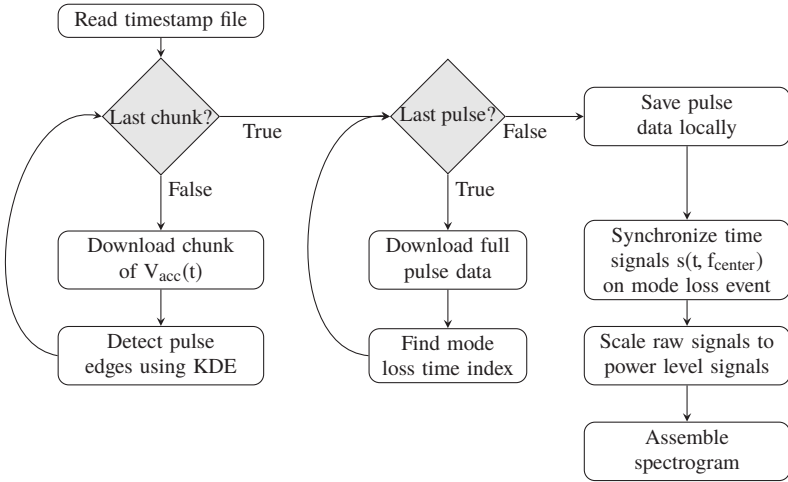


Figure 5.2: Simplified post-processing workflow for the gyrotron pulse spectrogram acquisition with time signal synchronization on the mode loss event

This way, the time signals for the different center frequencies can be synchronized on a common defined event. This is done in order to guarantee a consistent spectrogram and to compensate for small time shifts between the acquired time signals. Finally, the raw vertical output voltage signal of the spectrum analyzer is rescaled to a power level signal and the spectrogram is assembled.

Typically a spectrogram consists of hundreds of time signals belonging to the same number of consecutive gyrotron pulses. The time resolution is $40\mu\text{s}$ given by the 25 kHz sampling rate of the W7-X data acquisition. The maximum frequency resolution is given by the minimum resolution bandwidth (RBW) of the spectrum analyzer which is 300 kHz. For a rough overview, a frequency resolution of 10 MHz to cover a frequency range of up to 16 GHz is used. The results obtained with this method are presented in the following sections.

5.1.3 Spectrogram of the Nominal Mode

In order to validate the method, a spectrogram of the nominal gyrotron TE_{28,8} mode was acquired. Figure 5.3 shows clearly the frequency chirp of the gyrotron nominal mode due to thermal cavity expansion and neutralization. The center frequency increment was set to the minimum possible resolution bandwidth of 300 kHz. This result is in quantitative and qualitative agreement with the measurement of the nominal mode frequency over time using the PSA system by Schlaich in [Sch15]. The nominal mode frequency is changing mainly during the first 500 ms of the pulse and is stabilizing later-on, undergoing only a very slow change (1.5 MHz per min [Sch15]) afterwards during very long pulse or cw-operation.

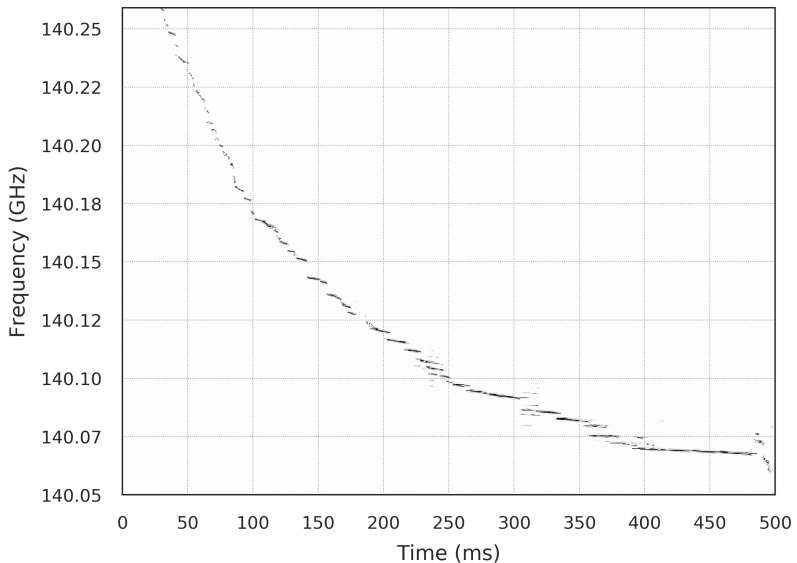


Figure 5.3: Spectrogram (frequency resolution $\Delta f = 300$ kHz) of a 500ms pulse with a voltage ramp for the last 20ms performed with the Bravo 5 gyrotron. The spectrogram was assembled of 695 time signals belonging to the same number of consecutive gyrotron pulses.

5.1.4 Spectrogram of Mode Switching Behaviour

To identify a possible mode loss precursor in the stray radiation spectrum, an overview spectrogram with 16 GHz frequency range was acquired for a 500 ms pulse performed with the Bravo 5 (TED SN002i) tube shown in Figure 5.4. The central frequency increment was set to 10 MHz resulting in 1600 gyrotron pulses required to obtain the spectrogram over the full frequency range. For the last 20 ms of the pulse, the body voltage was ramped up in order to provoke a loss of the nominal operating mode and hence mode switching behaviour. After the provoked mode switch, on average, modes at 130.26 GHz, 133.01 GHz, 134.57 GHz, 135.76 GHz, 137.34 GHz and 142.81 GHz appeared beside the weakened nominal gyrotron mode $TE_{28,8}$ at 140.02 GHz. The latter two parasitic modes can be identified as the azimuthal neighbour or satellite modes $TE_{27,8}$ and $TE_{29,8}$ of the nominal mode. The measured frequencies are close to the predicted frequencies by the cold-cavity code COLDC [Ker96] and by the multi-mode gyrotron interaction code EURIDICE [APIV12]. The observed parasitic mode frequencies are consistent with previous findings by Schlaich in [Sch15]. This result is in qualitative agreement with the simulation results presented in chapter 2. The multi-moding behaviour was observed with both satellites being active simultaneously with the weakened nominal mode before the satellite becomes the dominant mode.

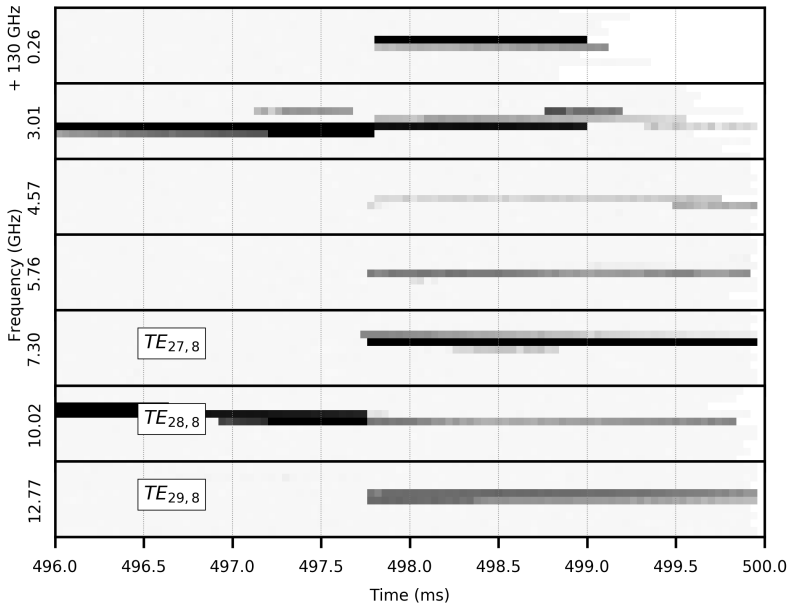


Figure 5.4: Excerpts of an overview spectrogram ($\Delta f = 10$ MHz) of a 500 ms pulse with the Bravo 5 (TED SN002i) tube. The gyrotron nominal mode $TE_{28,8}$, its satellites $TE_{27,8}$ and $TE_{29,8}$ and other parasitic modes are observed around a provoked mode switch by ramping up the body voltage for the last 20 ms. The satellite $TE_{27,8}$ is found to be dominant after the mode switch.

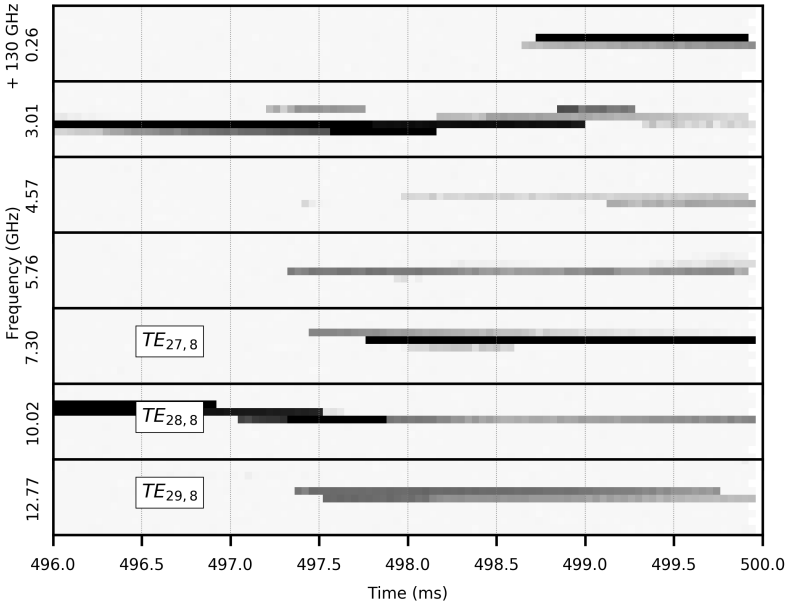


Figure 5.5: Same spectrogram as in Figure 5.4, but the time signals are not synchronized to the mode loss event, but to the pulse startup.

5.2 Explorative Measurements

The gyrotron interaction simulations exhibited an increasing satellite mode activity with multi-moding behaviour prior to a loss of the nominal gyrotron mode. Consequently, experiments were performed to clarify whether the same behaviour can be observed in reality.

In this section, the results of first exploratory satellite mode activity measurements for the Bravo 5 (TED 2i) and Alpha 5 (TED 5i) gyrotrons are presented. The stray radiation was measured with a very simple setup consisting of a D-band detector diode (TST BD7 S/N 922x), a differential amplifier with low pass ($f_c = 1$ MHz), a 20dB fixed attenuator to protect the diode and either a high pass or a notch filter. A WR7 waveguide adapter was attached to the WG16 diagnostic flange between the relief load and the relief window to pick up the gyrotron stray radiation from the relief window.

5.2.1 TED #2i Gyrotron with 142 GHz High Pass Filter

A 142 GHz high pass filter was placed before the diode to measure the activity of the upper azimuthal neighbour or satellite mode $TE_{29,8}$ only. Figure 5.6 shows the measurement setup using the high pass filter.

In total, more than 3000 pulses with a target duration of 1 s were acquired on 13th and 14th July 2016 with the Bravo 5 gyrotron at constant (nominal) fields ($I_{\text{main}} = 83.9$ A, $I_{\text{gun}} = -3.2$ A), but for various points in the working point plane (U_{acc} , I_{cath}) at various output power levels. The depression ratio was in the range between 0.46 and 0.53 representing a variation of up to 15 %. The experimental data was automatically aggregated to a small searchable database using the aforementioned SAGE framework. Figure 5.7 shows the result of the stray radiation measurement with the 142 GHz high pass filter and a single diode. The average measured diode signal is plotted against the average output power at the gyrotron output window. Every dot represents a gyrotron pulse of 1 s duration. The average measured diode signal could be interpreted as the average activity A of the upper satellite mode $TE_{29,8}$ during the pulse.

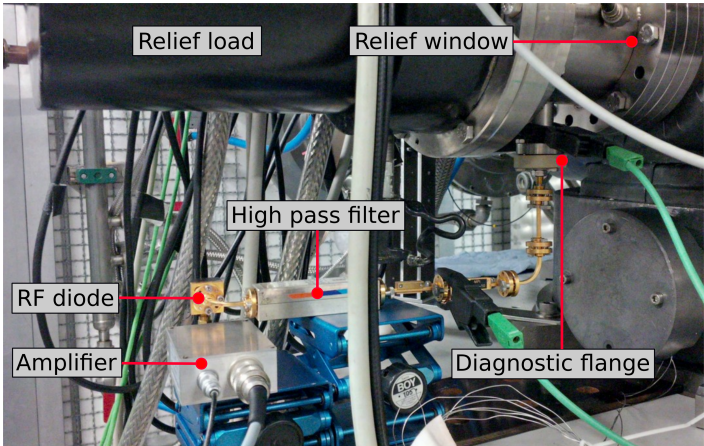


Figure 5.6: Setup for the single diode measurement of the stray radiation using a 142 GHz high pass filter

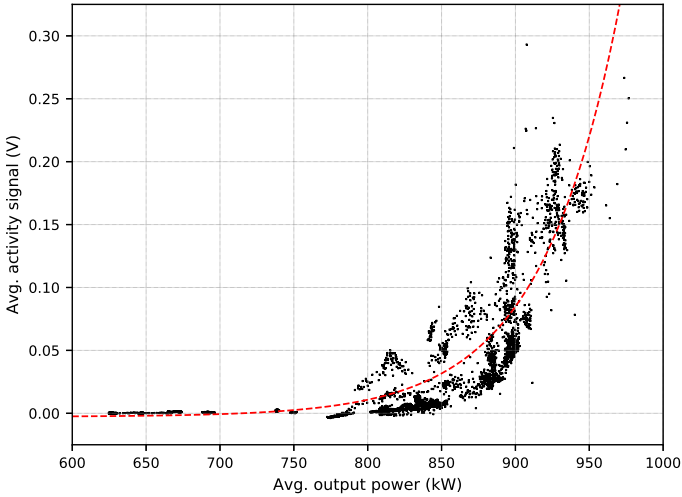


Figure 5.7: Average diode signal measured with 142 GHz high pass filter plotted against the power at the gyrotron output window. Each dot represents a gyrotron pulse with a duration of 1 s. The red dashed line is an exponential fit of the data.

The red dashed line fits the data using the ordinary least squares (OLS) (see e.g [KNNL04]) method with the function

$$A(P) = \alpha + \beta e^{\gamma(P+\delta)} \quad (5.1)$$

where $\alpha = -2.744 \cdot 10^{-3}$, $\beta = 4.89 \cdot 10^{-9}$, $\gamma = 1.867 \cdot 10^{-2}$, $\delta = -6.064$ and P being the gyrotron output power. For the sake of simplicity, the quality of a fit or a model will be evaluated using the normalized root-mean-square error (NRMSE). There are other more appropriate quality measures for non-linear models like e.g. the Akaike information criterion (AIC) [Aka74], but this would be an overkill for this application. The NRMSE is defined as

$$\text{NRMSE} = \frac{\sqrt{\text{MSE}}}{p_{90\%}(Y) - p_{10\%}(Y)} = \frac{\sqrt{\frac{1}{N} \sum_{i=1}^N (y_i - \hat{y}_i)^2}}{p_{90\%}(Y) - p_{10\%}(Y)} \quad (5.2)$$

Here, N is the total number of values in the data set, $y_i \in Y$ is the observed value (dependent or explanatory variable) and $\hat{y}_i = f(\hat{x}_i, \hat{\Theta})$ are the values predicted by the model f with \hat{x}_i being the input vector (assumed independent variables) and $\hat{\Theta}$ the model parameter vector. The root-mean-square error (RMSE) is normalized by the percentile (see chapter 2.3.1 for an explanation) difference of the data set allowing for a better comparability of the NRMSE across different models and data sets. In this case, the obtained NRMSE of the fit was 0.181. The fraction of variance explained (FVE) by the model is defined by

$$\text{FVE} = 1 - \frac{\text{MSE}}{\text{Var}(Y)} \quad (5.3)$$

which accounts here to 78.3%. The average activity signal grows exponentially above a gyrotron output power of 800 kW. This coincides with the practical output power limit of the gyrotron lying in the range between 800 to 950 kW where the operational reliability is significantly decreased (see chapters 3.3.1 and 3.3.5). The deviations from the activity fit curve can be explained better when the acceleration voltage and cathode current are used as explanatory variables.

Figure 5.8 shows a three-dimensional visualization of the data (U_{acc}, I_{cath}, A) where the average activity is shown over the average working point of each gyrotron pulse in Figure 5.8. The data is fitted using the OLS method with the exponential function

$$A(U_{acc}, I_{cath}) = \alpha + \exp(\beta U_{acc} + \gamma I_{cath} + \delta U_{acc} I_{cath} + \epsilon) \quad (5.4)$$

where $\alpha = -1.004 \cdot 10^{-2}$, $\beta = 4.824$, $\gamma = 6.84$, $\delta = -8.234 \cdot 10^{-2}$ and $\epsilon = -4.010 \cdot 10^2$ are the fit parameters. The activity increases exponentially with the acceleration voltage, but also an increasing slope with increasing cathode current is visible. Figure 5.9 shows the same data, but projected on the (U_{acc}, A)-plane. Already just visually judging, the activity variation is clearly explained better when the acceleration voltage and cathode current are taken into account. The NRMSE decreased, to 0.147 (before: 0.181) and the FVE now accounts to 85.7 % (before: 78.3 %).

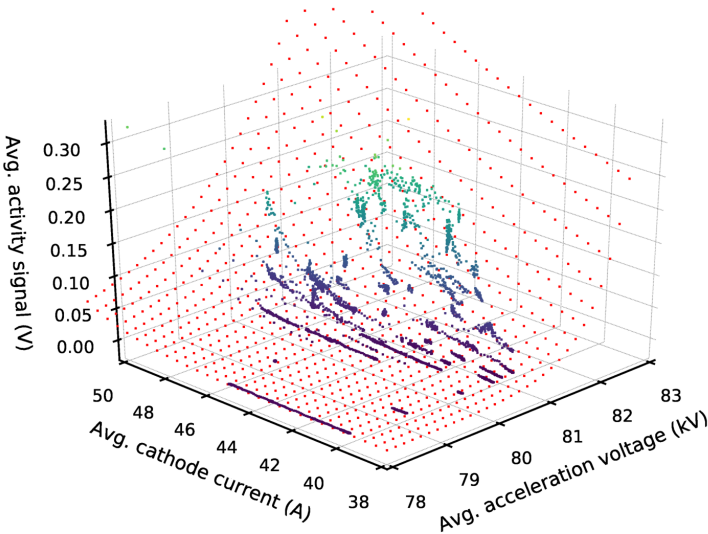


Figure 5.8: Average measured activity in the working point plane for all gyrotron pulses performed with Bravo 5 using the high pass filter (activity signal level is also color encoded). Red dot plane fits the data with an exponential function.

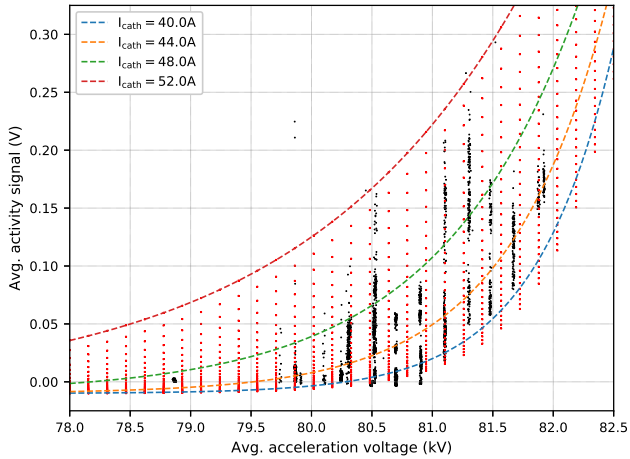


Figure 5.9: Two-dimensional projection of the experimental data and the fit from Figure 5.8. Dashed lines denote the fit results for different constant cathode currents for visualization purposes only.

Note that the W7-X gyrotrons use a diode-type MIG. Consequently, an increasing acceleration voltage means an increasing pitch factor (for an explanation, see chapter 1.5.1) The increased pitch factor can explain the increased parasitic activity level, as similar behaviour is observed in gyrotron interaction simulations presented in chapter 2 of this thesis.

Of course, one could argue that the general average stray radiation level was expected to increase with increasing output power anyway: Since the quasi-optical output coupler or beam launcher in the gyrotron is not 100 % efficient and the Gaussian beam created by the quasi-optical output coupler is the result of a superposition of the field distributions of multiple modes [TYA⁺05], an increase of the general stray radiation level could be expected. But even when the result for the activity signal from Figure 5.7 is taken and normalized by the output power, the evidence is still indisputable (the result is shown in Figure A.1 in the appendix).

In order to examine the behaviour of the activity signal in the time domain, the time signals for the RF power at the gyrotron output window and the activity are shown in Figure 5.10 for three gyrotron pulses combined. Pulse 1 and 2 were performed above 900 kW and pulse 3 around 800 kW output power. Up

to an output power of 800 kW, the general activity level is low and decays within a time scale of ≤ 100 ms. The beam space charge neutralization acts on a similar time scale. Above the output power threshold of 800 kW, the activity level is significantly increased and does not fully decay over time even after the gyrotron has reached a stationary state for $t \geq 500$ ms. The average activity level is affected by multiple effects on different time scales. First the electron beam pitch factor, which reaches for a constant acceleration voltage a lower stationary value after 50 to 100 ms (depending on the pressure inside the tube), implying a lower activity level. Second, as shown in Figures 5.8 and 5.9, the activity level depends on the cathode current as well.

The cathode current itself depends on the acceleration voltage (diode-type MIG, hence the Shockley diode equation holds) and on the emitter temperature via the filament heating current. The cathode current reacts almost instantaneously on a μs time scale to changes of the acceleration voltage. On the other hand, the emitter cooling effect is dominant on longer time scales ($\gg 100$ ms), reducing the cathode current.

Figures 5.8 and 5.9 are implying - on average - a lower activity level over the pulse duration for a lower cathode current. Taking also the simulation results from chapter 2 and the experimental results shown in Figure 3.5 into account, this simple relation is questioned: A decreasing cathode current can imply a lower time-averaged activity, but simultaneously, if the gyrotron working point was already close to the nominal mode loss (the red dashed fit line in Figure 3.5), the break current for the working mode is approached further and hence the mode loss probability increased. If the parasitic mode activity signal has any predictive power for a loss of the nominal working mode, we would expect to see an increasing activity level, although the cathode current decreases, when the nominal mode loss is approached.

This behaviour is in fact observed in experiments: Looking again at Figure 5.10, pulse 1 and 2 only differ in their acceleration voltage signal phase, leading to a later increase of the voltage towards the end at a slightly lower cathode current for pulse 1. This slight difference seems to be sufficient to result in an increased activity towards the end of the pulse. Figure 5.11 is a zoom into the last 200 ms of pulse 1 from Figure 5.10. An interesting, reproducible observation is the coincidence of peaks in the activity signal with dips in the RF signal of the nominal mode. The red dashed lines denote the beginning and end of a peak or a dip respectively.

The hypothetical, but physically motivated explanation for this coincidence is: parasitic modes temporarily draw power from the nominal mode expressed by

dips in the RF and simultaneous peaks in the activity signal. It supports the existence of temporary, reversible multi-mode behaviour due to mode competition during the high-power operation of the gyrotron close to the nominal mode loss. Since the cathode current drops while the acceleration voltage increases towards the end of the pulse (due to supply voltage ripple and emitter cooling), the mode loss region in the working point plane is approached further which is indicated by the suddenly increasing activity and the sequence of dips and spikes in the activity and RF signals.

The reversibility of the multi-moding behaviour and the time scale of the observed pattern could be explained by the acceleration voltage noise and its non-gaussian probability distribution which was examined in section 2.3.1. A result from section 2.3.1 was that a noise voltage ≥ 0.5 kV occurs with a probability of 0.43 % or every 9.3 ms assuming a sample rate of 25 kHz. The higher the overshoot noise voltage, the lower is the probability and the bigger is the time distance between such temporary multi-moding events and vice versa. In Figure 5.11, the average time distance between onsets of peaks in the activity signal and respectively dips in the RF signal is 14 ms. Therefore, a noise voltage ≥ 0.5 kV is probably responsible for the observed phenomenon at this momentary working point. This coincides with the time scale for the time distance between noise voltage peaks implied by the empirical noise voltage probability distribution. So as long as a certain time distance threshold for noise voltage peaks is not exceeded, depending on the hysteresis or the taken path in the gyrotron parameter space during the pulse, the multi-moding behaviour is probably reversible and a bigger spike from noise on the acceleration voltage does not immediately cause an irreversible switch to the neighbouring satellite mode.

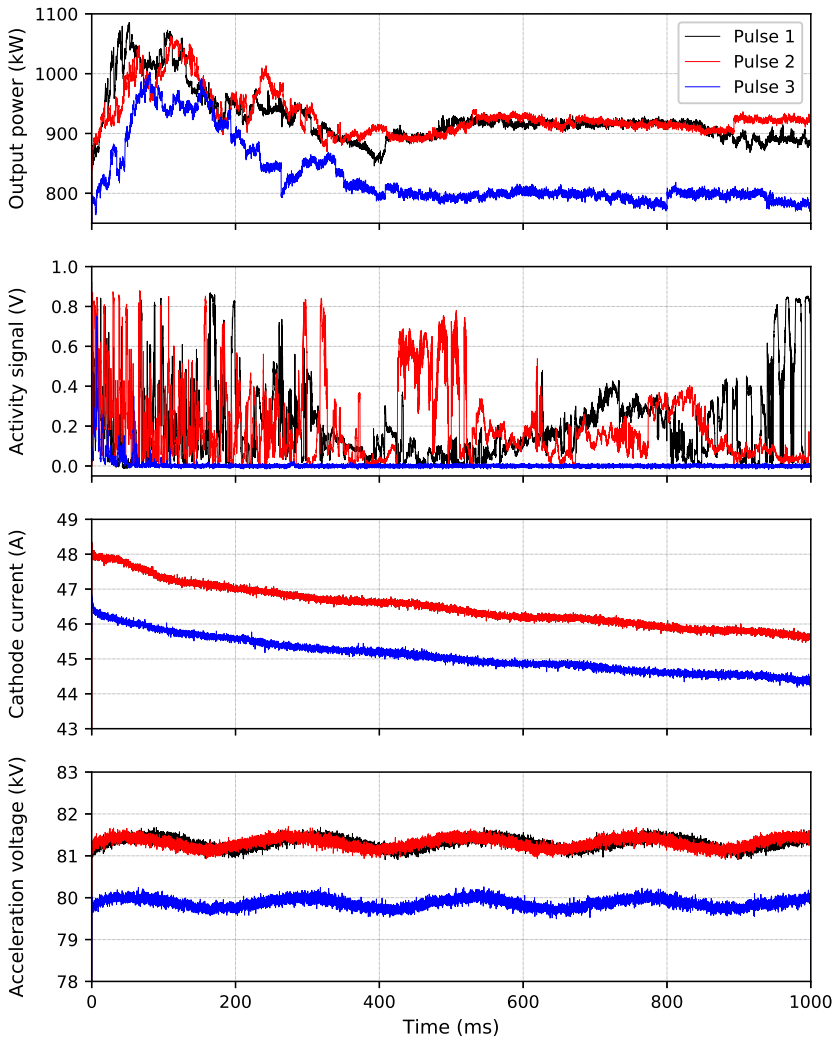


Figure 5.10: Exemplary gyrotron pulses around and above 800 kW output power: fast decaying activity signal within neutralization time scale (≤ 100 ms) below 800 kW. Activity signal shows non-decaying high parasitic activity above 800 kW.

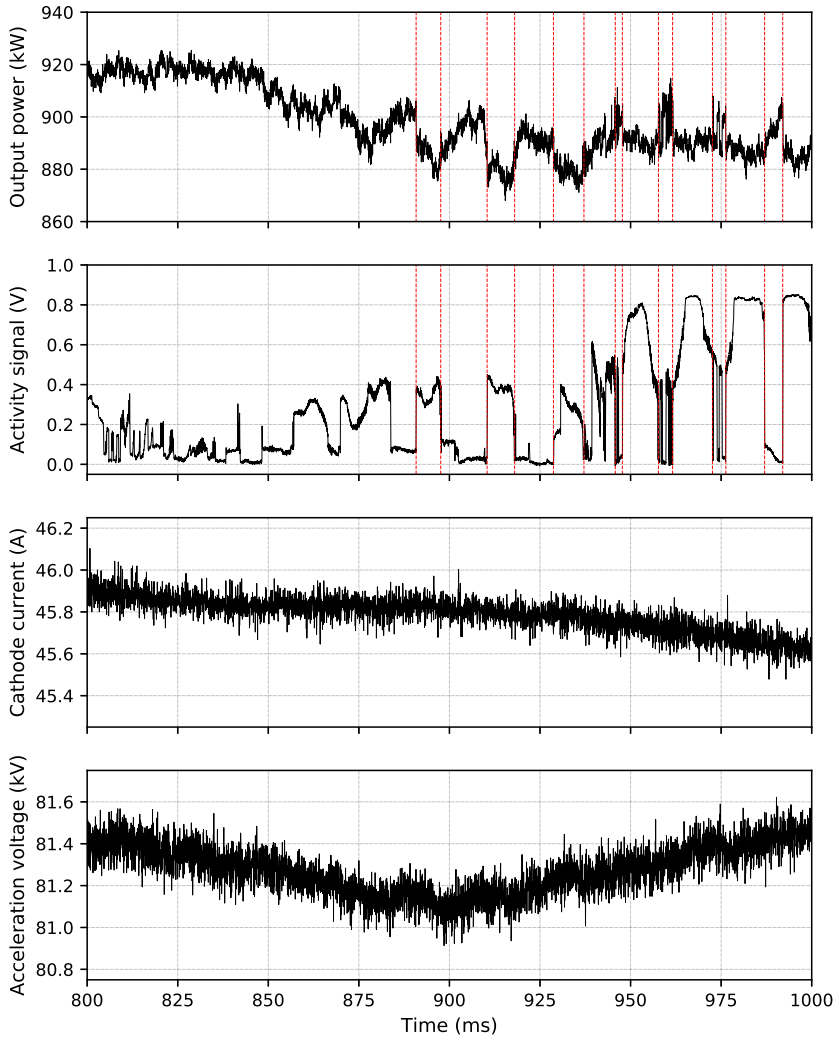


Figure 5.11: Zoom into the last 200 ms of figure 5.10. Coincidence of peaks in the activity signal with dips in the RF signal (red dashed lines) indicating temporary, reversible multi-mode behaviour due to increased mode competition close to the nominal mode loss.

5.2.2 TED #5i Gyrotron with 142 GHz High Pass Filter

On the 29th and 30th September 2016, 1240 gyrotron pulses with a duration of 1 s were performed in total with the Alpha 5 tube at various working points with different output power levels. The coil currents were the same for all gyrotron pulses. A 142 GHz high pass filter was used to measure the activity of the upper satellite mode $TE_{29,8}$ only. A preattenuation of 20dB was used and the amplifier for the measurement diode was calibrated to 10 V for a RF power of 1 mW produced by a 140 GHz test sender. Since the measurements were performed between the site acceptance test (SAT) of the gyrotron and the following experimental campaign OP1.2a, the power calibration of the gyrotron output power signal has a lower accuracy here of $\pm 10\%$.

Figure 5.12 shows the average diode signal versus the average output power of all performed gyrotron pulses. Each dot in the plot represents a gyrotron pulse. The red dashed line denotes an exponential fit of the data with the function 5.1 as used in the previous section. The achieved NRMSE increased to 0.475 and the FVE is lowered to 79.8 % compared to the fit for the experimental data obtained with Bravo 5.

Qualitatively, the same exponential growth of the activity beyond a certain output power level is observed. The qualitative behaviour seems to be similar across different gyrotrons of the same model series. The difference for Alpha 5 is that the power threshold level for which the activity growth begins, is lower and its steepness is increased compared to the result obtained with Bravo 5.

Again, a three dimensional plot (U_{acc}, I_{cath}, A) of the data, a fit and their projection on the (U_{acc}, A)-plane are presented with Figures 5.14 and 5.13. The same exponential function 5.4 was used to fit the data. The achieved NRMSE was 0.108 and a high FVE of 92.2 % was achieved in this case.

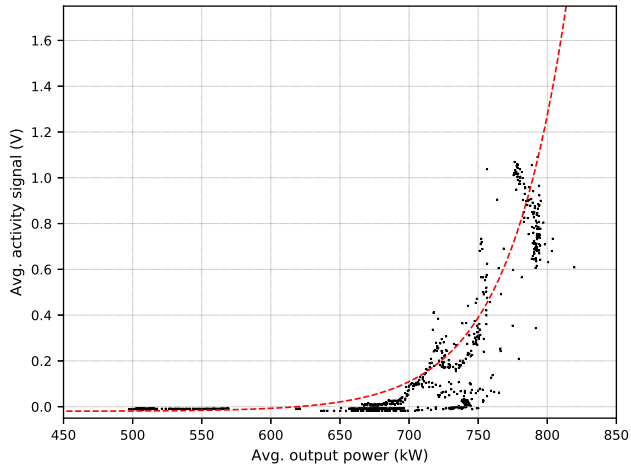


Figure 5.12: Average diode signal measured with the 142 GHz high pass filter. Each dot represents a gyrotron pulse with a duration of 1 s. The red dashed line fits the data with an exponential function. Again, an exponential growth for the activity is observed.

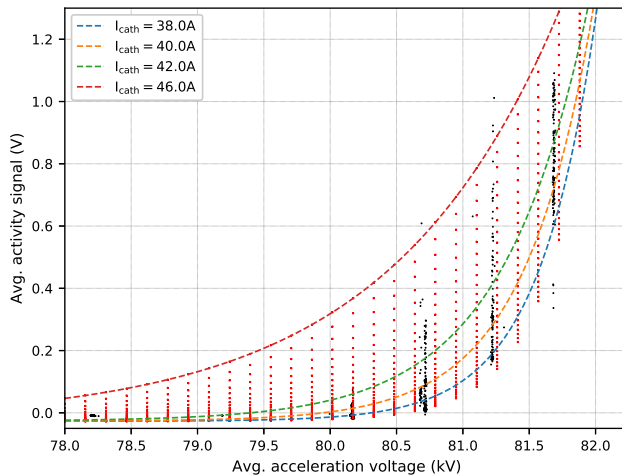


Figure 5.13: Two-dimensional projection of the experimental data and the fit from Figure 5.14. Dashed lines denote the fit results for different constant cathode currents for visualization purposes only.

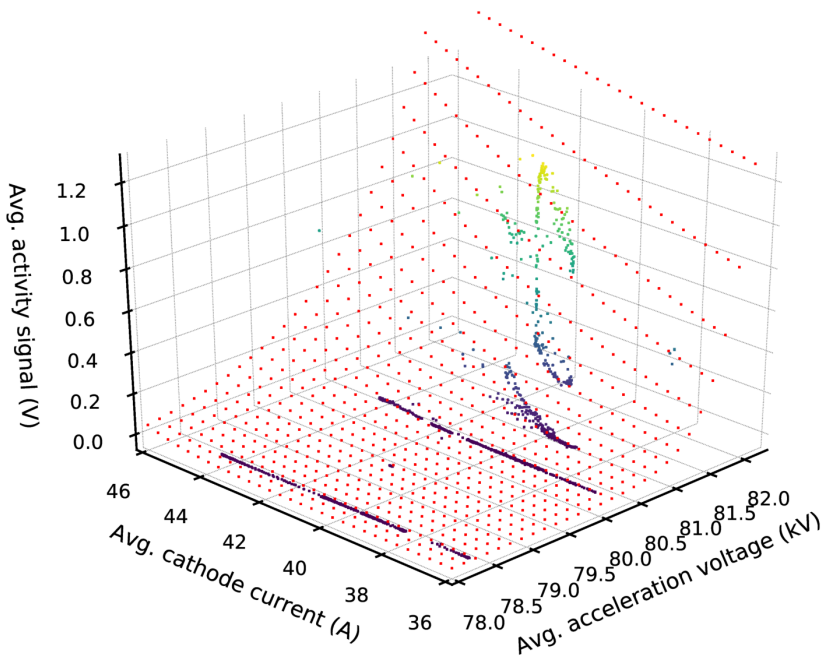


Figure 5.14: Average measured activity in the working point plane for all gyrotron pulses performed with Alpha 5 using the high pass filter (activity signal level is also color encoded). Red dot plane fits the data with an exponential function.

5.2.3 TED #5i Gyrotron with 140 GHz Notch Filter

1200 gyrotron pulses at various output power levels with a duration of 1 s were performed with the Alpha 5 tube on the 11th January 2017. In this experiment, a 140 GHz notch filter was used which is normally a part of the W7-X electron cyclotron emission (ECE) diagnostic. It was possible since the gyrotron experiments were performed in between the experiment campaigns of W7-X. The W7-X ECE notch filter was built as Bragg reflector with stacked rings introducing a corrugation in an oversized waveguide (see Figure A.2 in the appendix).

Figure 5.15 illustrates the working principle of a filter realized by a Bragg reflector: The TE_{11} mode is converted by the corrugation to a backward propagating high-order TM_{1p} mode, if the Bragg condition is met. Since the mode is reflected between the up- and down-tapers of the oversized waveguide, it is converted back to a backward propagating TE_{11} mode which can pass the input taper. The measured transmission shows in a very deep (-40 dB) and comparably wide (around 1 GHz) notch as shown in Figure 5.16 [DWF⁺15].

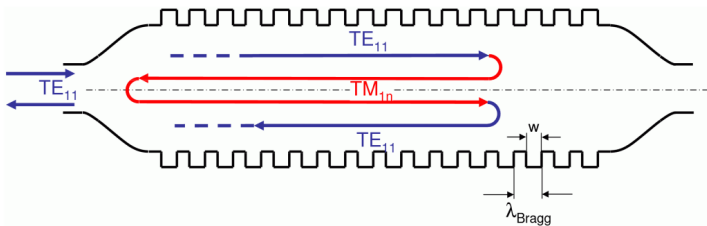


Figure 5.15: Illustrated working principle of the filter using high-order Bragg resonances with w being the slot width and λ_{Bragg} the corrugation period (from [DWF⁺15]).

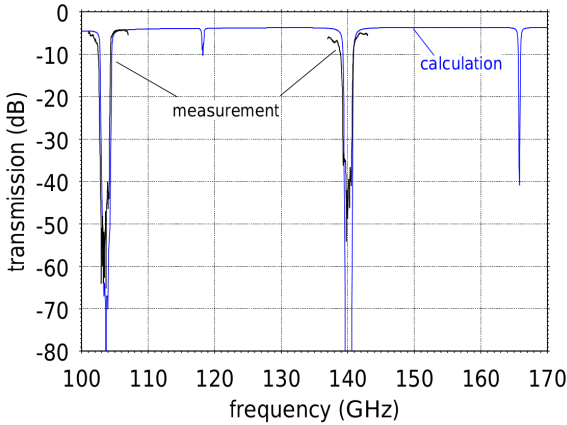


Figure 5.16: Comparison of the computed and measured transmission of the W7-X ECE notch filter (from [DWF⁺15]).

Therefore, the nominal gyrotron mode should hardly contribute to the measured activity signal and it is guaranteed that only all other parasitic modes should be measured. The same pre-attenuation and calibration for the activity measurement diode was used. The power calibration of the gyrotron RF output power signal was unchanged compared to the measurement with the high pass filter.

Figure 5.17 shows the measurement results where again every dot represents a 1 s gyrotron pulse. An even steeper growth of the average activity is observed with the notch filter compared to the previous measurements using the notch filter. This could be explained by the activity of the lower satellite and other parasitic modes also contributing to the signal as well as by better characteristics of the W7-X ECE notch filter (e.g. attenuation for the nominal gyrotron mode and hence a better signal-noise ratio) compared to the high pass filter. The attempt to fit the data with the simple exponential function (5.1) obviously failed and is unable to capture the sudden growth and variation of the activity. This result is reflected by the increased NRMSE of 0.247 and the low FVE accounting to 49.9 %. Looking at Figures 5.19 and 5.18 where the data (U_{acc}, I_{cath}, A) was again plotted in three dimensions and then projected on the (U_{acc}, A)-plane, the exponential function (5.4) fits much better the data and captures the steep growth in activity. This is accounted for in the small achieved NRMSE of 0.066 and the very high FVE of 96.5 %.

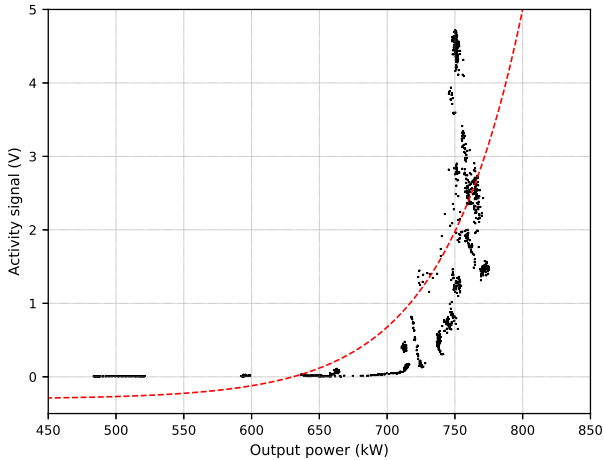


Figure 5.17: Average diode signal measured with the W7-X ECE notch filter. Each dot represents a gyrotron pulse with a duration of 1 s. The simple exponential function (5.1) fails to fit the data and to explain the variation and growth of the activity.

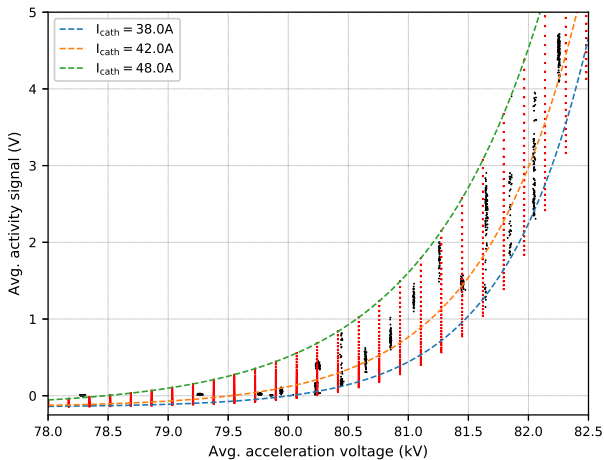


Figure 5.18: Two-dimensional projection of the experimental data and the fit from figure 5.19. Dashed lines denote the fit results for different constant cathode currents for visualization purposes only. The exponential function (5.4) captures much better the variation and growth of the activity.

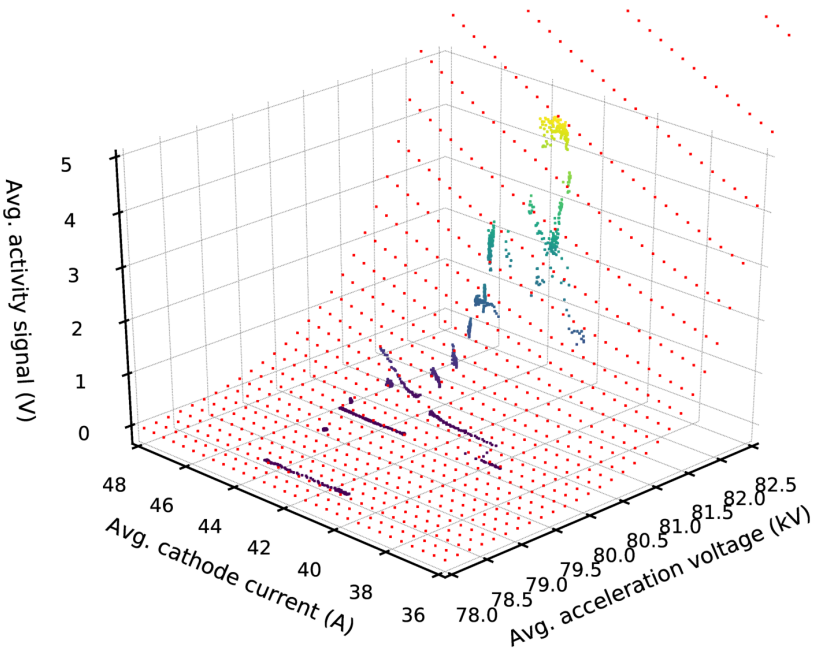


Figure 5.19: Average diode signal measured with the W7-X ECE notch filter. Each dot represents a gyrotron pulse with a duration of 1 s (activity signal level is also color encoded). A very steep growth of the activity is visible around an output power of 750 kW.

5.3 Advanced Measurements

The preliminary satellite mode stray radiation measurements were performed using a single RF pickup. Since the stray radiation field is to some degree stochastic in nature (dynamic speckle patterns, see Figure 4.7) and it was measured only at a single position in space, a highly fluctuating, unstable time signal is expected and also finally measured in experiments (see e.g. Figure 5.10). Additionally, experimental observations were hinting a connection between the probability distribution of the acceleration voltage noise and patterns in the activity and RF output power signals close to the loss of the nominal mode. In the contrary, a stable signal proportional to the power content in the parasitic modes is desired to serve as a feedback signal and mode loss precursor for a gyrotron controller. In an attempt to achieve a more stable activity signal, two more advanced measurement setups were developed and evaluated in experiments. In order to evaluate the predictive power of the activity signal for mode losses, the stray radiation measurements were performed while MORE was active. This way, possible relations between the mode losses and their probability to occur and (statistical) properties in the activity time signal could be identified more easily.

5.3.1 Mono-mode Setup

Figures 5.20 and 5.21 show the mono-mode measurement setup for the satellite mode activity. The setup uses 4 open-ended WR7 waveguides as RF pickups which are positioned in front of the gyrotron relief window. The idea is that the sum signal of multiple RF pickups is likely to be more stable, so it would be better suited to be used as feedback for a gyrotron controller. Ideally, for future version of the measurement setup, a (slot) antenna array covering the area of the gyrotron relief window could be used (see e.g. [GJ97,TKSX18]). In order to achieve the required frequency selectivity of our measured signal, a 136 GHz high pass filter which was fabricated for this thesis and two 140 GHz tuneable notch filters were concatenated. Finally, 10 dB pre-attenuation with a single RF detector diode and an amplifier are used to measure the activity signal. The design, fabrication and verification of the high pass filter is described in chapter 4.2.

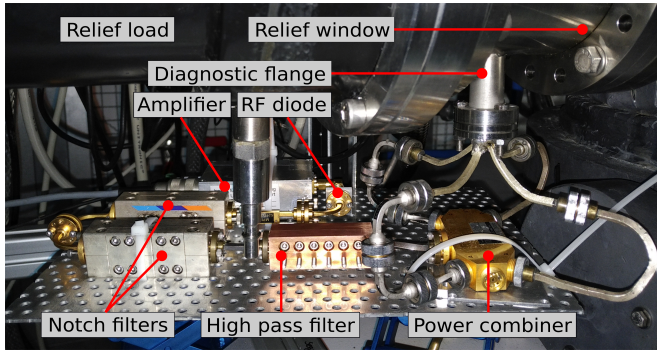


Figure 5.20: Photograph of the mono-mode satellite mode activity measurement setup.

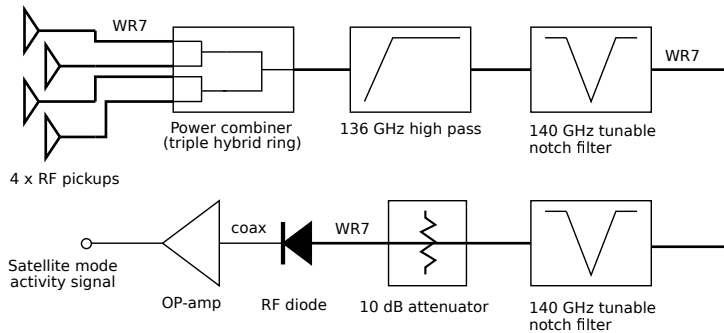


Figure 5.21: Schematic of the mono-mode satellite mode activity measurement.

174 gyrotron pulses were acquired with this setup in total on 21st March, 26/27th April and 2nd May 2018 with a target duration of 20 s with the Alpha 1 tube (TED SN007) mostly at high-power working points. MORE was active during the pulses which were performed at nominal and at changed main and gun coil fields, hence changed I_{main} and I_{gun} . Figure 5.22 shows the average values of the activity signals of whole gyrotron pulses $\overline{A_i(t)} = \overline{A_i}$ measured with the mono-mode setup plotted against the average criticality, hence the minimum distance of the average gyrotron working point during the pulse to the nominal mode-loss line (Equation 3.1) from Figure 3.5. Every marker represents a gyrotron pulse with 20 s target duration.

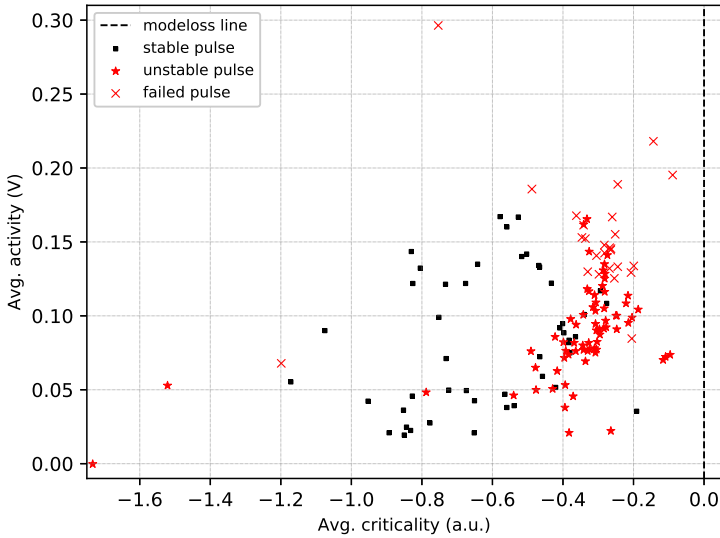


Figure 5.22: Average activity measured with the mono-mode setup over the average criticality. Every marker represents a gyrotron pulse with 20 s target duration. Explanation of gyrotron pulse categories: stable (zero MORE cycles), unstable (≥ 1 MORE cycle, pulse finished normally) and failed (≥ 1 MORE cycle, pulse terminated prematurely with RF interlock). MORE cycles have been removed from the time signals to avoid any bias (an explanation is given in the text).

The gyrotron pulses are again classified into one of the following categories as in chapter 3: stable (no MORE cycle, pulse finished normally), unstable (≥ 1 MORE cycle, pulse finished normally) or failed (≥ 1 MORE cycle, pulse terminated prematurely with RF interlock). In the latter case, the last MORE cycle triggered by the last mode loss could not recover the nominal mode within the RF grace time (typ. 2 ms). The activity signal was observed to be extremely high (often the amplifier even saturated) compared to the remaining signal during MORE cycles. In order to remove the possible bias for the result of the analysis which would result from that, MORE cycles have been removed from the time signal, if present. Only gyrotron pulses with constant main and gun coil currents being close to those used for the fit of the mode losses in the working point plane (in Figure 3.5) were selected for this analysis. Otherwise, the experimental conditions would not be comparable.

pulse category	μ_A [V]	$\varrho(\bar{C}, \bar{A})$
stable	0.082	0.362
unstable	0.088	0.46
failed	0.153	0.05
all		0.38

Table 5.1: Comparison of the correlation coefficients ϱ and means of the average pulse activities μ_A for the three gyrotron pulse categories.

Figure 5.22 shows the expected trend, that unstable and failed gyrotron pulses seem to occur more frequently towards the nominal mode loss around zero criticality. The shift in criticality, the earlier activity increase in the presented data set, can be explained by the fact that the average working points ($\overline{U_{\text{acc}}(t)} = \bar{U}$, $\overline{I_{\text{cath}}(t)} = \bar{I}$) over whole gyrotron pulses are used here to compute the criticality C (see Equation 3.3). In contrast, the nominal mode-loss line from Figure 3.5 was fitted to the mode losses and their momentary, last working point before the mode loss. The group of failed pulses close to the nominal mode loss exhibits an increased average activity compared to the group of unstable pulses where the mode could be still successfully recovered.

The correlation coefficient $\rho(X, Y)$ for two sample sets X and Y is defined as

$$\rho(X, Y) = \frac{\text{Cov}(X, Y)}{\sigma_X \sigma_Y} = \frac{\sum_i^n (x_i - \bar{x})(y_i - \bar{y})}{\sqrt{\sum_i^n (x_i - \bar{x})^2 \cdot \sum_i^n (y_i - \bar{y})^2}} \quad (5.5)$$

which is the covariance normalized by the product of the variable's standard deviations. The correlation coefficient takes the value of ± 1 for two ideally linearly correlated data sets. The mean of the average activities $\mu_A = (1/N) \sum_{n=1}^N \overline{A_i(t)}$ and the correlation coefficient $\varrho(C(\bar{U}, \bar{I}), \bar{A})$ were computed for the samples of the three gyrotron pulse categories (stable, unstable or failed) in order to identify a (linear) trend.

Table 5.1 shows an increased mean activity for the groups of unstable and failed pulses and an overall weak positive correlation between the average criticality and the average pulse activity. The correlation coefficient was unable to identify a linear relationship for the group of failed pulses. A better representation of the results is achieved showing the median of the pulse activities along with their 10 % and 90 % percentiles as vertical error bars over the criticality median

in Figure 5.23 (for an explanation of the term percentile, see section 2.3.1). The percentiles were chosen since the popular mean and standard deviation are only meaningful for normally-distributed data. The activity data is obviously not normally-distributed since the shown percentiles are not symmetric. It's clearly visible in Figure 5.23 that the activity is low most of the time during the pulses since the activity median is much lower than the 90 % percentile of the measured activity $p_{90\%}(A_i(t))$.

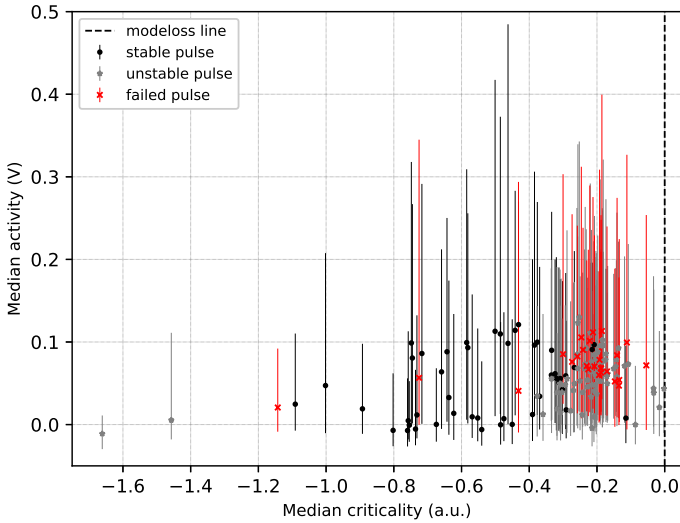


Figure 5.23: Median pulse activities measured with the mono-mode setup over the median criticalities of whole gyrotron pulses. Every marker represents a gyrotron pulse with 20 s target duration. The lower and upper bounds of the error bars represent the 10 % and 90 % percentiles of the measured activity for each pulse.

Figure 5.23 shows less discrimination between the stable and unstable or failed pulses regarding the median activity. But the 90 % percentile $p_{90\%}$ shows a clear decreasing trend for stable pulses approaching the mode loss. This could be interpreted as decreasing tolerated parasitic activity when the nominal mode loss is approached. In comparison, unstable and failed pulses exhibit an increased $p_{90\%}$ compared to stable pulses. The same holds for the comparison of the 90 % percentiles between failed and unstable pulses.

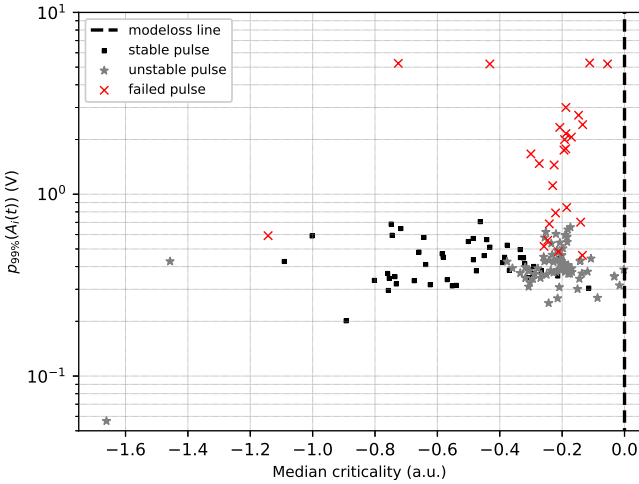


Figure 5.24: 99 % percentiles of the activity measured with the mono-mode setup over the criticality median. The three pulse groups are now clearly separated. Failed pulses have more frequently, a much higher activity during the pulses (meaning the distribution is also broader) compared to the other pulse groups.

The separation between the pulse groups is improved looking at the 99 % percentiles of the activity signals in Figure 5.24. The group of failed pulses exhibits more frequently, much higher activity levels. The activity signal measured with a 142 GHz high pass filter was shown in Figures 5.10 and 5.11 together with the RF output power signal. Both signals suddenly exhibited simultaneously a temporal pattern (dips in the RF output power signal and peaks in the activity signal) on a timescale of 10 ms to 200 ms approaching the output power limit of the gyrotron. It was hypothesized that the reason for this pattern could be possible multi-mode behavior of the nominal mode and other parasitic or satellite modes in agreement with the probability distribution of the technical noise on the supply voltages. Since the correlation coefficient is only suitable to capture linear relationships between two variables, the mutual information (MI) or information gain is proposed here to detect a possible non-linear coupling between the RF output power and the measured activity signal.

The mutual information or information gain $MI(X, Y)$ of two random variables X and Y measures the mutual statistical dependence and quantifies the amount of information gained about X when Y is observed and vice versa. The Mutual Information (MI) can be expressed as difference of the Shannon entropies H as [Sha48a, Sha48b]

$$H(X) = - \sum_{a \in X} p(X = a) \log_2(p(X = a)) \quad (5.6)$$

$$H(X, Y) = - \sum_{b \in Y} \sum_{a \in X} p(X = a, Y = b) \log_2(p(X = a, Y = b)) \quad (5.7)$$

$$MI(X, Y) = MI(Y, X) = H(X) + H(Y) - H(X, Y) \geq 0 \quad (5.8)$$

where $p(X = a)$ is the probability for $a \in X$ and $H(X)$ is the entropy or the expectation value of the point-wise information of elements in X . The joint probability distribution $p(X, Y)$ is used for the computation of $H(X, Y)$. In case of a sampled time series and for large sample sizes, the probability distributions can be approximated by the normalized histograms (a 2D histogram in case of the joint probability distribution).

Figures 5.25 and 5.27 show the resulting pulse-wise mutual information $MI(\text{RF}(t), A(t))$ between the RF output power signal and the measured activity signal over the criticality median and respectively the 99 % percentile of the measured average activity signal over whole gyrotron pulses. The MI of the failed pulses scales linear with the increasing activity and is clearly distinct from the stable and unstable pulses. The correlation coefficient for the group of failed pulses amounts to $\rho(p_{99\%}(A), MI(\text{RF}, A)) = 0.882$ indicating a strong linear relation. The same linear relation is obtained in Figure 5.26 between the MI and the average pulse activity for the group of failed pulses. The correlation coefficient for the group of failed pulses in this case is $\rho(\bar{A}, MI(\text{RF}, A)) = 0.815$ indicating as well a strong linear relation. The pulse group means for the MI are 0.153 (stable), 0.171 (unstable) and 0.315 (failed). Furthermore, the MI over a gyrotron pulse increases when the modeloss line is approached, indicating that the RF output power and the activity signal are increasingly coupled for a working point approaching the modeloss line. The temporary multi-mode pattern discussed above from Figures 5.10 and 5.11 seems to be reflected in the increased MI for unstable and failed shots.

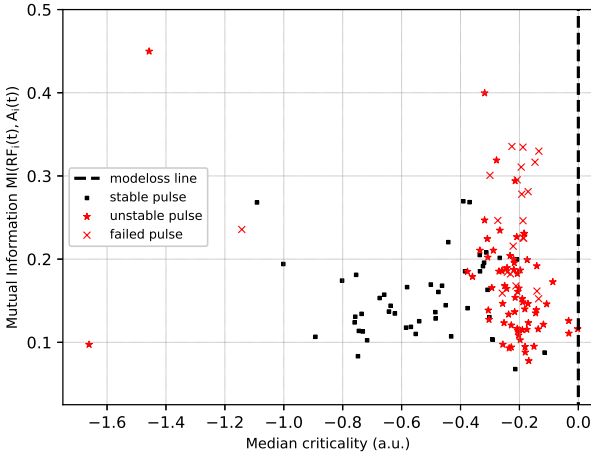


Figure 5.25: MI between the RF output power signal and the activity measured with the mono-mode setup over the criticality median. The RF output power signal and the activity signal are more strongly coupled approaching the modeloss line.

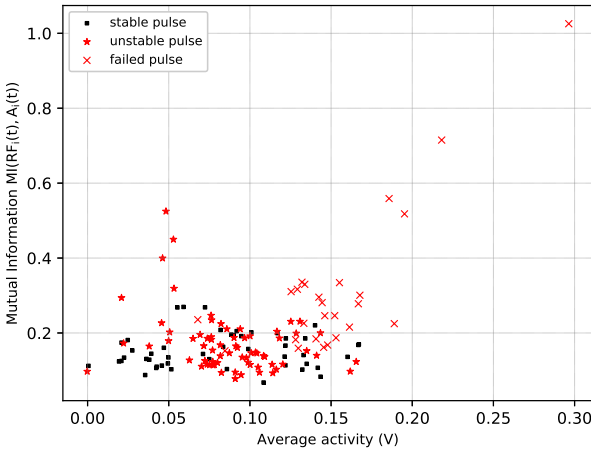


Figure 5.26: MI between RF output power signal and the activity measured with the mono-mode setup over the average activity during the pulses. The output power and activity are more strongly coupled for failed pulses. The MI and the average activity exhibit a linear relation for failed pulses.

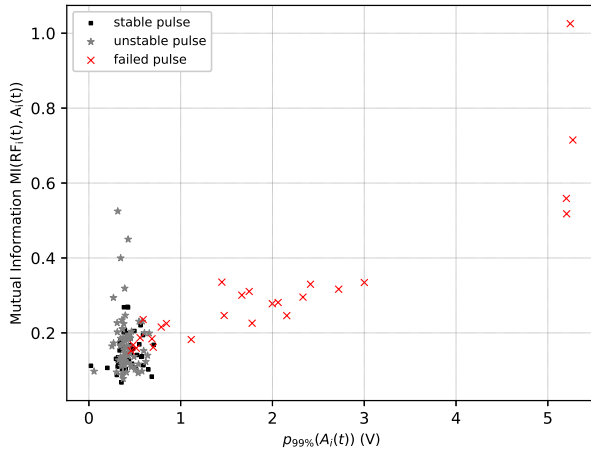


Figure 5.27: MI between the RF output power signal and the activity measured with the mono-mode setup over the 99 % percentiles of the pulse activity signals. The RF output power signal and the activity signal are more strongly coupled for unstable and failed pulses, in the latter case at significantly increased activity levels.

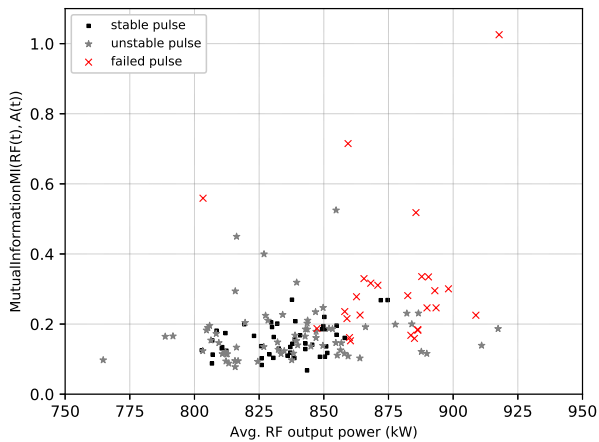


Figure 5.28: MI between the RF output power signal and the activity measured with the mono-mode setup over the average RF output power during the pulse. Good separation between the pulse groups with trend of increasing coupling towards higher output power.

5.3.2 Quasi-Optical Setup

Figures 5.29 and 5.30 show the quasi-optical measurement setup for the satellite mode activity. This setup is overmoded and uses a multi-mode transparent quasi-optical band pass filter in an oversized circular waveguide for the stray radiation from the satellite modes $TE_{27,8}$ and $TE_{29,8}$ of the nominal gyrotron mode. The design, construction and verification of the quasi-optical band pass filter is described in chapter 4.3. The filtered stray radiation is then measured with five RF detector diodes which are located at the center of opposing faces of a mode-stirring volume.

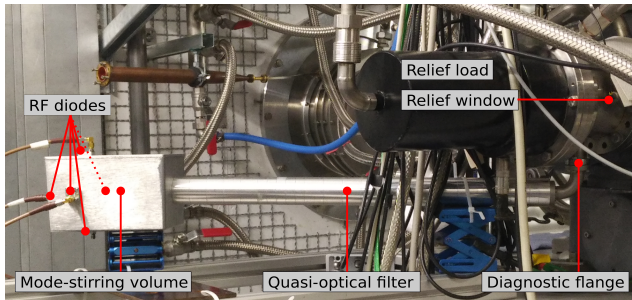


Figure 5.29: Photograph of the quasi-optical satellite mode activity measurement setup.

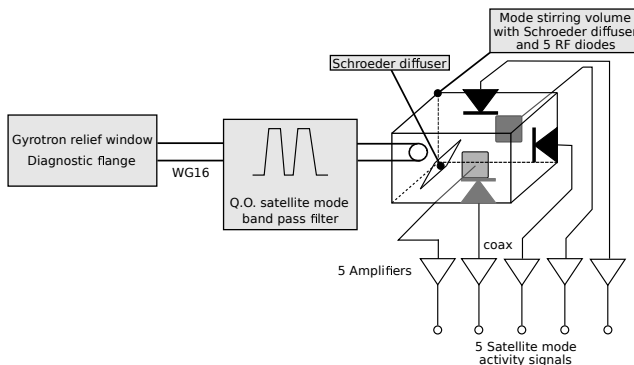


Figure 5.30: Schematic of the quasi-optical satellite mode activity measurement.

Experiments with acoustic mode-stirring chambers and Schroeder or reflection phase grating diffusers [DK84] exhibit improved microwave field homogeneity [PS98, PS99]. The idea roots back to the acoustic optimization of concert halls [Sch79, Sch75]. By chance, a Schroeder diffuser for 140 GHz was previously manufactured for another stray radiation measurement [Ger16]. Figure 5.31 shows a model of a Schroeder diffuser which is an array of square stubs of width $w = \lambda/2$. The number of stubs along each dimension should be an odd number. The stub depths d_n are chosen to be a quadratic-residue series [DK84] leading to different phase shifts between the reflected waves so that they ideally interfere in such a way that the incident waves are diffusely scattered over a broader angle (a proof is given in [Ger16]).

Figure 5.32 compares the measured normalized scattering amplitudes by a flat plate and a Schroeder diffuser, showing the best result for a reflection angle of around 45 degrees. Therefore, the Schroeder diffuser was positioned with an angle of 45 degrees in front of the input of the mode-stirring volume to further diffuse and homogenize the stray radiation field. The resulting signal measured by the RF diodes should then be more stable and fluctuating less over time.

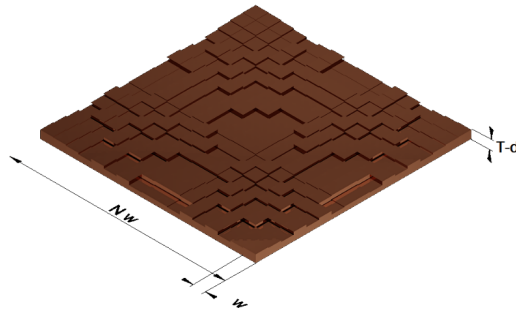


Figure 5.31: Exemplaric Schroeder diffuser design with N^2 (here $N = 17$) stubs of width $w = \lambda/2$ and height $T - d_n$ where T is the thickness of the base plate and d_n the depth of each stub (from [Ger16]).

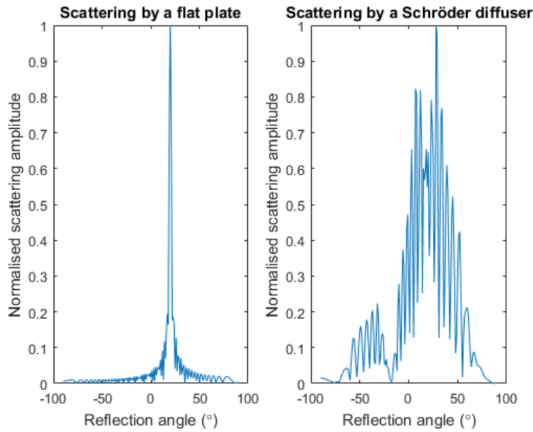


Figure 5.32: Comparison between the measured normalized scattering amplitudes by a flat plate and a Schroeder diffuser. The Schroeder diffuser leads to a scattering over a broader angle range (from [Ger16]).

Between the 12th to 15th March and on 16th April 2018, 170 pulses with a target duration of 20 s were performed with the Alpha 1 tube (TED SN007) at mostly high-power working points together with MORE being active. 37 pulses of 170 were performed at the same fields and parameters as the pulse data used to fit the model loss line (Equation 3.3).

Since the quasi-optical measurement setup has five RF diodes, we obtain five activity signals $A_j(t)$. In order to exploit and represent the full information, the quantities averaged over the activity channels are presented. The mean mutual information (Equation 5.6) between the RF output signal $RF_i(t)$ and the N measured activity signals $A_{ij}(t)$ is defined by

$$\overline{\text{MI}(RF(t), A_j(t))}_i = \frac{1}{N} \sum_{j=1}^N \text{MI}(RF_i(t), A_{ij}(t)) \quad (5.9)$$

and the mean mutual information between the N activity signals $MI(A_{ij}(t), A_{ik}(t))$ is defined by

$$\overline{MI(A_j(t), A_k(t))}_i = \frac{2}{N^2 - N} \sum_{j=1}^N \sum_{j < k}^N MI(A_{ij}(t), A_{ik}(t)) \quad (5.10)$$

with i being the gyrotron pulse index and j, k being the activity channel indices. $(N^2 - N)/2$ is the number of desired unique index permutations since $MI(A_{ij}, A_{ij})$ and other duplicate values due to the symmetry property of the mutual information $MI(X, Y) = MI(Y, X)$ should be avoided. Here for $N = 5$, the number of unique index permutations amounts to 10 (which are $\{(1, 2), (1, 3), (1, 4), (1, 5), (2, 3), (2, 4), (2, 5), (3, 4), (3, 5), (4, 5)\}$).

Additionally, the total mean mutual information (TMMI) which is the mean mutual information across the RF output power signal, the measured activity signals and between unique pairs of the measured activity signals defined as

$$\begin{aligned} \text{TMMI}_i = \\ \frac{2}{N^2 + N} \left(\sum_{j=1}^N MI(\text{RF}_i(t), A_{ij}(t)) + \sum_{j=1}^N \sum_{j < k}^N MI(A_{ij}(t), A_{ik}(t)) \right) \end{aligned} \quad (5.11)$$

is used here with N being the number of activity signals, i the pulse index and j, k being the activity channel indices.

First, results including only 37 pulses out of 170 are shown to not mix up gyrotron pulses performed at different magnetic fields (set by the gun coil current and/or main coil current) with a changed modeloss line compared to Figure 3.5.

Figure 5.33 shows the mean pulse activity signal averaged over the five activity channels versus the average criticality. Using this information alone, a satisfactory separation between the three pulse groups is achieved. But taking the mean mutual information (or non-linear coupling degree) between the RF output power and the measured activity signals into account (Equation 5.9) in Figure 5.34, a good separation is achieved. An even better separation is achieved when the mutual information among the activity channels (Equation 5.10) is also taken into account in Figure 5.35 and combined to the TMMI (Equation 5.11) in Figure 5.36. Clearly, the TMMI is significantly higher for failed pulses compared to unstable and stable pulses and it grows with

increasing criticality approaching the modeloss line. Therefore, not only the non-linear coupling or mutual information between the RF output power signal and the activity signals increases during an unstable operation state, but as well the mutual information among the activity signals. Figure 5.37 shows the same trend and very good separation for the TMMI over the average RF output power during the pulses. The TMMI of the failed pulses is not only significantly increased, but also grows with increasing output power.

Figures 5.39 and 5.40 show the results of all 170 gyrotron pulses acquired with the quasi-optical measurement setup with varying magnetic fields for the gyrotron. The TMMI over the average RF output power and the average activity signal during the pulses is presented. Even here, where multiple data sets for different fields are mixed, a fairly good separation for the three pulse groups is achieved, most importantly for the group of failed pulses. Again, the trend between the increasing TMMI with increasing RF output power and increasing activity signal is observed, discarding outliers in the mixed data set. Exploiting the additional data from multiple stray radiation measurement channels using the TMMI seems to be an advantage since the separation of the pulse groups is improved compared Figure to 5.25 which was obtained with the mono-mode measurement setup having only one stray radiation measurement channel.

Therefore, the TMMI using the data from multiple stray radiation measurement channels seems to be a promising candidate to characterize unstable gyrotron operation states and to predict a likely modeloss.

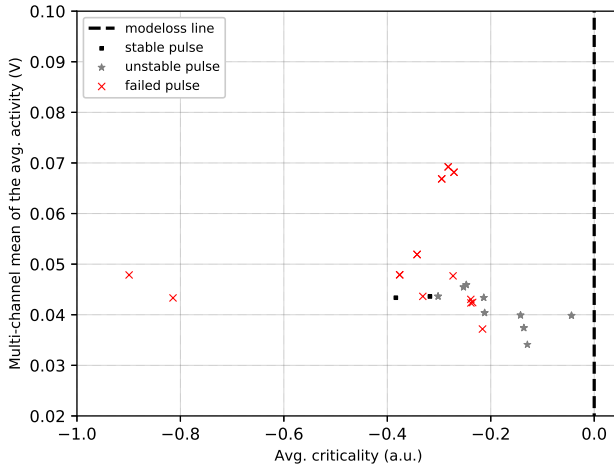


Figure 5.33: Multi-channel mean of the average pulse activity measured with the quasi-optical setup versus the average criticality of the working point. Satisfactory separation for failed pulses is observed.

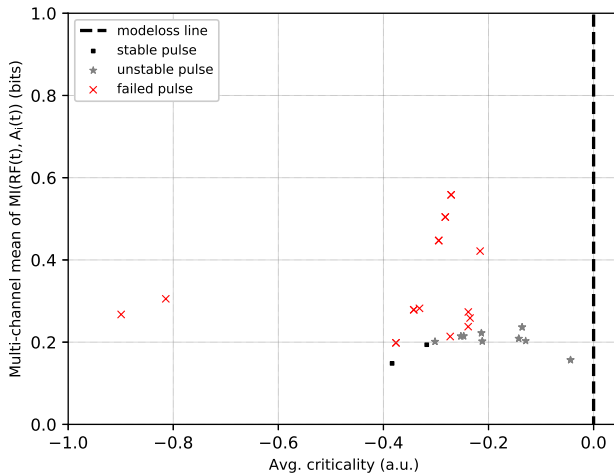


Figure 5.34: Multi-channel mean of the MI between the RF output power signal and the five activity signals over the average criticality of the working point. Good separation for failed pulses is observed.

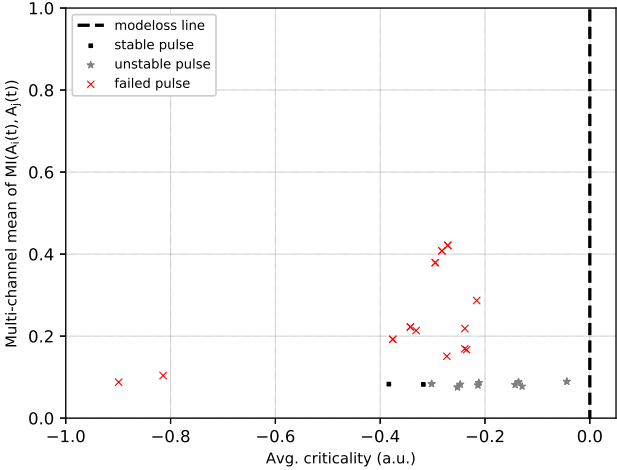


Figure 5.35: Multi-channel mean of the MI among the unique permutations of the five activity signals over the average criticality of the working point. Very good separation for failed pulses is observed.

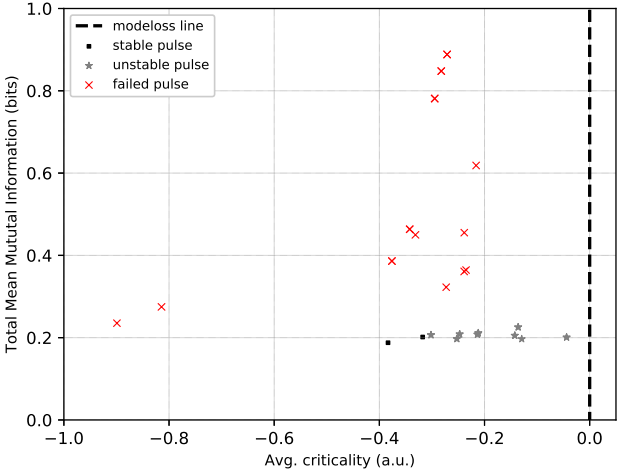


Figure 5.36: Total mean mutual information over the average criticality of the working point. Excellent separation for failed pulses is observed.

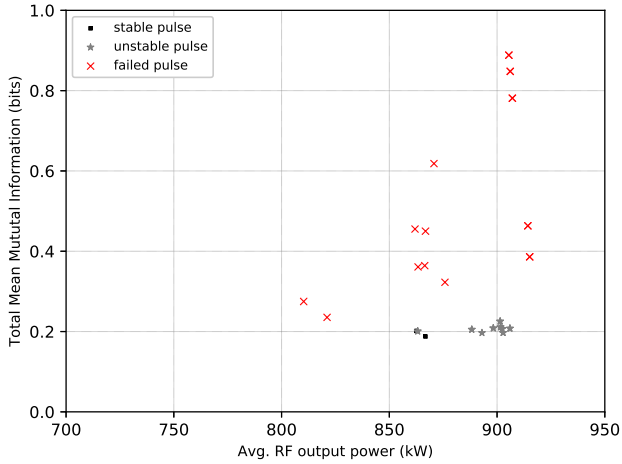


Figure 5.37: Total mean mutual information over the average RF output power during the pulse. A trend for an increasing TMMI with increasing output power is observed for failed pulses.

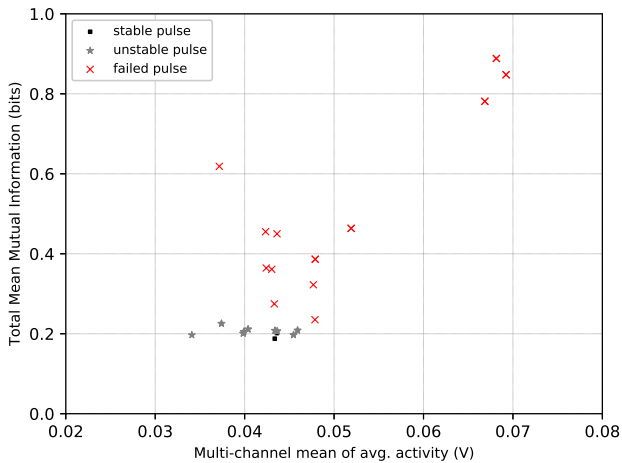


Figure 5.38: Total mean mutual information over the average pulse activity measured with the quasi-optical setup. Failed pulses are well separated and a trend of a growing TMMI with increasing average pulse activity is visible.

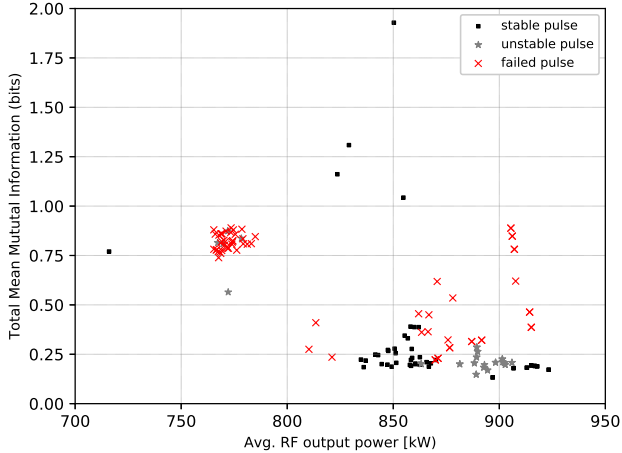


Figure 5.39: Total mean mutual information over the average RF output power during the pulse using the quasi-optical measurement setup for varying magnetic fields of the gyrotron. Despite the mixed data set, failed pulses are still separated.

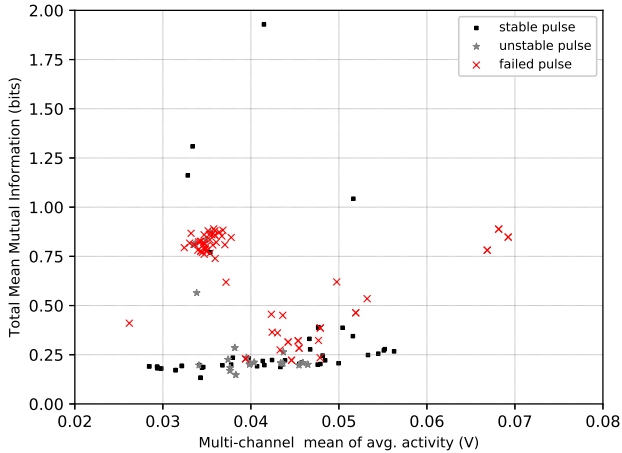


Figure 5.40: Total mean mutual information over the average pulse activity measured with the quasi-optical setup for varying magnetic fields of the gyrotron. Despite the mixed data set, failed pulses are still separated. Again, a trend between average activity and the TMMI is visible.

5.4 Summary

Stray radiation measurements using one RF pickup show that the average stray radiation level during gyrotron pulses increases exponentially approaching the practical output power limit of the gyrotron of around 900 kW. Comparing the measurements with two different gyrotrons and filter types (a 142 GHz high pass and a 140 GHz notch filter), the hypothesis is supported that mainly the satellite modes and/or other parasitic modes are contributing to the growing stray radiation signal.

Reproducible sequences of simultaneous dips in the RF output power and peaks in the stray radiation signal are observed close to the loss of the nominal mode (see Figure 5.11). The time scale of the phenomenon coincides with the time scale implied by the (slightly non-Gaussian) probability distribution of the technical noise found on the acceleration voltage in section 2.3. Therefore, the hypothesis is supported that this could be temporary, reversible multi-mode behaviour due to mode competition caused by the acceleration voltage noise prior to a likely loss of the nominal mode.

A mono-mode setup and a quasi-optical measurement setup are presented using up to five RF diodes to measure the stray radiation from the satellite modes. The activity measurements were performed with MORE being active during the gyrotron pulses, allowing for the distinction into the three groups of stable, unstable and failed pulses. Using simply the averaged activity signals, a good separation of the three gyrotron pulse groups is not achieved. But analyzing the non-linear coupling degree between the RF output power signal and the measured activity signal(s) by computing the mutual information (MI), a satisfactory to good separation for the group of failed pulses is achieved plotting the MI against the criticality, the average activity or the average output power during the pulse using the mono-mode setup. The trend of an increasing MI with increasing average pulse activity and average output power is observed for failed pulses.

The quasi-optical measurement setup has five RF diodes to measure the stray radiation. Computing the Total Mean Mutual Information (TMMI) between the RF output power signal, the five activity signals and among unique pairs of the activity signals, an excellent separation for the group of failed pulses was achieved from the groups of stable and unstable pulses. Failed pulses have a much higher TMMI compared to stable and unstable pulses. The clear trend of an increasing TMMI was observed for a growing average activity and

average output power particularly for the group of failed pulses, approaching the modeloss line with increasing criticality. Therefore, exploiting the additional data from multiple stray radiation measurement channels seems to help to detect and discriminate an unstable gyrotron operation state. The TMMI is therefore a promising candidate for a mode loss precursor.

6 Moving-Window Activity Data Statistics

The findings presented in sections 5.2 and 5.3 hold for the aggregated time-series data over whole gyrotron pulses. In contrast, a real-time precursor for mode loss as feedback during the pulse duration is required for an electronic stability control for gyrotrons. Therefore analyses using a moving window over the time series data are required to simulate the signal processing during the gyrotron pulse. In order to choose the adequate (minimum) duration for the moving window, methods originally used to identify the proper embedding parameters for a phase space reconstruction are applied to whole gyrotron pulses first. The phase space is the reconstruction of the high-dimensional state space of a complex dynamical system from a low- or even one-dimensional time series. The moving window analyses are then performed with the goal to identify a (statistical) precursor for the loss of the nominal mode during the gyrotron pulse. The data obtained with both measurement setups presented in sections 5.3.1 and 5.3.2 is evaluated using the (total mean) mutual information of a moving window over the data.

6.1 Time-Delayed Mutual Information

The Mutual Information (MI) (Equation 5.6) of a sampled time series $x(t_n)$ with its time-delayed (or shifted) version $x(t_{n+\tau})$ is called Time-Delayed Mutual Information (TDMI) defined as

$$X_t = \{x(t_n), x(t_{n+1}), \dots, x(t_{n+\Delta})\} \quad (6.1)$$

$$\text{TDMI}(x(t), \tau) = \text{MI}(X_t, X_{t+\tau}) \quad (6.2)$$

with Δ being the length of the signal (window) and τ being the applied time delay or shift. The TDMI was first used by Fraser [FS86] to find an optimum

time delay τ_{opt} for the time-delay embedding $\hat{x}(t_n)$ of the time series defined by

$$\hat{x}(x_n) = (x(t_n), x(t_{n-\tau}), x(t_{n-2\tau}), \dots, x(t_{n-(d_{\min}-2)\tau}), x(t_{n-(d_{\min}-1)\tau})) \quad (6.3)$$

where $\hat{x}(t_n)$ are the reconstructed points in phase space, τ is the chosen time delay and d_{\min} the (minimum) embedding dimension.

The optimum time delay is located by convention at the first local minimum of the TDMI computed for an interval of time shifts. The minimum embedding dimension can be determined by using e.g. the False Next Neighbour (FNN) ratio by Kennel [KBA92]. According to Takens' delay embedding theorem [Tak81], the time-delay embedding is one way to reconstruct the high-dimensional state or phase space of a complex dynamical system. The manifold of all phase space trajectories of a system as a whole is called "attractor".

A prominent example for an attractor is e.g. the Lorenz attractor [Lor63] which is often mentioned as example for deterministic chaos. If the right time delay was chosen for the embedding, the attractor of the system should properly unfold, occupy a maximum volume in the high-dimensional phase space and neighboring phase space trajectories should be separated as shown for the Lorenz attractor in Figure A.3. Therefore using the TDMI, it can be shown that a time series which seems to be purely random or stochastic, is in fact governed by deterministic chaos and has serial non-linear correlations. Furthermore, its behavior becomes predictable using its reconstructed phase space as several applications of this technique in various different fields (e.g. in Psychology and Medicine [CFZ14], Hydrology [SJF02], Meteorology [SW18, WLGL17, HRY15], Geophysics, Economics, Machine Learning etc.) demonstrate.

The TDMI is computed here for the data of whole gyrotron pulses to determine the length of serial correlations and hence the adequate minimum and maximum reasonable window duration for the moving window statistical analyses of the pulse data in the following section of this thesis. The optimum time delay τ_{opt} is determined for the activity signals obtained with both measurement setups, a mono-mode setup and a quasi-optical setup, which were presented in section 5.3.

Figures 6.1 and 6.2 show plots of the computed TDMI for a time delay range of up to 200 ms for the RF output power signal and the activity signal(s) of an unstable gyrotron pulse example for both measurement setups. The local minima and maxima are clearly visible in both plots. The TDMI is also shown for white noise to illustrate the meaning of the TDMI. The TDMI of white noise is always zero since the values in a sequence of random values are ideally uncorrelated, hence random white noise has no serial correlations. The first local minimum of the TDMI is located around 10 ms to 15 ms in both cases. The TDMI decays faster for the data obtained with the quasi-optical measurement setup in this case. The TDMI approaches a low value for all signals after 100 ms to 200 ms giving an upper limit for the reasonable window duration.

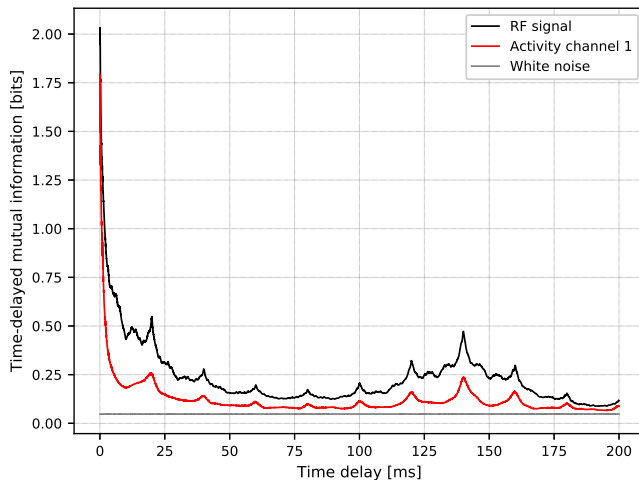


Figure 6.1: Computed TDMI for an unstable gyrotron pulse example using data obtained with the mono-mode measurement setup. Clear local minima and maxima are visible with decaying mutual information with increasing time delay.

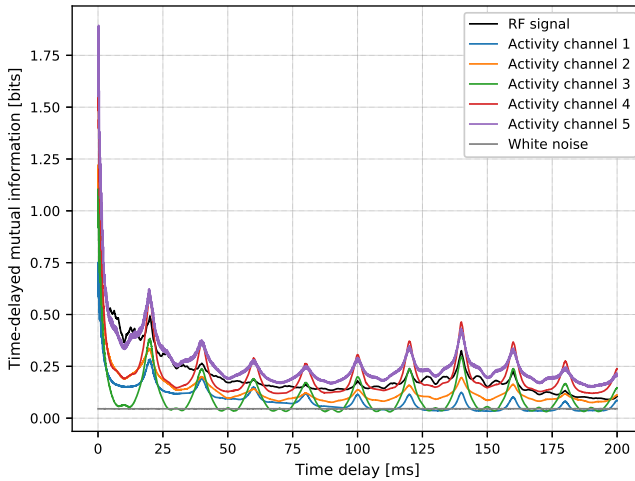


Figure 6.2: Computed TDMI for an unstable gyrotron pulse example using data obtained with the quasi-optical measurement setup. Clear local minima and maxima are visible with decaying mutual information with increasing time delay.

Figures 6.3 and 6.4 show stacked histograms of the optimum time delays τ_{opt} found for the activity signals of the gyrotron pulses presented for the three gyrotron pulse categories (stable, unstable and failed). Again, the MORE cycles in the unstable and failed pulses have been removed from the time signals used for the analysis to avoid any bias for the computed quantities. In both cases, an accumulation for the optimum time delay τ_{opt} in the range between 10 ms and 20 ms is visible with a tendency towards slightly higher τ_{opt} for unstable and failed gyrotron pulses.

This confirms again the characteristic time scale of the hypothesized, temporary multi-mode phenomenon shown in Figure 5.11. This time delay is also in agreement with the time scale implied by the empirically found probability distribution (see Figures 2.16 and 2.17) of the technical acceleration voltage noise in section 2.3.1.

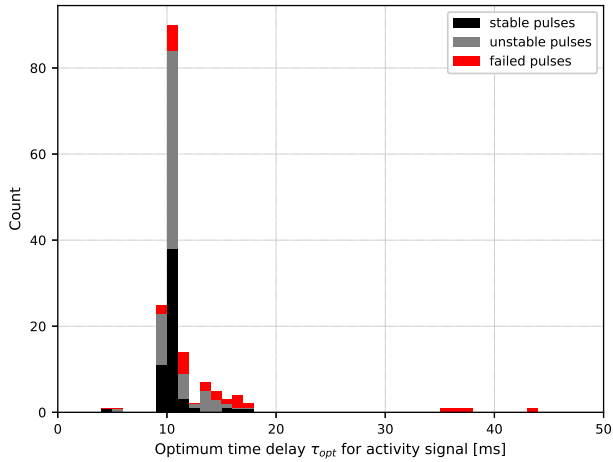


Figure 6.3: First local minima of the TDMI using all available gyrotron pulse data (at same magnetic field) for the activity signal obtained with the mono-mode measurement setup. Clear shift towards higher time delay for the group of unstable and failed pulses.

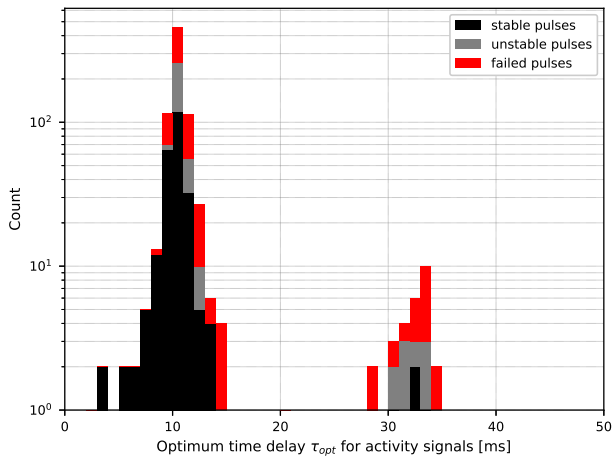


Figure 6.4: First local minima of the TDMI using all available gyrotron pulse data (at various magnetic fields) for the activity signals obtained with the quasi-optical measurement setup. A shift towards higher time delays for the group of unstable and failed pulses is visible.

The higher count and the bigger time delay for unstable and failed pulses in Figure 6.4 can be explained: Firstly by the fact that all available pulse data was used where the gyrotron was operated at different magnetic fields. Secondly, the five activity signals were processed and counted separately. Figure 6.5 shows the same analysis result but distinguished for the five activity channels.

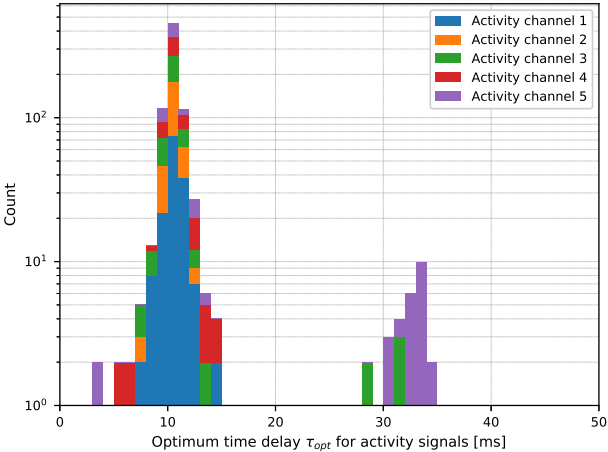


Figure 6.5: Optimum time delays using the first local minimum of the TDMI using all available gyrotron pulse data (at various magnetic fields) for the activity signals obtained with the quasi-optical measurement setup. Clear shift towards higher time delay for one activity channel.

6.2 Moving Mutual Information

This section presents the results of the moving window analysis for the gyrotron pulse data for both stray radiation measurement setups. The moving window analysis simulates the statistical analysis of FIFO (First-In First-Out) buffers (e.g. implemented on a FPGA) containing the data of the measured activity signals and the RF output power signal of the nominal mode during a gyrotron pulse. Statistical patterns in the moving (total) mutual information are identified which would be a suitable precursor for the loss of the nominal mode of the gyrotron.

6.2.1 Mono-mode Setup

In case of the mono-mode setup (presented in section 5.3.1), the mutual information $MI(\text{RF}(t_n, d), A(t_n, d))$ between the RF output power signal $\text{RF}(t_n)$ and the measured activity or stray radiation signal $A(t_n)$ is computed for moving data windows defined by

$$\text{RF}(t_n, d) = \{\text{RF}(t_{n-d}), \dots, \text{RF}(t_{n-1}), \text{RF}(t_n)\} \quad (6.4)$$

$$A(t_n, d) = \{A(t_{n-d}), \dots, A(t_{n-1}), A(t_n)\} \quad (6.5)$$

where d is the window length (or duration) and n is the running index for the gyrotron pulse time signals. The moving data window simulates a FIFO buffer in a possible future FPGA implementation. The mutual information is not recomputed for every new incoming value, but recomputed only every $480 \mu\text{s}$ or 12 samples with a sample rate of 25 kHz as it is the case for the W7-X data acquisition. This is done in order to firstly reduce the computational effort for this analysis and secondly to simulate the required processing time in a future FPGA implementation.

The same data as in section 5.3.1, 174 gyrotron pulses with a target duration of up to 20 s, was used in this analysis. Based on the findings in the previous section 6.1, the window durations were chosen to be 15 ms, 25 ms, 50 ms and 100 ms. Figures 6.6 and 6.7 show the median and the 10 % percentile of the mutual information computed for a window duration of 50 ms over the criticality intervals. The difference between the figures is the data selection used for the analyses.

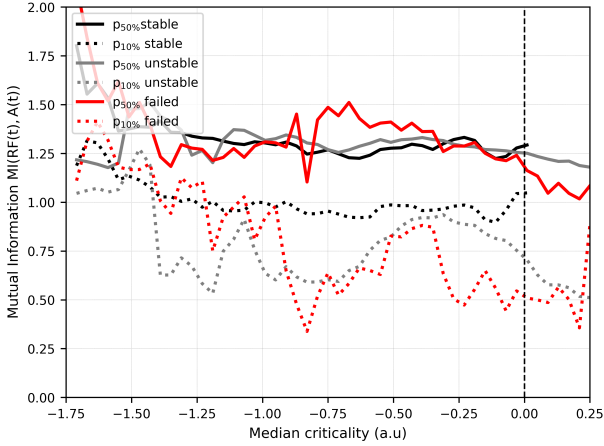


Figure 6.6: Median of the mutual information MI (RF, A) over the criticality intervals. The quantities were computed for a window duration of 50 ms. The three gyrotron pulse groups (stable ($2.07 \cdot 10^6$ values), unstable ($2.84 \cdot 10^6$ values) and failed ($2.51 \cdot 10^5$ values)) are again distinguished.

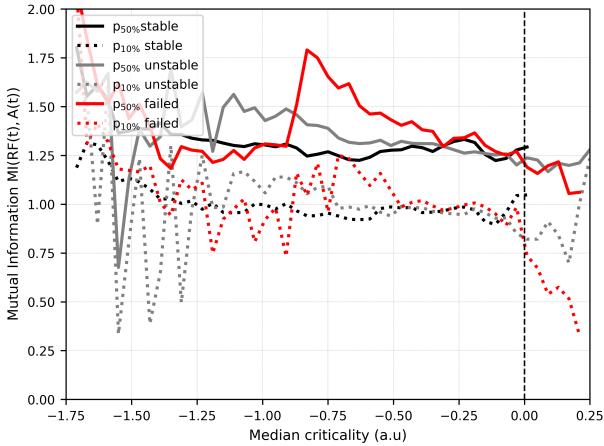


Figure 6.7: Median of the mutual information MI (RF, A) over the criticality intervals but only data up to the first mode loss is used from each pulse. The quantities were computed for a window duration of 50 ms. The three gyrotron pulse groups (stable ($2.07 \cdot 10^6$ values), unstable ($9.23 \cdot 10^5$ values) and failed ($1.63 \cdot 10^5$ values)) are distinguished.

In the latter case, only gyrotron pulse data up to the first mode loss in each gyrotron pulse is used for the group of unstable and failed pulses. An increased median mutual information far away from the modeloss line is visible for the group of failed pulses with the trend of a decreasing MI towards the mode loss line. In contrast, the group of unstable pulses exhibits only a slightly increased median MI, but also a decreasing median MI towards the mode loss line. The group of stable pulses as control group hardly varies over the criticality, but has a dip close to the mode loss line. This observation is still in agreement with the results presented in sections 5.3.1 and 5.3.2.

More interestingly, the 10 % percentiles for the pulse groups differ significantly with a nearly constant lower percentile for the group of stable pulses, but lowered percentiles for the groups of unstable and failed pulses. The explanation is that even an increased average MI over whole gyrotron pulses was observed in sections 5.3.1 and 5.3.2, the phenomenon of interest leads locally in time to a suddenly decreased MI (a peak in the RF output power signal and a dip in the measured stray radiation signal). Since the percentage of these events of interest compared to the pulse duration is small (this should be the case if these events are supposed to have any predictive power in this case), it cannot be reflected well by an average or median value. But it is reflected by the asymmetry of the data distribution and hence by the distance to the median. Hence, the median decreases since the events occur more frequently approaching the mode loss line.

The accumulation of the hypothesized multi-mode event is much more clearly visible in Figures 6.8, 6.9, 6.10 and 6.11. Histograms of the mutual information MI (RF, A) computed for moving windows versus the time distance to the next or first mode loss are shown depending on the data selection for the analysis. Figure 6.8 shows the result for data from the group of unstable pulses over the Time distance Till to the next Mode Loss (TTML). The time periods where the false mode was active have been removed from the data to avoid any bias. The median and the 90 % percentile of MI (RF, A) show just a slight increase towards the mode loss in agreement with the findings of the whole pulse analysis. But the 10 % and 1 % percentiles are decreasing towards the mode loss with local minima at 125 ms, 250 ms, 400 ms and 500 ms. These are probably the time periods between mode losses and the effect of the slow voltage ripple of around 4 Hz observed in section 2.3.1. The distribution is as well asymmetric towards lower values of the MI with respect to the median MI when the distances between the median and the 90 % and 10 % percentiles are compared.

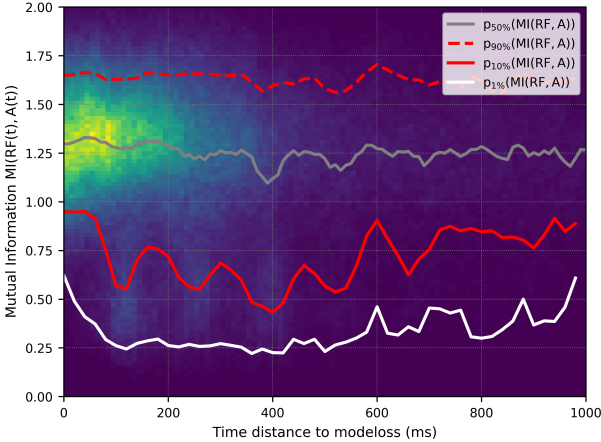


Figure 6.8: 2D histogram for the mutual information $MI(RF,A)$ and the time distance to the next mode loss computed for a moving window duration of 50 ms using data from 75 unstable gyrotron pulses. The MORE cycles have been stripped from the data to avoid any bias.

This is the effect of the periodically, shortly decreased MI due the hypothesized phenomenon leading to an accumulation for a lowered MI in the histogram. This is even stronger visible in Figure 6.9 where only data from the group of failed pulses was used since the data from the multi-mode events has a higher percentage of the total amount of data. The multi-mode events are visible as clusters with lowered MI around 0.25 to 0.5 in the histogram up to 200 ms before a mode loss. The median and the percentiles of the MI decrease up to 400 ms in advance and reach a local minimum between 40 ms and 150 ms before the next mode loss. If only the pulse data up to the first mode loss is used as in Figures 6.10 and 6.11, in order to avoid the bias from the time periods between mode losses, a similar distinct asymmetry and decrease of the 10 % and 1 % percentiles of the MI is observed in advance. The horizontal axis shows the Time distance Till the First Mode Loss (TTFML) in these cases. In order to examine the influence of the chosen window duration, the analyses were performed for window durations of 15 ms, 25 ms, 50 ms and 100 ms. The results are summarized in Figures 6.12 and 6.13. Figure 6.12 compares the median of $MI(RF,A)$ over the TTFML for a variable window duration.

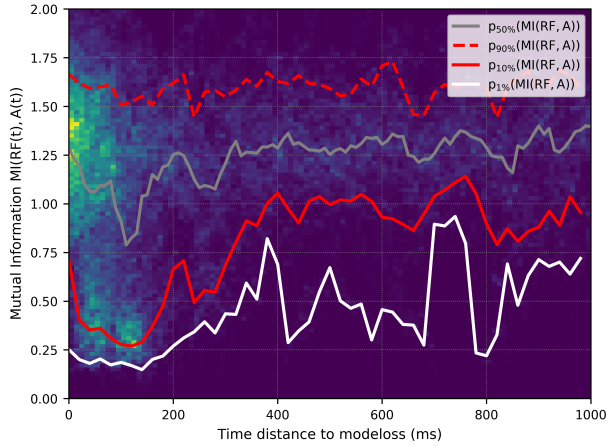


Figure 6.9: 2D histogram for the mutual information $MI(RF,A)$ and the time distance to the next mode loss computed for a moving window duration of 50 ms using data from 26 failed gyrotron pulses. The MORE cycles have been stripped from the data to avoid any bias.

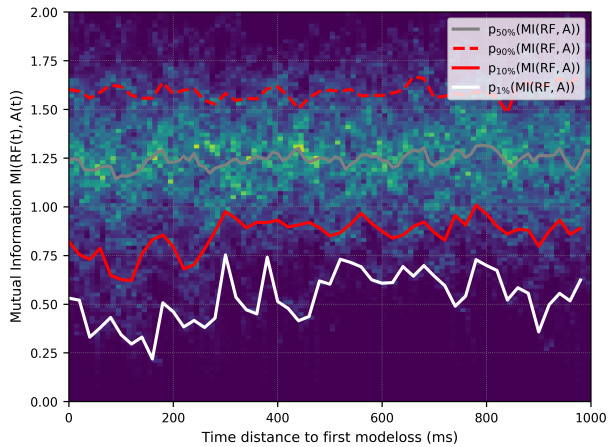


Figure 6.10: 2D histogram for the mutual information $MI(RF,A)$ computed for a moving window duration of 50 ms using data from 75 unstable gyrotron pulses up to the first mode loss.

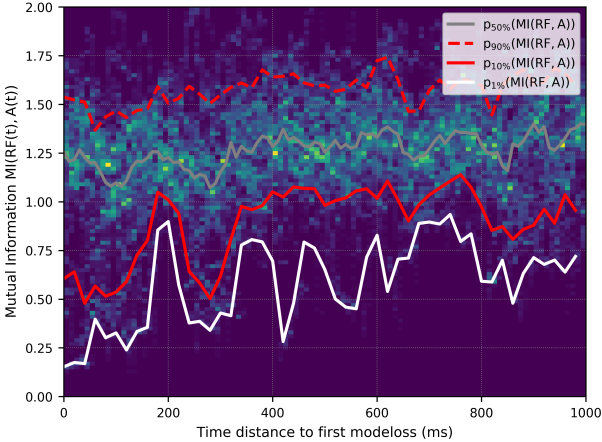


Figure 6.11: 2D histogram for the mutual information $MI(RF, A)$ computed for a moving window duration of 50 ms using data from 26 failed gyrotron pulses up to the first mode loss.

Obviously, the median MI depends more strongly on the TTMFL with increasing window duration. The explanation is that the characteristic time scale of the hypothesized multi-mode phenomenon is mostly in the range of 10 ms to 20 ms as shown in section 6.1. The closer the window duration is to this time scale, only single events will be captured more likely by the moving window leaving the median MI unaffected. If the moving window duration is much bigger than the time scale of the single event, it is more likely that multiple of such events are captured affecting the median MI, leading to this dependency of the median MI against the TTFML. This is also reflected by Figure 6.13 showing the 1 % and 10 % (lower/upper boundary of the shaded areas) percentiles for multiple window durations. The percentile difference decreases with increasing moving window duration. In all cases, either the percentile difference (shaded area) increases or both MI percentiles decrease for a $TTFML \leq 400$ ms indicating a temporal accumulation of the multi-mode events prior to a mode loss.

Therefore, the moving window MI of the RF output power signal and the measured stray radiation signal (which should reflect the activity of parasitic and satellite modes) could be used as precursor for mode loss in a fast gyrotron controller.

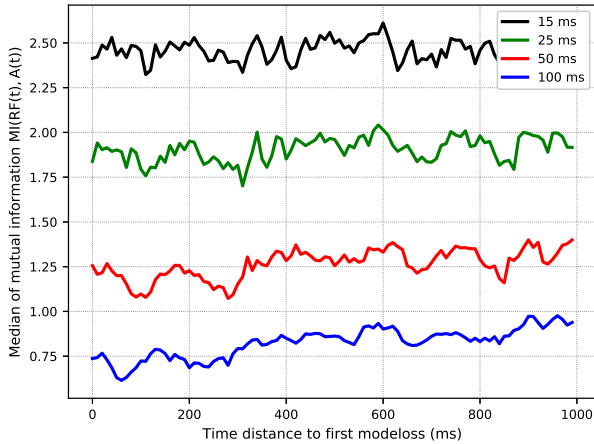


Figure 6.12: Median mutual information $MI(RF,A)$ for each time distance interval for various window durations using data from 26 failed gyrotron pulses up to the first mode loss.

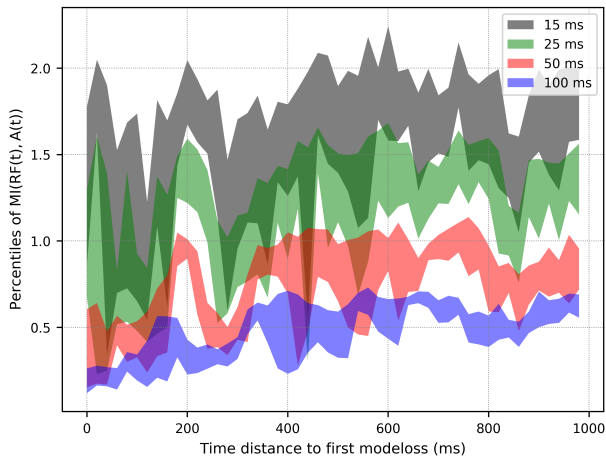


Figure 6.13: 1 % and 10 % percentiles of the mutual information $MI(RF,A)$ for each time distance interval for various window durations using data from 26 failed gyrotron pulses up to the first mode loss. The area between the percentiles is shaded to illustrate the asymmetry of the MI distribution.

6.2.2 Quasi-optical Setup

In case of the quasi-optical setup (presented in section 5.3.2) three quantities were computed for the moving windows: The mean mutual information between the RF output power signal $RF(t_n)$ and the five measured activity or stray radiation signals $A_i(t_n)$ defined by Equation 5.9, the mean mutual information between unique permutations of activity channel pairs defined by Equation 5.10 and the Total Mean Mutual Information (TMMI) using Equation 5.11.

The same data as in section 5.3.2, up to 170 gyrotron pulses with a target duration of up to 20 μ s, was used in this analysis. 37 pulses of 170 were performed at the same fields and parameters as the pulse data used to fit the modelless line (Equation 3.3). Based on the findings in the previous section 6.1, the window durations were again chosen to be 25 ms, 50 ms and 100 ms.

Figures 6.14, 6.15 and 6.16 show histograms for each of the three computed quantities using a window duration of 50 ms over the Time distance Till First Mode Loss (TTFML) in the moving window analysis for data from 75 unstable gyrotron pulses up to the first mode loss. The median of all three quantities hardly changes over the time distance. The lower percentiles only slightly decrease up to 400 ms prior to a mode loss for the TMMI and the mean mutual information between the RF output power signal and the five measured activity signals $MI(RF, A_i)$. In contrast, the mean mutual information among the activity channel pairs $MI(A_i, A_j)$ exhibits a strong sudden decrease around 50 ms to 200 ms. A possible explanation is that the sudden decrease of $MI(RF, A_i)$ during a multi-mode events vanishes more likely due to the averaging. In contrast, the activity channels seem to be decoupled (or exhibit a phase shift with events similar to the hypothesized multi-mode event) with an increasing stray radiation level leading to a drop of $MI(A_i, A_j)$.

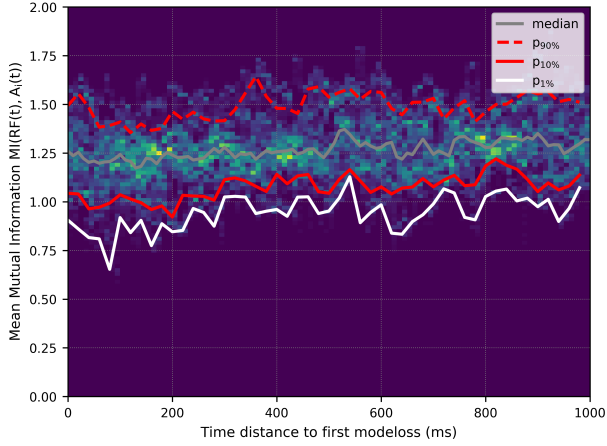


Figure 6.14: 2D histogram for the mean mutual information $MI(RF, A_i)$ over the activity channels computed for a moving window duration of 50 ms using data from 75 unstable gyrotron pulses ($2.68 \cdot 10^5$ values) up to the first mode loss.

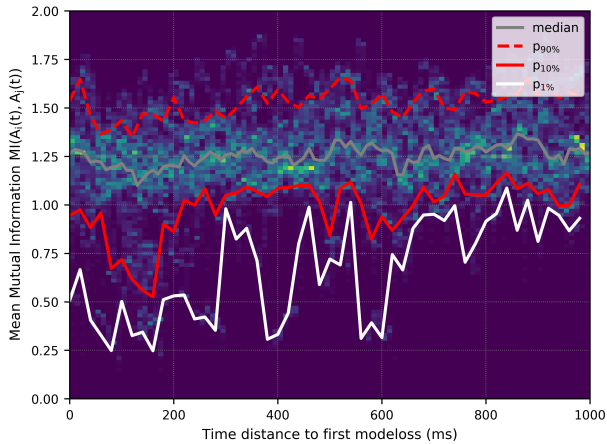


Figure 6.15: 2D histogram for the mean mutual information $MI(A_i, A_j)$ over unique activity channel pairs (A_i, A_j) computed for a moving window duration of 50 ms using data from 75 unstable gyrotron pulses ($2.68 \cdot 10^5$ values) up to the first mode loss.

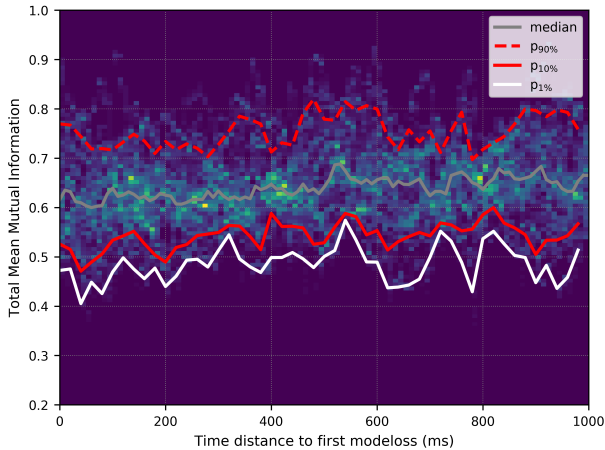


Figure 6.16: 2D histogram for the total mean mutual information over the activity channels computed for a moving window duration of 50 ms using data from 75 unstable gyrotron pulses ($2.68 \cdot 10^5$ values) up to the first mode loss.

Figures 6.14, 6.15 and 6.16 show the results of the same analyses for data from 69 failed gyrotron pulses up to the first mode loss. In case of the TMMI and the mean MI $MI(RF, A_i)$, the lower percentiles decrease slightly up to 200 ms prior to a mode loss, but more significantly for the mean MI $MI(A_i, A_j)$ around 150 ms prior to a mode loss. Possible solutions to obtain a stronger precursor would be to avoid the averaging of the pairs $MI(RF, A_i)$, but to select the minimum $MI(RF, A_i)$ for each moving data window or to increase the window duration.

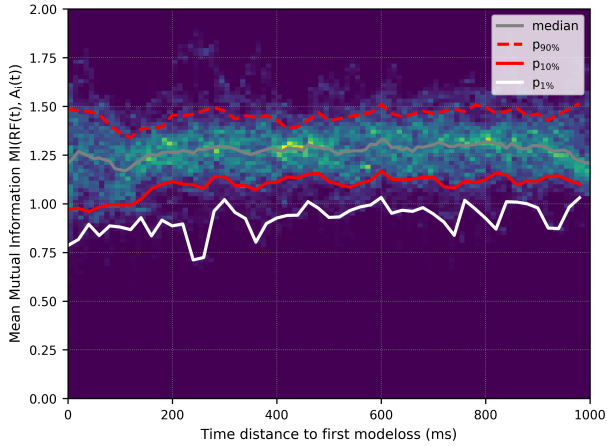


Figure 6.17: 2D histogram for the mean mutual information $MI(RF, A_i)$ over the activity channels computed for a moving window duration of 50 ms using data from 69 failed gyrotron pulses ($3.84 \cdot 10^5$ values) up to the first mode loss.

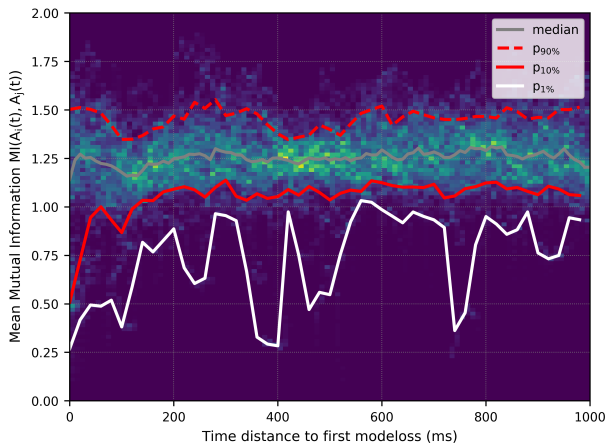


Figure 6.18: 2D histogram for the mean mutual information $MI(A_i, A_j)$ over unique activity channel pairs (A_i, A_j) computed for a moving window duration of 50 ms using data from 69 failed gyrotron pulses ($3.84 \cdot 10^5$ values) up to the first mode loss.

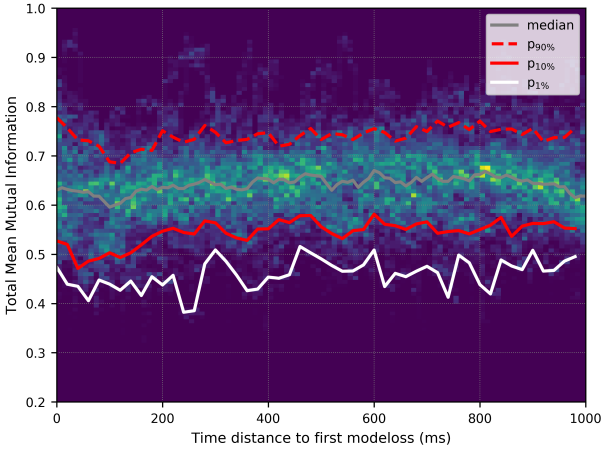


Figure 6.19: 2D histogram for the total mean mutual information over the activity channels computed for a moving window duration of 50 ms using data from 69 failed gyrotron pulses ($3.84 \cdot 10^5$ values) up to the first mode loss.

6.3 Summary

The RF output power signal of the nominal mode and the stray radiation signals from parasite and satellite modes measured with two different setups were analyzed in the time-domain in order to identify exploitable statistical properties for the prediction of mode losses. Relevant data for the analysis could be acquired since the automated mode recovery was active during unstable and failed gyrotron pulses. This allowed the repeated observation of partly stochastic, but reproducible patterns on the RF output power and stray radiation signals prior to a mode loss.

Since a low-latency mode loss precursor is desired as feedback, the analyses were performed over moving windows (simulating a FIFO buffer) for the time signals. In order to determine the minimum adequate window size, the Time-Delayed Mutual Information (TDMI) was computed for time delays of up to 200 ms using the RF output power signal and the activity signals from the gyrotron pulses. The minimum window size was found to be around 10 ms to 15 ms with the tendency to slightly higher time delays up to 40 ms for the groups of unstable and failed gyrotron pulses. The found time delay reflects the characteristic time scale of the hypothesized multi-mode event (see Figures 5.10 and 5.11) where simultaneous dips in the RF output power signal and peaks in the measured stray radiation signal were observed. The time scale of these events (duration and time distance between the events) is in agreement with the time scale implied by the probability distribution for the technical noise on the gyrotron supply voltage (see section 2.3.1).

The moving Mutual Information (MI) between the RF output power signal and the measured stray radiation signals was computed for the data from the three gyrotron pulse groups (stable, unstable and failed). The analysis of data from failed (and unstable) gyrotron pulses obtained with the mono-mode setup yielded a decreasing median MI with decreasing Time distance Till the First Mode Loss (TTFML) for moving window durations ≥ 50 ms up to 400 ms in advance prior to a mode loss. In contrast, the median MI hardly varies over the TTFML for moving window durations around the characteristic time scale of the hypothesized multi-mode event. In contrast, the 1 % and 10 % percentiles are significantly decreased in this case. The explanation is that if the moving window size is chosen to be comparable to the characteristic time scale of the phenomenon, only single events are likely captured by the moving window, leaving the median MI unaffected. In contrast, it is more likely for bigger

window durations that the moving window captures multiple events, hence yielding a lowered MI averaged over the window duration. In both cases, the multi-mode events are captured by the windowed mutual information and the decreasing MI shows that they occur more frequently and accumulate in time when a mode loss is imminent.

In case of the quasi-optical measurement setup with its five stray radiation measurement signals, the mean MI between the RF and the activity channels, the mean MI between unique pairs of the activity channels and the total mean mutual information were computed in the moving window analysis. Similar qualitative observations were made as for the mono-mode setup. The mean MI between unique pairs of the activity channels showed the strongest trend. The results for the TMMI and the mean MI between the RF and the activity channels were less distinct due to the fact that a sudden drop of the MI for one channel pair (RF, A_i) vanishes in averaging over all pairs. Using the minimum MI of the channel pairs (RF, A_i) could solve the problem.

The moving window MI could therefore serve as a fast feedback or precursor signal for mode loss during the gyrotron pulse implemented on a fast gyrotron controller.

Nevertheless, also non-parametric clustering algorithms like e.g. DBSCAN [SSE⁺17], a neural network suitable for time-series regression or classification (e.g. Convolutional Neural Network (CNN) or Long-Short Term Memory (LSTM)) or other machine learning methods should be evaluated as well.

7 Conclusion and Outlook

An automated mode recovery (MORE) for gyrotrons was successfully demonstrated at Wendelstein 7-X. MORE is able to recover the nominal working mode in 99 % of the cases in dedicated test experiments across two gyrotrons. During the last experimental campaign, MORE was able to recover the nominal mode in 91 % of the cases across seven gyrotrons. The reliable output power was increased by up to 100 kW per gyrotron for the same pulse length and the same level of the mean failure probability. Being a mere software update for the already existing gyrotron controllers, a kind-of free power upgrade was achieved for nine out of ten gyrotrons being part of the W7-X ECRH facility. The automated mode or fast oscillation recovery during the gyrotron pulse is therefore a significant contribution to ensure the required reliable heating power for future fusion experiments and in particular for possible fusion power plants.

The stray radiation of the azimuthal neighbor or satellite modes $TE_{27,8}$ and $TE_{29,8}$ at the gyrotron relief window was identified as a possible mode loss precursor in stray radiation spectrograms of the mode-switching behavior. Exploratory measurements with a single detector found an exponential growth of the average measured activity during the pulse while approaching the practical output power limit of the gyrotron. A more in detail analysis of the stray radiation signal in the time domain revealed a simultaneous pattern which is interpreted as temporary, reversible multi-moding of the nominal working mode and other parasitic and satellite modes. The pattern is reproduced when the nominal mode loss is approached and its time scale is explained by the probability distribution of the acceleration voltage noise and the residual voltage ripple on the gyrotron supply voltages.

The time scale implied by the probability distribution of the voltage noise is also in agreement with the characteristic time scale of 10 ms to 20 ms identified for the phenomenon applying the Time-Delayed Mutual Information (TDMI) on the measured stray radiation signals. This result was then used as minimum adequate window duration for a moving window analysis of the gyrotron pulse

data obtained with both measurement setups. The moving window analysis was performed in order to simulate the signal processing during the gyrotron pulse in a possible future implementation in a fast gyrotron controller. The Mutual Information (MI) was computed between the RF output power and the measured stray radiation signals to determine the non-linear coupling degree and to identify the bespoke hypothesized multi-mode phenomenon. Indeed, the moving window analysis revealed a statistical accumulation for a lowered mutual information up to 400 ms in advance prior to a mode loss compared to the rest of the gyrotron pulses. The mutual information could be therefore used as precursor for the mode loss during the gyrotron pulse in a possible, future electronic stability control for gyrotrons. A neural network or other machine learning methods could be applied to predict the loss of the nominal operating mode during the pulse.

A Appendix

A.1 Data Normalization Methods

Data normalization methods are commonly applied in data science and in the data preprocessing step for machine learning algorithms, e.g. see [MG16].

A.1.1 Min-Max Normalization

Let X be a set of n data samples and $x = (x_0, x_1, \dots, x_m) \in X \subset \mathbb{R}^m$ a sample with m features. X_{ij} denotes the j -th feature of the i -th data sample and $X_j \in \mathbb{R}^n$ the feature vector containing the j -th feature of each of the n samples. The min-max normalized sample where each feature is normalized individually, is then given by (see e.g. [FPP07] or [Gru15])

$$x'_j = \frac{x_j - \min(X_j)}{\max(X_j) - \min(X_j)} \quad (\text{A.1})$$

where X_j denotes the set containing the j -th feature of each sample (also called feature vector). To rescale the features to an arbitrary interval $[a, b]$, the expression changes to

$$x'_j = a + \frac{(x_j - \min(X_j)) (b - a)}{\max(X_j) - \min(X_j)} \quad (\text{A.2})$$

A.1.2 Z-Score Normalization

Let X be a set of n data samples and $x = (x_0, x_1, \dots, x_m) \in X \subset \mathbb{R}^m$ a sample with m features. X_{ij} denotes the j -th feature of the i -th data sample and $X_j \in \mathbb{R}^n$ the feature vector containing the j -th feature of each of the n samples. The z-score normalized sample where each feature is normalized individually, is then given by (see e.g. [FPP07] or [Gru15])

$$\bar{X}_j = \frac{1}{N} \sum_{i=1}^N X_{ij} \quad (\text{A.3})$$

$$\sigma(X_j) = \sqrt{\text{Var}(X_j)} = \sqrt{\frac{1}{N} \sum_{i=1}^N (X_{ij} - \bar{X}_j)^2} \quad (\text{A.4})$$

$$x'_j = \frac{x_j - \bar{X}_j}{\sigma(X_j)} \quad (\text{A.5})$$

A.2 Implemented Expressions in MMWFR

A.2.1 Circular Waveguide

The conductive loss attenuation constant α_{cmn} for a TE_{mn} mode in an arbitrary circular waveguide with inner radius R is computed using

$$\beta_{mn} = \sqrt{k_{mn}^2 \epsilon_r - k_{cmn}^2} \quad (A.6)$$

$$R_S = \sqrt{\frac{\omega \mu_0}{2 \sigma_c}} \quad (A.7)$$

$$\psi_1 = \frac{\pi \operatorname{Re}(\beta_{mn}) \mu_0 \mu_r}{2 k_{cmn}^4} \quad (A.8)$$

$$I = \int_0^R \frac{n^2}{\rho} J_n(k_{cmn} \rho)^2 + k_{cmn}^2 \rho J_n'(k_{cmn} \rho)^2 d\rho \quad (A.9)$$

where R_S is the surface resistance of the waveguide wall, β_{mn} the propagation constant, k_{mn} the mode wavenumber and k_{cmn} the cutoff wavenumber of the mode. The total power flow P_0 and the conductive power loss per length P_1 are then obtained with

$$P_0^{(TE)} = \psi_1 I \quad (A.10)$$

$$P_1^{(TE)} = \frac{R_S \pi R}{2} \left(\frac{\beta_{mn}^2 n^2}{k_{cmn}^4 R^2} \right) \quad (A.11)$$

$$\alpha_{cmn}^{(TE)} = \frac{P_1^{(TE)}}{2P_0^{(TE)}} \quad (A.12)$$

For a TM_{mn} mode holds deviating from above

$$\psi_2 = \frac{\pi \operatorname{Re}(\beta_{mn}) \omega \epsilon_0 \epsilon_r}{2 k_{cmn}^4} \quad (A.13)$$

The total power flow P_0 and the conductive power loss per length P_l are then obtained with

$$P_0^{(\text{TM})} = \psi_2 I \quad (\text{A.14})$$

$$P_l^{(\text{TM})} = \frac{R_S \pi R}{2} \left(\frac{\omega \epsilon_0 \epsilon_r}{k_{c_{mn}}} J'_n(k_{c_{mn}} R) \right)^2 \quad (\text{A.15})$$

$$\alpha_{c_{mn}}^{(\text{TM})} = \frac{P_l^{(\text{TM})}}{2P_0^{(\text{TM})}} \quad (\text{A.16})$$

A.2.2 Rectangular Waveguide

The conductive loss attenuation constant $\alpha_{c_{mn}}$ for a TE_{mn} mode in an arbitrary rectangular waveguide with inner dimensions a and b is computed using

$$\psi = \frac{1}{2} \frac{\omega \mu_0 \mu_r n^2 \pi^2 \text{Re}(\beta_{mn})}{k_{c_{mn}}^4 a^2} \quad (\text{A.17})$$

$$I_1(n, a) = \int_0^a \cos\left(\frac{n\pi x}{a}\right)^2 dx \quad (\text{A.18})$$

$$I_2(n, a) = \int_0^a \sin\left(\frac{n\pi x}{a}\right)^2 dx \quad (\text{A.19})$$

$$I_3(m, n, a, b) = \int_0^a \int_0^b \left\{ \left(\frac{m}{a}\right)^2 \cos\left(\frac{m\pi x}{a}\right)^2 \sin\left(\frac{n\pi y}{b}\right)^2 + \left(\frac{n}{b}\right)^2 \cos\left(\frac{n\pi y}{b}\right)^2 \sin\left(\frac{m\pi x}{a}\right)^2 \right\} dx dy \quad (\text{A.20})$$

$$P_0^{(\text{TM})} = \psi \text{Re}(I_1(n, a)) \text{Re}(I_2(m, b)) \quad (\text{A.21})$$

$$P_l^{(\text{TM})} = R_S \left\{ I_1(m, b) + \frac{\beta_{mn}^2 n^2 \pi^2}{k_{c_{mn}}^4 a^2} I_2(n, a) + I_1(n, a) \right\} \quad (\text{A.22})$$

$$\alpha_{c_{mn}}^{(\text{TM})} = \frac{P_l^{(\text{TM})}}{2P_0^{(\text{TM})}} \quad (\text{A.23})$$

with R_S being the surface resistance of the waveguide wall, P_0 being the total power flow and P_1 the conductive power loss per length.

A.3 Supplementary Figures

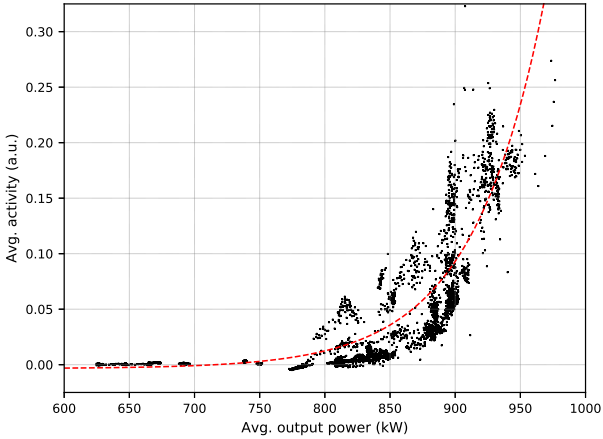


Figure A.1: Power-normalized average diode signal measured with 142 GHz high pass filter plotted against the power at the gyrotron output window. Each dot represents a gyrotron pulse with a duration of 1 s. The red dashed line is an exponential fit of the data.

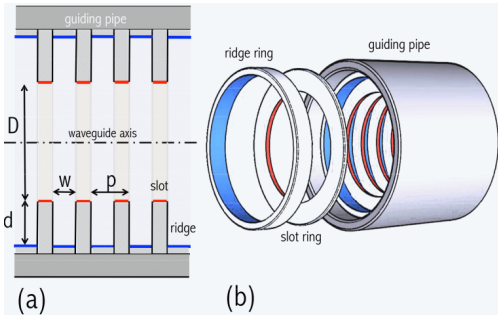


Figure A.2: Schematic of the W7-X ECE notch filter. A Bragg reflector was realized with a corrugated waveguide assembled of stacked rings (from [DWF⁺ 15]).

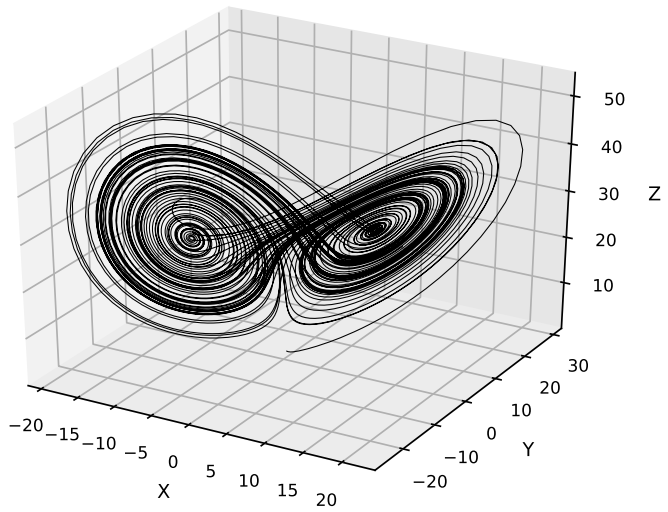


Figure A.3: 3D plot of the reconstructed phase space trajectories of the Lorenz attractor.

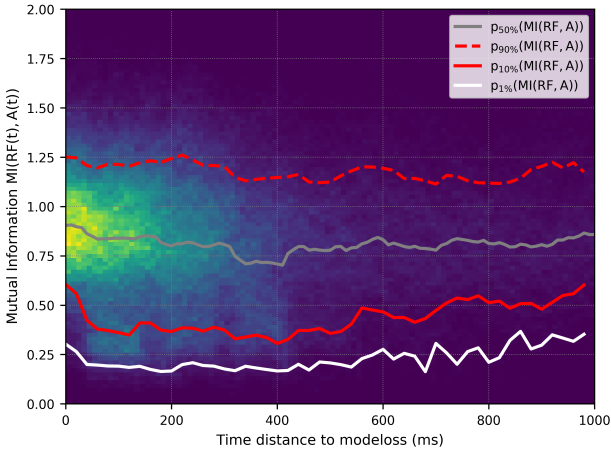


Figure A.4: 2D histogram for the mutual information $MI(RF,A)$ computed for a moving window duration of 100 ms using data from 75 unstable gyrotron pulses.

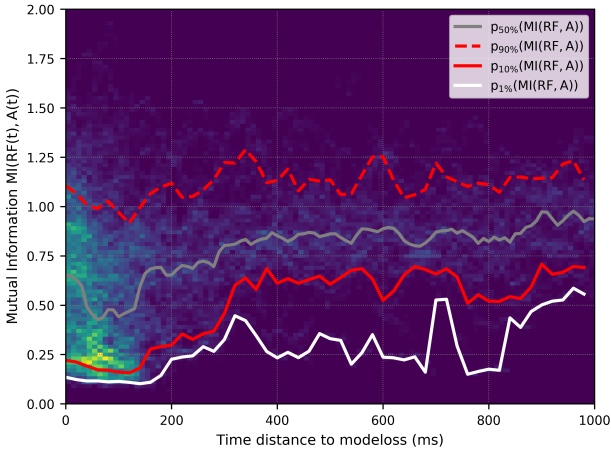


Figure A.5: 2D histogram for the mutual information $MI(RF,A)$ computed for a moving window duration of 100 ms using data from 26 failed gyrotron pulses.

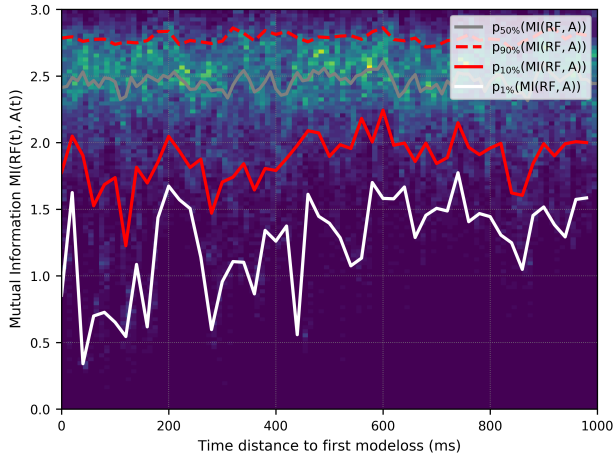


Figure A.6: 2D histogram for the mutual information $MI(RF, A)$ computed for a moving window duration of 15 ms using data from 26 failed gyrotron pulses up to the first mode loss.

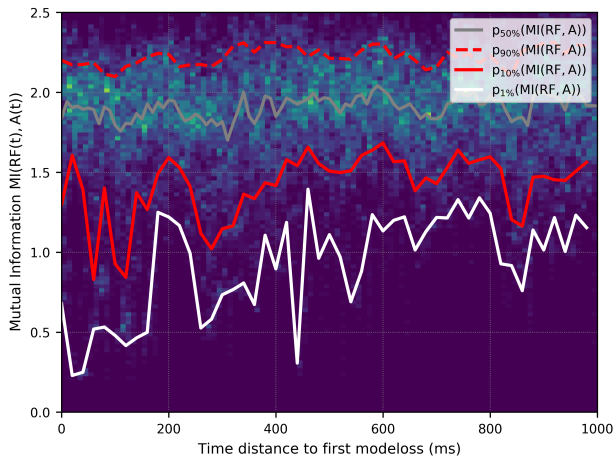


Figure A.7: 2D histogram for the mutual information $MI(RF, A)$ computed for a moving window duration of 25 ms using data from 26 failed gyrotron pulses up to the first mode loss.

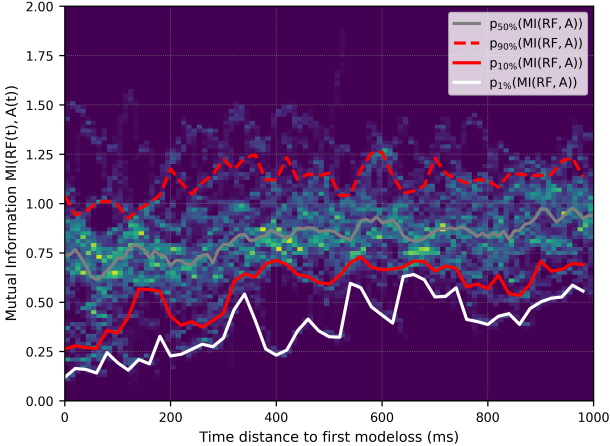


Figure A.8: 2D histogram for the mutual information $MI(RF,A)$ computed for a moving window duration of 100 ms using data from 26 failed gyrotron pulses up to the first mode loss.

Bibliography

- [AAA⁺12] S. Alberti, J.-Ph. Ansermet, K. A. Avramides, F. Braunmueller, P. Cuanillon, J. Dubray, D. Fasel, J.-Ph. Hogge, A. Macor, E. de Rijk, M. da Silva, M. Q. Tran, T. M. Tran, and Q. Vuillemin. Experimental study from linear to chaotic regimes on a terahertz-frequency gyrotron oscillator. *Physics of Plasmas*, 19(12):123102, 2012.
- [ABA⁺18] K. A. Avramidis, A. Bertinetti, F. Albajar, F. Cau, F. Cismondi, G. Gantenbein, S. Illy, Z. C. Ioannidis, J. Jelonnek, F. Legrand, I. G. Pagonakis, Y. Rozier, T. Rzesnicki, L. Savoldi, M. Thumm, and R. Zanino. Numerical studies on the influence of cavity thermal expansion on the performance of a high-power gyrotron. *IEEE Transactions on Electron Devices*, 65(6):2308–2315, June 2018.
- [AC94] Mohammed Nurul Afsar and Hua Chi. Window materials for high power gyrotron. *International Journal of Infrared and Millimeter Waves*, 15(7):1161–1179, Jul 1994.
- [AD02] M. I. Airila and O. Dumbrajs. Spatio-temporal chaos in the transverse section of gyrotron resonators. *IEEE Transactions on Plasma Science*, 30(3):846–850, June 2002.
- [AD03] M.I Airila and O Dumbrajs. Stochastic processes in gyrotrons. *Nuclear Fusion*, 43(11):1446–1453, nov 2003.
- [ADRS01] M. I. Airila, O. Dumbrajs, A. Reinfelds, and U. Strautiņš. Nonstationary oscillations in gyrotrons. *Physics of Plasmas*, 8(10):4608–4612, 2001.
- [ADV08] K. A. Avramides, O. Dumbrajs, and J. L. Vomvoridis. Mode selection for a 170 ghz, 1 mw gyrotron. *35th EPS Conference on Plasma Phys.*, 32D, 2008.
- [AIK⁺15] K. A. Avramidis, Z. C. Ioannidis, S. Kern, A. Samartsev, I. Gr. Pagonakis, I. G. Tigelis, and J. Jelonnek. A comparative study

- on the modeling of dynamic after-cavity interaction in gyrotrons. *Physics of Plasmas*, 22(5):053106, 2015.
- [Aka74] H. Akaike. A new look at the statistical model identification. *IEEE Transactions on Automatic Control*, 19(6):716–723, December 1974.
- [APIT13] K. A. Avramidis, I. G. Pagonakis, Z. C. Ioannidis, and I. G. Tigelis. Numerical investigations on the effects of electron beam misalignment on beam-wave interaction in a high-power coaxial gyrotron. In *2013 38th International Conference on Infrared, Millimeter, and Terahertz Waves (IRMMW-THz)*, pages 1–2, Sep. 2013.
- [APIV12] Avramides, K. A., Pagonakis, I. Gr., Iatrou, C. T., and Vomvoridis, J. L. Euridice: A code-package for gyrotron interaction simulations and cavity design. *EPJ Web of Conferences*, 32:04016, 2012.
- [APPV07] K. A. Avramides, I. G. Pagonakis, B. Piosczyk, and J. L. Vomvoridis. Possible excitation of radial satellites in high-power gyrotrons. In *2007 Joint 32nd International Conference on Infrared and Millimeter Waves and the 15th International Conference on Terahertz Electronics*, pages 700–701, Sep. 2007.
- [ARM⁺19] Avramidis, Konstantinos A., Ruess, Tobias, Mentgen, Felix, Jin, Jianbo, Wagner, Dietmar, Gantenbein, Gerd, Illy, Stefan, Ioannidis, C., Laqua, Heinrich P., Pagonakis, Ioannis Gr., Rzesnicki, Tomasz, Thumm, Manfred, Wolf, Robert C., and Jelonnek, John. Studies towards an upgraded 1.5 mw gyrotron for w7-x. *EPJ Web Conf.*, 203:04003, 2019.
- [ATA⁺11] S. Alberti, T. M. Tran, K. A. Avramides, F. Li, and J. . Hogge. Gyrotron parasitic-effects studies using the time-dependent self-consistent monomode code twang. In *2011 International Conference on Infrared, Millimeter, and Terahertz Waves*, pages 1–2, Oct 2011.
- [Avr15] K. A. Avramidis. Investigations and advanced concepts on gyrotron interaction modeling and simulations. *Physics of Plasmas*, 22(12):123114, 2015.
- [Avr19] K. Avramidis. Personal communication, 08 2019.

- [BAA⁺17] A. Bertinetti, K.A. Avramidis, F. Albajar, F. Cau, F. Cismondi, Y. Rozier, L. Savoldi, and R. Zanino. Multi-physics analysis of a 1mw gyrotron cavity cooled by mini-channels. *Fusion Engineering and Design*, 123:313 – 316, 2017. Proceedings of the 29th Symposium on Fusion Technology (SOFT-29) Prague, Czech Republic, September 5-9, 2016.
- [BAL⁺98] M. Botton, T. M. Antonsen, B. Levush, K. T. Nguyen, and A. N. Vlasov. Magy: a time-dependent code for simulation of slow and fast microwave sources. *IEEE Transactions on Plasma Science*, 26(3):882–892, June 1998.
- [BBK⁺05] H Braune, P Brand, R Krampitz, W Leonhardt, D Mellein, G Michel, G Mueller, J Sachtleben, M Winkler, the W7-X ECRH teams at IPP IPF, and FZK. HV-system for CW-gyrotrons at w7-x and the relevance for ITER. *Journal of Physics: Conference Series*, 25:56–65, jan 2005.
- [Ber11] Matthias Hermann Beringer. *Design studies towards a 4 MW 170 GHz coaxial-cavity gyrotron*. PhD thesis, 2011. 31.30.03; LK 01.
- [Bet39] H. A. Bethe. Energy production in stars. *Phys. Rev.*, 55:434–456, Mar 1939.
- [Big18] Bernard Bigot. Iter construction and manufacturing progress toward first plasma. *Fusion Engineering and Design*, 2018.
- [BSL⁺17] K. J. Brunner, T. Stange, H. P. Laqua, S. Marsen, ECRH group, and W7-X team. W7-x ecrh developments towards op1.2. In *W7-X OP1.2a Program Workshop, Greifswald*. Max Planck Institute for Plasmaphysics, April 2017.
- [Bus26] H. Busch. Berechnung der bahn von kathodenstrahlen im axial-symmetrischen elektromagnetischen felde. *Annalen der Physik*, 386(25):974–993, 1926.
- [BWA⁺13] H.-S. Bosch, R.C. Wolf, T. Andreeva, J. Baldzuhn, D. Birus, T. Bluhm, T. Bräuer, H. Braune, V. Bykov, A. Cardella, F. Durodié, M. Endler, V. Erckmann, G. Gantenbein, D. Hartmann, D. Hathiramani, P. Heimann, B. Heinemann, C. Henig, M. Hirsch, D. Holtum, J. Jagielski, J. Jelonnek, W. Kasparek, T. Klinger, R. König, P. Kornejew, H. Kroiss, J.G. Krom, G. Kühner, H. Laqua, H.P. Laqua, C. Lechte, M. Lewerentz,

J. Maier, P. McNeely, A. Messiaen, G. Michel, J. Ongena, A. Peacock, T.S. Pedersen, R. Riedl, H. Riemann, P. Rong, N. Rust, J. Schacht, F. Schauer, R. Schroeder, B. Schweer, A. Spring, A. Stäbler, M. Thumm, Y. Turkin, L. Wegener, A. Werner, D. Zhang, M. Zilker, T. Akijama, R. Alzbutas, E. Ascasibar, M. Balden, M. Banduch, Ch. Baylard, W. Behr, C. Beidler, A. Benndorf, T. Bergmann, C. Biedermann, B. Bieg, W. Biel, M. Borchardt, G. Borowitz, V. Borsuk, S. Bozhenkov, R. Brakel, H. Brand, T. Brown, B. Brucker, R. Burhenn, K.-P. Buscher, C. Caldwell-Nichols, A. Cappa, A. Cardella, A. Carls, P. Carvalho, Ł. Ciupiński, M. Cole, J. Collienne, A. Czarnicka, G. Czymek, G. Dammertz, C.P. Dhard, V.I. Davydenko, A. Dinklage, M. Drevlak, S. Drotziger, A. Dudek, P. Dumortier, G. Dundulis, P.v. Eeten, K. Egorov, T. Estrada, H. Faugel, J. Fellingner, Y. Feng, H. Fernandes, W.H. Fietz, W. Figacz, F. Fischer, J. Fontdecaba, A. Freund, T. Funaba, H. Fünfgelder, A. Galkowski, D. Gates, L. Giannone, J.M. García Regaña, J. Geiger, S. Geissler, H. Greuner, M. Grahl, S. Gross, A. Grosman, H. Grote, O. Grulke, M. Haas, L. Haiduk, H.-J. Hartfuss, J.H. Harris, D. Haus, B. Hein, P. Heitzenroeder, P. Helander, R. Heller, C. Hidalgo, D. Hildebrandt, H. Höhnle, A. Holtz, E. Holzhauer, R. Holzthüm, A. Huber, H. Hunger, F. Hurd, M. Ihrke, S. Illy, A. Ivanov, S. Jablonski, N. Jaksic, M. Jakubowski, R. Jaspers, H. Jensen, H. Jenzsch, J. Kacmarczyk, T. Kaliatk, J. Kallmeyer, U. Kamionka, R. Karaleviciu, S. Kern, M. Keunecke, R. Kleiber, J. Knauer, R. Koch, G. Kocsis, A. Könies, M. Köppen, R. Koslowski, J. Koshurinov, A. Krämer-Flecken, R. Krampitz, Y. Kravtsov, M. Krychowiak, G. Krzesinski, I. Ksiazek, M. Kubkowska, A. Kus, S. Langish, R. Laube, M. Laux, S. Lazerson, M. Lennartz, C. Li, R. Lietzow, A. Lohs, A. Lorenz, F. Louche, L. Lubyako, A. Lumsdaine, A. Lyssoivan, H. Maassberg, P. Marek, C. Martens, N. Marushchenko, M. Mayer, B. Mendelevitch, Ph. Mertens, D. Mikkelsen, A. Mishchenko, B. Missal, T. Mizuuchi, H. Modrow, T. Mönnich, T. Morizaki, S. Murakami, F. Musielok, M. Nagel, D. Naujoks, H. Neilson, O. Neubauer, U. Neuner, R. Nocentini, J.-M. Noterdaeme, C. Nührenberg, S. Obermayer, G. Offermanns, H. Oosterbeek, M. Otte, A. Panin, M. Pap,

- S. Paquay, E. Pasch, X. Peng, S. Petrov, D. Pilopp, H. Pirsch, B. Plaum, F. Pompon, M. Povilaitis, J. Preinhaelter, O. Prinz, F. Purps, T. Rajna, S. Récsei, A. Reiman, D. Reiter, J. Rummel, S. Renard, V. Rhode, J. Riemann, S. Rimkevicius, K. Risse, A. Rodatos, I. Rodin, M. Romé, H.-J. Roscher, K. Rummel, Th. Rummel, A. Runov, L. Ryc, J. Sachtleben, A. Samartsev, M. Sanchez, F. Sano, A. Scarabosio, M. Schmid, H. Schmitz, O. Schmitz, M. Schneider, W. Schneider, L. Scheibl, M. Scholz, G. Schröder, M. Schröder, J. Schruff, H. Schumacher, I.V. Shikhovtsev, M. Shoji, G. Siegl, J. Skodzik, M. Smirnow, E. Speth, D.A. Spong, R. Stadler, Z. Sulek, V. Szabó, T. Szabolics, T. Szetefi, Z. Szökefalvi-Nagy, A. Tereshchenko, H. Thomsen, M. Thumm, D. Timmermann, H. Tittes, K. Toi, M. Tournianski, U.v. Toussaint, J. Tretter, S. Tulipán, P. Turba, R. Uhlemann, J. Urban, E. Urbonavicius, P. Urlings, S. Valet, D. Van Eester, M. Van Schoor, M. Vervier, H. Viebke, R. Vilbrandt, M. Vrancken, T. Wauters, M. Weissgerber, E. Weiss, A. Weller, J. Wendorf, U. Wenzel, T. Windisch, E. Winkler, M. Winkler, J. Wolowski, J. Wolters, G. Wrochna, P. Xanthopoulos, H. Yamada, M. Yokoyama, D. Zacharias, J. Zajac, G. Zangl, M. Zarnstorff, H. Zeplien, S. Zoletnik, and M. Zuin. Technical challenges in the construction of the steady-state stellarator wendelstein 7-x. *Nuclear Fusion*, 53(12):126001, nov 2013.
- [CCE⁺17] Mirela Cengher, Xi Chen, Robert Ellis, Yuri Gorelov, John Lohr, Charles Moeller, Dan Ponce, and Antonio Torrezan. Advances in technology and high power performance of the ech system on diii-d. *Fusion Engineering and Design*, 123:295 – 298, 2017. Proceedings of the 29th Symposium on Fusion Technology (SOFT-29) Prague, Czech Republic, September 5-9, 2016.
- [CFZ14] Minyou Chen, Yonghui Fang, and Xufei Zheng. Phase space reconstruction for improving the classification of single trial eeg. *Biomedical Signal Processing and Control*, 11:10 – 16, 2014.
- [CG01] W. N. Cottingham and D. A. Greenwood. *An Introduction to Nuclear Physics*. Cambridge University Press, 2 edition, 2001.
- [Che15] Francis Chen. *Introduction to Plasma Physics and Controlled Fusion*. Springer, 2015.

- [Chu04] K. R. Chu. The electron cyclotron maser. *Rev. Mod. Phys.*, 76:489–540, May 2004.
- [Coh03] J. E. Cohen. Human population: The next half century. *Science*, 302:1172–1175, 2003.
- [Cro65] C.R. Crowell. The richardson constant for thermionic emission in schottky barrier diodes. *Solid-State Electronics*, 8(4):395 – 399, 1965.
- [CSD⁺11] A. R. Choudhury, A. Schlaich, D. D’Andrea, S. Kern, and M. Thumm. Influence of non-uniform magnetic field distribution on gyrotron spurious oscillations. In *2011 International Conference on Infrared, Millimeter, and Terahertz Waves*, pages 1–2, Oct 2011.
- [DAB⁺05] G. Dammertz, A. Arnold, E. Borie, S. Illy, S. Alberti, D. Bariou, P. Brand, H. Braune, V. Erckmann, G. Gantenbein, E. Giguët, R. Heidinger, J. P. Hogge, W. Kasperek, K. Koppenburg, H. Laqua, F. Legrand, W. Leonhardt, C. Lievin, G. Michel, G. Muller, G. Neffe, B. Piosczyk, M. Schmid, M. Thumm, and M. Q. Tran. Experimental results on the 140 ghz, 1 mw, cw gyrotrons for the stellarator w7-x. In *2005 Joint 30th International Conference on Infrared and Millimeter Waves and 13th International Conference on Terahertz Electronics*, volume 1, pages 235–236 vol. 1, Sep. 2005.
- [Dam95] Günter Dammertz. Vacuum requirements in high power microwave tubes. *Vacuum*, 46(8):785 – 788, 1995.
- [DeV16] Jeanne Jackson DeVoe. Pppl, princeton university physicists join german chancellor angela merkel at wendelstein 7-x celebration. Website, 2016.
- [DFG⁺17] G. G. Denisov, A. P. Fokin, M. Y. Glyavin, G. Y. Golubiatnikov, L. V. Lubyako, M. V. Morozkin, B. Z. Mowshevich, and A. I. Tsvetkov. High precision frequency stabilization of a 100w/263 ghz continuous wave gyrotron. In *2017 Eighteenth International Vacuum Electronics Conference (IVEC)*, pages 1–2, April 2017.
- [DI08] O. Dumbrajs and T. Idehara. Hysteresis in Mode Competition in High Power 170 GHz Gyrotron for ITER. *International Journal of Infrared and Millimeter Waves*, 29(3):232–239, Mar 2008.

- [DII⁺03] O. Dumbrajs, T. Idehara, Y. Iwata, S. Mitsudo, I. Ogawa, and B. Piosczyk. Hysteresis-like effects in Gyrotron Oscillators. *Physics of Plasmas*, 10(5):1183 – 1186, 2003.
- [DIP⁺05] G. Dammertz, S. Illy, B. Piosczyk, M. Schmid, and D. Bar-iou. Collector sweeping systems for high power gyrotrons. In *2005 Joint 30th International Conference on Infrared and Millimeter Waves and 13th International Conference on Terahertz Electronics*, volume 1, pages 293–294 vol. 1, Sep. 2005.
- [DK81] A. T. Drobot and K. Kim. Space charge effects on the equilibrium of guided electron flow with gyromotion. *International Journal of Electronics*, 51(4):351–367, 1981.
- [DK84] Peter D’Antonio and John H. Konnert. The reflection phase grating diffusor: Design theory and application. *J. Audio Eng. Soc.*, 32(4):228–238, 1984.
- [DN97] O. Dumbrajs and G. S. Nusinovich. Effect of technical noise on radiation linewidth in free-running gyrotron oscillators. *Physics of Plasmas*, 4(5):1413–1423, 1997.
- [DN13] O. Dumbrajs and G. S. Nusinovich. Effect of electron beam misalignments on the gyrotron efficiency. *Physics of Plasmas*, 20(7):073105, 2013.
- [DWF⁺15] D. Wagner, W. Kasperek, F. Leuterer, A. Marcor, F. Monaco, M. Münich, E. De Rijk, H. Schütz, J. Stober, M. Thumm, and A. Zeitler. Sub-thz notch filters based on photonic bandgaps in overmoded waveguides. In *2015 40th International Conference on Infrared, Millimeter, and Terahertz waves (IRMMW-THz)*, pages 1–2, Aug 2015.
- [EBB⁺07] V. Erckmann, P. Brand, H. Braune, G. Dammertz, G. Ganzenbein, W. Kasperek, H. P. Laqua, H. Maassberg, N. B. Marushchenko, G. Michel, M. Thumm, Y. Turkin, M. Weissgerber, A. Weller, W7-X ECRH Team at IPP Greifswald, W7-X ECRH Team at FZK Karlsruhe, and W7-X ECRH Team at IPF Stuttgart. Electron cyclotron heating for w7-x: Physics and technology. *Fusion Science and Technology*, 52(2):291–312, 2007.
- [Edg93] C. J. Edgecombe. *Gyrotron oscillators: their principles and practice*. Taylor & Francis Ltd, 1993.

- [Ein35] Albert Einstein. Elementary derivation of the equivalence of mass and energy. *Bull. Amer. Math. Soc.*, 41:223–230, 1935.
- [FGG⁺18] Andrey Fokin, Mikhail Glyavin, German Golubiatnikov, Lev Lubyako, Mikhail Morozkin, Boris Movshevich, Alexander Tsvetkov, and Gregory Denisov. High-power sub-terahertz source with a record frequency stability at up to 1 Hz. *Scientific Reports*, 8(4317), 2018.
- [FGN15] A. P. Fokin, M. Yu. Glyavin, and G. S. Nusinovich. Effect of ion compensation of the beam space charge on gyrotron operation. *Physics of Plasmas*, 22(4):043119, 2015.
- [FGPY77] V. A. Flyagin, A. V. Gaponov, I. Petelin, and V. K. Yulpatov. The gyrotron. *IEEE Transactions on Microwave Theory and Techniques*, 25(6):514–521, Jun 1977.
- [FPP07] David Freedman, Robert Pisani, and Roger Purves. *Statistics: Fourth International Student Edition*. W.W. Norton & Company, 2007.
- [Fra17] Joachim Franck. *Systematic study of key components for a coaxial-cavity gyrotron for DEMO*. PhD thesis, Karlsruher Institut für Technologie (KIT), 2017.
- [FS86] Andrew M. Fraser and Harry L. Swinney. Independent coordinates for strange attractors from mutual information. *Phys. Rev. A*, 33:1134–1140, Feb 1986.
- [GDA⁺06] G. Gantenbein, G. Dammertz, S. Alberti, A. Arnold, V. Erckmann, E. Giguët, R. Heidinger, J. P. Hogge, S. Illy, W. Kasperek, K. Koppenburg, H. Laqua, F. Legrand, W. Leonhardt, C. Lievin, G. Michel, G. Neffe, B. Piosczyk, M. Schmid, M. Thumm, and M. Q. Tran. Status of the 1-mw, 140-ghz, cw gyrotron for w7-x. In *2006 IEEE International Vacuum Electronics Conference held Jointly with 2006 IEEE International Vacuum Electron Sources*, pages 533–534, April 2006.
- [GDF⁺10] G. Gantenbein, G. Dammertz, J. Flamm, S. Illy, S. Kern, G. Latsas, B. Piosczyk, T. Rzesnicki, A. Samartsev, A. Schlaich, M. Thumm, and I. Tigelis. Experimental investigations and analysis of parasitic rf oscillations in high-power gyrotrons. *IEEE Transactions on Plasma Science*, 38(6):1168–1177, June 2010.

- [Gei91] T. Geist. Linewidth measurement on a 140 GHz gyrotron. In Minh Quang Tran, editor, *16th International Conference on Infrared and Millimeter Waves*, volume 1576, pages 327 – 328. International Society for Optics and Photonics, SPIE, 1991.
- [Gei98] Thomas Geist. Simple millimeter wave dielectric disc filter with very flat passband characteristic. *International Journal of Infrared and Millimeter Waves*, 19(6):887–893, Jun 1998.
- [GEI⁺11] Gerd Gantenbein, Volker Erckmann, Stefan Illy, Stefan Kern, Walter Kasperek, Carsten Lechte, Wolfgang Leonhardt, Christophe Liévin, Andrey Samartsev, Andreas Schlaich, Martin Schmid, and Manfred Thumm. 140 ghz, 1 mw cw gyrotron development for fusion applications - progress and recent results. *Journal of Infrared, Millimeter, and Terahertz Waves*, 32(3):320–328, Mar 2011.
- [Ger16] R. W. L. Geraerts. Feasibility Study on a Schröder Diffuser for Creating Homogeneous Microwave Fields, for Measuring Isotropic Stray Radiation Absorption Coefficients, 09 2016.
- [GJ97] Guo-Xin Fan and Jian-Ming Jin. Scattering from a cylindrically conformal slotted waveguide array antenna. *IEEE Transactions on Antennas and Propagation*, 45(7):1150–1159, July 1997.
- [GKL⁺06] G. Yu. Golubiatnikov, A. F. Krupnov, L. V. Lubyako, A. G. Luchinin, A. B. Pavelyev, M. I. Petelin, and A. Fernandez Curto. Gyrotron frequency control by a phase lock system. *Technical Physics Letters*, 32(8):650–652, Aug 2006.
- [GLM⁺92] G. Grieger, W. Lotz, P. Merkel, J. Nührenberg, J. Sapper, E. Strumberger, H. Wobig, R. Burhenn, V. Erckmann, U. Gasparino, L. Giannone, H. J. Hartfuss, R. Jaenicke, G. Kühner, H. Ringler, A. Weller, and F. Wagner. Physics optimization of stellarators. *Physics of Fluids B: Plasma Physics*, 4(7):2081–2091, 1992.
- [GM93] G. Grieger and I. Milch. Das fusionsexperiment wendelstein 7-x. *Physikalische Blätter*, 49(11):1001–1005, 1993.
- [GR95] R. J. Goldston and P. H. Rutherford. *Introduction to Plasma Physics (Plasma Physics Series)*. Routledge, 1995.
- [GRS⁺14] Patrick Gerland, Adrian E. Raftery, Hana Sevcíková, Nan Li, Danan Gu, Thomas Spoorenberg, Leontine Alkema, Bailey K.

- Fosdick, Jennifer Chunn, Nevena Lalic, Guiomar Bay, Thomas Buettner, Gerhard K. Heilig, and John Wilmoth. World population stabilization unlikely this century. *Science*, 346(6206), 2014.
- [Gru15] Joel Grus. *Data Science from Scratch*. O'Reilly, 2015.
- [HAB⁺07] M.A. Henderson, S. Alberti, P. Benin, T. Bonicelli, R. Chavan, D. Campbell, S. Cirant, G. Dammertz, O. Dormicchi, O. Dumbrajs, D. Fasel, T.P. Goodman, R. Heidinger, J.-P. Hogge, W. Kasparek, C. Lievin, B. Piosczyk, E. Poli, G. Ramponi, G. Saibene, O. Sauter, A. Serikov, G. Taddia, M. Thumm, M.Q. Tran, A.G.A. Verhoeven, and H. Zohm. Eu developments of the iter ecrh system. *Fusion Engineering and Design*, 82(5):454 – 462, 2007. Proceedings of the 24th Symposium on Fusion Technology.
- [HBB⁺13] Dag Hathiramani, Roland Binder, Rudolf Brakel, Torsten Broszat, Bertram Brucker, Antonino Cardella, Michael Endler, Klaus Grosser, Matthias Hirsch, Heinrich Laqua, and Stefan Thiel. Microwave stray radiation: Measures for steady state diagnostics at wendelstein 7-x. *Fusion Engineering and Design*, 88(6):1232 – 1235, 2013. Proceedings of the 27th Symposium On Fusion Technology (SOFT-27); Liège, Belgium, September 24-28, 2012.
- [HFH⁺96] R. S. Hemsworth, J.-H. Feist, M. Hanada, B. Heinemann, T. Inoue, E. Kussel, A. Krylov, P. Lotte, K. Miyamoto, N. Miyamoto, D. Murdoch, A. Nagase, Y. Ohara, Y. Okumura, J. Paméla, A. Panasenkov, K. Shibata, M. Tanii, and M. Watson. Neutral beams for iter (invited). *Review of Scientific Instruments*, 67(3):1120–1125, 1996.
- [HG03] Albrecht Herrmann and Otto Gruber. Chapter 1: Asdex upgrade - introduction and overview. *Fusion Science and Technology*, 44(3):569–577, 2003.
- [HMG⁺16] Christine Hennig, Josef Maier, Martin Grün, Jon Krom, Torsten Blum, Michael Grahl, Peter Heimann, Heike Riemann, Heike Laqua, Marc Lewerentz, Anett Spring, and Andreas Werner. Archivedb—scientific and technical data archive for wendelstein 7-x. *Fusion Engineering and Design*, 112:984 – 990, 2016.

- [Hol07] N. Holtkamp. An overview of the iter project. *Fusion Engineering and Design*, 82(5):427 – 434, 2007. Proceedings of the 24th Symposium on Fusion Technology.
- [HRY15] Li Han, Carlos E. Romero, and Zheng Yao. Wind power forecasting based on principle component phase space reconstruction. *Renewable Energy*, 81:737 – 744, 2015.
- [HTA08] R. S. Hemsworth, A. Tanga, and V. Antoni. Status of the iter neutral beam injection system (invited). *Review of Scientific Instruments*, 79(2):02C109, 2008.
- [IKF⁺17] S. Illy, P. C. Kalaria, J. Franck, K. A. Avramidis, G. Gantenbein, I. G. Pagonakis, M. Thumm, and J. Jelonnek. Investigation on misalignment tolerances of 240-ghz demo gyrotrons. In *2017 Eighteenth International Vacuum Electronics Conference (IVEC)*, pages 1–2, April 2017.
- [IKO⁺15] Ryosuke Ikeda, Ken Kajiwara, Yasuhisa Oda, Koji Takahashi, and Keishi Sakamoto. High-power and long-pulse operation of te31,11 mode gyrotron. *Fusion Engineering and Design*, 96-97:482 – 487, 2015. Proceedings of the 28th Symposium On Fusion Technology (SOFT-28).
- [IKUK14] Toshitaka Idehara, Alexei Kuleshov, Keisuke Ueda, and Eduard Khutoryan. Power-stabilization of high frequency gyrotrons using a double pid feedback control for applications to high power thz spectroscopy. *Journal of Infrared, Millimeter, and Terahertz Waves*, 35(2):159–168, Feb 2014.
- [IPP16] Angela merkel switches on wendelstein 7-x fusion device. Website, 2016.
- [ite19] Iter organization website, May 2019.
- [Jac99] John D. Jackson. *Classical Electrodynamics*. Wiley, New York, 1999.
- [Jel00] J. Jelonnek. *Untersuchung des Lastverhaltens von Gyrotrons*. PhD thesis, Technische Universität Hamburg-Harburg, 2000.
- [JGC⁺16] Junkai Ji, Shangce Gao, Jiujun Cheng, Zheng Tang, and Yuki Todo. An approximate logic neuron model with a dendritic structure. *Neurocomputing*, 173:1775 – 1783, 2016.

- [JGS99] J. Jelonnek, A. Grudiev, and K. Schunemann. Rigorous computation of time-dependent electromagnetic fields in gyrotron cavities excited by internal sources. *IEEE Transactions on Plasma Science*, 27(2):374–383, April 1999.
- [KAB⁺16] T Klinger, A Alonso, S Bozhenkov, R Burhenn, A Dinklage, G Fuchert, J Geiger, O Grulke, A Langenberg, M Hirsch, G Kocsis, J Knauer, A Krämer-Flecken, H Laqua, S Lazerson, M Landreman, H Maassberg, S Marsen, M Otte, N Pablant, E Pasch, K Rahbarnia, T Stange, T Szepesi, H Thomsen, P Traverso, J L Velasco, T Wauters, G Weir, and T Windisch and. Performance and properties of the first plasmas of wendelstein 7-x. *Plasma Physics and Controlled Fusion*, 59(1):014018, oct 2016.
- [KAB⁺19] Thomas Klinger, Tamara Andreeva, Sergey A Bozhenkov, Christian Brandt, Rainer Burhenn, Birger Buttenschön, Golo Fuchert, Benedikt Geiger, Olaf Grulke, Heinrich Peter Laqua, Novimir Antoniuk Pablant, Kian Rahbarnia, Torsten Stange, Adrian von Stechow, Naoki Tamura, H Thomsen, Thomas Wegner, and Rene Bussiahn. Overview of first wendelstein 7-x high-performance operation. *Nuclear Fusion*, 2019.
- [KAC⁺10] S. Kern, K. A. Avramides, A. R. Choudhury, O. Dumbrajs, G. Gantenbein, S. Illy, A. Samartsev, A. Schlaich, and M. Thumm. Simulation and experimental investigations on dynamic after cavity interaction (aci). In *35th International Conference on Infrared, Millimeter, and Terahertz Waves*, pages 1–2, Sep. 2010.
- [KBA92] Matthew B. Kennel, Reggie Brown, and Henry D. I. Abarbanel. Determining embedding dimension for phase-space reconstruction using a geometrical construction. *Phys. Rev. A*, 45:3403–3411, Mar 1992.
- [KBB⁺76] Charles D. Keeling, Robert B. Bacastow, Arnold E. Bainbridge, Carl A. Ekdahl Jr., Peter R. Guenther, Lee S. Waterman, and John F. S. Chin. Atmospheric carbon dioxide variations at mauna loa observatory, hawaii. *Tellus*, 28(6):538–551, 1976.
- [KBR⁺19] P. C. Kalaria, P. T. Brucker, S. Ruess, S. Illy, K. A. Avramidis, G. Gantenbein, M. Thumm, and J. Jclonck. Design studies of mini-channel cavity cooling for a 170 ghz, 2 mw coaxial-cavity

- gyrotron. In *2019 International Vacuum Electronics Conference (IVEC)*, pages 1–2, April 2019.
- [KBT04] M. V. Kartikeyan, E. Borie, and M. K. A. Thumm. *Gyrotrons: High Power Microwave and Millimeter Wave Technology*. Springer, 1 edition, 2004.
- [KDST85] K. E. Kreischer, B. G. Danly, J. B. Schutkeker, and R. J. Temkin. The design of megawatt gyrotrons. *IEEE Transactions on Plasma Science*, 13(6):364–373, Dec 1985.
- [Ker96] Stefan Kern. *Numerische Simulation der Gyrotron- Wechselwirkung in koaxialen Resonatoren*. PhD thesis, 1996. 31.04.02; LK 01; Karlsruhe 1996. (Wissenschaftliche Berichte. FZKA. 5837.) Fak. f. Elektrotechnik, Diss. v. 12.7.1996.
- [KIK⁺15] E. M. Khutoryan, T. Idehara, A. N. Kuleshov, Y. Tatematsu, Y. Yamaguchi, Y. Matsuki, and T. Fujiwara. Stabilization of gyrotron frequency by pid feedback control on the acceleration voltage. *Journal of Infrared, Millimeter, and Terahertz Waves*, 36(12):1157–1163, Dec 2015.
- [KIKN05] H Kishimoto, S Ishida, M Kikuchi, and H Ninomiya. Advanced tokamak research on JT-60. *Nuclear Fusion*, 45(8):986–1023, aug 2005.
- [KLT12] M. Kikuchi, K. Lackner, and M. Q. Tran. *Fusion Physics*, volume 43. International Atomic Energy Agency, 2012.
- [KMT⁺05] A. Kasugai, R. Minami, K. Takahashi, N. Kobayashi, and K. Sakamoto. Development of a 170ghz high-power and cw gyrotron for fusion application. In *2005 Joint 30th International Conference on Infrared and Millimeter Waves and 13th International Conference on Terahertz Electronics*, volume 1, pages 287–288 vol. 1, Sep. 2005.
- [KMT⁺06] A. Kasugai, R. Minami, K. Takahashi, N. Kobayashi, and K. Sakamoto. Long pulse operation of 170ghz iter gyrotron by beam current control. *Fusion Engineering and Design*, 81(23):2791 – 2796, 2006. Proceedings of the Fifteenth International toki Conference on Fusion and Advanced Technology.
- [KNNL04] Michael Kutner, Christopher Nachtsheim, John Neter, and William Li. *Applied Linear Statistical Models*. McGraw-Hill/Irwin, 5th edition edition, 2004.

- [KPT83] C. Koch, T. Poggio, and V. Torre. Nonlinear interactions in a dendritic tree: Localization, timing, and role in information processing. *Proc. Natl. Acad. Sci. USA*, 80:2799–2802, 1983.
- [KSF⁺09] S. Kern, A. Schlaich, J. Flamm, G. Gantenbein, G. Latsas, T. Rzesnicki, A. Samartsev, M. Thumm, and I. Tigelis. Investigations on parasitic oscillations in megawatt gyrotrons. In *2009 34th International Conference on Infrared, Millimeter, and Terahertz Waves*, pages 1–3, Sep. 2009.
- [KYI⁺10] A. Komori, H. Yamada, S. Imagawa, O. Kaneko, K. Kawahata, K. Mutoh, N. Ohyabu, Y. Takeiri, K. Ida, T. Mito, Y. Nagayama, S. Sakakibara, R. Sakamoto, T. Shimosuma, K. Y. Watanabe, O Motojima, and LHD Experiment Group. Goal and achievements of large helical device project. *Fusion Science and Technology*, 58(1):1–11, 2010.
- [LAA⁺15] M. Lehnen, K. Aleynikova, P.B. Aleynikov, D.J. Campbell, P. Drewelow, N.W. Eidielis, Yu. Gasparyan, R.S. Granetz, Y. Gribov, N. Hartmann, E.M. Hollmann, V.A. Izzo, S. Jachmich, S.-H. Kim, M. Kočan, H.R. Koslowski, D. Kovalenko, U. Kruezi, A. Loarte, S. Maruyama, G.F. Matthews, P.B. Parks, G. Pautasso, R.A. Pitts, C. Reux, V. Riccardo, R. Roccella, J.A. Snipes, A.J. Thornton, and P.C. de Vries. Disruptions in iter and strategies for their control and mitigation. *Journal of Nuclear Materials*, 463:39 – 48, 2015. PLASMA-SURFACE INTERACTIONS 21.
- [Lam96] James W. Lamb. Miscellaneous data on materials for millimetre and submillimetre optics. *International Journal of Infrared and Millimeter Waves*, 17(12):1997–2034, Dec 1996.
- [Law57] J. D. Lawson. Some criteria for a power producing thermonuclear reactor. *Proceedings of the Physical Society. Section B*, 70(1):6–10, January 1957.
- [LBB⁺18] Laqua, H.P., Baldzuhn, J., Braune, H., Bozhenkov, S., Brunner, K.J., Kazakov, Ye.O., Marsen, S., Moseev, D., Stange, T., Wolf, R.C., Zanini, M., and Wendelstein7-X Team. Overview of w7-x ecrh results in op1.2a. *EPJ Web Conf.*, 187:01011, 2018.
- [LG75] C. Lanczos and B. Gellai. Fourier analysis of random sequences. *Computers & Mathematics with Applications*, 1(3):269 – 276, 1975.

- [Lor63] Edward N. Lorenz. Deterministic nonperiodic flow. *Journal of the Atmospheric Sciences*, 20(2):130–141, 1963.
- [LSSD11] Josef Lutz, Heinrich Schlangenotto, Uwe Scheuermann, and Rik De Doncker. *Semiconductor Power Devices*. Springer, 2011.
- [LST11] Alexander Litvak, Keishi Sakamoto, and Manfred Thumm. Innovation on high-power long-pulse gyrotrons. *Plasma Physics and Controlled Fusion*, 53(12):124002, nov 2011.
- [MAD⁺15] Joe Milnes, Nizar Ben Ayed, Fahim Dhalla, Geoff Fishpool, John Hill, Ioannis Katramados, Richard Martin, Graham Naylor, Tom O’Gorman, and Rory Scannell. Mast upgrade – construction status. *Fusion Engineering and Design*, 96-97:42 – 47, 2015. Proceedings of the 28th Symposium On Fusion Technology (SOFT-28).
- [MBB⁺13] Paul McNeely, Marek Barlak, Jürgen Baldzuhn, Sergey Bozhenkov, Michael Drevlak, Grzegorz Gawlik, Bernd Heineemann, Dieter Holtum, Jacek Jagielski, Roland Kairys, Riccardo Nocentini, Rudolf Riedl, Peter Rong, Norbert Rust, Ralf Schroeder, Eckehart Speth, Albrecht Stäbler, Andrzej Turos, and Robert Wolf. Current status of the neutral beam heating system of w7-x. *Fusion Engineering and Design*, 88(6):1034 – 1037, 2013. Proceedings of the 27th Symposium On Fusion Technology (SOFT-27); Liège, Belgium, September 24-28, 2012.
- [MBH98] Michael E. Mann, Raymond S. Bradley, and Malcolm K. Hughes. Global-scale temperature patterns and climate forcing over the past six centuries. *Nature*, 392:779–787, 1998.
- [MCL⁺17] S. Marsen, Y. Corre, H.P. Laqua, V. Moncada, D. Moseev, H. Niemann, M. Preynas, and T. Stange and. First results from protective ECRH diagnostics for wendelstein 7-x. *Nuclear Fusion*, 57(8):086014, jun 2017.
- [MDZP⁺18] Valérie Masson-Delmotte, Panmao Zhai, Hans-Otto Pörtner, Debra Roberts, Jim Skea, Priyadarshi R. Shukla, Anna Pirani, Wilfran Moufouma-Okia, Clotilde Péan, Roz Pidcock, Sarah Connors, J. B. Robin Matthews, Yang Chen, Xiao Zhou, Melissa I. Gomis, Elisabeth Lonnoy, Tom Maycock, Melinda Tignor, and Tim Waterfield. Global warming of 1.5°C: An ipcc special report on the impacts of global warming of 1.5°C above pre-industrial

levels and related global greenhouse gas emission pathways, in the context of strengthening the global response to the threat of climate change, sustainable development, and efforts to eradicate poverty. Technical report, IPCC, 2018.

- [MG16] Andreas C. Mueller and Sarah Guido. *Introduction to Machine Learning with Python*. O'Reilly Media, Inc., 2016.
- [MKL⁺14] A. Messiaen, A. Krivska, F. Louche, J. Ongena, P. Dumortier, F. Durodie, D. Van Eester, and M. Vervier. Coupling and matching study of the icrf antenna for w7-x. *AIP Conference Proceedings*, 1580(1):354–357, 2014.
- [MLM⁺16] D. Moseev, H. P. Laqua, S. Marsen, T. Stange, H. Braune, V. Erckmann, F. Gellert, and J. W. Oosterbeek. Absolute calibration of sniffer probes on wendelstein 7-x. *Review of Scientific Instruments*, 87(8):083505, 2016.
- [MNP⁺16] V. E. Miasnikov, V. O. Nichiporenko, L. G. Popov, S. V. Usachev, and Y. M. Yashnov. Endurance of the highly heat-stressed units exposed to cycling loading in 1MW/170 GHz CW gyrotron for ITER. *IRMMW-THz*, 12 2016.
- [Mot15] O. Motojima. The ITER project construction status. *Nuclear Fusion*, 55(10):104023, oct 2015.
- [MS64] Syukuro Manabe and Robert F. Strickler. Thermal equilibrium of the atmosphere with a convective adjustment. *Journal of the Atmospheric Sciences*, 21(4):361–385, 1964.
- [MS11] Georg Michel and Jürgen Sachtleben. An integrated gyrotron controller. *Fusion Engineering and Design*, 86(6):776 – 779, 2011. Proceedings of the 26th Symposium of Fusion Technology (SOFT-26).
- [MSS⁺19] D. Moseev, M. Stejner, T. Stange, I. Abramovic, H. P. Laqua, S. Marsen, N. Schneider, H. Braune, U. Hoefel, W. Kasparek, S. B. Korsholm, C. Lechte, F. Leipold, S. K. Nielsen, M. Salewski, J. Rasmussen, M. Weißgerber, and R. C. Wolf. Collective thomson scattering diagnostic at wendelstein 7-x. *Review of Scientific Instruments*, 90(1):013503, 2019.
- [Mue] Personal discussion with the Ampegon employee Mr. Mühle responsible for maintenance and upgrade of the high-voltage power supplies.

- [MWB⁺19] S. Marsen, F. Wilde, H. Braune, K. J. Brunner, H. P. Laqua, D. Moseev, N. Schneider, T. Stange, and W7-X Team. Reliability of the w7-x ecrh plant: Experience from the first experimental campaigns. 31th Russian-German Workshop on Gyrotrons, June 2019.
- [MWC⁺17] S. Marsen, F. Wilde, Y. Corre, H. P. Laqua, V. Moncada, D. Moseev, H. Niemann, T. Stange, and W7-X Team. Control and protection system for the w7-x ecrh plant - experience from the first and plans for the next campaign. *27th IEEE Symposium On Fusion Engineering (SOFE), Shanghai, China*, 2017.
- [NAH⁺90] H. Ninomiya, T. Ando, T. Horie, H. Horiike, K. Koizumi, T. Kushima, M. Matsukawa, Y. Neyatani, and M. Yamamoto. Jt-60 upgrade device for confinement and steady state studies. *Plasma Devices and Operations*, 1(1):43–65, 1990.
- [ND97] G. S. Nusinovich and O. Dumbrajs. Technical noise in gyrokystrons and phase-locked gyrotron oscillators. *Physics of Plasmas*, 4(5):1424–1433, 1997.
- [NSA⁺06] G. S. Nusinovich, O. V. Sinitsyn, T. M. Antonsen, A. N. Vlasov, S. R. Cauffman, and K. L. Felch. Slow processes in startup scenarios of long-pulse gyrotrons. *Physics of Plasmas*, 13(8):083106, 2006.
- [NSV⁺04] G. S. Nusinovich, O. V. Sinitsyn, L. Velikovich, M. Yeddulla, T. M. Antonsen, A. N. Vlasov, S. R. Cauffman, and K. Felch. Startup scenarios in high-power gyrotrons. *IEEE Transactions on Plasma Science*, 32(3):841–852, June 2004.
- [NT91] H.-U. Nickel and M. Thumm. Plane transverse waveguide windows: survey of formulas for reflection, transmission, and absorption. In Minh Quang Tran, editor, *16th International Conference on Infrared and Millimeter Waves*, volume 1576, pages 499 – 500. International Society for Optics and Photonics, SPIE, 1991.
- [Nus81] G. S. Nusinovich. Mode interaction in gyrotrons. *International Journal of Electronics*, 51(4):457–474, 1981.
- [Nus99] G. S. Nusinovich. Review of the theory of mode interaction in gyrodevices. *IEEE Transactions on Plasma Science*, 27(2):313–326, April 1999.

- [Nus04] G. S. Nusinovich. *Introduction to the Physics of Gyrotrons*. The John Hopkins University Press, 2004.
- [NZ86] J. Nührenberg and R. Zille. Stable stellarators with medium β and aspect ratio. *Physics Letters A*, 114(3):129 – 132, 1986.
- [OHA⁺11] T. Omori, M.A. Henderson, F. Albajar, S. Alberti, U. Baruah, T.S. Bigelow, B. Beckett, R. Bertizzolo, T. Bonicelli, A. Bruschi, J.B. Caughman, R. Chavan, S. Cirant, A. Collazos, D. Cox, C. Darbos, M.R. de Baar, G. Denisov, D. Farina, F. Gandini, T. Gassmann, T.P. Goodman, R. Heidinger, J.P. Hogge, S. Illy, O. Jean, J. Jin, K. Kajiwara, W. Kasperek, A. Kasugai, S. Kern, N. Kobayashi, H. Kumric, J.D. Landis, A. Moro, C. Nazare, Y. Oda, I. Pagonakis, B. Piosczyk, P. Platania, B. Plaum, E. Poli, L. Porte, D. Purohit, G. Ramponi, S.L. Rao, D.A. Rasmussen, D.M.S. Ronden, T. Rzesnicki, G. Saibene, K. Sakamoto, F. Sanchez, T. Scherer, M.A. Shapiro, C. Sozzi, P. Spaeh, D. Strauss, O. Sauter, K. Takahashi, R.J. Temkin, M. Thumm, M.Q. Tran, V.S. Udintsev, and H. Zohm. Overview of the iter ec h&cd system and its capabilities. *Fusion Engineering and Design*, 86(6):951 – 954, 2011. Proceedings of the 26th Symposium of Fusion Technology (SOFT-26).
- [OIT⁺12] I. Ogawa, R. Ikeda, Y. Tatematsu, T. Idehara, and T. Saito. Stabilization of gyrotron output power using feedback control. In *2012 37th International Conference on Infrared, Millimeter, and Terahertz Waves*, pages 1–2, Sep. 2012.
- [OMVE⁺14] J. Ongena, A. Messiaen, D. Van Eester, B. Schweer, P. Dumortier, F. Durodie, Ye. O. Kazakov, F. Louche, M. Vervier, R. Koch, A. Krivska, A. Lysoivan, M. Van Schoor, T. Wauters, V. Borsuk, O. Neubauer, O. Schmitz, G. Offermans, Y. Altenburg, C. Baylard, D. Birus, S. Bozhenkov, D. A. Hartmann, J. P. Kallmeyer, S. Renard, R. C. Wolf, and T. Fülöp. Study and design of the ion cyclotron resonance heating system for the stellarator wendelstein 7-x. *Physics of Plasmas*, 21(6):061514, 2014.
- [PAA⁺19] Pagonakis, Ioannis, Alberti, Stefano, Avramidis, Konstantinos, Legrand, Francois, Gantenbein, Gerd, Genoud, Jérémy, Hogge, Jean-Philippe, Illy, Stefan, Ioannidis, Zisis, Kalaria, Parth, Piosczyk, Bernhard, Ruess, Sebastian, Ruess, Tobias, Rzesnicki,

- Tomasz, Tran, Minh-Quang, Tran+, Trach-Minh, Thumm, Manfred, Vomvouridis, Ioannis, and Jelonnek, John. Overview on recent progress in magnetron injection gun theory and design for high power gyrotrons. *EPJ Web Conf.*, 203:04011, 2019.
- [Pag] I. Gr. Pagonakis. Personal communication.
- [PAH+98] M. Pedrozzi, S. Alberti, J. P. Hogge, M. Q. Tran, and T. M. Tran. Electron beam instabilities in gyrotron beam tunnels. *Physics of Plasmas*, 5(6):2421–2430, 1998.
- [PBC+18] D. Ponce, R. Brambila, M. Cengher, Y. Gorelov, W. Grosnickle, J. Lohr, and A. Torrezan. Interrupting an imminent body current fault and restoring full power in milliseconds on a diiii-d national fusion facility gyrotron. *Fusion Science and Technology*, 73(1):1–4, 2018.
- [PCFS80] N. H. Packard, J. P. Crutchfield, J. D. Farmer, and R. S. Shaw. Geometry from a time series. *Phys. Rev. Lett.*, 45:712–716, Sep 1980.
- [PdVH+18] G. Pautasso, P.C. de Vries, D. Humphreys, M. Lehnen, C. Rapson, G. Raupp, J.A. Snipes, W. Treutterer, A. Vergara-Fernandez, and L. Zabeo. The ITER disruption mitigation trigger: developing its preliminary design. *Nuclear Fusion*, 58(3):036011, jan 2018.
- [PIDT96] B. Piosczyk, C. T. Iatrou, G. Dammertz, and M. Thumm. Single-stage depressed collectors for gyrotrons. *IEEE Transactions on Plasma Science*, 24(3):579–585, June 1996.
- [PIT16] Ioannis Gr. Pagonakis, Stefan Illy, and Manfred Thumm. Influence of emitter ring manufacturing tolerances on electron beam quality of high power gyrotrons. *Physics of Plasmas*, 23(8):083103, 2016.
- [PLT+11] D. Ponce, J. Lohr, J.F. Tooker, R.C. O’Neill, C.P. Moeller, J.L. Doane, S. Noraky, K. Dubovenko, Y.A. Gorelov, M. Cengher, B.G. Penaflo, and R.A. Ellis. Ech system developments including the design of an intelligent fault processor on the diiii-d tokamak. *Fusion Engineering and Design*, 86(6):785 – 788, 2011. Proceedings of the 26th Symposium of Fusion Technology (SOFT-26).

- [POL⁺16] T. Sunn Pedersen, M. Otte, S. Lazerson, P. Helander, S. Bozhnikov, C. Biedermann, T. Klinger, R. C. Wolf, H. S. Bosch, and The Wendelstein 7-X Team. Confirmation of the topology of the wendelstein 7-x magnetic field to better than 1:100,000. *Nature Communications*, 7(13493), 2016.
- [Poz05] D. M. Pozar. *Microwave Engineering*. John Wiley & Sons, 2005.
- [PPZ⁺16] Ioannis Gr. Pagonakis, Bernhard Piosczyk, Jianhua Zhang, Stefan Illy, Tomasz Rzesnicki, Jean-Philippe Hogge, Konstantinos Avramidis, Gerd Gantenbein, Manfred Thumm, and John Jelonnek. Electron trapping mechanisms in magnetron injection guns. *Physics of Plasmas*, 23(2):023105, 2016.
- [PS98] M. Petirsh and A. Schwab. Improving a mode-stirred chamber utilizing acoustic diffusers. In *1998 IEEE EMC Symposium. International Symposium on Electromagnetic Compatibility. Symposium Record (Cat. No.98CH36253)*, volume 1, pages 39–43 vol.1, Aug 1998.
- [PS99] W. Petirsch and A. J. Schwab. Investigation of the field uniformity of a mode-stirred chamber using diffusers based on acoustic theory. *IEEE Transactions on Electromagnetic Compatibility*, 41(4):446–451, Nov 1999.
- [PV04] J. G. Pagonakis and J. L. Vomvoridis. The self-consistent 3d trajectory electrostatic code ariadne for gyrotron beam tunnel simulation. In *Infrared and Millimeter Waves, Conference Digest of the 2004 Joint 29th International Conference on 2004 and 12th International Conference on Terahertz Electronics, 2004.*, pages 657–658, Sep. 2004.
- [PW05] A. Pironti and M. Walker. Fusion, tokamaks, and plasma control: an introduction and tutorial. *IEEE Control Systems Magazine*, 25(5):30–43, Oct 2005.
- [RAG⁺18] T. Rzesnicki, K. A. Avramidis, G. Gantenbein, S. Illy, Z. C. Joannidis, J. Jin, I. G. Pagonakis, S. Ruess, T. Ruess, M. Schmid, M. Thumm, J. Weggen, and J. Jelonnek. Development and first operation of the 170 ghz, 2 mw longer-pulse coaxial-cavity modular gyrotron prototype at kit. In *2018 43rd International Conference on Infrared, Millimeter, and Terahertz Waves (IRMMW-THz)*, pages 1–2, Sep. 2018.

- [RBK85] P.H. Rebut, R.J. Bickerton, and B.E. Keen. The joint european torus: installation, first results and prospects. *Nuclear Fusion*, 25(9):1011–1022, sep 1985.
- [RC14] Amitavo Roy Choudhury. *Investigations of after cavity interaction in gyrotrons including the effect of non-uniform magnetic field*. PhD thesis, Karlsruhe, 2014. Zugl.: Karlsruhe, KIT, Diss., 2013.
- [REGK98] M Romé, V Erckmann, U Gasparino, and N Karulin. Electron cyclotron resonance heating and current drive in the w7-x stellarator. *Plasma Physics and Controlled Fusion*, 40(4):511–530, apr 1998.
- [RGI⁺13] T. Rzesnicki, G. Gantenbein, S. Illy, J. Jelonnek, J. Jin, I. G. Pagonakis, B. Piosczyk, A. Schlaich, and M. Thumm. 2 mw, 170 ghz coaxial-cavity short-pulse gyrotron - investigations on electron beam instabilities and parasitic oscillations. In *2013 38th International Conference on Infrared, Millimeter, and Terahertz Waves (IRMMW-THz)*, pages 1–2, Sep. 2013.
- [RGI⁺17] S. Ruess, G. Gantenbein, S. Illy, T. Kobarg, I. G. Pagonakis, T. Rzesnicki, M. Thumm, J. Weggen, and J. Jelonnek. Tolerance studies on an inverse magnetron injection gun for a 2-mw 170-ghz coaxial-cavity gyrotron. *IEEE Transactions on Electron Devices*, 64(9):3870–3876, Sep. 2017.
- [RGJ⁺14] T. Rzesnicki, G. Gantenbein, J. Jelonnek, J. Jin, I. G. Pagonakis, B. Piosczyk, A. Samartsev, A. Schlaich, and M. Thumm. 2 mw, 170 ghz coaxial-cavity short-pulse gyrotron — single stage depressed collector operation. In *2014 39th International Conference on Infrared, Millimeter, and Terahertz waves (IRMMW-THz)*, pages 1–2, Sep. 2014.
- [SBB⁺19] E.J. Strait, J.L. Barr, M. Baruzzo, J.W. Berkery, R.J. Buttery, P.C. de Vries, N.W. Eidietis, R.S. Granetz, J.M. Hanson, C.T. Holcomb, D.A. Humphreys, J.H. Kim, E. Kolemen, M. Kong, M.J. Lanctot, M. Lehnen, E. Lerche, N.C. Logan, M. Maraschek, M. Okabayashi, J.K. Park, A. Pau, G. Pautasso, F.M. Poli, C. Rea, S.A. Sabbagh, O. Sauter, E. Schuster, U.A. Sheikh, C. Sozzi, F. Turco, A.D. Turnbull, Z.R. Wang, W.P. Wehner, and L. Zeng. Progress in disruption prevention for ITER. *Nuclear Fusion*, 59(11):112012, jun 2019.

- [SBC⁺16] B. Schunke, D. Boilson, J. Chareyre, C.-H. Choi, H. Decamps, A. El-Ouazzani, F. Geli, J. Graceffa, R. Hemsworth, M. Kushwah, K. Roux, D. Shah, M. Singh, L. Svensson, and M. Urbani. Overview of the negative ion based neutral beam injectors for iter. *Review of Scientific Instruments*, 87(2):02C101, 2016.
- [SBG⁺01] V. D. Shafranov, B. D. Bondarenko, G. A. Goncharov, O. A. Lavrent'ev, and A. D. Sakharov. On the history of the research into controlled thermonuclear fusion. *Phys. Usp.*, 44(8):835–843, 2001.
- [SCG⁺11] A. Schlaich, A. R. Choudhury, G. Gantenbein, S. Illy, S. Kern, C. Liévin, A. Samartsev, and M. Thumm. Examination of parasitic after-cavity oscillations in the w7-x series gyrotron sn4r. In *2011 International Conference on Infrared, Millimeter, and Terahertz Waves*, pages 1–2, Oct 2011.
- [Sch75] M. R. Schroeder. Diffuse sound reflection by maximumlength sequences. *The Journal of the Acoustical Society of America*, 57(1):149–150, 1975.
- [Sch79] M. R. Schroeder. Binaural dissimilarity and optimum ceilings for concert halls: More lateral sound diffusion. *The Journal of the Acoustical Society of America*, 65(4):958–963, 1979.
- [Sch95] F C Schuller. Disruptions in tokamaks. *Plasma Physics and Controlled Fusion*, 37(11A):A135–A162, nov 1995.
- [Sch15] A. Schlaich. *Time-dependent spectrum analysis of high power gyrotrons*. PhD thesis, Karlsruhe Institute of Technology, 2015.
- [SCP⁺14] A. Schlaich, Chuanren Wu, I. Pagonakis, K. A. Avramidis, S. Illy, G. Gantenbein, J. Jelonnek, and M. Thumm. Separation of thermal expansion and beam charge neutralization effects in high power 140 ghz cw gyrotrons. In *2014 IEEE 41st International Conference on Plasma Sciences (ICOPS) held with 2014 IEEE International Conference on High-Power Particle Beams (BEAMS)*, pages 1–1, May 2014.
- [SDG⁺13] A. Samartsev, G. Dammertz, G. Gantenbein, J. Jelonnek, S. Illy, and M. Thumm. Influence of annular beam displacement on the performance of a high-power gyrotron. *IEEE Transactions on Plasma Science*, 41(4):872–878, April 2013.

- [SDP06] F. Sartori, G. de Tommasi, and F. Piccolo. The joint european torus. *IEEE Control Systems Magazine*, 26(2):64–78, April 2006.
- [SFG⁺10] A. Schlaich, J. Flamm, G. Gantenbein, S. Kern, G. Latsas, T. Rzesnicki, A. Samartsev, M. Thumm, and I. Tigelis. 2.4: Investigations on parasitic oscillations in megawatt gyrotrons. In *2010 IEEE International Vacuum Electronics Conference (IVEC)*, pages 33–34, May 2010.
- [SG64] Abraham. Savitzky and M. J. E. Golay. Smoothing and differentiation of data by simplified least squares procedures. *Analytical Chemistry*, 36(8):1627–1639, 1964.
- [SGI⁺15] A. Schlaich, G. Gantenbein, S. Illy, J. Jelonnek, and M. Thumm. Observation of discrete frequency hopping in mw-class gyrotrons during long-pulse operation. *IEEE Transactions on Electron Devices*, 62(9):3049–3055, Sep. 2015.
- [SGJT13a] A. Schlaich, G. Gantenbein, J. Jelonnek, and M. Thumm. Simulations of high power gyrotron operation during window arc. In *2013 38th International Conference on Infrared, Millimeter, and Terahertz Waves (IRMMW-THz)*, pages 1–2, Sep. 2013.
- [SGJT13b] A. Schlaich, G. Gantenbein, J. Jelonnek, and M. Thumm. Transient millimeter-wave signal analysis with unambiguous rf spectrum reconstruction. *IEEE Transactions on Microwave Theory and Techniques*, 61(12):4660–4666, Dec 2013.
- [Sha48a] C. E. Shannon. A mathematical theory of communication. *The Bell System Technical Journal*, 27(3):379–423, July 1948.
- [Sha48b] C. E. Shannon. A mathematical theory of communication. *The Bell System Technical Journal*, 27(4):623–656, Oct 1948.
- [Sha06] Cosma Rohilla Shalizi. *Methods and Techniques of Complex Systems Science: An Overview*, pages 33–114. Springer US, Boston, MA, 2006.
- [SID⁺07] M. Schmid, S. Illy, G. Dammertz, V. Erckmann, and M. Thumm. Transverse field collector sweep system for high power cw gyrotrons. *Fusion Engineering and Design*, 82(5):744–750, 2007. Proceedings of the 24th Symposium on Fusion Technology.
- [SJF02] B. Sivakumar, A.W. Jayawardena, and T.M.K.G. Fernando. River flow forecasting: use of phase-space reconstruction and

- artificial neural networks approaches. *Journal of Hydrology*, 265(1):225 – 245, 2002.
- [SKT⁺07] Keishi Sakamoto, Atsushi Kasugai, Koji Takahashi, Ryutaro Minami, Noriyuki Kobayashi, and Ken Kajiwara. Achievement of robust high-efficiency 1 mw oscillation in the hard-self-excitation region by a 170 ghz continuous-wave gyrotron. *Nature Physics*, 3:411–414, 2007.
- [SLB⁺17] Stange, Torsten, Laqua, Heinrich Peter, Beurskens, Marc, Bosch, Hans-Stephan, Bozhenkov, Sergey, Brakel, Rudolf, Braune, Harald, Brunner, Kai Jakob, Cappa, Alvaro, Dinklage, Andreas, Erckmann, Volker, Fuchert, Golo, Gantenbein, Gerd, Gellert, Florian, Grulke, Olaf, Hartmann, Dirk, Hirsch, Matthias, Höfel, Udo, Kasperek, Walter, Knauer, Jens, Langenberg, Andreas, Marsen, Stefan, Marushchenko, Nikolai, Moseev, Dmitry, Pablant, Novomir, Pasch, Ekkehard, Rahbarnia, Kian, Mora, Humberto Trimino, Tsujimura, Toru, Turkin, Yuriy, Wauters, Tom, and Wolf, Robert. Advanced electron cyclotron heating and current drive experiments on the stellarator wendelstein 7-x. *EPJ Web Conf.*, 157:02008, 2017.
- [SNA12] O. V. Sinitsyn, G. S. Nusinovich, and T. M. Antonsen. Stability of gyrotron operation in very high-order modes. *Physics of Plasmas*, 19(6):063114, 2012.
- [SPB10] H. R. Strauss, R. Paccagnella, and J. Breslau. Wall forces produced during iter disruptions. *Physics of Plasmas*, 17(8):082505, 2010.
- [Spi58] Lyman Spitzer. The stellarator concept. *The Physics of Fluids*, 1(4):253–264, 1958.
- [Spi06] Lyman Spitzer. *Physics of Fully Ionized Gases*. Dover Publications, 2006.
- [SSE⁺17] Erich Schubert, Jörg Sander, Martin Ester, Hans Peter Kriegel, and Xiaowei Xu. Dbscan revisited, revisited: Why and how you should (still) use dbscan. *ACM Trans. Database Syst.*, 42(3), July 2017.
- [SW18] Wei Sun and Yuwei Wang. Short-term wind speed forecasting based on fast ensemble empirical mode decomposition,

- phase space reconstruction, sample entropy and improved back-propagation neural network. *Energy Conversion and Management*, 157:1 – 12, 2018.
- [SWP⁺15] Andreas Schlaich, Chuanren Wu, Ioannis Pagonakis, Konstantinos Avramidis, Stefan Illy, Gerd Gantenbein, John Jelonnek, and Manfred Thumm. Frequency-based investigation of charge neutralization processes and thermal cavity expansion in gyrotrons. *Journal of Infrared, Millimeter, and Terahertz Waves*, 36(9):797–818, Sep 2015.
- [TAA⁺07] M. Thumm, S. Alberti, A. Arnold, P. Brand, H. Braune, G. Dammertz, V. Erckmann, G. Gantenbein, E. Giguet, R. Heidinger, J. Hogge, S. Illy, W. Kasperek, H. P. Laqua, F. Legrand, W. Leonhardt, C. Lievin, G. Michel, G. Neffe, B. Piosczyk, M. Schmid, K. Schworer, and M. Q. Tran. Eu megawatt-class 140-ghz cw gyrotron. *IEEE Transactions on Plasma Science*, 35(2):143–153, April 2007.
- [Tak81] Floris Takens. Detecting strange attractors in turbulence. In David Rand and Lai-Sang Young, editors, *Dynamical Systems and Turbulence, Warwick 1980*, pages 366–381, Berlin, Heidelberg, 1981. Springer Berlin Heidelberg.
- [TBB⁺08] M. Thumm, P. Brand, H. Braune, G. Dammertz, V. Erckmann, G. Gantenbein, S. Illy, W. Kasperek, H. P. Laqua, C. Lechte, W. Leonhardt, G. Michel, G. Neffe, B. Piosczyk, M. Schmid, and M. Weissgerber. Progress in the 10-mw 140-ghz ech system for the stellarator w7-x. *IEEE Transactions on Plasma Science*, 36(2):341–355, April 2008.
- [TDST19] Manfred Thumm, G G Denisov, Keishi Sakamoto, and Minh Quang Tran. High-power gyrotrons for electron cyclotron heating and current drive. *Nuclear Fusion*, 2019.
- [Thu97] M. K. Thumm. *Generation and Application of High Power Microwaves*, chapter Modes and mode conversion in microwave devices, pages 121–71. The Scottish Universities Summer School in Physics and Institute of Physics Publishing, 1997.
- [Thu11] M. Thumm. Progress on gyrotrons for iter and future thermonuclear fusion reactors. *IEEE Transactions on Plasma Science*, 39(4):971–979, April 2011.

- [Thu14] M. Thumm. Recent advances in the worldwide fusion gyrotron development. *IEEE Transactions on Plasma Science*, 42(3):590–599, March 2014.
- [Thu15] Manfred Thumm. State-of-the-art of high power gyro-devices and free electron masers. update 2014. (kit scientific reports ; 7693). Technical report, Karlsruher Institut für Technologie (KIT), 2015. 31.10.01; LK 01.
- [Thu20] Manfred Thumm. State-of-the-Art of High-Power Gyro-Devices and Free Electron Masers. *J Infrared Milli Terahz Waves*, 41:1–140, 2020.
- [TKSX18] J. Tak, A. Kantemur, Y. Sharma, and H. Xin. A 3-d-printed w-band slotted waveguide array antenna optimized using machine learning. *IEEE Antennas and Wireless Propagation Letters*, 17(11):2008–2012, Nov 2018.
- [TNN⁺00] Y Takeiri, Y Nakamura, N Noda, M Osakabe, K Kawahata, Y Oka, O Kaneko, K Tsumori, M Sato, T Mutoh, T Shimozuma, M Goto, K Ida, S Inagaki, S Kado, S Masuzaki, S Morita, Y Nagayama, K Narihara, B J Peterson, S Sakakibara, K Sato, M Shoji, K Tanaka, P C de Vries, S Sudo, N Ohyabu, and O Motojima. Plasma characteristics of long-pulse discharges heated by neutral beam injection in the large helical device. *Plasma Physics and Controlled Fusion*, 42(2):147–159, jan 2000.
- [Tsi01] Sh.E. Tsimring. Gyrotron electron beams: Velocity and energy spread and beam instabilities. *International Journal of Infrared and Millimeter Waves*, 22(10):1433–1468, Oct 2001.
- [Tsi07] Shulim E. Tsimring. *Electron beams and microwave vacuum electronics*. Wiley, 2007.
- [TSK⁺10] H. Takahashi, T. Shimozuma, S. Kubo, S. Ito, S. Kobayashi, Y. Yoshimura, H. Igami, Y. Mizuno, Y. Takita, T. Mutoh, T. Kariya, R. Minami, and T. Imai. The development of a 77-ghz, 1-mw ecrh system for the large helical device. *Fusion Science and Technology*, 57(1):19–26, 2010.
- [TYA⁺05] M. Thumm, X. Yang, A. Arnold, G. Dammertz, G. Michel, J. Pretterebner, and D. Wagner. A high-efficiency quasi-optical mode converter for a 140-ghz 1-mw cw gyrotron. *IEEE Transactions on Electron Devices*, 52(5):818–824, May 2005.

- [WAA⁺17] R.C. Wolf, A. Ali, A. Alonso, J. Baldzuhn, C. Beidler, M. Beurskens, C. Biedermann, H.-S. Bosch, S. Bozhenkov, R. Brakel, A. Dinklage, Y. Feng, G. Fuchert, J. Geiger, O. Grulke, P. Helander, M. Hirsch, U. Höfel, M. Jakubowski, J. Knauer, G. Kocsis, R. König, P. Kornejew, A. Krämer-Flecken, M. Krychowiak, M. Landreman, A. Langenberg, H.P. Laqua, S. Lazerson, H. Maassberg, S. Marsen, M. Marushchenko, D. Moseev, H. Niemann, N. Pablant, E. Pasch, K. Rahbarnia, G. Schlisio, T. Stange, T. Sunn Pedersen, J. Svensson, T. Szepesi, H. Trimino Mora, Y. Turkin, T. Wauters, G. Weir, U. Wenzel, T. Windisch, G. Wurden, D. Zhang, I. Abramovic, S. Äkäs-lompolo, P. Aleynikov, K. Aleynikova, R. Alzbutas, G. Anda, T. Andreeva, E. Ascasibar, J. Assmann, S.-G. Baek, M. Banduch, T. Barbui, M. Barlak, K. Baumann, W. Behr, A. Bendorf, O. Bertuch, W. Biel, D. Birus, B. Blackwell, E. Blanco, M. Blatzheim, T. Bluhm, D. Böckenhoff, P. Bolgert, M. Borchardt, V. Borsuk, J. Boscary, L.-G. Böttger, H. Brand, Ch. Brandt, T. Bräuer, H. Braune, S. Brezinsek, K.-J. Brunner, B. Brünner, R. Burhenn, B. Buttenschön, V. Bykov, I. Calvo, B. Cannas, A. Cappa, A. Carls, L. Carraro, B. Carvalho, F. Castejon, A. Charl, F. Chernyshev, M. Cianciosa, R. Citarella, Ł. Ciupiński, G. Claps, M. Cole, M.J. Cole, F. Cordella, G. Cseh, A. Czarnecka, A. Czermak, K. Czerski, M. Czerwinski, G. Czymek, A. da Molin, A. da Silva, G. Dammertz, J. Danielson, A. de la Pena, S. Degenkolbe, P. Denner, D.P. Dhard, M. Dostal, M. Drevlak, P. Drewelow, Ph. Drews, A. Dudek, G. Dundulis, F. Durodie, P. van Eeten, F. Effenberg, G. Ehrke, M. Endler, D. Ennis, E. Erckmann, H. Esteban, T. Estrada, N. Fahrenkamp, J.-H. Feist, J. Fellingner, H. Fernandes, W.H. Fietz, W. Figacz, J. Fontdecaba, O. Ford, T. Fornal, H. Frerichs, A. Freund, M. Führer, T. Funaba, A. Galkowski, G. Gantenbein, Y. Gao, J. García Regaña, M. Garcia-Munoz, D. Gates, G. Gawlik, B. Geiger, V. Giannella, N. Gierse, A. Gogoleva, B. Goncalves, A. Gorjaev, D. Gradic, M. Grahl, J. Green, A. Grosman, H. Grote, M. Gruca, C. Guerard, L. Haiduk, X. Han, F. Harberts, J.H. Harris, H.-J. Hartfuss, D. Hartmann, D. Hathiramani, B. Hein, B. Heinemann, P. Heitzenroeder, S. Henneberg, C. Hennig, J. Hernandez Sanchez, C. Hidalgo,

H. Hölbe, K.P. Hollfeld, A. Hölting, D. Höschen, M. Houry, J. Howard, X. Huang, M. Huber, V. Huber, H. Hunger, K. Ida, T. Ilkei, S. Illy, B. Israeli, A. Ivanov, S. Jablonski, J. Jagielski, J. Jelonnek, H. Jenzsch, P. Junghans, J. Kacmarczyk, T. Kalitka, J.-P. Kallmeyer, U. Kamionka, R. Karalevicius, H. Kasahara, W. Kasperek, N. Kenmochi, M. Keunecke, A. Khilchenko, D. Kinna, R. Kleiber, T. Klinger, M. Knaup, Th. Kobarg, F. Köchl, Y. Kolesnichenko, A. Könies, M. Köppen, J. Koshurinov, R. Koslowski, F. Köster, R. Koziol, M. Krämer, R. Krampitz, P. Kraszewsk, N. Krawczyk, T. Kremeyer, Th. Krings, J. Krom, G. Krzesinski, I. Ksiazek, M. Kubkowska, G. Kühner, T. Kurki-Suonio, S. Kwak, R. Lang, S. Langish, H. Laqua, R. Laube, C. Lechte, M. Lennartz, W. Leonhardt, L. Lewerentz, Y. Liang, Ch. Linsmeier, S. Liu, J.-F. Lobsien, D. Loesser, J. Loizu Cisuella, J. Lore, A. Lorenz, M. Losert, L. Lubyako, A. Lücke, A. Lumsdaine, V. Lutsenko, J. Majano-Brown, O. Marchuk, M. Mardenfeld, P. Marek, S. Massidda, S. Masuzaki, D. Maurer, K. McCarthy, P. McNeely, A. Meier, D. Mellein, B. Mendelewitsch, Ph. Mertens, D. Mikkelsen, O. Mishchenko, B. Missal, J. Mittelstaedt, T. Mizuuchi, A. Mollen, V. Moncada, T. Mönich, T. Morizaki, R. Munk, S. Murakami, F. Musielok, G. Náfrádi, M. Nagel, D. Naujoks, H. Neilson, O. Neubauer, U. Neuner, T. Ngo, R. Nocentini, C. Nührenberg, J. Nührenberg, S. Obermayer, G. Offermanns, K. Ogawa, J. Ongena, J.W. Oosterbeek, G. Orozco, M. Otte, L. Pacios Rodriguez, W. Pan, N. Panadero, N. Panadero Alvarez, A. Panin, D. Papenfuss, S. Paqay, A. Pavone, E. Pawelec, G. Pelka, X. Peng, V. Perseo, B. Peterson, A. Pieper, D. Pilopp, S. Pingel, F. Pisano, B. Plaum, G. Plunk, M. Povilaitis, J. Preinhaelter, J. Proll, M.-E. Puiatti, A. Puig Sitjes, F. Purps, M. Rack, S. Récsei, A. Reiman, D. Reiter, F. Rempffel, S. Renard, R. Riedl, J. Riemann, S. Rimkevicius, K. Risse, A. Rodatos, H. Röhlinger, M. Romé, P. Rong, H.-J. Roscher, B. Roth, L. Rudischhauser, K. Rummel, T. Rummel, A. Runov, N. Rust, L. Ryc, S. Ryosuke, R. Sakamoto, A. Samartsev, M. Sanchez, F. Sano, S. Satake, G. Satheeswaran, J. Schacht, F. Schauer, T. Scherer, A. Schlaich, K.-H. Schlüter, J. Schmitt, H. Schmitz, O. Schmitz, S. Schmuck, M. Schneider, W. Schneider, M. Scholz, P. Scholz, R. Schritt

twieser, M. Schröder, T. Schröder, R. Schroeder, H. Schumacher, B. Schweer, B. Shanahan, I.V. Shikhovtsev, M. Sibilia, P. Sinha, S. Sipliä, J. Skodzik, C. Slaby, H. Smith, W. Spiess, D.A. Spong, A. Spring, R. Stadler, B. Standley, L. Stephey, M. Stoneking, U. Stridde, Z. Sulek, C. Surko, Y. Suzuki, V. Szabó, T. Szabolics, Z. Szökefalvi-Nagy, N. Tamura, A. Terra, J. Terry, J. Thomas, H. Thomsen, M. Thumm, C.P. von Thun, D. Timmermann, P. Titus, K. Toi, J.M. Travere, P. Traverso, J. Tretter, H. Tsuchiya, T. Tsujimura, S. Tulipán, M. Turnyanskiy, B. Unterberg, J. Urban, E. Urbonavicius, I. Vakulchuk, S. Valet, B. van Millingen, L. Vela, J.-L. Velasco, M. Vergote, M. Vervier, N. Vianello, H. Viebke, R. Vilbrandt, A. Vorkörper, S. Wadle, F. Wagner, E. Wang, N. Wang, F. Warmer, L. Wegener, J. Weggen, Y. Wei, J. Wendorf, A. Werner, B. Wiegel, F. Wilde, E. Winkler, V. Winters, S. Wolf, J. Wolowski, A. Wright, P. Xanthopoulos, H. Yamada, I. Yamada, R. Yasuhara, M. Yokoyama, J. Zajac, M. Zarnstorff, A. Zeitler, H. Zhang, J. Zhu, M. Zilker, A. Zimbal, A. Zocco, S. Zoletnik, and M. Zuin. Major results from the first plasma campaign of the wendelstein 7-x stellarator. *Nuclear Fusion*, 57(10):102020, jul 2017.

[WA19]

R. C. Wolf, A. Alonso, S. Äkäslompolo, J. Baldzuhn, M. Beurskens, C. D. Beidler, C. Biedermann, H.-S. Bosch, S. Bozhentkov, R. Brakel, H. Braune, S. Brezinsek, K.-J. Brunner, H. Damm, A. Dinklage, P. Drewelow, F. Effenberg, Y. Feng, O. Ford, G. Fuchert, Y. Gao, J. Geiger, O. Grulke, N. Harder, D. Hartmann, P. Helander, B. Heinemann, M. Hirsch, U. Höfel, C. Hopf, K. Ida, M. Isobe, M. W. Jakubowski, Y. O. Kazakov, C. Killer, T. Klinger, J. Knauer, R. König, M. Krychowiak, A. Langenberg, H. P. Laqua, S. Lazerson, P. McNeely, S. Marsen, N. Marushchenko, R. Nocentini, K. Ogawa, G. Orozco, M. Osakabe, M. Otte, N. Pablant, E. Pasch, A. Pavone, M. Porkolab, A. Puig Sitjes, K. Rahbarnia, R. Riedl, N. Rust, E. Scott, J. Schilling, R. Schroeder, T. Stange, A. von Stechow, E. Strumberger, T. Sunn Pedersen, J. Svensson, H. Thomson, Y. Turkin, L. Vano, T. Wauters, G. Wurden, M. Yoshinuma, M. Zanini, and D. Zhang. Performance of wendelstein 7-x stellarator plasmas

- during the first divertor operation phase. *Physics of Plasmas*, 26(8):082504, 2019.
- [WBD⁺18] R C Wolf, S Bozhenkov, A Dinklage, G Fuchert, Y O Kazakov, H P Laqua, S Marsen, N B Marushchenko, T Stange, M Zanini, I Abramovic, A Alonso, J Baldzuhn, M Beurskens, C D Beidler, H Braune, K J Brunner, N Chaudhary, H Damm, P Drewelow, G Gantenbein, Yu Gao, J Geiger, M Hirsch, U Höfel, M Jakubowski, J Jelonnek, T Jensen, W Kasperek, J Knauer, S B Korsholm, A Langenberg, C Lechte, F Leipold, H Trimino Mora, U Neuner, S K Nielsen, D Moseev, H Oosterbeek, N Pablant, E Pasch, B Plaum, T Sunn Pedersen, A Puig Sitjes, K Rahbarnia, J Rasmussen, M Salewski, J Schilling, E Scott, M Stejner, H Thomsen, M Thumm, Y Turkin, and F Wilde and. Electron-cyclotron-resonance heating in wendelstein 7-x: A versatile heating and current-drive method and a tool for in-depth physics studies. *Plasma Physics and Controlled Fusion*, 61(1):014037, nov 2018.
- [WBDa16] F Warmer, C D Beidler, A Dinklage, and R Wolf and. From w7-x to a HELIAS fusion power plant: motivation and options for an intermediate-step burning-plasma stellarator. *Plasma Physics and Controlled Fusion*, 58(7):074006, jun 2016.
- [Wel67] P. Welch. The use of fast fourier transform for the estimation of power spectra: A method based on time averaging over short, modified periodograms. *IEEE Transactions on Audio and Electroacoustics*, 15(2):70–73, June 1967.
- [WHL⁺17] R. C. Wolf, D. Hartmann, H. P. Laqua, O. Neubauer, J. Ongena, and J. Baldzuhn. Heating and pellets. In *W7-X Workshop, Greifswald*. Max Planck Institute for Plasmaphysics, 04 2017.
- [WLGL17] Deyun Wang, Hongyuan Luo, Olivier Grunder, and Yanbing Lin. Multi-step ahead wind speed forecasting using an improved wavelet neural network combining variational mode decomposition and phase space reconstruction. *Renewable Energy*, 113:1345 – 1358, 2017.
- [WLM⁺17] F. Wilde, H. P. Laqua, S. Marsen, T. Stange, K. A. Avramidis, G. Gantenbein, J. Jelonnek, S. Illy, I. G. Pagonakis, and M. Thumm. Measurements of satellite modes in 140 ghz wendelstein 7-x gyrotrons: An approach to an electronic stability

- control. In *2017 Eighteenth International Vacuum Electronics Conference (IVEC)*, pages 1–2, April 2017.
- [WMS⁺19] F. Wilde, S. Marsen, T. Stange, D. Moseev, J.W. Oosterbeek, H.P. Laqua, R.C. Wolf, K. Avramidis, G. Gantenbein, I.Gr. Pagonakis, S. Illy, J. Jelonnek, M.K. Thumm, and W7-X team. Automated mode recovery for gyrotrons demonstrated at Wendelstein 7-X. *Fusion Engineering and Design*, 148:111258, 2019.
- [WSL⁺16] D. Wagner, J. Stober, F. Leuterer, F. Monaco, S. Müller, M. Münich, C. J. Rapson, M. Reich, M. Schubert, H. Schütz, W. Treutterer, H. Zohm, M. Thumm, T. Scherer, A. Meier, G. Gantenbein, J. Jelonnek, W. Kasperek, C. Lechte, B. Plaum, T. Goodman, A. G. Litvak, G. G. Denisov, A. Chirkov, V. Zapevalov, V. Malygin, L. G. Popov, V. O. Nichiporenko, V. E. Myasnikov, E. M. Tai, E. A. Solyanova, S. A. Malygin, and AS-DEX Upgrade Team. Status, operation, and extension of the ecrh system at asdex upgrade. *Journal of Infrared, Millimeter, and Terahertz Waves*, 37(1):45–54, Jan 2016.
- [Wu19] Chuanren Wu. *Conceptual Studies of Multistage Depressed Collectors for Gyrotrons*. PhD thesis, Karlsruher Institut für Technologie (KIT), 2019. 31.03.02; LK 01.
- [YEW14] H. L. Yap, A. Eftekhari, M. B. Wakin, and C. J. Rozell. A first analysis of the stability of takens' embedding. In *2014 IEEE Global Conference on Signal and Information Processing (GlobalSIP)*, pages 404–408, Dec 2014.
- [Zha16] Jianghua [VerfasserIn] Zhang. *Influence of emitter surface roughness and emission inhomogeneity on efficiency and stability of high power fusion gyrotrons*. Karlsruher Forschungsberichte aus dem Institut für Hochleistungsimpuls- und Mikrowellentechnik ; Band 9. KIT Scientific Publishing, Karlsruhe, 2016.
- [ZIP⁺17] J. Zhang, S. Illy, I. G. Pagonakis, T. Rzesnicki, K. A. Avramidis, A. Malygin, S. Ruess, A. Samartsev, G. Dammertz, B. Piosczyk, G. Gantenbein, M. Thumm, and J. Jelonnek. Evaluation and influence of gyrotron cathode emission inhomogeneity. *IEEE Transactions on Electron Devices*, 64(3):1315–1322, March 2017.

- [ZRZ16] Richard E. Zeebe, Andy Ridgwell, and James C. Zachos. Anthropogenic carbon release rate unprecedented during the past 66 million years. *Nature Geoscience*, 2016.

Acknowledgement

First of all I would like to thank sincerely my supervisors Prof. Dr.-Ing. J. Jelonnek at the Karlsruhe Institute of Technology and Dr. H. P. Laqua at the Max Planck Institute of Plasmaphysics for giving me the opportunity to work on such a challenging and innovative subject and their patient guidance, support and constructive criticism along this journey. I'd also like to express my deepest gratitude to Prof. Dr. R. C. Wolf for being the co-referee of this thesis and for his continuous support and supervision.

I'm deeply indebted to Dr. T. Stange and Dr. S. Marsen for the countless discussions, the practical suggestions and the successful collaboration in performing microwave measurements, the implementation of the gyrotron control algorithms and the proof-reading of this thesis.

I'd like to extend my deepest gratitude to Dr. K. Avramidis and Dr. I. Gr. Pagonakis for their moral support in general and for sharing their scientific expertise in particular with regard to numerous discussions related to various gyrotron interaction simulations.

Another much appreciated colleague is Dr. J. W. Oosterbeek who provided a first initial MATLAB script to compute the frequency response of a single dielectric window which inspired the Python code used in this thesis to develop the microwave filters for the stray radiation measurements.

Furthermore, i'd like to thank Prof. Dr. M. K. Thumm for his efforts in discussions and the proof-reading of this thesis and Dr. W. Kasperek from IGVP of the university of Stuttgart for his suggestions of how to possibly construct a D-band high-pass filter. Thanks should also go to Dr. S. Illy for coming up first with the idea to investigate the gyrotron stray radiation at the relief window.

Finally, i'd like to gratefully acknowledge the support of the institutes involved, the Max Planck Institute of Plasmaphysics (IPP) in Greifswald and the Institute for Pulsed Power and Microwave Technology (IHM) at the Karlsruhe Institute of Technology for allowing me to use their infrastructure and resources for this work.

I'd also like to mention that i had the pleasure to work with the gyrotron operators N. Schneider, F. Noke and F. Purps who proved themselves to be very patient even in performing repetitive and tedious gyrotron experiments during a lot of days for this thesis. Thanks goes also to M. Radau and S. Moseev of the administrative staff of E3 at IPP who always helped me patiently with any bureaucratic issue and carefully prepared every business travel. The same holds true of course for M. Huber and M. Mai of IHM at KIT who i'd like to thank for all their efforts.

At the end of this acknowledgement, i'd like to mention the people who are important to me and to whom this thesis is dedicated. Without their friendship, their moral and emotional support, this thesis wouldn't exist.

I owe a big part of my motivation and morale support for this work to my colleagues in Karlsruhe and Greifswald:

I'd like to thank my office mate Joachim Franck in Karlsruhe for his company and friendship together with Sebastian Ruess, Chuanren Wu, Parth Kalaria, Vasilis Ramopoulos and others for their company and conversations during our lunch breaks. I want to thank my office mate Udo Hoefel for his company in Greifswald while working till nine or ten o'clock in the evening. I also would like to thank him for the fruit- and insightful conversations about politics, philosophy and mathematics, we had. I'm grateful for the time spent together and the friendship of my colleagues Lukas Boettger, Lukas Rudischhauser and Daniel Böckenhoff. Furthermore i want to thank my friends Tiziano Fulceri and Marco Zanini for the company during numerous lunch and coffee breaks, the discussions about emerging gravitation and space-time or history and politics respectively. They reminded me often to take care of myself and to take a break for that reason.

And finally and most importantly, i owe a lot to those who were closest to me during this time:

I owe my grandparents a lot who always supported me, who covered my university fees as a student, even if they didn't understand what i was studying and why. I have to thank my old friends from school in Hannover who never ceased to believe in me and who were there to support me. And finally and most importantly, i owe my deepest gratitude to Katharina for her relentless empathic and supportive attitude, her emotional support and affection even during my darkest times.

Your life is your life

(...)

Be on the watch.

There are ways out.

There is light somewhere.

It may not be much light but

it beats the darkness.

(...)

The Laughing Heart, Charles Bukowski